INVESTIGATION OF NOVEL AMMONIA PRODUCTION OPTIONS USING PHOTOELECTROCHEMICAL HYDROGEN

By
YUSUF BICER

A Thesis Submitted in Partial Fulfillment
of the Requirements for the degree of Doctor of Philosophy
in
Mechanical Engineering

University of Ontario Institute of Technology
Faculty of Engineering and Applied Science

Oshawa, Ontario, Canada

ABSTRACT

Hydrogen and ammonia are two of the most significant clean fuels, energy carriers and storage media in the near future. Production of these chemicals are desired to be environmentally friendly. Renewable energy, in particular solar energy-based hydrogen and ammonia production technologies bring numerous attractive solutions for sustainable energy production, conversion and utilization. The energy of the sun is endless and the water is a substance which is always accessible and renewable. Ammonia is currently one of the mostly used chemicals throughout the world due to many applications, such as fertilizers, cooling agents, fuel, etc. The Haber-Bosch process is the most dominant ammonia synthesis process which requires very high temperatures and pressures to operate and consumes massive amounts of fossil fuels mainly natural gas leading a non-sustainable process in the long-term. Therefore, alternative methods for ammonia production are in urgent need of development.

This study theoretically and experimentally investigates the photoelectrochemical production of hydrogen and electrochemical synthesis of ammonia in a cleaner and integrated manner. In this respect, the main objective of this thesis is to develop a novel solar energy based ammonia production system integrated to photoelectrochemical hydrogen production. The hybrid system enhances the utilization of sunlight by splitting the spectrum and combining the photovoltaic and photoelectrochemical processes for electricity, hydrogen and ammonia production. The photoelectrochemical reactor is built by electrodeposition of the photosensitive semiconductor (copper oxide) on the photocathode. The characterization of the reactor under solar simulator light, ambient irradiance and concentrated light is accomplished. Furthermore, an electrochemical ammonia synthesis reactor is built using molten salt electrolyte, nickel electrodes and iron-oxide catalyst. The electrochemical synthesis of ammonia is succeeded using hydrogen and nitrogen feed gases above 180°C and at ambient pressures. The photoelectrochemically produced hydrogen is then reacted with nitrogen in the electrochemical reactor to produce clean ammonia.

The comprehensive thermodynamic, thermoeconomic, electrochemical and life cycle models of the integrated system are developed and analyses are performed. The results obtained through models and experiments are comparatively assessed. The spectrum of solar light can be separated for various applications to enhance the overall performance of energy conversion from solar to other useful commodities such as electricity, fuels, heating and cooling. The results of this thesis show that under concentrated and split spectrum, the photoelectrochemical hydrogen production rates and efficiencies are improved. The overall integrated system exergy efficiencies are found to be 7.1% and 4.1% for hydrogen and ammonia production, respectively. The total cost rate of the experimental system for hydrogen and ammonia production is calculated to be 0.61 $/h from exergoeconomic analyses results. The solar-to-hydrogen conversion efficiency of the photoelectrochemical process increases from 5.5% to 6.6% under concentrated and split spectrum. Similarly, the photovoltaic module efficiency can be increased up to 16.5% under concentrated light conditions. Furthermore, the maximum coulombic efficiency of electrochemical ammonia synthesis process is calculated as 14.2% corresponding to NH_3 formation rate of 4.41×10^{-9} mol s^{-1} cm^{-2}.

ACKNOWLEDGEMENTS

First of all, I would to express my sincerest appreciation and gratitude to my supervisor, Prof. Dr. Ibrahim Dincer, for his endless, full-time, highly exergetic support and truthful guidance throughout my PhD thesis voyage. He provided me this unique opportunity to work with him in this research area under his excellent supervision and guidance. He has a very wide vision and mind to mentor and supervise his students in an extremely smart manner. This PhD thesis would not be possible without his supervision, patience, understanding, enthusiasm, and support.

I am also grateful to Dr. Calin Zamfirescu for his support and help in critical times. I would also like to thank the examining committee members, Dr. Yasar Demirel, Dr. Martin Agelin-Chaab, Dr. Ali Grami and Dr. Yuping He for their valuable feedbacks and comments in improving this thesis.

Financial support provided by the Natural Sciences and Engineering Research Council of Canada, Mitacs and Hydrofuel Inc. are gratefully acknowledged.

Although it is not possible to mention all the names here, I have to thank all my friends and colleagues as a past or present member of Dr. Dincer's Research Group at ACE3030 and Clean Energy Research Laboratory (CERL) namely; Farrukh Khalid, Dr. Hasan Ozcan, Murat Emre Demir, Muhammad Ezzat, Abdullah Al-Zahrani, Maan Al-Zareer, Ahmed Hasan, Huseyin Karasu, Reza Mohammadali zadeh, Dr. Canan Acar, Dr. Rami Salah El-Emam in addition to Murat Bahadir Ozkan. Special thanks go to Janettte Hogerwaard, Ghassan Chedade, André Felipe Vitorio Sprotte, Lowell Bower and Rodrigo Siliceo for their generous supports in the experimentation process. Karasu, Dereci, Ozkan, Zamfirescu and Khalili families are gratefully acknowledged for their kind friendships during my stay in Canada.

I am also thankful to the managers of my previous employer, UGETAM, especially to Prof. Dr. Umit Dogay Arinc and Serkan Keleser in addition to Dr. Cevat Ozarpa for their valuable mentorship, advices and encouragements before and during this PhD.

Sacrifice and patience are precious blessings and not easy to perform, therefore special thanks and love go to my dear chemist wife and mother of my children, Elif Derya, and my daughters, Erva Hatice and Zumra Ayse (who was born in the last moments of this thesis and was so quiet for her father to finish the thesis), for their generous sacrifice and endless encouragement. This work wouldn't have been accomplished without their patience and support.

Last but not the least, I would like to gratefully thank my dear parents; Mehmet Bicer and Sema Bicer who raised, educated and shaped me, and my siblings; Zehra Betul Bicer and Zeynep Bicer for their love, prayers and support.

TABLE OF CONTENTS

LIST OF FIGURES

LIST OF TABLES

NOMENCLATURE

A	Area (m^2)
A_λ	Spectral absorbance
B	Warburg element time constant ($s^{0.5}$)
c	Cost per unit exergy ($/kWh), Photonic constant (mK)
c	Speed of light (3×10^8 m/s)
$\dot{C}_D$	Cost rate of exergy destruction ($/h)
$\dot{C}$	Cost rate ($/h)
CC	Capital cost ($)
CRF	Capital recovery factor
CPE	Constant phase element parameter ($S\ s^a\ /cm^2$)
CPV	Concentrated photovoltaic
D	Diffusion coefficient (cm^2/s^1)
D_P	Depletion factor
e	Charge of an electron ($1.60217657 \times 10^{19}$ C)
$\dot{E}$	Energy rate (W)
E	Cell Voltage (V)
$\dot{E}x$	Exergy rate (W)
ex	Specific exergy (kJ/kg)
f	Fugacity coefficient
F	Faraday constant (C/mol)
f	Exergoeconomic factor
G	Gibbs free energy (kJ)
h_c	Heat transfer coefficient (W/m^2 K)
h	Specific enthalpy (kJ/kg)
H	Enthalpy (kJ)
h	Planck's constant ($6.62606957 \times 10^{-34}$ m^2kg/s)
I	Current (A)
I	Irradiance (W/m^2)
i	Interest rate (%)
J	Current density (A/m^2)
J_0	Exchange current density (A/m^2)
J_L	Limiting current density (A/m^2)
K	Equilibrium constant
k	Boltzmann constant (1.3806488×10^{23} J/K)
k_t	Thermal conductivity (W/mK)
k	Extinction coefficient
$\dot{m}$	Mass flow rate (kg/s)
m	Mass (kg)
M	Molarity (M)
$\dot{n}$	Mol flow rate (mol/s)
n	Refraction index, Number of transferred electrons
n	Diode ideality factor, Total operating time of the system (h)
N	Number
OM	Operating and maintenance cost ($)
P	Power (W)
P	Pressure (kPa)

$\dot{Q}$	Heat transfer rate (W)
$\boldsymbol{R_i}$	Random error
R	Universal gas constant (8.314 kJ/kmol K)
R	Reflectance
$\mathcal{R}$	Resistance (Ohm)
R_s	Internal series resistance of PV cell
S_{T_o}	Total amount of normal radiation (W/m^2)
$\dot{S}$	Entropy rate (W/K)
S_T	Global solar radiation (W/m^2)
$\boldsymbol{S_i}$	Systematic error
s	Specific entropy (kJ/kg K)
S	Entropy (kJ/K)
S	Siemens
T	Temperature (°C or K)
$\boldsymbol{T_W}$	Warburg time constant ($s^{0.5}$)
$\mathcal{T}$	Transmittance
t	Time (s)
U	Overall heat transfer coefficient (W/m^2K)
U	Uncertainty
V	Voltage (V)
$\boldsymbol{y_i}$	Molar fraction of species
$\boldsymbol{Y_0}$	Warburg element parameter ($S\ s^{0.5}/cm^2$)
v	Wind speed (m/s)
$\dot{V}$	Volume flow rate (mL/h)
V	Volume (L)
$\dot{W}$	Work rate (W)
W	Work (kJ)
$\boldsymbol{X_i}$	Conversion rate
$\dot{Z}$	Cost of owning and operating the system ($/h)
Z	Impedance (ohm)

Greek letters

α	Transfer coefficients
β	Temperature coefficient
δ	Nernst diffusion layer thickness (cm)
β_i	Fugacity coefficient
λ_m	Degree of membrane hydration (mole H_2O/mole SO_3^-)
δ	Membrane thickness (cm)
δ	Temperature induced efficiency
Δ	Change
η	Efficiency
λ	Wavelength (nm)
ν	Dimensionless voltage
π	Pi number
ρ	Density (kg/m^3)
σ	Conductivity of the membrane ($1/\Omega$ cm)
Φ	Spectral quantum efficiency
φ	Phase angle (°)

ω	Angular frequency (rad/s)

Subscripts

0	Ambient condition
a	Anode
abs	Absorbed
act	Activation or actual
AR	Ammonia reactor
b	Blackbody
c	Cathode or cell
C	Capacitance
cas	Casing
ch	Chemical
co	Coating
conc	Concentration
d	Destruction or diode
eff	Effective
el	Electricity
Elec	Electrolyzer
en	Energy
ex	Exergy
g	Band gap
gen	Generation
i	State number
in	Input
j	Imaginary
L	Inductance
m	Maximum
max	Maximum
mem	membrane
min	Minimum
oc	Open circuit
ohm	Ohmic
out	Outlet
ov	Overall
p	Product
p	Partial pressure
pce	Power conversion efficiency
ph	Physical or photon
POA	Plane of array
r	Reactor, reactant, reference, real, reversible
R	Resistance
rad	Radiation
rev	Reversible
s	Source, sink, sun, series,
sc	Short circuit
sh	Shunt
tot	Total

waf	Wafer

Acronyms

AC	Alternative current
ADF	Abiotic depletion factor
AM	Air mass
AOI	Angle of incidence
AP	Acidification potential
APE	Average photon energy
AR	Anti-reflective or ammonia reactor
BWR	Boiling water reactor
CAN	Calcium ammonium nitrate
CBD	Chemical bath deposition
CCD	Charge coupled device
CCS	Carbon capture storage
CEPCI	Chemical engineering plant cost index
CERL	Clean energy research laboratory
CF	Coefficient factor
CFBG	Circulating fluidized bed gasifier
CML	Center of Environmental Science of Leiden University
CPE	Constant phase element
CPV	Concentrated photovoltaic
CSP	Concentrated solar power
CV	Coefficient of variation
DAFC	Direct ammonia fuel cell
DAP	Ammonium phosphate
DC	Direct current
DG	Downdraft gasifier
DNI	Direct normal irradiance
DOE	Department of energy
ED	Electrodeposition
EEPROM	Electrically erasable programmable read-only memory
EES	Engineering equation solver
EIS	Electrochemical impendence spectroscopy
EQE	External quantum efficiency
FC	Fuel cell
FF	Fill factor
FKM	Fluorocarbon material
FOF	Field output factor
FOF	Field output factor
FS	Full scale
FTO	Fluorine-doped tin oxide
GHG	Greenhouse gas
GWP	Global warming potential
HDPE	High density polyethylene
HHV	Higher heating value
HTP	Human toxicity potentials
ICE	Internal combustion engine
IEA	International energy agency

IPCC	Intergovernmental panel on climate change
IQE	Internal quantum efficiency
IR	Infrared
ISO	International organization for standardization
ITO	Indium-doped tinoxide
LCA	Life cycle assessment
LCD	Liquid crystal display
LCI	Life cycle inventory
LDPE	Low density polyethylene
LHV	Lower heating value
LPG	Liquefied petroleum gas
MAX	Maximum
MLS	Middle latitude summer
MLW	Middle latitude winter
MOP	Muriate of potassium.
MPC	Microbial photoelectrochemical cell
MPEA	Membrane photo electrode assembly
MSE	Mercury sulfate electrodes
MW	Molecular weight
NIR	Near infrared
NOCT	Nominal operating cell temperature
NP	Nitrification potential
NTC	Negative temperature coefficient
OTEC	Ocean thermal energy conversion
PEC	Photoelectrochemical
PEM	Proton exchange membrane
PSU	Power supply unit
PtB	Platinum black
PTC	Parabolic trough collector
PV	Photovoltaic
PV/T	Photovoltaic/thermal
PWR	Pressurized water reactor
RH	Relative humidity
RHE	Reversible hydrogen electrode
RMS	Root mean square
RSD	Relative standard deviation
S&F	Shettle and Fenn
SCE	Saturated calomel electrode
SCFM	Standard cubic feet per minute
SD	Standard deviation
SDC	Samarium doped cerium oxide
SF	Shape factor
SFCN	SmFeCuNi
SI	Sustainability index
SLM	Standard liters per minute
SMARTS	The simple model of the atmospheric radiative transfer of sunshine
SMR	Steam methane reforming
SOFC	Solid oxide fuel cell
SSAS	Solid state ammonia synthesis

SSPC	Solid state proton conductors
STH	Solar-to-hydrogen
TSP	Triple superphosphate
UCG	Underground coal gasification
UOIT	University of Ontario Institute of Technology
UV	Ultraviolet
VB	Valance band
VIS	Visible
VOC	Volatile organic compound
ZRA	Zero resistance ammeter

CHAPTER 1: INTRODUCTION

In the introduction chapter, the fundamental information about the energy issues of the world is explained. The importance of the alternative energy production and storage options are emphasized by special focus on the hydrogen and ammonia.

1.1 Importance of Renewable Energy

As the energy consumption of mankind increases, seeking for various power generation and storage alternatives emerges. Rather than conventional sources, renewable energy resources are main solution for a cleaner and sustainable world. At the end of year 2015, renewable energy share of global electricity generation remains about 7.3% (having 1% increase compared to previous year) corresponding to 785 GW installed power capacity excluding hydropower as illustrated in Fig. 1.1. The share of wind energy and solar PV in global electricity production is approximately 3.1% and 0.9%, respectively. Fossil fuels and nuclear sources constitute still 77.2% of the global electricity production.

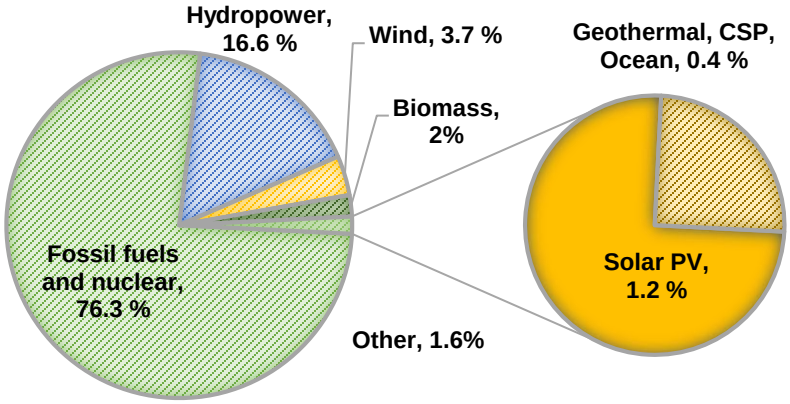

Fig. 1.1 Renewable energy share of global electricity generation at the end of 2015 (data from [1]).

The key benefits of renewable energy can be listed as follows:

- Renewable energy technologies are inexhaustible compared to conventional resources.
- Renewable energy resources are clean and environmentally friendly.
- Renewable energy is independent from any type of fossil fuel crisis.
- In terms of energy security, they compromise a unique importance.
- Being a crucial way of implementing sustainable development of society, renewables will continue to be cost effective solution.

On the whole, renewable energy resources constitute a significant role because of being undepleted, environmentally friendly and allowing decentralized energy generation.

1.2 Hydrogen Energy

Hydrogen element is considered as one of the most important energy carriers in this century. However, producing hydrogen form conventional resources brings more environmental side-

effects and less alternative solutions. Primarily, producing hydrogen from renewable energy sources is the best solution for supplying the energy requirements of hydrogen society. Sustainable development obliges a stream of energy resources which are sustainably available at reasonable cost and grounds either minimal or zero negative effects. Extensive utilization of green energy based hydrogen energy systems will be extremely important for achieving global stability and sustainability in both developing and industrialized countries. Hydrogen energy strategies, policies and programs are certainly essential to guarantee the stability of world using hydrogen energy and sustainability by decreasing the destructive effects of the fossil based energy consumption. The increase in hydrogen production capacities in the world can be seen in Fig. 1.2.

The significant advantages of hydrogen energy utilization can be written as follows:

- In comparison with electricity, hydrogen can be stored over longer periods of time.
- Hydrogen can be utilized as a fuel for transportation sector in combustion engines, electricity generation source through fuel cells and in all sections of the economy
- Hydrogen is a clean energy carrier having a high specific energy on a mass basis.
- Combustion product of hydrogen is only non-toxic exhaust emissions.
- Hydrogen can be transported in pipelines in safe and secure manner.
- There are multiple pathways for hydrogen production from various energy sources including renewables.
- Hydrogen with a low carbon footprint has the potential to assist noteworthy declines in energy associated CO_2 emissions.
- Hydrogen can support new connections between energy supply and demand, in both a centralized or decentralized manner by improving overall energy system flexibility.

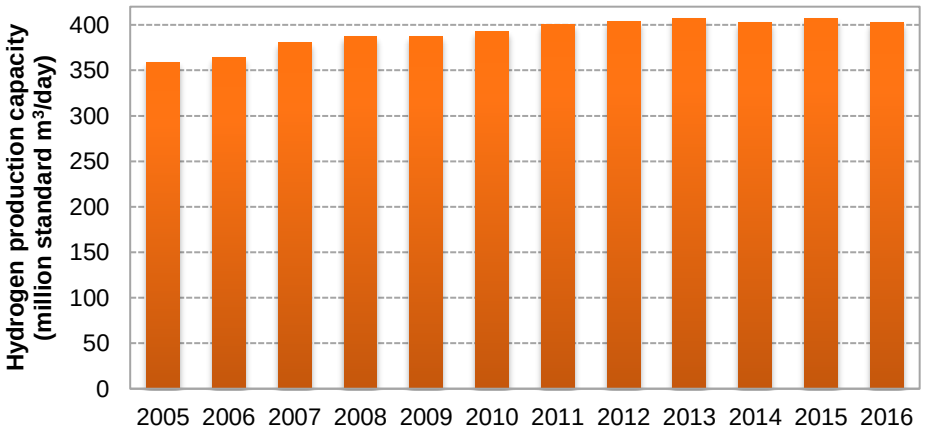

Fig. 1.2 Worldwide hydrogen production capacity at refineries as of 2016 (data from [2]).

Two of the major uses of hydrogen are for methanol and ammonia production. These chemicals are crucial for the world economy because they are the feedstock for many other major products such as formaldehyde, plywood, paints, textiles, fertilizers, and pharmaceutical substances. Furthermore, ammonia and methanol can be used as fuels in fuel cells and engines.

1.3 Hydrogen Production Methods

Hydrogen can be produced from a variety of feedstocks containing fossil resources, such as natural gas and coal, as well as renewable resources, such as solar, wind, etc. Currently, there are numerous pathways for hydrogen production including conventional and renewable sources as shown in Fig. 1.3.

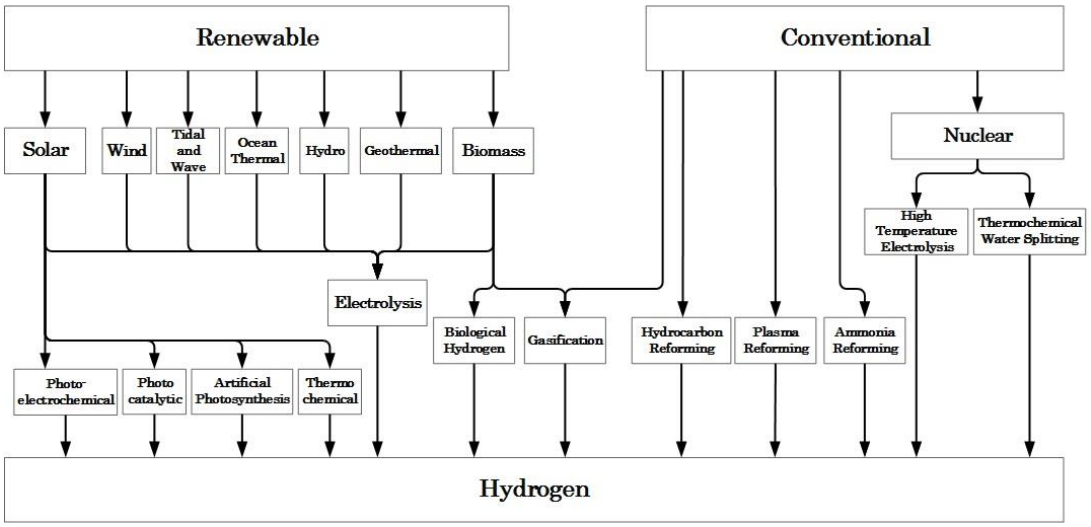

Fig. 1.3 Various renewable and conventional resources based hydrogen production methods

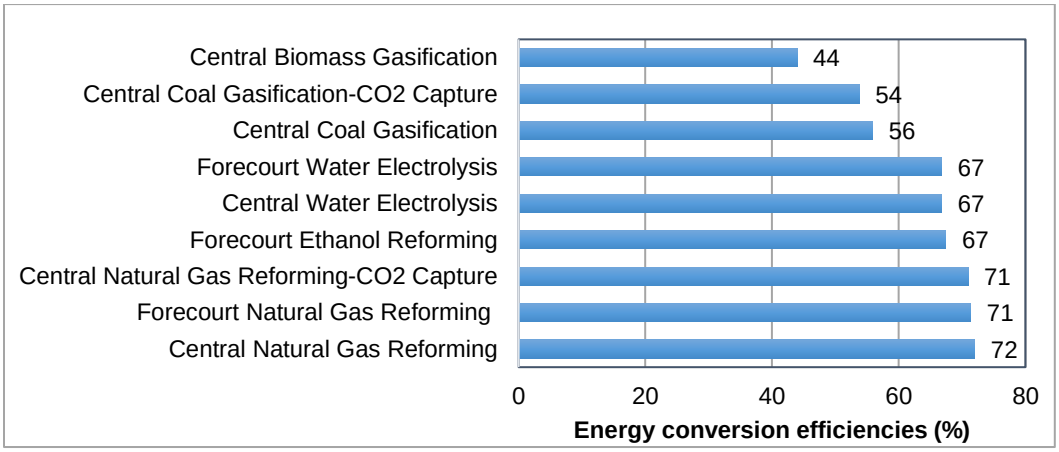

Fig. 1.4 Energy conversion efficiencies of various hydrogen production technologies (data from [2]).

An illustration of average efficiencies for current hydrogen production methods is shown in Fig. 1.4. Since steam methane reforming technology is developed and mature, its efficiency is higher however, water electrolysis efficiency is also very close corresponding to approximately 67%.

1.3.1 Hydrogen from nuclear energy

Hydrogen can be generated by thermochemical water splitting cycles which function at temperatures of around 500°C or more using nuclear reactors. Thermochemical water splitting is the transformation of water into hydrogen and oxygen by a series of thermally driven chemical reactions. Numerous different high temperature water-splitting thermochemical

reactions have been proposed for thermochemical water splitting [3]. For the moment, one of the significant challenges is obtaining high efficiencies with respect to lower temperature levels [4]. However, thermochemical cycles yield promising results to be considered as potential method to produce hydrogen.

1.3.2 Hydrogen from natural gas

Steam methane reforming is the conversion of methane and water vapor into hydrogen and carbon monoxide which is an endothermic reaction. The heat can be supplied from the combustion of the methane feed gas. The process temperature and pressure values are generally 700 to 850°C and pressures of 3 to 25 bar, respectively. The reacting products are heated up to 750-850°C to deliver the required heat for the endothermic methane-steam reaction [5]. The mixture then enters the secondary reformer. The oxygen taken from the air reacts with the hydrogen. This process enables raising the temperature in the reformer to 1,000°C, which shifts the equilibrium of the methane steam reaction to reduce the methane content to approximately 0.3% on a dry basis [5].

1.3.3 Hydrogen from coal

There are mainly two type of coal gasification. The one is called as underground coal gasification which take place below earth level and the other one is coal gasification which takes place above earth level. Coal gasification is the second most commonly used process for hydrogen production. There are a variety of gasification processes such as fixed bed, fluidized bed or entrained flow. In practice, high temperature entrained flow processes are preferred to make best use of carbon conversion to gas, consequently preventing the formation of substantial amounts of char, tars and phenols. Since this reaction is endothermic, additional heat is required, as with methane reforming. Besides surface coal gasification, underground coal gasification (UCG) is a promising alternative for the future use of un-worked coal. As opposed to mining coal reserves, UCG can eventually propose unreached coal reserves reachable. UCG is one of the un-mined type of electricity production having quite less greenhouse gas emission compared to coal fired power plant. It avoids environmental impacts, safety and health risks of coal extraction process. Carbon capture and storage of carbon dioxide technologies are considered as two operative methods. In this process, underground coal is expended by partial combustion with air, oxygen, steam, or any combination of these to generate syngas. The syngas formed via the gasification process consists of primarily hydrogen and CO.

1.3.4 Partial oxidation of heavy oils

The partial oxidation method is utilized for the gasification of heavy feedstocks such as residual oils and coal. Exceedingly viscous hydrocarbons and plastic wastes can also be utilized as elements of the feed. The essential oxygen can be manufactured in an air separation unit. In order to eliminate contaminations from the syngas and to obtain the needed hydrogen/nitrogen ratio in the syngas, nitrogen is supplied in the liquid nitrogen wash. The partial oxidation gasification is a non-catalytic process which occurs at high pressures above 50 bar and temperatures in the range of 1,400°C. Steam addition is also required for temperature control.

The partial oxidation process is an alternative source of waste utilization. CO_2 is generally detached by an absorption mediator which could be the same as in the sulphur elimination process.

1.3.5 Hydrogen from biomass

Hydrogen can be generated from diverse kinds of biomass such as animal, forestry, industrial and municipal waste, and agricultural and industrial crops. Frequently employed methods to generate hydrogen from biomass are gasification, thermochemical, and biochemical processes. In biomass conversion methods, a hydrogen containing gas, which is generally called as syngas, is usually manufactured similar to the gasification of coal. The chemical reactions occurring in biomass based hydrogen generation are very similar to fossil fuel based methods. Gasification and pyrolysis are evaluated one of the most encouraging medium-term methods for the commercialization of hydrogen generation from biomass. Biomass is considered as an abundant renewable source and it carries a potential to decrease CO_2 emissions because of fossil fuel utilization.

1.3.6 Hydrogen from wind energy

Wind turbines transform the energy of wind to mechanical work. Using an alternator, mechanical work is then transformed into to alternating current (AC) electricity. Produced electricity is either transmitted to the power grid or directly delivered to the electrolyzer for hydrogen generation. For hydrogen production system from wind, there are two key steps: a wind turbine generating the electricity and a water electrolysis system producing hydrogen. Wind energy based hydrogen production brings a significant potential amongst renewable options for generating non-polluting hydrogen, particularly for distributed systems.

1.3.7 Hydrogen from solar energy

Hydrogen production using solar energy can be executed through electrolysis, artificial photosynthesis, photoelectrolysis, thermochemical, photocatalytic and photoelectrochemical water splitting etc. methods. Though, each method has few specific advantages and drawbacks, photoelectrolysis, photocatalysis, and photoelectrochemical hydrogen production methods are more promising among the available solar hydrogen routes [6]. The detailed explanation about solar based hydrogen production is presented in next sections.

1.3.8 Hydrogen from other renewable resources

Hydrogen can be produced from water electrolysis which uses the electricity produced by renewable sources such as geothermal, tidal and wave, ocean thermal and hydro energy. Compared to conventional methods, they are more environmentally friendly and many of them have started to be cost competitive in terms of electricity prices.

Geothermal energy: The geothermal power plant generates the electricity for the electrolysis plant as well as providing energy to the water to reduce the amount of energy required to produce the hydrogen. The opportunity of worldwide small-medium scale production of electricity from geothermal systems may be in the future an option for distributed hydrogen production in many countries.

Ocean thermal energy (OTEC): Solar energy heats the top 50-100 m of ocean to a temperature of 27-30°C. At the same time, the water at a depth of 1,000 m stays at or below 5°C near the equator regions [7]. An OTEC plant is a solar energy based source of harvesting the temperature change between the ocean surface and deep ocean waters. In order to extract the energy from these temperature difference, generally a vapor-power cycle is built by using the hot and cold heat reservoirs of ocean water. OTEC is the one of the regular availability of the renewable resources during every day of the year different than other renewable energy sources.

Tidal and wave energy: Tidal energy is one of the oldest types of energy utilized by humanity. Tidal power is pollution free and the amount of energy that can be produced is predictable. Tidal energy is generally characterized by low capacity factors, in the range of 20-35%. The required technology to convert tidal energy into electrical work is quite similar to the technology used in conventional hydropower plants.

1.4 Solar Light Based Hydrogen Production Methods

As a renewable and abundant supply, solar energy is a prospective sustainable solution to the growing energy demand of the world with an addition of a storage technique. Solar energy is intermittent source with day/night cycles. Therefore, solar energy is desired to be stored in a different form of energy in order to deliver an uninterrupted supply. As a chemical fuel, hydrogen is an encouraging storage medium because of its high energy storage capacity. A classification of main solar light based hydrogen production methods is given in Table 1.1.

Table 1.1 Main solar light based hydrogen production methods.

Method	Temperature level	Process	Description
Concentrated solar thermal	High temperature (200-2500°C)	Thermolysis	Thermal disassociation of water
		Thermochemical cycles	Thermochemical cycles using metal oxides
		Gasification	Steam gasification of coal
		Cracking	Thermal disassociation of natural gas and hydrocarbons
		Steam reforming	Steam reforming of natural gas and hydrocarbons
		Electrolysis	Water electrolysis using high temperature and solar thermal electricity
PV	Low temperature (0-200°C)	Electrolysis	Water electrolysis
Photocatalytic		Photo catalysis	Water photo catalysis
Photoelectrochemical		Photo electrolysis	Water photo electrolysis
Photobiological		Photo biolysis	Plant and algal photosynthesis

Source: (modified from [8])

Photoelectrochemical water splitting brings various advantages over other methods mainly; avoiding safety concerns, reducing energy necessities, and improving system control by selecting low temperature processes instead of the high temperature techniques.

1.5 Photoelectrochemical Hydrogen Production

Photoelectrochemical cells transform solar energy to hydrogen using light enthused electrochemical processes. In a photoelectrochemical cell, solar light is absorbed by one or both of the photo electrodes in which one of them is at least a semiconductor. Photoelectrochemical cells may generate either chemical or electrical energy depending on the desire of the usage.

Light utilization ability can be decided by band gap of the material for the photo electrode. There are natural losses related with any solar energy transformation methods including materials. The losses related with natural emissions affect the efficiency of the applied system [9, 10].

Photochemical water reduction requires the flat-band potential of the semiconductor exceeding the oxidation potential of water of +1.23 V at pH = 0 or +0.82 V at pH = 7. A single band gap device requires, at a minimum, a semiconductor with a 1.6 to 1.7 eV band gap in order to produce the open circuit potential required to split water. When other voltage loss issues are also taken into account, a band gap above 2 eV is usually essential [11]. The utilization of two semiconductor materials stays as an attractive choice for capturing a large share of the solar spectrum, with the two band gaps tuned to absorb corresponding sections of the solar spectrum [11]. Alternatively, using spectrum splitters, the multi-product generation can be increased leading higher overall efficiencies.

1.6 Ammonia as a Sustainable Energy Carrier

Ammonia is considered not only as a feedstock but also evaluated as an energy carrier. Due to its many advantages over hydrogen it can be a medium to store and carry energy. Currently, more than 90% of the world ammonia synthesis is realized by the Haber-Bosch synthesis process. This process is called for Fritz Haber and Carl Bosch who developed the method in 1913 [12, 13]. It is important to note that natural gas is the main feedstock used for manufacturing ammonia worldwide. In Canada, there are about 11 ammonia plants operating and producing an average of 4–5 million metric tonnes yearly [14]. Haber-Bosch process is based on combining hydrogen and nitrogen over an iron oxide catalyst at high temperature and pressures. On the other hand, novel techniques such as solid state synthesis and electrochemical procedures are currently being advanced to decrease the cost and enhance the efficiency of ammonia production process.

Ammonia is one of the largest produced industrial chemical in the world. The increase in ammonia production per year is shown in Fig. 1.5. Production of ammonia consumes almost 1.2% of total primary energy and adds about 1% of global GHGs [15]. Approximately 1.5 to 2.5 tons of CO_2 is emitted to the atmosphere during the production of 1 tonne of ammonia depending on the feedstock use [15].

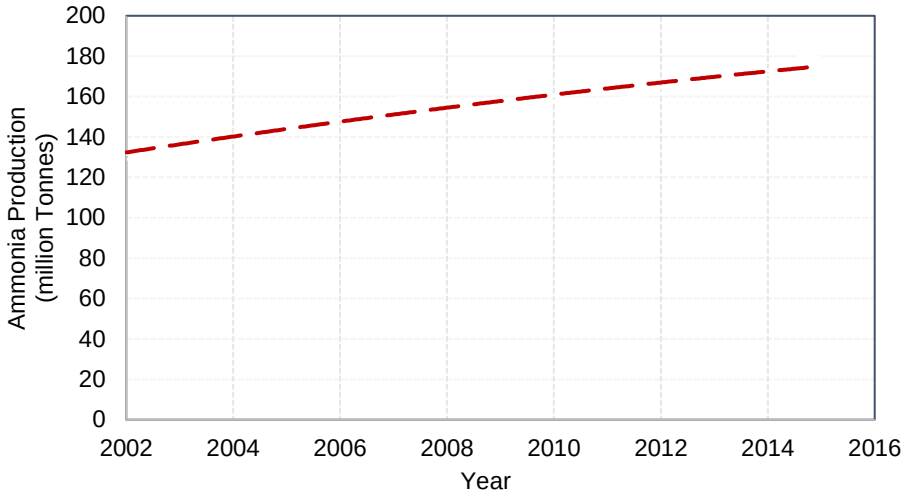

Fig. 1.5 World ammonia production growth (data from [16]).

1.7 Ammonia Production Methods

Globally, 72% of ammonia is produced using steam reforming of natural gas (SMR) as clarified in Fig. 1.6. Considering the conventional sources, naphtha, heavy fuel oil, coal, natural gas coke oven gas and refinery gas could be utilized as feedstock in ammonia synthesis. In China, coal is the main source of ammonia production, therefore the energy consumption and greenhouse gas emissions are higher than the rest of the world. For steam methane reforming method, natural gas costs represent almost 70-90% of the production cost of ammonia. Since, ammonia production is based on natural gas in SMR method, rising natural gas prices causes an increase in production costs of ammonia [17, 18].

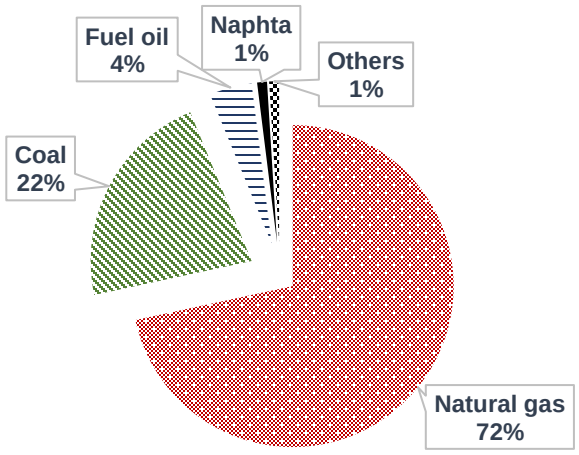

Fig. 1.6 Sources of ammonia production based on feedstock use (data from [17, 18]).

Although there are many methods for ammonia synthesis, commonly two different ammonia production methods are available in the world namely; Haber-Bosch process and solid state ammonia synthesis process as exemplified in Fig. 1.7. In both procedures, nitrogen is delivered via air separation process. Cryogenic air separation is currently the most effective and economical expertise for producing bulky amount of oxygen, nitrogen, and argon [19].

Cryogenic method can likewise yield high-purity nitrogen as a useful by-product stream at relatively low incremental cost. Among other air separation methods, cryogenic air separation has most established and industrialized expertise. Since ammonia is manufactured at high quantities, required nitrogen ought to be manufactured in a low cost and high effective manner. Required electricity for air separation could be supplied either from conventional or alternative resources.

The Haber-Bosch process is the most common method to produce ammonia [20]. It is an exothermic process combining hydrogen and nitrogen in 3:1 ratio to yield ammonia. The reaction is assisted by catalyst and the optimal temperature range is 450-600°C [20–22]. The Haber–Bosch process was developed at the beginning of the twentieth century to combine hydrogen and nitrogen thermo-catalytically according to the following reaction:

$$\frac{3}{2}\,H_2 + \frac{1}{2}N_2 \rightarrow NH_3 + 45.2\ \mathrm{kJ/mol} \qquad (1.1)$$

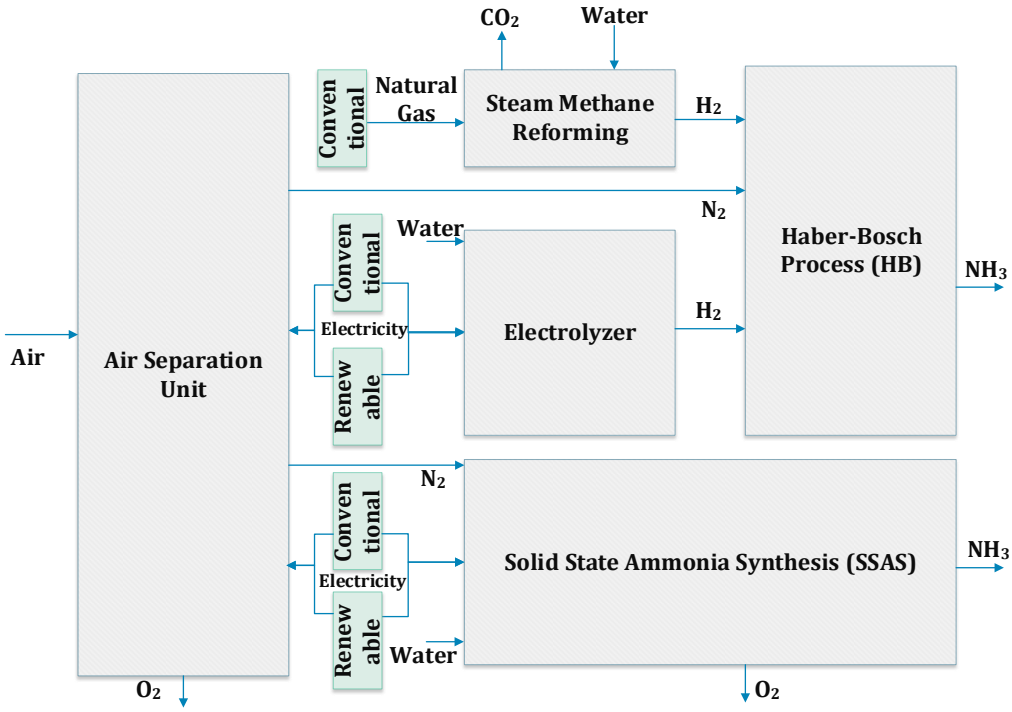

Fig. 1.7 Main ammonia production routes via conventional and renewable sources.

The characteristics of this method is based on rising the temperature of the reactants such that the nitrogen molecule accepts enough energy to be cracked. The catalyst breaks the nitrogen bonds at the surface. In case the temperature is not high enough, nitrogen atoms endure toughly bound at the surface and constrain the catalyst from carrying out a new catalytic cycle. Nevertheless, since 2 mol of reactants produces 1 mol of products in the reaction, the forward reaction is expedited by low temperatures and high pressures. Since the reaction temperature is not desired to be set low because of catalyst poisoning, the working pressure is quite high. Typically, the operating temperature and pressure are 450°C to 600°C and 100 to 250 bar, respectively, for 25% to 35% conversion rate [21].

A frequently used conversion loop in Haber-Bosch plant is presented in Fig. 1.8 and operates as follows. Make-up gas consisting of hydrogen and nitrogen is delivered as input and compressed up to an intermediate pressure. The make-up gas is joined with unreacted gases returned from the loop and compressed additionally up to the conversion pressure. The feed is sent toward the catalytic converter that covers primarily iron-based catalysts. The resulting gases comprehending converted ammonia product arrive the ammonia separator operating at the intermediary pressure. There, ammonia is separated by condensation and collected as liquid from the bottom of the separator. A refrigeration plant based on ammonia is used to cool, condensate, and separate the product. The residual gases, containing mainly unreacted nitrogen and hydrogen, are partly recycled by recompressing together with the make-up gas and partly used in a combustor to produce process heat.

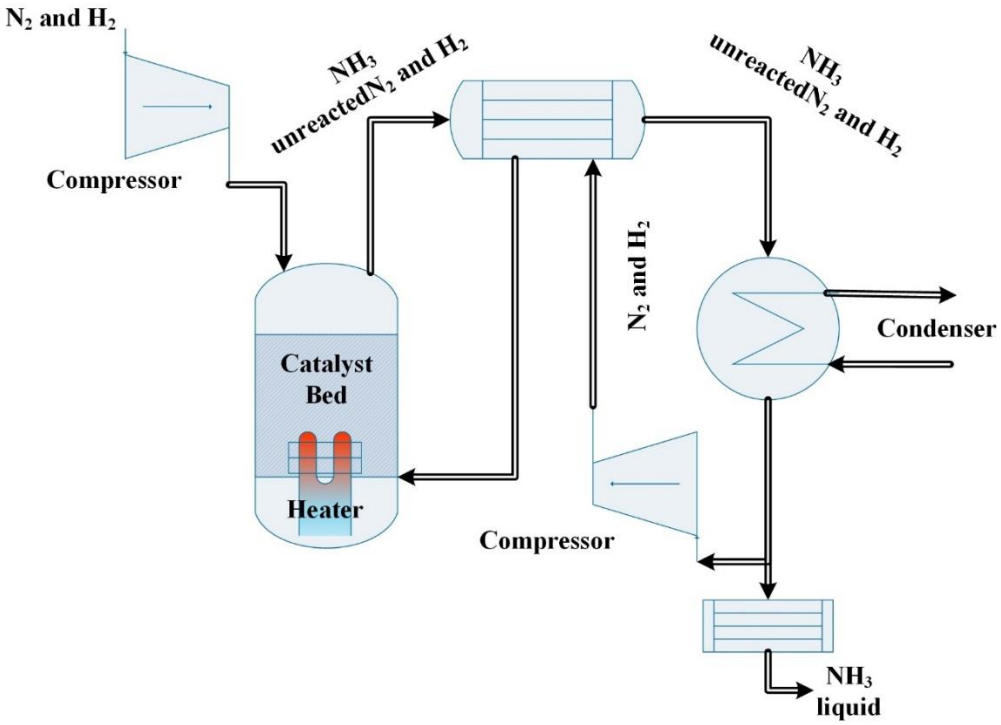

Fig. 1.8 Simple layout of Haber-Bosch ammonia synthesis process (modified from [23,24]).

In Haber-Bosch process, the impact of ammonia production basically depends on the methods used to produce hydrogen and nitrogen. The nitrogen and hydrogen gas mixture is compressed to 100-220 bar, depending on the particular plant, before it enters the ammonia synthesis loop [25]. Only a portion of the mixture gas is converted to ammonia in a single pass through the converter due to thermodynamic equilibrium of the ammonia synthesis reaction. The residual gas which is not reacted is passed through the converter once more, creating a flow loop for the unreacted gas. The ammonia in gas form and unconverted mixture gas then arrives the ammonia recovery section of the synthesis loop. Using the refrigeration coolers, the temperature of the gases is decreased to -10˚C to -25˚C which condenses ammonia out of the mixture and leave unreacted synthetic gas behind [5].

Each of the main factors affecting the world such as population increase, upgrading of the world's food source and biomass utilization to supply energy, will cause additional demand for nitrogen as fertilizer. If the production of ammonia and other fertilizers continue to be dependent on fossil fuels, Earth will become a place with polluted air, increased human health risks decreased biodiversity and more GHGs [26]. Conversion of feed gases to ammonia is thermodynamically limited (10–15%) ending up with some disadvantages of Haber-Bosch process [27]. In addition, environmental contamination is severe and energy consumption is high [26, 27]. The way of improving Haber-Bosch is mostly via modifications in the catalyst and heat recovery. Ruthenium-based catalyst instead of an iron-based catalyst is one of the catalytic improvements which has recently started to be used [30]. In this way, better catalyst enables more ammonia to be formed per pass over the converter at lower temperatures and pressures which also bring lower energy consumption.

The average energy use and environmental impact of various commercial ammonia plants in the world is exemplified in Table 1.2. It is remarked that including the extra emissions for manufacture and transportation of fossil fuels leads a significant growing effect of ammonia manufactured. Moreover, a variance in global regions consuming miscellaneous fossil fuel mixtures and different ammonia manufacture efficiencies yield a more explicit variety in emissions per tonne ammonia manufactured [13]. Based on the type of feedstock, the greenhouse gas emission differ. The number of life cycle assessment studies for specifically ammonia generation is quite limited. Hence, the values for comparing the emissions of various fertilizer production processes are listed in Table 1.3. Here, DAP represents ammonium phosphate, TSP: triple superphosphate, CAN: calcium ammonium nitrate and MOP: muriate of potassium. In China, coal is the fundamental feedstock for hydrogen generation required for ammonia synthesis. Hence, the average GHG emissions are quite higher than world average and natural gas feedstock.

Table 1.2 The average energy use and GHG emissions of ammonia production in various global regions.

Region	**MJ/tonne NH_3**	**tonne CO_2 eq/tonne of NH_3**
Western Europe	41.6	2.34
North America	45.5	2.55
Russia and Central Europe	58.9	3.31
China and India	64.3	5.21
Rest of the World	43.7	2.45
World Average	52.8	3.45

Source: (data from [13])

The other developing ammonia production method is solid state ammonia synthesis (SSAS). This type of ammonia production system uses a solid state electrochemical process to produce ammonia from nitrogen, water, and electricity. SSAS consumes less energy and yields higher efficiencies. The required electricity for SSAS process is 7,000-8,000 kWh/tonne-NH_3, whereas it is 12,000 kWh/tonne-NH_3 for the combination of electrolyzer and Haber-Bosch

synloop The capital cost is approximately 200,000 $/tonne-day-$NH_3$. Compared with electrolyzer with a Haber-Bosch synloop which is about 750,000 $/tonne-day-$NH_3$, it is considerably less [20,31].

Table 1.3 Comparison of various literature results for different fertilizers production including ammonia.

Product	**GHG emissions (kg CO_2 eq./kg product)**	**Remarks**	**Reference**
Ammonia	1.83	Feedstock: Natural gas	SimaPro Database [32]
Ammonia	1.44	Feedstock: Natural gas	Makhlouf et al. [33]
CAN/MOP/DAP	1.37	Fertilizer	Hasler et al. [34]
Urea/MOP/TSP	1.30	Fertilizer	Hasler et al. [34]
CAN/MOP/TSP	1.76	Fertilizer	Hasler et al. [34]
Ammonia	5.22	Feedstock: Anthracite coal	Kahrl et al. [35]
Urea and ammonium bicarbonate	2.57	Feedstock: Anthracite coal	Kahrl et al. [35]

In SSAS, a proton-conducting membrane is heated to about 550˚C. Under same pressures, nitrogen and water vapor is supplied to each side of the membrane to initiate the reaction. In this regard, the schematic diagram of SSAS process is illustrated in Fig. 1.9.

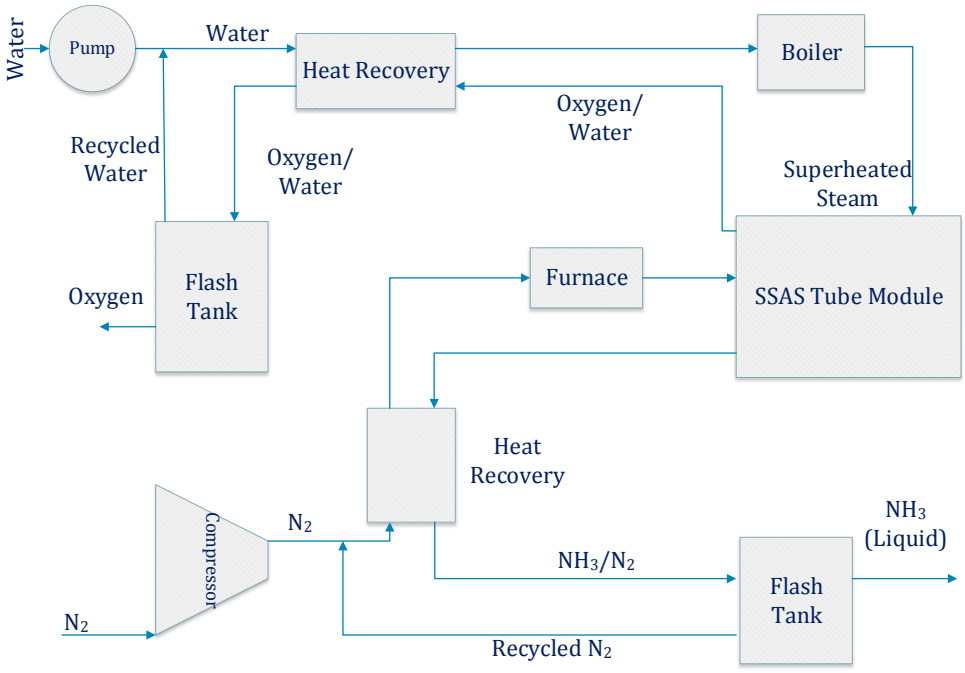

Fig. 1.9 Ammonia production via solid state ammonia synthesis (adapted from [31]).

The water vapor separates into protons and oxygen. By applying an external voltage, the protons are transferred through the membrane, and on the nitrogen side of the membrane, NH_3 is being formed as a result of nitrogen and protons reaction. Since the energy consumption of the SSAS process is lower, it is evaluated that it will enable producing ammonia at a lower cost than the Haber-Bosch process. On the other hand, it does not consume fossil fuel which brings significant environmental advantage. Since the electrolyzer and Haber-Bosch synloop are eliminated when SSAS system is used, the SSAS technology is thought to be suitable for renewable energy sources which results in many energetic and financial advantages [31].

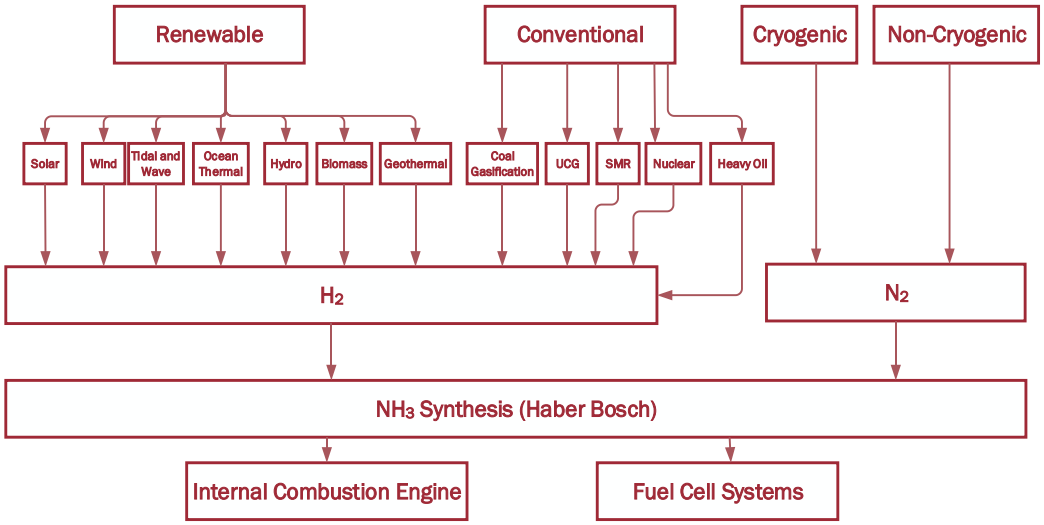

Fig. 1.10 Main ammonia production and utilization methods by the Haber-Bosch method.

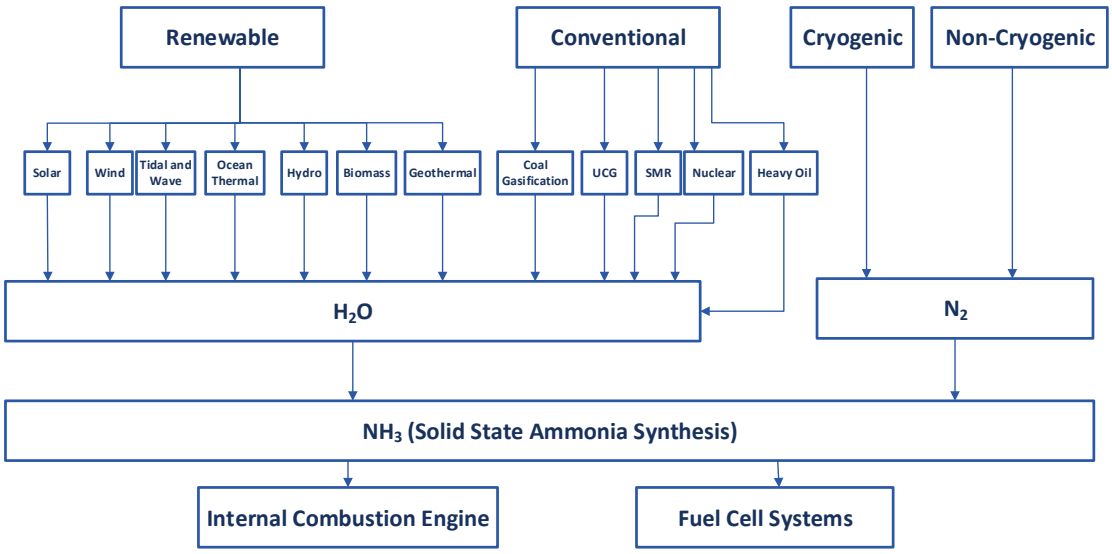

Fig. 1.11 Main ammonia production and utilization routes by SSAS method.

For the Haber-Bosch process, production of ammonia is based on various hydrogen production techniques as shown in Fig. 1.10. In contrast, in SSAS process, it is based on generating super-heated steam as illustrated in Fig. 1.11.

1.8 Ammonia Utilization

There are various alternatives for ammonia usage in various applications as illustrated in Fig. 1.12. It is mostly used as a fertilizer and refrigerant in the current market. There are also ammonia-fueled vehicle prototypes using either engines or fuel cells.

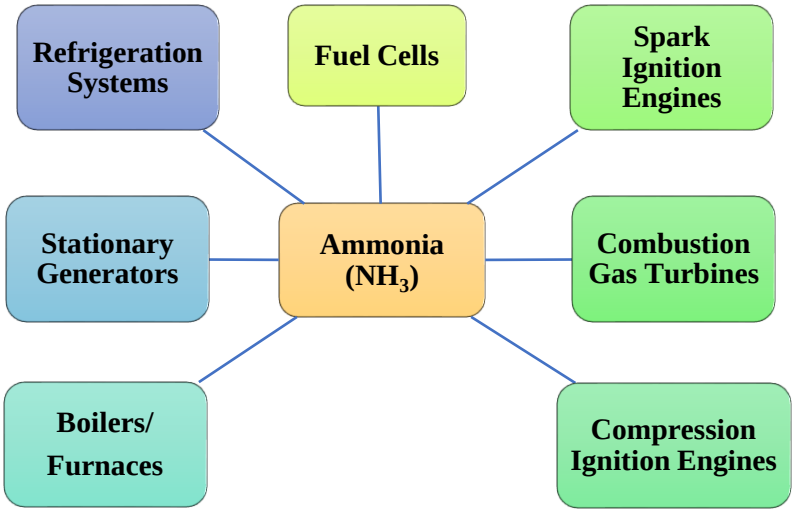

Fig. 1.12 Some of the main ammonia utilization systems.

The demand for ammonia is forecasted to grow at an average annual rate of approximately 3% over the next five years globally in which they are used in many applications as illustrated in Fig. 1.13. The historical growth rate was 1%. Therefore, currently it is 2% above the historical growth rate. It is expected that agricultural essentials will be first responsible of this growth as fertilizer utilization accounts for nearly 80% of global ammonia request [36, 37].

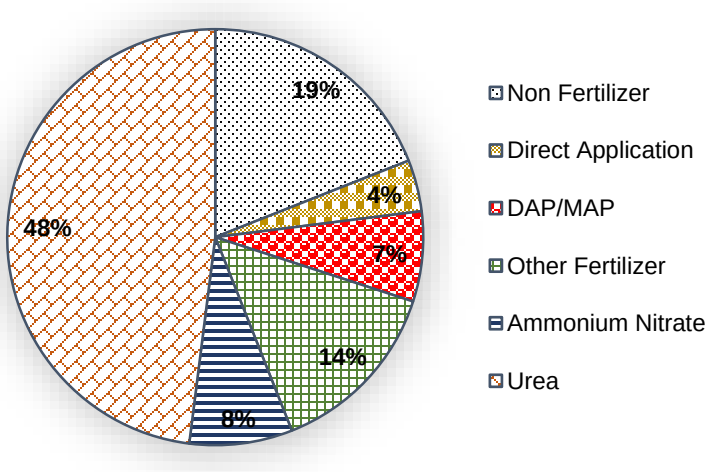

Fig. 1.13 World ammonia usage as an average of 2010-2013 (data from [34, 35]).

The storage and delivery substructure of ammonia is comparable to LPG process. Under intermediate pressures, both of the materials are in liquid state that is an important benefit. Principally, ammonia is an appropriate candidate for vehicular uses which can be used in different systems as illustrated in Fig. 1.14. In the present day, vehicles running on propane are commonly recognized and it is a decent model for ammonia fueled vehicle occasions. An ammonia pipeline from the Gulf of Mexico to Minnesota and with divisions to Ohio and Texas has worked for the ammonia industry for several years. Ammonia is an appropriate material to be transported using steel pipelines with minor changes which are presently used for natural gas and oil. In this way, the availability issue of ammonia can be eliminated. A pipeline may deliver almost 50% more energy when transporting liquid ammonia than carrying compressed natural gas [38].

Ammonia as a sustainable fuel can be utilized in all types of combustion engines, gas turbines, and burners with only small amendments and directly in fuel cells that is a very significant advantage in comparison with other type of fuels. In an ammonia economy, the accessibility of a pipeline to the residential area could supply ammonia to fuel cells, stationary generators, furnaces/boilers and even vehicles which will bring a non-centralized power generation and enable smart grid applications. Ammonia could basically be reformed to hydrogen for any application due to very low energy prerequisite of reforming. Ammonia is at the same time a very suitable fuel solid oxide fuel cells and direct ammonia fuel cells. These medium-temperature fuel cells promise to be low cost, highly efficient and very robust [38].

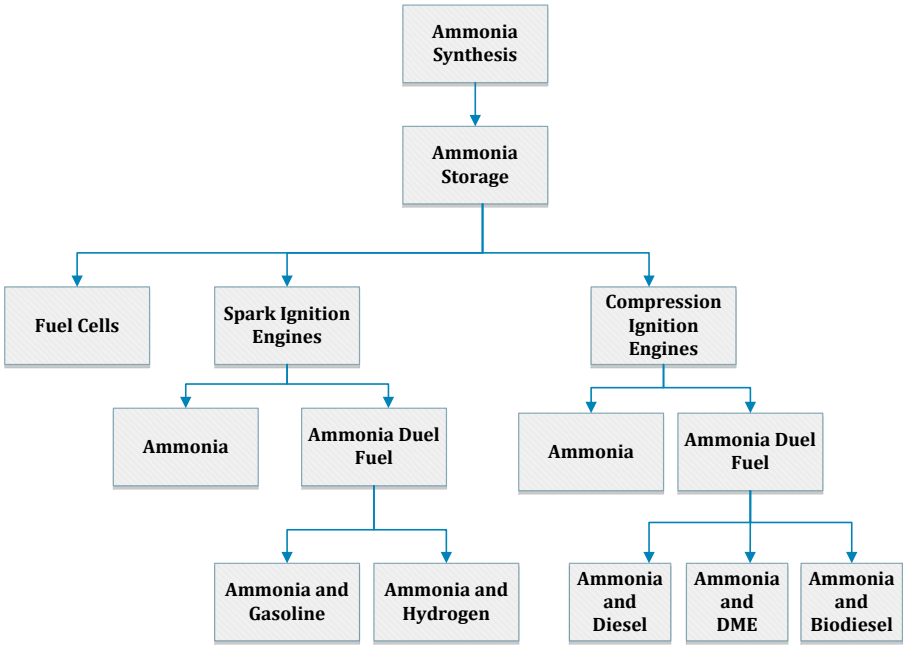

Fig. 1.14 Some of the ammonia usage routes in transportation applications.

As ammonia can function as a storage medium, the use of ammonia for concentrated solar energy storage with solar dish systems has been proposed by Lovegrove et. al. [39] based on the fact that the reaction is reversible and there are no side products. The forward reaction

$NH_3 \rightarrow 1.5\ H_2 + 0.5\ N_2$ receives thermal energy when sun is present and the reverse reaction $1.5\ H_2 + 0.5\ N_2 \rightarrow NH_3$ provides heat on demand. This process is satisfactorily well understood and its thermodynamics are very favorable up to pressure of 200 bar. The receiver temperature is kept high as the reaction progresses at a constant temperature.

In addition, ammonia is a fuel for Direct Ammonia Fuel Cell (DAFC) which is a type of the SOFC+ with selected catalysts at the anode where gaseous ammonia is fed as a source of hydrogen. The schematic of a DAFC is shown in Fig. 1.15. Ammonia fed at the anode decomposes thermo-catalytically and generates protons that diffuse through the porous electrolyte.

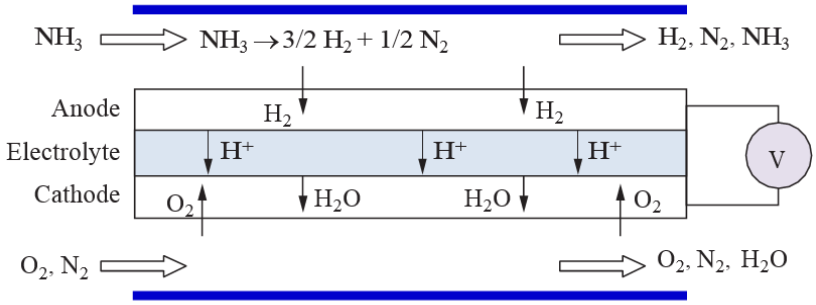

Fig. 1.15 Direct ammonia fuel cell illustration (modified from [40]).

Water is formed at the cathode where protons encounter the oxygen. The achievable DAFC efficiency is on the order of SOFC+ fueled with hydrogen, i.e., over 55%. The system half-reactions are then given as follows:

$$\text{Anode: } NH_3(g) \rightarrow N_2(g) + 3H^+ + 3e^- \quad (1.2)$$

$$\text{Cathode: } 1.5\ O_2(g) + 3H^+ + 3e^- \rightarrow 1.5\ H_2O(g) \quad (1.3)$$

Ammonia has also been a principal refrigerant in the industrial segment because of its exceptional thermal properties, zero ozone depletion and global warming potential (GWP). Ammonia bears the utmost refrigerating outcome per unit mass compared to all refrigerants being used counting the halocarbons. The notable benefits of ammonia over R-134a could be inferior overall operating costs of ammonia systems, the flexibility in meeting complex and numerous refrigeration requirements, and inferior initial costs for plentiful applications [41]. Producing ammonia in a clean way and using in various applications will enable a cleaner community. These systems are not necessarily centralized large-scale applications. In contrast, they can be stand-alone and small/medium scale applications which can contribute de-centralized smart energy systems. Ammonia can also be decomposed into hydrogen and nitrogen easily using heat input for further usage.

1.9 Thesis Outline

This thesis comprises of six main chapters. In the first chapter, a comprehensive introduction and background information on energy, renewable energy, energy storage, hydrogen and ammonia systems are presented. The importance of clean and sustainable energy carriesr are emphasized. In addition, the production and utilization techniques of ammonia are explained

in detail. Chapter 2 focuses on detailed literature review on utilized sub-systems in this thesis namely; solar energy, photoelectrochemical hydrogen production, solar light concentration and splitting, electrochemical ammonia production routes, reactor design, membrane assemblies, and system hybridization. The motivation and objectives of the thesis are presented at the end of Chapter 2 where the main gaps in the open literature are explained. In this section, the originality of the thesis is further emphasized. Chapter 3 explains the developed and utilized experimental apparatus and procedures. In this chapter, each device used in the experiments are written together with the experimental procedure followed during the experiments. The experimental diagrams for photoelectrochemical hydrogen production and electrochemical ammonia production are separately introduced. The design parameters for the selection of the materials are also expressed. The detailed thermodynamic analyses, electrochemical modeling, photocurrent generation modeling, holistic photovoltaic analyses, efficiency assessment, life cycle assessment, exergoeconomic and optimization study of the systems are presented in Chapter 4. Some of the measured parameters are used in the analysis, therefore Chapter 4: Analysis and Modeling is written after introducing the experimental apparatus and procedure. Chapter 5 provides the obtained results as well as their comprehensive comparison by giving detailed information on main findings from this thesis. In this chapter, the model results are comparatively shown with experimental results. The results are divided into 8 main sub-sections as follows; photovoltaic system results, photocatalyst electrodeposition results, photoelectrochemical hydrogen production results, electrochemical ammonia production results, integrated system results, exergoeconomic results, optimization study results and environmental impact assessment study results. In Chapter 6, conclusions are presented showing the main findings from this thesis. Moreover, the recommendations to further develop the system and technology are presented in the final chapter.

CHAPTER 2: BACKGROUND AND LITERATURE REVIEW

In this chapter, a comprehensive review of the systems and technologies used in this thesis is presented. In this thesis, solar energy based electrochemical hydrogen and ammonia production system is developed, tested and analyzed. Therefore, the system mainly includes solar concentrator, photovoltaics, photoelectrochemical hydrogen production, electrochemical ammonia synthesis and spectrum splitters. The topics covered in the literature review include the followings:

- Solar and photoelectrochemical energy based hydrogen production
- Photosensitive materials and electrodeposition
- Electrochemistry of the photoelectrochemical cells
- Solar spectrum effect on PV and photoelectrochemical hydrogen
- Spectrum splitting mechanisms and applications
- Solar PV and PV/T systems
- Life cycle assessment of hydrogen and ammonia production
- Novel ammonia production methods

2.1 Solar and Photoelectrochemical Based Hydrogen Production Technologies

Zamfirescu et al. [42] studied a thermodynamic model to investigate the exergy part of instance solar irradiation hitting on the surface of Earth that could be utilized to generate power via dual cascaded thermodynamic cycle. The realization of the model was shown and confirmed by computing the exergy of solar irradiation based on measurements. Their model explains that whole Earth performs as a heat engine combined to a brake such that the insolation and also the climate are foreseeable as a constructal design of the global flow system.

He et al. [43] worked on a light-driven microbial photoelectrochemical cell (MPC) system, which consists of a TiO_2 photocathode and a microbial anode. It was an integration of microbial anode and semiconductor photocathode. In the microbial anode, electrons are electrochemically produced by active microorganisms from organic matters and are then transported to cathode side. On the other hand, in the photocathode, semiconductor absorbs photon to produce electrons at its conduction-band and holes at its valence-band. They concluded that the efficiency of the MPC system should be improved and the cost needs to be decreased.

Tseng et al. [44] conducted studies about the heat transfer in a photoelectrochemical hydrogen production reactor. They spitted solar spectrum into short and long wavelength parts depending on the energy band gap of the photoelectrode. The short wave energy is directed to the anode to generate electron and hole pairs, and the long wave energy is utilized for heating purposes of the reactor. Their results concluded that using the excess higher wave length energy to heat up the reactor can increase the solar to hydrogen efficiency.

Lopes et al. [45] studied a PEC cell for testing different photoelectrodes configurations, appropriate for continuous operation and for easily collect the produced gases. Photocurrent–voltage characteristics were obtained for all samples characterized under three different conditions namely no membrane separating the anode and the cathode evolution; using a

Teflon® diaphragm and using a Nafion®212 membrane. The proposed Teflon diaphragm was successfully implemented in the new PEC cell, with approximately 47% photocurrent density enhancement when transparent WO_3 photoelectrode was used.

Abe [46] prepared a review about the recent progress in photocatalytic and photoelectrochemical water splitting field by concentrating on approaches that utilize visible light such as two-step photoexcitation systems that were inspired by photosynthesis in nature, band engineering for producing novel photocatalysts that have both a high visible light absorption and suitable energy stages for water splitting, the improvement of new co catalysts for efficient H_2 or O_2 manufacture, assembly of effective photoelectrodes based on visible-light-responsive semiconductors, and the construction of tandem-type PEC water-splitting arrangements. Water splitting under visible light has been confirmed in numerous heterogeneous photocatalytic arrangements over the last decade and highly effective photoelectrodes have been advanced. The goal quantum yield for splitting water into H_2 and O_2 is 30% at 600 nm, which means a solar energy conversion efficiency of about 5%

Minggu et al. [47] expressed in their study that the main requirement for the photocell or photoreactor is to allow maximum light to reach the photoelectrode. They studied an overview of the photoelectrode configurations and the possible photocell and photoreactor design for hydrogen production by PEC water splitting. The ideal design of the photocell and photoreactor is such that the photoelectrode has a maximum exposure to light.

Gibson et al. [48] assessed the efficiency of the PV-electrolysis system and optimized the system by matching the voltage and maximum power output of the photovoltaics to the operational voltage of proton exchange membrane (PEM) electrolyzers. The optimization practice improved the hydrogen production efficiency to 12% for a solar powered PV-PEM electrolyzer which can deliver enough hydrogen to drive a fuel cell vehicle. They found that the solar to hydrogen effectiveness of PV-electrolyzer systems is maximized in case the voltage of the PV system matches the operational voltage of the electrolyzer.

Ismail et al. [49] indicated in their review that hydrogen generation from water splitting by UV and visible light-driven photocatalysis has made new advances. A number of synthetic amendment methods for adapting the electronic structure to improve the charge separation in the photocatalyst materials were discussed in that study. The studies concerning the development of new co-catalysts can provide supplementary breakthroughs in obtaining highly efficient photocatalysts. The quantum efficiency of photocatalyst materials upon visible and UV illumination were also reviewed.

Gibson et al. [50] proposed a mathematical model for predicting the efficiency of a PV-electrolyzer combination based on operating parameters including voltage, current, temperature, and gas output pressure. The model could predict PV-electrolyzer efficiency within ±0.4% accuracy and allow design of optimized solar hydrogen production systems from a range of PV and electrolyzer choices. They concluded that the efficiency of solar energy to electric conversion by PV modules decreases with increasing operating temperature, therefore a temperature control mechanism would be necessary.

Shi et al. [51] made a review on recent progress of some promising photoelectrode materials, including $BiVO_4$, α-Fe_2O_3, Ta_3N_5 photoanodes and Cu_2ZnSnS_4 photocathodes.

Among these three photoanode materials, onset potential of a $BiVO_4$ photoanode is the lowest, a Ta_3N_5 photoanode has the highest photocurrent, while α-Fe_2O_3 is superior for low cost and high stability. Since water splitting reaction occurs at electrode/electrolyte interface, which is very important for a PEC cell, the current problems need to be resolved for these three photoanode materials.

Kelly et al. [52] measured the light focusing features of two kinds of PEC reactors with curved surfaces and holding a clear aqueous fluid that resulted in the focusing of solar irradiance within the reactor. One reactor was a teardrop shaped plastic-film bag reactor, and the other was an acrylic spherical tank reactor. They concluded that a Fresnel lens could increase the photo enhancement in either the bag reactor or the spherical tank reactor. Increasing the solar irradiance on the PEC photoelectrode which is evaluated as the most expensive part of the overall system, can help to reduce the system cost, therefore a light-focusing reactor is an important system component.

Jacobsson et al. [53] performed analysis by theoretically designing a number of intermediate devices, successively going from PEC-cells to PV-electrolyzers. The analysis was performed by reviewing the physics behind the process of solar hydrogen production, and a number of intermediate devices were theoretically designed which illustrate how a classical PEC-device stepwise and gradually could be converted into a conventional PV-electrolyzer.

Tseng et al. [54] studied thermodynamic analysis of photoelectrochemical (PEC) hydrogen production. Because the energy required for splitting water decreases as temperature is increased, heating the system by using the long wavelength energy will increase the system efficiency. In their conclusion they indicated that in order to rise the maximum hydrogen production rate and the maximum solar to hydrogen efficiency, it is more effective to increase the quantum efficiency than raising the reaction temperature. On the other hand, increasing temperature also helps to increase the hydrogen production rate and solar to hydrogen efficiency.

James et al. [55] studied about multi-junction PV cells covered by thin films, which absorbs direct and diffuse radiations, with electrodes immersed in water solution closed by a transparent material in order to prevent the escape of gases. Furthermore, the electrodes were put in same the vessel although separated by cell's junctions in order to avoid mixture of the resulted gases in this process. In regard to H_2 production efficiency, although it is nominally 10%, it ranges between 8% and 12.4%. Moreover, future projections indicate the efficiency may change between 25% and 31%.

Acar et al. [54, 55] conducted energy, exergy and cost analyses studies for a continuous type hybrid photoelectrochemical hydrogen production system which generates Cl_2 and NaOH as useful commodities in addition to hydrogen. The efficiency of the integrated system is calculated as 4% with annual production of 2.8 kg of hydrogen per square meter of heliostat. The proposed system brings low hydrogen production cost and zero GHG emissions during operation in addition, the hybrid system has a potential to further lower production costs and rise energy and exergy efficiencies as photoelectrochemical cell technologies develop. Acar et al. [57] also analyzed a continuous type hybrid system thermodynamically for hydrogen manufacture which photoelectrochemically splits water and realizes chloralkali electrolysis.

Throughout the night time, the scheme can function fully with electricity and on cloudy days when solar irradiation is not satisfactory, electricity can be applied to help the photoelectrochemical process.

There is a conflict between two key necessities of a front photoelectrode in a tandem cell arrangement, namely, high transparency and high photocurrent density. To attain a solar-to-hydrogen efficiency beyond 10%, the photoelectrode of the front cell in tandem devices desires to be absorptive to efficiently use photons from the sunlight while also being transparent enough to feed the rear cell for unaided operation.

Shi et al. [58] demonstrated a 7.1% solar-to-hydrogen conversion efficiency without any external potential mentioning one of the highest efficiency to date for a PEC/solar cell tandem device. Doscher et al. [59] proposed a standardized PEC characterization to provide crucial insights and guidance for developing tandem devices. The IPCE analysis shows a practical maximum of about 10% solar-to-hydrogen efficiency for the classical upright epitaxial GaInP/GaAs tandem PEC design.

Li and Wu [60] prepared a review for the current status of the PEC water splitting semiconductors. TiO_2 is photochemically stable under harsh condition. However, owing to its large band gap, it can only absorb the ultraviolet (UV) light, which accounts for <5% of solar radiation. This leads to a very low theoretical maximum STH efficiency ranging between 1.3% and 2.2%. Therefore, different doping mechanism are under investigation. Fe_2O_3 has an ideal band gap (1.9-2.2 eV) thus can achieve a theoretical maximum solar-to-hydrogen (STH) of 12.9%, Deposition of IrO_2 on hematite surface has led to a photocurrent of 3.3 mA/cm^2 at 1.23 V (vs. RHE), shifted the on-set potential by 200 mV.

Reece et al. [61] have developed an amorphous silicon based triple junction PEC with earth abundant metals and Co-Pi as the catalyst. The cell has achieved an efficiency of 4.7% for solar water splitting. Also, Brillet et al. [62] have successfully constructed a tandem cell with hematite or WO_3 as the photoanode. The cell reached a solar-to-hydrogen efficiency of 3.1%. However, achieving a 10% solar-to-hydrogen efficiency is very difficult so far with a single material. Hence, improving this efficiency would be possible to combine multiple materials together to form a composite which can utilize the strengths of individual materials and compensate their shortcomings and even create new functionality. The other option to increase the solar-to-hydrogen efficiency is to use developed integrated systems for maximum solar light utilization as proposed in this thesis. In this way, overall solar-to-product efficiencies can be enhanced.

2.2 Photosensitive Materials and Electrodeposition

One of the most environmental-friendly processes for hydrogen production is the use of solar energy via photoelectrochemical (PEC) water splitting where a potential difference of at least 1.23 V, in addition to over potentials, is required. The required voltage can be partly supplied by the potential difference created within the photoelectrode (photocathode or photoanode depending on the photosensitive material) when there is sunlight illumination. The copper oxide is one of the alternative materials for PEC hydrogen production applications.

Various studies have been conducted in the literature for CuO/Cu_2O and other photo-

sensitive materials electrodeposition [63–73]. Electrodeposition process to obtain cuprous oxide is quite cheap with a possibility of making large area coatings. Zhao et al [74] reported that electrodeposition conditions of the Cu_2O thin films have important effects on the surface morphology, crystal quality, photocatalysis and photoelectric properties. However, the response to sunlight of Cu_2O thin films has been rarely reported. According to their results, the deposition potential has an important effect on the crystallographic orientation and particle size. They used different morphologies of cuprous oxide (Cu_2O) thin film electrodes which were electrodeposited on indium-doped tinoxide (ITO) substrates. Their study identified the dendritic morphology as superior to the granular morphology in producing photoelectrodes with good electrical continuity at a temperature of 20°C, slightly acidic medium and photocurrent density of 0.06 mA/cm^2. Amano et al. [75] used indirect photoelectrochemical water splitting achieved by using a Cu_2O electrode, catalyst and redox couple as an electron mediator from the electrode to the catalyst. The study highlighted the crystalline composition of the outermost surface of Cu_2O films as important factor in regulating photo-cathodic reactions.

The photo-energy conversation efficiency was about 0.01% under the visible illumination. Cu_2O may only be deposited electrochemically in a restricted voltage limits, at pH 9-11 between approximately -0.1 to -0.6 V vs SCE as reported by Jongh et al.[64]. The pH of the electrodeposition mixture carried a solid impact on the characteristics of the layers. At pH 7 and 8, copper was made at upper current densities. For pH 9-12, well-defined layers of faceted Cu_2O crystals can be obtained. Georgieva and Ristov [76] performed the study by preparing semi-conductor copper oxide layers with electrodeposition onto viable conducting glass covered with indium tin oxide coated by spraying method. The copper oxide layers were electrodeposited with a galvanostatic process from an alkaline $CuSO_4$ bath comprising lactic acid and sodium hydroxide at a temperature of 60°C. The film thickness was in the range of 4–6 μm. The best values of V_{oc}=340 mV and I_{sc}=245 mA/cm^2 were obtained by depositing graphite paste and illumination by an artificial white light source of 100 mW/cm^2 The total cell active area was 1 cm^2 with current density of 0.57 mA/cm^2. The efficiency of the cell was found to be 0.0234%. The cell showed photovoltaic features after heat management of the layers for 3 h at 130°C.

ZnO/Cu_2O heterojunction solar cells were made by consecutive cathodic electrodeposition of ZnO and Cu_2O on glass plates covered with a SnO_2 transparent conductive oxide layer (Asahi glass) in the study by Jeong et al.[68]. The impact of the electro deposition situations (pH/temperature) on the performance of the cell has been examined with film thickness changing between 2-4 μm. The cells made with a Cu_2O layer deposited at high pH about 12 and moderate temperature about 50°C and current density 0.75 mA/cm^2 for Cu_2O and 1 mA/cm^2 for ZnO shown conversion efficiency as high as 0.41%.

Bao et al. [77] deposited Cu_2O films using a ZF-8 potentiostat, completed with a standard three-electrode electrochemical cell. A platinum piece and a saturated calomel electrode (SCE) were utilized as a counter electrode and a reference electrode, respectively. A well-polished stainless steel with a 2 cm^2 surface area was used as a work electrode. The Cu_2O films were deposited electrochemically at a persistent deposition potential of −0.1 and −0.2 V,

measured with respect to SCE. The chemical solution confined 0.1 M Cu (II) salt and 0.75 M lactic acid as chelating mediator to alleviate the Cu^{2+} ion. Its pH was set to 9 with sodium hydroxide. The temperature of the bath was 50°C. Three or more films were deposited under each deposition circumstance to confirm reproducibility. The electrodeposition conditions include a pH of 9 and a temperature of 50°C where they recorded a photocurrent density of 0.57 mA/cm^2. However, the efficiency and the electrodeposition current values were neither specified nor provided. CuO nanoparticles were deposited by Chiang et al. [78] in a solution based process and used to prepare photoactive porous nanostructured CuO thin film electrodes for hydrogen generation via a photoelectrochemical cell. The particle and film morphologies were well controlled in the processes. The porous structure of the CuO film made by this process (powder prepared at 60°C and sintered at 600°C for 1 h) had increased surface area and a high photocurrent and charge carrier density. These films were demonstrated to have 0.91% solar conversion efficiency at applied voltage of -0.55 V vs. Ag/AgCl in 1 M KOH electrolyte with 1 sun (AM1.5G) illumination. Electrodeposition of Cu_2O was also investigated by Haller et al. [79] for potentials of deposition ranging from −0.7 to −1.05 V vs. MSE with electrolyte at pH 9 and 12.5. The effect of chloride addition either from $CuCl_2$ or KCl and hence annealing has also been studied. Crystal quality was found to depend on the potential of deposition and an optimum was found for deposition at −0.9 V vs. MSE in an electrolyte at pH 12.5 and free of chloride. In the best conditions, ZnO–Cu_2O heterojunction could reach efficiency up to 0.33%.

Casallas et al. [80] also conducted electrodeposition to acquire a photocathode by deposition of copper oxide semiconductors on the surface of the cathode of a membrane electrode assembly entailing of a NAFION® membrane with two surfaces of which were coated with carbon layers and doped with electro-catalysts.

Because of having higher absorption coefficient in the visible region of the solar light spectrum, Cu_2O is preferred in applications for solar energy conversion and photoelectrochemical hydrogen production applications. Cu_2O is a p-type semiconductor with direct band-gap of 1.9 to 2.2 eV. However, there are some potential drawbacks of copper oxide coatings, such as probability of photo-corrosion which might be caused since oxidation and reduction potentials of Cu_2O and CuO drop within the bandgap [81]. The other drawback may be the diffusion length of photo-generated charge carriers due to having shorter than light absorption depth. In order to overcome the photo-corrosion, different techniques have been proposed in the literature such as formation of composite coatings or deposition of thin protective layers such as the one performed by Tran et al. [82] by applying a composite with reduced graphene oxide.

There are various ways for photosensitive material coating in the literature such as chemical bath deposition (CBD), electrodeposition (ED) and thermal evaporation [81, 82]. Nevertheless, some of the methods require harsh coating environments, such as an ultra-high vacuum, higher temperatures, quite lengthy period of time, and complex phases. Consequently, considering large scale hydrogen production plants from photoelectrochemical methods will necessitate to develop lower temperature, atmospheric, and modest solution-based techniques for Cu_2O coatings. Hence, electrodeposition technique is a promising method to make

photoelectrochemical cells and also dye sensitized solar cells. Because, this method is a low cost, simple, and environmentally friendly [85].

Some researchers performed electrodeposition of different chemicals, such as Fe_3O_4 [86] where they highlighted the advantage of using low-temperature electrochemical deposition methods to make high-performance Fe_3O_4 electrodes. Dubal et al. [87] studied copper oxide multilayer nano-sheets for synthesizing in a simple and inexpensive chemical bath deposition method. They resulted that the chemically deposited copper oxide thin films appear to be promising electrode material for electrochemical capacitors. Daltin et al. [88] deposited in potentiostatic way cuprous oxide nanowires in polycarbonate membrane by cathodic reduction of alkaline cupric lactate solution where they defined the optimum parameters for the deposition of nanowires as temperature of 70°C, pH of 9.1, and applied potential of 0.9 V vs. SSE. Zhou and Switzer [89] conducted polycrystalline copper (I) oxide films on stainless steel substrate by galvanostatic electrodeposition method where the substrate, which were used as cathodes, were disks of 430 stainless steel with 15 mm in diameter. In this thesis, copper oxide is electrodeposited on the cathode electrode having a very larger area than literature studies.

2.3 Electrochemistry of the Photoelectrochemical Cells

Gomadam and Weidner [90] reviewed electrochemical impedance spectroscopy (EIS) analyses for proton exchange membrane fuel cells. They showed various type of EIS models of PEM fuel cells by emphasizing the importance of continuum mechanics-based analyses. Lopes et al. [91] measured photocurrent features of PEC cell for solar hydrogen production via EIS method. They used a photoanode with Fe_2O_3 and obtained photocurrent density of about 89.7 $\mu A/cm^2$ at an applied voltage of 1.23 V_{RHE}. Their impedance analysis showed that the charge transfer resistances are lower under irradiation.

Siracusano et al. [92] also conducted experimental EIS study for a 5 cm^2 PEM cell electrolyzer in a temperature range from 25 to 80°C and under atmospheric pressure. They heated the deionized water before entering the cell with a flow rate of 2 mL/min. They observed a low series resistance corresponding to 0.13 Ω cm^2 the sulfonated Polysulfone membrane at 80°C at 1.8 V. Bohra and Smith [93] studied the photoelectrochemical performance of $CuWO_4$ as photo-anode for hydrogen production. They applied EIS ranging from 0 V to 0.5 V vs. Ag/AgCl and observed that charge separation is the dominant limitation for this material. They obtained a photocurrent density of 0.13 mA/cm^2 at 1.23 V vs. RHE. Dedigama et al. [94] examined the association of flow inside the PEM cell and electrochemical performance of the cell using thermal imaging and EIS. They obtained EIS results for the applied potentials of 1.5 V to 2.5 V. They explained that the EIS results showed better mass transport properties related with an increase in cell voltage/current density.

Rong and Han [95] developed a monolithic quasi-solid-state dye-sensitized solar cell based on carbon-counter electrode. Using EIS method, they showed the activity of normal carbon-counter electrode enhanced afterward being improved with graphene. Because it compromises rich defects and adequate functional groups. Yi and Song [96] presented an EIS study for PEM fuel cell and showed the size of the semicircle can change by altering the oxygen

transport resistances within the catalyst layer. They obtained AC impedance at constant current with a maximum current density of 0.3 A/cm^2 where the applied AC voltage was 10 mV from 0.05 to 10 kHz frequency. Cho et al. [97] collected EIS data and plotted Nyquist graphs for the PEM fuel cell stack having a capacity of 1 kW assembled with graphite, AISI 316, TiN/316 bipolar plates. The applied voltage was 0.85V and the operating temperature was about 80°C with 1 atm pressure. Jia et al. [98] studied for dye synthesized solar cells with the impedance spectra at frequencies ranging from 1 MHz to 0.1 Hz. In their study, they found that the nitrogen doped hollow carbon nanoparticles yield better electro-catalytic action for I_3^- reduction, higher than that of the platinum catalyst.

2.4 Solar Concentrators and Solar Spectrum Effect on PV and Photoelectrochemical Hydrogen Production

Faine et al. [99] specified in their study that solar spectral irradiance deviations are influenced by the bandgap of the device as well as on the number of junctions. Turbidity and air mass variations impact the efficiencies of high-bandgap devices more than those of low-bandgap devices. Nevertheless, water-vapor differences have very slight influence on high-bandgap devices compared with low-bandgap devices.

Nagae et al. [100] confirmed that the FOF (field output factor) of a-Si PV components are considerably influenced by the difference of the instance spectrum of light. In their study, for stacked a-Si PV modules, slight effect of both average photon energy and panel temperature on FOF was perceived. Minemoto et al. [101] examined the impacts of spectral irradiance scatterings on the outside functioning of amorphous Si/thin-film crystalline Si stacked photovoltaic (PV) modules mounted at Shiga-prefecture in Japan. They revealed that more than 95% of yearly total spectra were blue-rich in comparison to AM (Air mass) 1.5 standard solar spectrum.

Nann and Emery [102] showed in their experiments that efficacies of amorphous silicon cells differ by 10% between winter and summer months due to spectral effects only. Since the PV efficiency depends on solar spectra in the field, the PV assembly must be designed so as to attain the most effective performance in natural outside sunlight.

Gottschalg et al. [103] presented that there is a main impact that results from disparities in the total irradiance in the spectrally beneficial collection of the device, and a secondary effect observed in double junction devices which is related to details of their structure. Saloux et al. [104] developed electrical and thermal models of PV/T system operating under different environmental conditions such as solar intensity and ambient temperature, where irreversibility in addition to energy and exergy efficiencies were taken into account.

Sudhakar et al. [105] conducted energy and exergy analyses of PV modules to govern exergy destruction in the process of PV taking into account the different operational and electrical factors. They determined that the exergy destructions increased with up surging cell temperature and the exergy efficiency could be improved in case the heat could be successfully extracted from the PV module surface. They found the energy and exergy efficiencies for PV panel as 6.4% and 8.5%, respectively.

Sahin et al. [106] performed thermodynamic analysis of solar photovoltaic cells using exergetic approach. Applying the exergy analysis into a PV module, they found the possible losses and evaluated the efficiencies. Their energy efficiency was calculated in the range of 7% to 12% while exergy efficiency variations from 2% to 8%. Rabady [107] studied theoretically hybrid thermo-photovoltaic system optimization that employs a 90% efficient solar thermal convertor with 82% solar to hydrogen conversion efficiency. They concluded that increasing the absorber thermal efficiency by using better materials and technologies would contribute significantly to the hydrogen production efficiency because of the close to quadratic relation between the two efficiencies based on the optimization model and theoretical findings of their work. Khamooshi et al. [108] reviewed solar photovoltaic concentrator technologies and their characteristics and properties such as their fundamental functions, efficiencies, concentration ratio, tracking systems, cooling systems, and brief comparison in some parts. They concluded that choosing the complete CPV containing the concentrator, tracking system, and cooling system is highly dependent on some limitation factors such as the climate conditions, geographical conditions, budget limits, and space limits.

A Fresnel lens can be combined into a projection lens structure to diminish the number of apparatuses, cost, dimension, and mass cost. They are also frequently used as part of the screen system in rear projection monitors. Fresnel lenses consist of a series of concentric grooves imprinted into plastic. Fresnel lens solar concentrators remain to fulfill a market requirement as a system component in high volume cost effective concentrating photovoltaic (CPV) power generation [107, 108]. Wu et al. [110] experimentally studied the effect of various parameters such as temperature and solar intensity, different ambient air temperatures, and natural and forced convection on the system. They mainly analyzed the thermal behavior of Fresnel lens and PV with respect to various ambient conditions where the solar intensity was varied between 200 W/m^2 to 1000 W/m^2.

2.5 Spectrum Splitting Mechanisms and Applications

It is known that electromagnetic radiation surrounds everything on earth and space. This basic form of interaction does not require a material support to propagate; it can pass through a true vacuum and travel distances measured in light years without attenuation [111]. Solar light, consisting of a spectrum of photons with a temperature around 6000 K, travels about 8 min before reaching earth. Life on earth depends on light and the photo physical and photochemical processes induced by light upon the earth's systems. When photon interacts with matter, a multitude of photo physical processes may occur [111]. At wavelengths shorter than a few mm, electromagnetic waves behave as quanta of energies, or photons. The infrared photons extend from micrometer to mm wavelengths. The visible spectrum is 400–700 nm. The ultraviolet spectrum extends in the range of 10 pm to 400 nm. The X-ray photons have wavelengths from 10 fm to a few pm. Gamma ray photons have wavelengths of pm scale and below. Solar spectrum splitting is a recent approach for maximum harvesting of solar energy. Instead of wasting some portion of the incoming photons which are not utilized in the system, they are separated before entering the mechanism. In this way, only useful photons interact with the system which decreases the destruction and losses.

Spectral splitting applications are partially studied in the literature for various purposes. Mojiri et al. [112] introduced a method which filters sunlight for high temperature hybrid solar receivers and is employed in linear solar concentrators. The researchers combined a semiconductor doped glass with propylene glycol to work instantaneously as the heat transfer fluid and a band pass filter to set the optimal wavelength band, 700–1100 nm, in order to fulfill the silicon solar cells requirements of operation. This combination resulted in low reflection fatalities because of effective optical matching between the optical mechanisms. An et al. [113] investigated experimentally solar spectrum splitting through the utilization of a Cu_9S_5 nano fluid as an optical filter for solar PV/T collectors. In this method, it was possible to reach efficiencies about 34.2% which is practically the double of the ones analyzed in non-filtered experiments. Furthermore, it was compared monocrystalline and polycrystalline cells under different prepared solutions by concentrating the light using Fresnel lens.

In another research, Stanley et al. [114] developed a spectral beam splitting mechanism where the wavelength was directed between 700-1100 nm to the PV cells. It was achieved high grade heat thermal efficiencies of 31% relative to the thermal beam splitting fraction at a receiver temperature of 120°C in addition to a total system efficiency of 50%. Crisostomo et al. [115] studied an optical model for PV/T collectors using beam splitters. In their research, the wavelengths were directed to the optimal values located between 732 nm to 1067 nm, which represent the region of the spectrum that should be directed to the PV cells, for the spectrum division in the collector. Their method indicated that, under this particular partition, 47% more power can be delivered from the collector in relation to a concentrated PV stand-alone system under the same concentration ratio. Moreover, the design of the beam splitting devices was addressed by using SiN_x and SiO_2 as, respectively, high and low refractive index materials in the profile of a multilayer thin film filter that was included in the ray tracing mode.

Kim et al. [116] emphasized that using an appropriate technique for cooling of PV module by means of heat dissipation process is important. The energy efficiency of a common photovoltaic panel usually falls at a rate of 0.5%/°C based on the temperature increase. Vorndran et al. [117] designed a holographic module to split light into two spectral bands for hybrid solar energy conversion. This design was applied to PV/T collectors in order to evaluate their performances together with losses. By other means, Willars-Rodríguez et al. [118] investigated the utilization of Fresnel lenses for thermoelectric generators and PV applications in the way it was obtained a combined electrical efficiency of approximately 20% and thermal efficiency of 40%. In addition, it was evaluated the economic aspects of the unit for practicability. Xu et al. [119] also investigated the hybrid systems for solar PV and thermoelectric generators for better photon management. It was performed multiple simulations to study the optical parameters such as absorptivity and reflectivity which demonstrated that better photon management in full spectrum can also be appointed for many other types of thin-film PV strategies used in the hybrid system.

Although, solar light splitting has been studied by many researchers for various applications, it has not been employed for integrated hydrogen, ammonia and electricity production in a combined manner so far. Therefore, this thesis uses the advantages of spectrum splitting for higher integrated system performance.

2.6 Solar PV and PV/T Systems

Different attitudes to exergy efficiency descriptions of PV and PV/T systems have been implemented in the literature. In addition, various experimental studies were conducted to assess energy and exergy efficiencies of PV and PV/T systems.

Akyuz et al. [120] determined the exergetic efficiency of a PV cell based on the position of the sun and time in addition to incidence angle and the day of the year to calculate the PV exergy efficiency. Ceylan et al. [121] performed experimental studies for PV module efficiency finding an overall exergy efficiency of about 17% for 45˚C set temperature and 21% for 55˚C set temperature.

Cotfas et al. [122] analyzed three types of photovoltaic cells under medium concentrated sunlight: mono and polycrystalline silicon and CdTe. Three parameters of photovoltaic cells, Io the reverse saturation current, series resistance Rs and the ideality factor of diode m, decrease with the illumination. The short circuit and the photo generated currents present a growth which is proportional with the illumination, while the open circuit voltage has a logarithmic dependence. Rawat et al. [123] presented a study for energy and exergy efficiencies of PV schemes to describe the long-term operation in actual working conditions. The degradation rate of 3.2 kWP CdTe PV system is found to be 0.18% per year after 23 months of operation in composite climate which is lower than the reported degradation rate of former CdTe technology.

Green et al. [124] report the recent efficiencies on different type of PV cells. Presently Si (multi-crystalline) PV cell set effectiveness can increase up to 26.3 % while thin film (GaAs) kinds can be more effective getting up to 28.8% for terrestrial cells. Moreover, for a concentration of 508 suns, GaInAsP/GaInAs based multi-junction cell effectiveness was measured as 46% for an actually small cell with an area of 0.0520 cm^2. Wu et al. [125] prepared a wide review and methodical categorization of methodology for computing heat and exergy fatalities of standard PV/T systems. They highlighted the significance of detecting the reasons and places of the thermodynamic restriction, detection of exergy loss within mechanisms and scatterings in PV/T system. They resulted that for the computation of heat and exergy losses in these systems, still more work is required. Royne et al. [126] overviewed numerous systems that can be utilized for cooling of photovoltaic cells particularly under concentrated light. They implied that cooling system desires a scheme to keep the cell temperature low and uniform, be simple and reliable, keep reliant power consumption to a minimum and permit the utilization of removed thermal heat.

2.7 Life Cycle Assessment (LCA) of Hydrogen and Ammonia Production

In the open literature, various studies were performed for LCA of hydrogen production options but ammonia production has not been intensively researched. Zamfirescu and Dincer [127] investigated the use of ammonia as a sustainable fuel in comparison with other conventional fuels. They analyzed the possible benefits and technical benefits of using ammonia as a sustainable fuel for power generation on vehicles based on some performance indicators including the system efficiency, the driving distance, fuel tank compactness and the cost of driving. Verma and Kumar [128] offered a study to evaluate life cycle GHG emissions in H_2

manufacture from UCG with and without CCS. Employment of CCS method permits a substantial decrease in total LCA releases in H_2 generation from UCG. Purge gas combustion and venting of gases in the CO_2 elimination unit are the main influences in the life cycle GHG emissions. Kalinci et al. [129] completed a life cycle evaluation of hydrogen generation from CFBG/DG biomass to use the generated hydrogen in PEM fuel cell cars by investigating the costs of GHG emissions decrease. The supreme consumption rate of energy was perceived in the compression and transport of hydrogen phases for the CFBG option. Koroneos et al. [130] showed life cycle evaluation for numerous hydrogen generation systems counting conventional and non-conventional selections. The usage of wind, hydropower and solar thermal power for the generation of hydrogen are the greatest eco-friendly techniques among the other studied options in their study. Ammonia is an alternative source for transportation sector although electric vehicles are one of the competitors. Granovskii et al. [131] studied life cycle assessment of hydrogen and gasoline vehicles by containing fuel generation and utilization in vehicles powered by fuel cells and internal combustion engines. They evaluated and compared the efficiencies and environmental impacts by resulting that wind electrolysis based hydrogen and PEM fuel cell vehicle is the most environmentally benign method. Kahr et al. [35] studied estimation of GHG emissions from synthetic nitrogen fertilizer utilization in Chinese agriculture and investigate the prospective for GHG emission decreases from performance enhancements in nitrogen fertilizers including ammonia generation and utilization. China's ammonia generation is mainly dependent on coal at the moment. Hacatoglu et al. [132] reported life cycle assessment of a nuclear-based copper-chlorine hydrogen generation method, containing approximations of fossil fuel energy use and greenhouse gas (GHG) emissions. They compared also other paths indicating that the performance of the method is similar to hydrogen produced by wind-based water electrolysis.

In the study by Utgikar and Thiesen [133] the GWP of high temperature electrolysis was found to be about 2 kg CO_2 per kilogram of hydrogen produced corresponding to one sixth of SMR method. It was also shown that high temperature electrolysis plant efficiency connecting with high temperature gas cooled reactor can yield over 53% hydrogen production efficiency at 800°C operation. Acar and Dincer [134] performed an extensive study for economic, environmental and social impacts of various hydrogen production methods including solar based options.

Ozbilen et al. [135–137] considered nuclear based hydrogen production via thermochemical water splitting in a CuCl cycle for the environmental effects. They performed exergetic LCA on the CuCl hydrogen production and the results imply that uranium treating has the largest exergy destruction share in the process. Cetinkaya et al. [138] calculated inclusive life cycle assessment for five different approaches of hydrogen production counting steam methane reforming, coal gasification, water electrolysis via wind and solar, and thermochemical water splitting with a Cu-Cl cycle. In their conclusions, the lowest polluting options is found to be wind electrolysis based hydrogen production, which is then followed by solar PV based electrolysis process. Both of the renewable energy systems can be used in appropriate places.

Makhlouf et al. [33] studies a life cycle assessment of 1 tonne of ammonia formed in Algeria for anhydrous liquid ammonia. They designated that Algerian ammonia plant requires in general more power than world average. Also, they implied that reformer processes are the key reasons of over consumption of energy and GHG emissions meaning that there is low effective catalytic reaction in which the catalysts were utilized more than 10 years. Recently, multiple studies have been performed for life cycle assessment ammonia production and utilization by Bicer et. al. [16, 137–139].

2.8 Novel Ammonia Production Methods

There are multiple pathways for ammonia synthesis besides mostly used Haber-Bosch process within the literature. For the electrolytic routes, required hydrogen can be sourced from natural gas like the Haber-Bosch process or electrolysis of water, or even decomposition of an organic liquid such as ethanol. When hydrogen is produced from water electrolysis utilizing a renewable energy source such as wind or solar, environmentally pollutant emissions would noticeably diminish for ammonia production. Water can also be utilized as a source of hydrogen inside the electrolytic cell through its reaction in the electrochemical process. The use of water as a source of hydrogen would also be helpful in eliminating any issues of catalyst poisoning due to traces of Sulphur compounds or CO which are common impurities in hydrogen produced via steam reforming of natural gas. The process can be carried out under ambient conditions or at higher temperatures depending on the type of the electrolyte material used. For high temperature electrolytic routes of ammonia production, the use of waste heat from thermal or nuclear power plants or heat from renewable energy sources like solar would make the overall process more environmentally friendly. Ammonia production from hydrogen and nitrogen is exothermic in nature and is facilitated by high pressures and low temperatures. Thus a balance between the operating temperature, pressure and the ammonia yield needs to be proven for each electrochemical system in determining ammonia production rates.

There are four main categories of electrolytes used for ammonia production as shown schematically in Fig. 2.1. These are listed as follows:

- Liquid electrolytes which operate near room temperature
- Molten salt electrolytes operating at intermediate temperatures (300-500˚C)
- Composite electrolytes consisting of a traditional solid electrolyte mixed with a low melting salt (300-700˚C)
- Solid electrolytes with a wide operating temperature range from near room temperature up to 700-800˚C depending on the type of electrolyte membrane used.

Electrochemical synthesis of ammonia is made possible by research and advances in materials at the anode, cathode, and electrolyte. One of the major significant developments have been the test with proton exchange membranes and specific combinations of anode and cathode materials which have resulted in significant results. Xu et al. [142] investigated synthesis of ammonia at atmospheric pressure and low temperature electrochemically, using the SFCN materials as the cathode, a Nafion membrane as the electrolyte, nickel-doped SDC (Ni-SDC) as the anode and silver-platinum paste as the current collector. Ammonia was produced from 25 to 100℃ temperature levels when the SFCN materials were utilized as cathode, with

$SmFe_{0.7}Cu_{0.1}Ni_{0.2}O_3$ which gives the maximum rates of ammonia formation. The maximum rate of formation of ammonia was 1.13×10^{-8} mol·cm^{-2}·s^{-1} at 80℃, and the current efficiency is obtained as high as 90.4%.

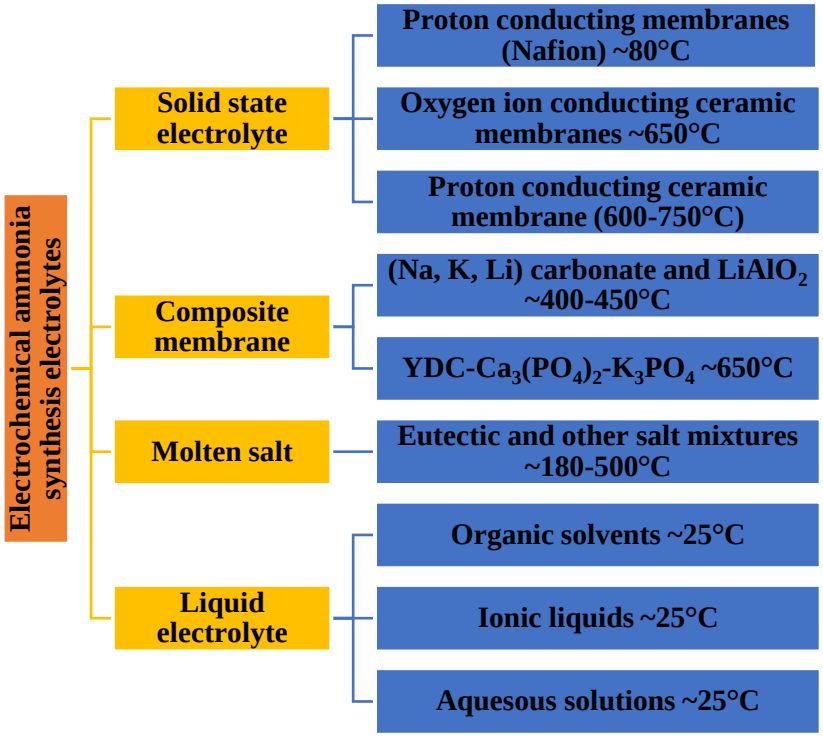

Fig. 2.1 Main electrochemical ammonia synthesis electrolyte types (modified from [143]).

Other electrolyte based systems have been researched as well and the results are shown in [143]. A comparison of current (coulombic) efficiency values from open literature is illustrated in Fig. 2.2.

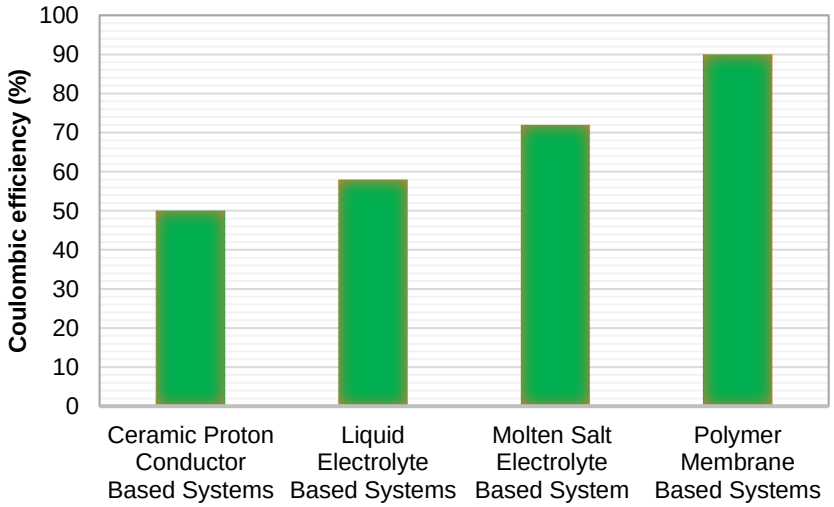

Fig. 2.2 Coulombic efficiencies of different electrochemical synthesis methods (data from Refs. [63-69]).

Murakami et al. [144] proposed an electrolytic ammonia synthesis method from methane and nitrogen gases in molten salt under atmospheric pressure. Their experiments confirmed that ammonia was synthesized by potentiostatic electrolysis using a methane gas electrode at 2.1 V and 773 K. Another way of producing ammonia electrochemically is by reducing nitrate in aqueous solutions. As discussed by Fanning [145] this nitrate is available from drinking water supplies and even nuclear waste. Not only ammonia is produced in some cases but also hydrogen and nitrite can be produced with high reduction efficiencies with respect to current supply.

Other considerations with current state of the art are important to note. When hydrogen is used as a reactant in ammonia synthesis the source must be considered which is majorly from fossil fuels and a small portion from electrolysis which has an efficiency of about 65-80% [146]. Ammonia cracking is also required when supplying fuel cells that require pure hydrogen gas, this must be done at temperatures above 500°C [146]. Li et al. [147] reported an appliance of electrochemical ammonia production through an iron intermediate in which H_2 and NH_3 are cogenerated by different electron transmission paths. At 200 mA/cm^2, over 90% of applied current drives hydrogen, rather than ammonia, formation. Lower temperature supports greater electrolyte hydration. To synthesize ammonia by electrolysis in hydroxide, water, N_2 (or air), and nanoscopic Fe_2O_3 are simultaneously required. Lan et al. [148] reported an artificial ammonia synthesis bypassing N_2 separation and H_2 production phases. A maximum ammonia production rate of 1.14×10^{-5} mol m^{-2} s^{-1} was realized when a voltage of 1.6 V was applied. They implied that in the future, other low cost ammonia synthesis catalysts such as Co_3Mo_3N and $Ni_2Mo_3N_{41}$ can be used to exchange Pt for selective ammonia synthesis under minor situations. A brief description of the novel studies for ammonia production is given in Table 2.1.

Table 2.1 The novel studies for ammonia synthesis in the literature.

Method	**Reference**	**Results**
Molten Salt Electrolyte Based System	Licht et al. [149]	Upwards of 30% current efficiency using water, and air as reactants. Using molten NaOH-KOH mixture with nanoscale Fe_2O_3 as catalyst. Nickel monel mesh with nickel electrodes.
Liquid Electrolyte Based Systems	Giddey et al. [143]	Iron is used at the cathode at operating temperature of 50°C when nitrogen was supplied to cathode at a pressure of 50 atm producing 58% current efficiency
Ceramic Proton Conductor Based Systems	Giddey et al. [143]	Ceramic proton conductor systems use vacancies in the chemical structures to conduct charged species, the net conversion efficiency was found at about only 50% because of the decomposition of ammonia back to hydrogen and nitrogen
Polymer Membrane Based Systems.	Garagounis et al. [150]	The highest product yield was demonstrated from a solid Nafion membrane with a mixed oxide ($SmFe_{0.7}Cu_{0.1}Ni_{0.2}O_3$). The rate of ammonia formation reported was 1.13×10^{-8} mol s^{-1} cm^{-2}, obtained at 80°C.

A variety of factors need to be analyzed when selecting the cell material such as system operating temperature, current density, pressure, and conductivity which all affect the ammonia production rate. It is important to note that conductivity of a solid electrolyte increases exponentially with temperature and by reducing cell thickness as reported by Giddey et al. [143].

Garagounis et al. [150] summarized the test results of studies within the last 15 years using electrolyte cells. More than 30 electrolyte materials with 15 catalysts that were used as working electrodes (cathode) were tested. The polymer Nafion yielded the highest rate of ammonia formation at a very low temperature. Nafion can also be used as a proton conductor with and a Ru/C cathode which yielded NH_3 from H_2O and N_2 at 90°C. These low operating temperatures are sought after when designing new systems because of the reduced energy input required and lower rate of decomposition of the ammonia formed. As an alternative approach, the use of oxygen ion (O_2^-) conductors where steam and nitrogen are introduced together at the cathode should be considered. The rate of NH_3 production was however very small in a demonstration at 500°C but improved by up to two orders of magnitude at higher temperatures as reported by Skodra et al. [151]. Furthermore, NH_3 synthesis using molten salt electrolyte based systems can yield high conversion ratios similar to that of polymer based membranes.

Serizawa et al. [152] reported conversion ratios as high as 70% of Li_3N into NH_3 using a molten LiCl–KCl-CsCl system at temperatures between 360 and 390°C. These conversion ratios have been achieved despite the side reactions where parts of NH_3 were dissolved in the melt in the form of imide (NH_2^-) and amide (NH_2^-) anions resulting in a lower NH_3 yield. Kyriakou et al. [153] recently reported extensive literature data about low temperature, medium temperature and high temperature electrochemical NH_3 synthesis routes showing that the synthesis rates can reach up to 3.3×10^{-8} mol/s cm^2. Shipman and Symes [154] presented the recent developments in electrochemical NH_3 production and they categorized the sources of proton as water, hydrogen and sacrificial proton donors. They resulted that the techniques keeping the temperatures in the range of 100°C and 300°C such as molten salt may well demonstrate to be the most efficient.

2.8.1 Liquid electrolyte based systems

In this method, Lithium perchlorate ($LiClO_4$ (0.2 M)) in tetrahydrofuran as the electrolyte and ethanol (0.18 M) as the hydrogen source can be used. In the previous studies [155], a low current efficiency of 3-5% was achieved considering that the current density was also low (2 mA/cm^2). The current efficiency may improve under a different set of experimental conditions by varying the pressure and temperature values, however, under the conditions of test, breakdown of the ionic liquid electrolyte was observed indicating severe distresses about the long term capability of the process. Furthermore the solubility of Li salts has been reported to be low in many ionic liquids [155].

Kim et al. [154, 155] also performed electrochemical synthesis of ammonia in molten LiCl-KCl-CsCl electrolyte by a mixture of catalysts as nano-Fe_2O_3 and $CoFe_2O_4$. Their maximum formation rate was 3×10^{-10} mol/s cm^2 where they used water and nitrogen for the reaction.

2.8.2 Composite membrane based systems

The composite electrolytes consist of one or more different ionic conducting phases and the second or third phase is added to the parent phase to modify electrical, thermal or mechanical properties. For example, an alkali metal carbonate and an oxide such as $LiAlO_2$ or Sm_2O_3 doped CeO_2 have been shown to have oxygen-ion, carbonate ion and even proton conductivity under certain conditions (e.g. in the presence of hydrogen) [156, 157]. Such materials have been under investigation as potential electrolytes for intermediate temperature (400-800°C) fuel cells and are also being employed to study ammonia production rates under a range of operating conditions.

2.8.3 Solid state electrolyte

A number of different systems, based either on proton or mixed proton/oxygen-ion conducting solid electrolytes, are undergoing research and development for application in electrochemical ammonia synthesis. The key instruments of the solid-state electrochemical system are two porous electrodes anode and cathode divided by a compact solid electrolyte, which permits ion transport of either protons or oxide ions and supports as a barrier to gas diffusion [158, 159]. Solid-state proton conductors (SSPC) denote a class of ionic solid electrolytes which have the ability to transfer hydrogen ions (H^+) [162]. However, this method has some disadvantages such as high temperature necessities and creation of secondary phases [163–165]. A schematic diagram of solid state ammonia synthesis is shown in Fig. 2.3. Hydrogen can also be directly used in the SSAS process. The SSAS system can be coupled to photoelectrochemical hydrogen production as illustrated in Fig. 2.4.

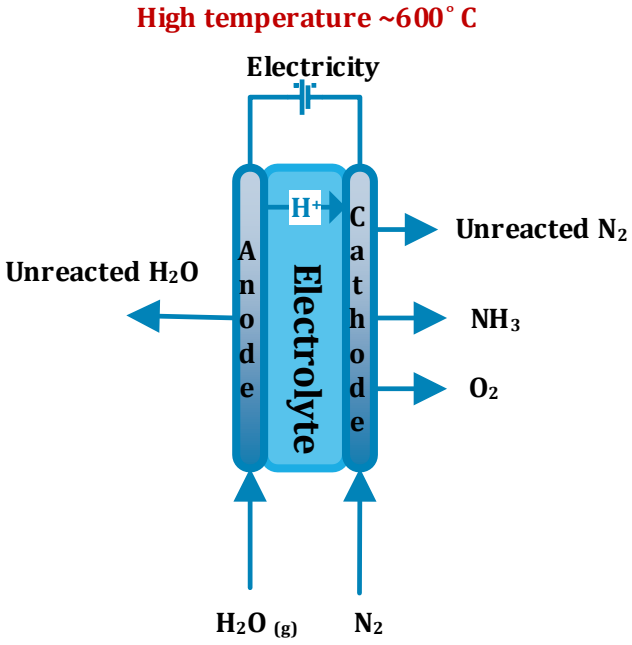

Fig. 2.1 Steam based SSAS in a high temperature electrochemical ammonia synthesis cell.

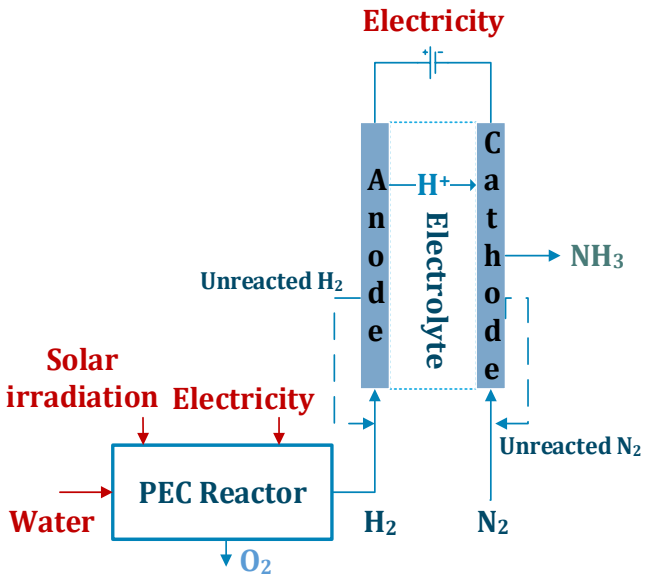

Fig. 2.2 SSAS using photoelectrochemically generated hydrogen.

2.8.4 Ceramic/inorganic proton conducting solid electrolyte based systems

A typical electrolytic cell for ammonia synthesis is fabricated by depositing electrode (catalyst) coatings on both sides of the proton conducting membrane. These porous electrodes are typically screen printed or brush coated on ceramic proton conductor membranes followed by heat treatment. Water or hydrogen is fed to the anode and nitrogen to the cathode, and ammonia is produced on the cathode side of the cell. The current collection is achieved by placing metallic meshes or sheets in contact with these electrodes. The proton conducting ceramic membrane, along with cathode or ammonia synthesis catalyst, are most important components in these systems. These membranes are required to reveal substantial proton conductivity at temperatures above 400˚C [143]. In another study, researchers used a proton-conducting solid electrolyte at 450°C to 700°C with Ru based catalyst. They resulted that the conversion rates are lower compared to nitrogen or steam because of the low conductivity of the working electrode [166].

2.8.4.1 Polymer membrane based systems

There are various types of polymer ion exchange membranes available that can be used as an electrolyte in electrochemical ammonia synthesis cells. These membranes can be operated in the temperature range from room temperature to 120˚C. Nafion membranes are the most popular proton conducting membranes being used in the chlor-alkali industry, and in the polymer electrolyte membrane (PEM) based fuel cells and electrolysis cells [143]. Despite some stability issues for polymer membranes in the presence of ammonia, there are many advantages of using these membranes due to their high proton conductivities at lower temperatures and a large amount of information available for cell construction and assembly due to their usage in fuel cells. The low temperature operation would reduce the rate of decomposition of ammonia formed and avoid several other high temperature materials related

issues. In another study with a Nafion divider in aqueous 2 M KOH and a Ru on cathode allowed ammonia generation from water and nitrogen at a rate of 2.8×10^{-12} mol NH_3 s^{-1} cm^{-2} and coulombic efficiency of 0.9% at 20°C. Also, at 90°C, a maximum rate of 2.1×10^{-11} mol s^{-1} cm^{-2} at 0.2% efficiency was observed [167]. Membrane based applications can be performed at quite lower temperatures than molten salt electrolyte based methods. Having Pt/C on a gas diffusion layer at both electrodes and room temperature, using Nafion as the electrolyte produced NH_3 at a developed rate of 1.1×10^{-9} mol s^{-1} cm^{-2}, which expended water at the anode and air at the cathode at 0.6% coulombic efficiency [148].

2.8.4.2 O_2^- conducting membrane materials and ammonia synthesis systems

A large number of O_2^- conducting ceramic electrolytes are available and have been used in oxygen sensors, solid oxide fuel cells and for high temperature steam electrolysis. These include fully and partially stabilized ZrO_2 with different dopant types and levels, doped CeO_2, doped $LaGaO_3$ at A- and B-sites, and doped Bi_2O_3 [168]. The O^{2-} conductivity feature varies significantly with the type of material used. Although some of these materials retain O_2^- conductivity over a wide range of temperatures, oxygen partial pressures and gas compositions, others develop either electronic or even proton conductivity in the presence of water and similar to those reported for doped $BaSrO_3$ and $SrCeO_3$ [161, 167].

Typically, electrochemical routes, investigated so far require operation at much lower pressures than those used in the Haber-Bosch process with operating temperatures from near room temperature for liquid and polymer electrolyte systems to between 400 and 800˚C for other solid electrolytic routes. The low temperature operation has the potential to decrease material and operating costs and increase life time of the electrochemical reactor provided high ammonia production rates and high current efficiency can be achieved. However, one of the significant advantages of ammonia production by medium-high temperature electrolytic routes such as molten salt is that such systems can be integrated with renewable energy, thermal or nuclear power plants to provide the waste heat for high temperature operation thus reducing the overall energy input especially if water is used as the hydrogen source. In addition to natural gas being a source of hydrogen, it can also be supplied by water electrolysis using renewable electricity.

2.8.5 Ammonia synthesis via molten salt based electrochemical system

The synthesis of ammonia from electrochemistry is based on electrolysis where electric current is supplied to a reactor consisting of a cathode, anode, and ionic conducting membrane. The chemical reactions consist of reduction on one side and oxidation on the other with an important component being the membrane which will only conduct a special kind of ion such as protons in the form of H^+, this allows the reactor to work continuously. There are many variations of types of cathodes, anodes, and membranes however the principle remains the same where two reactants and an activation potential are applied to generate a chemical reaction resulting in ammonia synthesis. These reactions have been shown to work in a wide range of pressures and temperatures making it viable when working with atmospheric conditions.

Using water and atmospheric air, combining them into a molten salt of NaOH-KOH with nano-Fe_2O_3 as the catalyst to produce a 30% current efficiency was observed [149]. The systems were using an open pot system with no separator, two nickel electrodes and a nickel monel mesh as the set up for their data. Although the efficiency seems to be lower than proton conducting membranes, its materials are inexpensive and could see improvements if the reactor set up is enhanced. In this method, the electrodes and mesh need to be continuously inspected and replaced due to corrosion in the reactor. Electrolyte salts must be tested periodically for reactivity. When including a catalyst inside the mixture such as nano-iron oxide [149], the particles must be kept in a consistent concentration throughout the salt mixture. In order to realize this method, a number of concepts have been demonstrated on small cells in laboratory experiments of short duration as using hydrogen, methane or water as the reactants. The technology being developed with a good current efficiency of 72% reported for hydrogen oxidation reaction and ammonia synthesis rates of about 3.3×10^{-9} mol cm^{-2} s^{-1} [144].

2.9 Main Gaps in the Literature and Motivation

Solar energy based hydrogen and ammonia production arises as one of the most sustainable solutions of today's critical energy, environmental and sustainability issues. The use of photochemical and catalytic hydrogen production systems is developing but the practicality of these methods at scaled up production rates needs to be investigated. In photoelectrochemical routes, a photosensitive material such as a semiconductor is needed in which electrodeposition technique is mostly used. As reported in the literature, there are different types of deposition methods where some of them require the moderate and high temperatures above 100°C. Here, the employed electrodeposition techniques require about 55°C and simple chemicals. In addition, the literature studies mainly performed electrodeposition on FTO (fluorine-doped tin oxide) glass substrates having a very small surface area. Therefore, there is a gap in the open literature to investigate the copper oxide electrodeposition on large surface metal plates for practicability under different conditions comparatively such as under solar simulator light and concentrated light. Furthermore, the electrodeposition of copper oxide has not been conducted so far on such a large area stainless steel plate and characterized under concentrated light for hydrogen production. Different than the literature studies, in this thesis, copper oxide is deposited on a large area steel and stainless steel metals under different experimental conditions by changing the temperature, pH and durations. Furthermore, the effects of these conditions are investigated for photoelectrochemical hydrogen production system under concentrated light, solar simulator light and no-light conditions, comparatively. After obtaining the photocathode, a new PEC cell for hydrogen production is developed and tested under concentrated light to measure the impacts of solar concentration on the performance which has not been studied in the literature. Although there are several studies for EIS measurements of PEM fuel cells and PEC cells, the effects of solar concentration on the cell performance is not investigated and not reported comparatively under concentrated light and no-light conditions in the literature. The PEC cell has a large membrane surface area corresponding to 930 cm^2 in total. Hence, it is known as one of the largest reactors in this area which can produce up to 7.5 L/h hydrogen compared to previous PEC reactors in the literature. Furthermore, in this thesis,

a novel approach to the processes inside a PV cell is addressed. In the previous studies, although there are exergy analysis for PV cells, they did not focus on exergy losses and destructions caused by internal processes of the PV cell. In this new approach, absorption, radiation, reflection, heat dissipation, heat penetration and electrical power transmission processes are exegetically analyzed and irreversibility caused by these processes are comparatively assessed. This enables a wider perspective inside the PV cell processes and for the proposed integrated system here.

Since solar energy cannot be directly stored or continuously supplied, it is required to convert solar energy to a storable type of energy. Ammonia is a significant candidate as a sustainable energy carrier. However production of ammonia is mostly dependent on natural gas in the world. Alternative ammonia production methods are being investigated in which there are less environmental emissions and energy consumption. Electrochemical ammonia synthesis is one of the highly developing technologies. Assisting electrochemical process with solar energy will contribute an environmentally friendly method. In order to utilize a solar irradiation as efficiently as possible, all wavelengths of light are desired to be used, and the efficiency of each section of the energy conversion steps should be improved. The absence of practical solar based integrated hydrogen and ammonia production systems which are environmentally benign, low cost, efficient, and safe is one of the main complications for the transition to a solar energy based economy. There has been no study for photoelectrochemical hydrogen based molten salt electrolytic ammonia synthesis process so far. There have been some studies using water as hydrogen source, however, in this thesis, hydrogen will directly be used in electrochemical ammonia synthesis where hydrogen is produced from photoelectrochemical process. Coupling of solar based hydrogen production with electrochemical ammonia synthesis has never been proposed in the literature.

The underlying motivation of this thesis is the potential for combining photoelectrochemical hydrogen production system with electrolytic ammonia synthesis processes to increase the solar spectrum utilization and ammonia production yield. Although synthesis of NH_3 using water as hydrogen source in electrochemical process reduces additional step, for the cases where ammonia and hydrogen is individually required as alternative fuels, H_2 can be directly utilized in the electrochemical NH_3 formation as investigated in this thesis. In addition, the required voltage is higher when water is used because of the water splitting potential.

Most of the literature used water as hydrogen source which also requires water splitting process at the same time with ammonia synthesis. Specifically, for solar energy storage applications, H_2 can act as short-term storage whereas NH_3 can serve as long-term storage medium (because of thermal properties) which reduces the storage losses significantly. In this thesis, the electrochemical synthesis of ammonia using H_2 and N_2 at ambient pressure in a molten hydroxide ambient with nano-Fe_3O_4 catalyst is achieved. The active surface areas of the Nickel mesh electrodes are increased to allow higher formation rates. The effects of various parameters such as applied potential, current density and reaction temperature on ammonia formation rates are investigated. The reaction temperatures are quite lower than the conventional Haber-Bosch process.

The originality of this thesis can be itemized as follows:

- The designed and developed photoelectrochemical hydrogen production reactor is one of the largest scale reactors in the literature.
- The copper oxide deposited photocathode has the largest surface area coated on stainless steel.
- The solar light splitting and concentrator has firstly been used for photoelectrochemical hydrogen production and electrochemical ammonia synthesis.
- It is the first study integrating the photoelectrochemical hydrogen into the electrochemical ammonia synthesis.
- The ammonia formation rate in the molten salt based electrochemical synthesis is one of the highest observed in the literature.
- This study includes the most comprehensive life cycle assessment of ammonia production containing 25 different methods including the newly tested photoelectrochemical hydrogen based ammonia synthesis option.
- There is a new exergetic approach in this study developed for photovoltaic cell considering all photo-thermo-electrical processes occurring in the cell.
- The characterization of the photoelectrochemical hydrogen production reactor has been performed comparatively under solar simulator light, ambient and concentrated light conditions using multiple techniques such as electrochemical impedance spectroscopy for the first time.

2.10 Objectives

The main objective of this thesis study is to develop and investigate a novel solar based hydrogen and ammonia production system. The proposed hybrid system enhances the utilization of solar spectrum by employing solar spectrum splitting mirrors and by integrating generated hydrogen as a reactant in the electrochemical ammonia synthesis process.

The specific objectives of this thesis are listed as follows:

- To design, develop, build and test a prototype of a large scale photoelectrochemical reactor for hydrogen production.
- To perform experiments on the developed photoelectrochemical hydrogen production reactor under various operating conditions namely; light intensity, temperature, spectral distribution, applied voltage and active area.
- To apply electrodeposition of copper oxide on large scale stainless steel electrode for photoelectrochemical hydrogen production applications and to investigate the effects of various process parameters of copper oxide deposition under different scenarios such as
    - concentrated light and no-light conditions,
    - stainless steel and steel plates,
    - smaller surface area and larger surface area,
    - duration of electrodeposition process, and electrodeposition temperature
- To comparatively evaluate the photoactivity of the developed photoelectrochemical cell under solar simulator light and concentrated sunlight.

- To design, develop, build and test an integrated system using concentrated light and spectrum splitting mirrors for hydrogen, ammonia and electricity production considering the following tasks:
    - investigating the solar spectrum splitting mechanism for better solar energy utilization,
    - building an experimental setup which concentrates the sun and produces multi-products; electricity, hydrogen, ammonia and heat.
    - measuring the concentrated solar radiation at each component of the system in order to calculate the amount of energy,
    - assessing the performance of the PV and PEC processes under concentrated and non-concentrated conditions, and determining the hydrogen production amount produced by photoelectrochemical reactor.
- To perform experiments and conduct holistic analyses for the photovoltaic cell under concentrated solar light using energy and exergy analysis methodologies on each of the sub-processes in the photovoltaic cell.
- To design, develop, build and test a prototype of molten salt based electrochemical ammonia synthesis experimental system.
- To perform experiments on the developed molten salt based electrochemical ammonia production process under various conditions such as
    - Reaction temperature,
    - Applied current,
    - Electrode area,
    - Catalyst and electrolyte
    - Inlet gas feed rates,
- To investigate other electrochemical ammonia production methods and to assess the efficiencies for comparison purposes.
- To conduct various experimental studies on each process type based on different parameters and ambient conditions to examine how light intensity, operation temperature, concentrations affect the hydrogen and ammonia production rate, energy requirements and losses within the system.
- To conduct energy and exergy analyses of photoelectrochemical hydrogen and electrochemical ammonia production systems
- To compare the results of the developed electrochemical model calculations with experimental outputs, and highlight any inconsistencies and their importance.
- To calculate the energy and exergy efficiencies of the integrated system for hydrogen and ammonia production processes.
- To determine the entropy generation and irreversibilities with their magnitudes and identify the effects of different parameters on them.
- To perform environmental impacts assessment of various ammonia production methods including the experimentally tested electrochemical ammonia synthesis route
    - to perform a life cycle assessment of various conventional and renewable resources based ammonia production pathways,

    - to define ecological effects of conventional and renewable ammonia production paths in global warming, human toxicity, depletion of abiotic sources, acidification/eutrophication and, climate change categories,
    - to define the most and least ecologically benign ammonia production option including the electrochemical ammonia production route.
- To conduct exergoeconomic analysis of the system in order to relate exergy with cost.
- To perform a scale-up analyses of the experimentally tested system for large scale clean hydrogen and ammonia production.
- To perform a multi-objective optimization technique on the system parameters to find the optimal operating parameters.

CHAPTER 3: EXPERIMENTAL APPARATUS AND PROCEDURE

In this chapter, the detailed explanation of experimental setups is presented. In addition, materials and devices used in the experiments are briefly described for better evaluation of the systems.

3.1 Devices and Materials

Photoelectrochemical hydrogen production system consists of mainly a photoelectrochemical reactor, light source, power source and optical tools. The PEC reactor is tested both under artificial light by using solar simulator and under actual sunlight outside using solar concentrator and optical filters.

3.1.1 Solar simulator

The TSS-208 Trisol Solar Simulator from OAI Instruments is a Class AAA system designed to provide highly accurate, collimated beams. The specifications for collimation half-angle, spatial uniformity, and temporal instability of irradiance are from a performance report provided by OAI [170]. The solar simulator has special air mass filters and lamps to simulate the sun's solar spectrum. Artificial light measurements are taken in the CERL Laboratory of University of Ontario Institute of Technology (43.9448° N, 78.8917° W) under solar simulator (OAI Trisol TSS-208 Class AAA) with an irradiance range of 800-1100 W/m^2 as shown in Fig. 3.1.

Fig. 3.1 Vernier pyranometer and OAI Trisol TSS-208 Class AAA solar simulator.

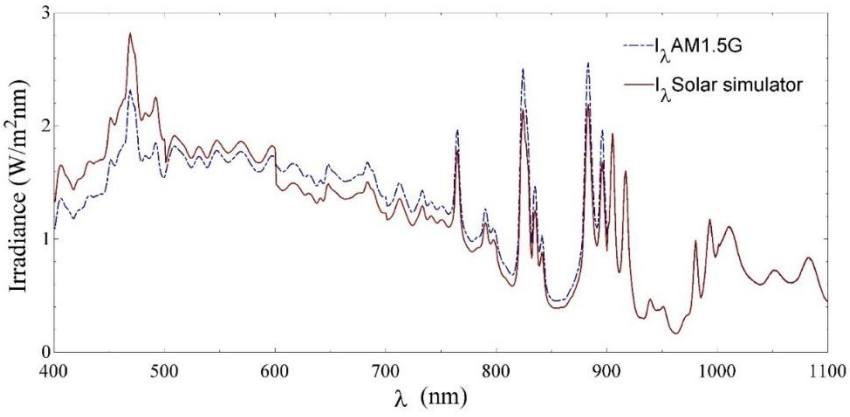

Fig. 3.2 Comparison of spectra of OIA solar simulator and Air Mass 1.5 G.

The comparison of spectra for Air Mass 1.5 G and OAI solar simulator can be seen in Fig. 3.2. The spectrum distributions are quite close to each other which indicates the accuracy of solar simulator.

3.1.2 Potentiostat

A potentiostat is an equipment which apply a voltage across a pair of electrodes and simultaneously measures the current which flows through a solution of an anolyte. Fig. 3.3 shows the potentiostat used in this thesis. The potentiostat used for this research is the Gamry 3000 high-performance Potentiostat/Galvanostat/ZRA which has a maximum current of ±3 A and a maximum voltage of ± 32 Volts. The outputs from the PV module were measured by the potentiostat in linear voltammetry mode and the photoelectrochemical process is assisted electrically by potentiostat.

Fig. 3.3 Gamry Instruments Reference 3000 and Reference 30k booster.

The Reference 3000 can operate as a potentiostat, a galvanostat, or a ZRA. Some of the features which the Reference 3000 include [171]:

- Physical Electrochemistry
- Electrochemical Frequency Modulation
- Electrochemical Impedance Spectroscopy
- DC Corrosion
- Pulse Voltammetry

3.1.3 Spectrometer

In order to examine the spectral irradiance scattering, solar spectra with the wavelength range of 350–1000 nm are logged by Ocean Optics Red Tide USB 650 spectrometer. It is compatible with Spectrasuite spectrometer operating software from Ocean Optics. A UV-VIS type fiber cable is utilized with a core diameter of 400 µm which is connected to the spectrometer in order to measure the intensity of the light. The transmission values of the fiber cable can be seen in Fig. 3.4 which is accounted for the light intensity calculations.

Features of the spectrometer shown in Fig. 3.5 are listed as follows [172]:

- Sony ILX511 linear silicon CCD array detector
- Responsive from 350 to 1000 nm
- Sensitivity of up to 75 photons/count at 400 nm
- An optical resolution of ~2.0 (FWHM)
- Integration times from 3 ms to 65 seconds (15 seconds typical maximum)

- Embedded microcontroller allows programmatic control of all operating parameters
- Wavelength calibration coefficients
- Linearity correction coefficients
- Other configuration parameters
- Low power consumption of only 450 mW
- 12 bit, 1MHz A/D Converter

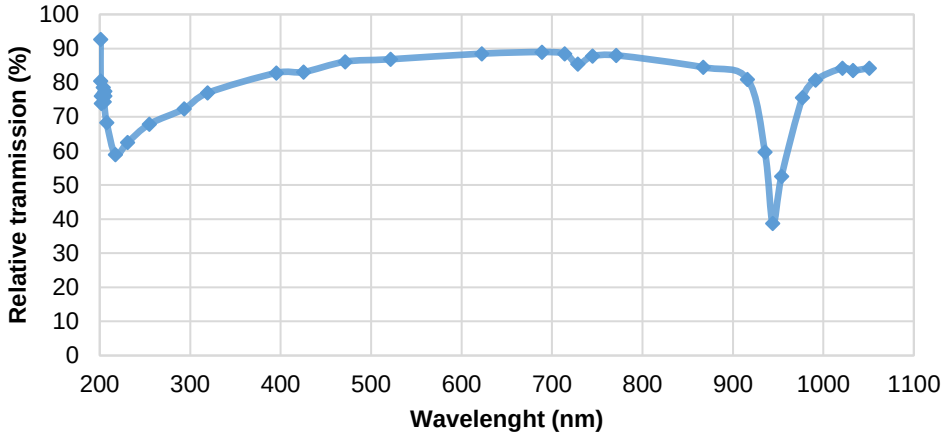

Fig. 3.4 Relative transmission of the fiber cable used with the spectrometer.

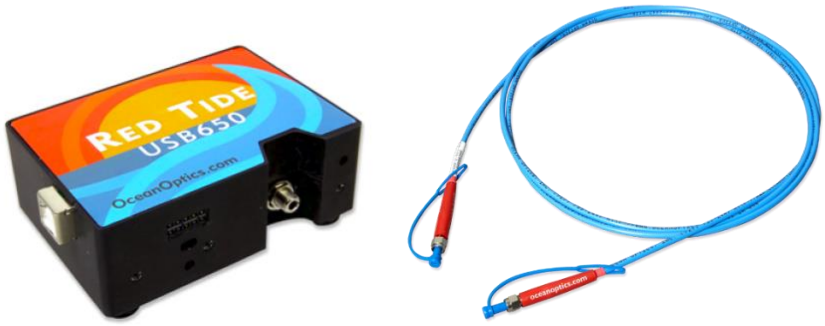

Fig. 3.5 Ocean Optics Red Tide USB 650 Spectrometer and UV-VIS optical fiber cable.

3.1.4 Irradiance meter and temperature measurement

Solar radiation at Earth's surface is characteristically defined as total irradiation across a wavelength range of 280 to 4000 nm. Total solar radiation, which is a summation of direct beam and diffuse, incident on a horizontal surface is defined as global shortwave radiation, or shortwave irradiance, and is given in W/m^2. Pyranometers are sensor devices which measure global shortwave radiation. The utilized pyranometer is silicon-cell pyranometer which is only sensitive to a part of the solar spectrum, approximately 350-1100 nm. This range of spectrum represents around 80% of total shortwave radiation. But, silicon-cell pyranometers are calibrated to estimate total shortwave radiation across the entire solar spectrum.

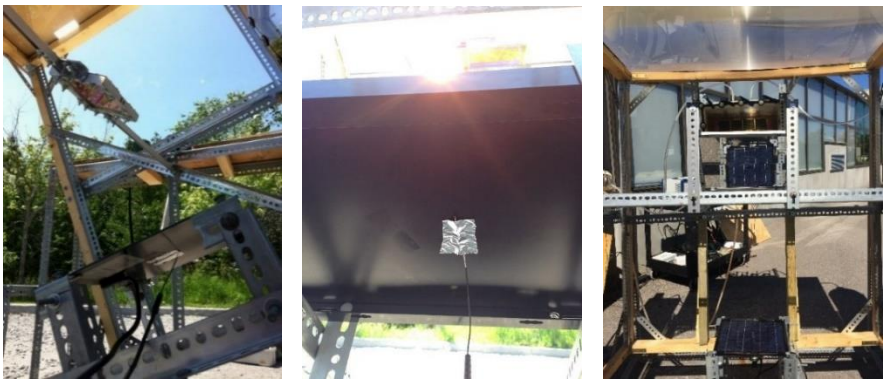

Fig. 3.6 The performance measurements of the PV under actual concentrated sunlight.

The surface temperature of PV panels is measured with surface temperature sensor (Vernier STS-BTA) and ambient temperature is measured with probe temperature sensor (Vernier GO-TEMP) by a data logger unit (Vernier LabQuest) as shown in Fig. 3.6. The surface temperature sensor as shown in Fig. 3.7 is aimed for use in conditions in which low thermal mass or flexibility is required. Special features contain an exposed thermistor that results in an enormously quick response. The specifications of the surface temperature sensor are listed as follows [173]:

- Temperature range: –25 to 125°C
- Temperature that the sensor can tolerate without damage: 150°C
- Temperature sensor: 20 kΩ NTC Thermistor
- Accuracy: ±0.2°C at 0°C, ±0.5°C at 100°C
- Probe dimensions: Probe length (handle plus body) 15.5 cm

The specifications of the ambient temperature sensor are as follows:

- Range –20 to 115°C
- Maximum temperature tolerated without damage to the sensor 150°C
- Resolution 0.07°C
- Accuracy ±0.5°C
- Response time 4 s (to 90% of full reading in water)

The specifications of the pyranometer used in the experiments are listed in Table 3.1.

Table 3.1 Specifications of the Vernier PYR-BTA pyranometer

Calibration factor	5.0 W/m^2 per mV (reciprocal of sensitivity)
Calibration uncertainty	± 5 %
Measurement repeatability	< 1 %
Non-stability (Long-term Drift)	< 2 % per year
Non-linearity	< 1 % (up to 1750 W/m^2)
Response time	< 1 ms
Field of view	180°
Spectral range	360 nm to 1120 nm (wavelengths where response is 10% of maximum) with same angle of PV modules to measure total global irradiance.

Source: [174]

In ammonia production experiments, OM-DAQPRO-5300 data logger with K-type thermocouple is used displayed in Fig 3.7. This device is an eight-channel portable data acquisition and logging system with graphic display and built-in analysis functions. The accuracies of the device is listed for K type thermocouple in Table 3.2. The OM-DAQPRO-5300 system also comes with the DaqLab software which shows the rates of up to 100/s, and automatic downloads can be carried out at higher rates.

Fig. 3.7 (a) The surface temperature sensor used in PV cell, (b) LAB QUEST data acquisition unit and (c) OM-DAQPRO-5300 temperature logger.

Table 3.2 Specifications of OM-DAQPRO-5300 temperature measurement device.

Temperature thermocouple K Type	-250 to 1200ºC
Resolution	0.1ºC (1μV)
Accuracy	
(-250) – (-50) ºC	±0.5%
50 – 1200 ºC	±0.5%
(-50) – 50 ºC	±0.5 ºC
Cold junction compensation	±0.3ºC

Source: [175]

3.1.5 Mass and volume flow meters

The FMA-1600A Series mass and volumetric flow meters (shown in Fig. 3.8) use the theory of differential pressure within a laminar flow field to govern the mass flow rate where the specifications are tabulated in Table 3.3. A laminar flow division inside the meter commands the gas into laminar flow. Inside this area, the Poiseuille equation orders that the volumetric flow rate be linearly correlated to the pressure drop. A differential pressure sensor is utilized to measure the pressure drop along a fixed distance of the laminar flow element. This, along with the viscosity of the gas, is employed to precisely govern the volumetric flow rate. Detached absolute temperature and pressure sensors are combined and they are used to correct the volumetric flow rate to a set of normal circumstances. The standard flow rate is usually named as the volume flow rate and is described in units such as standard cubic feet per minute (SCFM) or standard liters per minute (SLM).

Fig. 3.8 The mass flow meters used in the experiments (OMEGA FMA 1600 and FMA 1800 Series).

Table 3.3 Specifications of FMA-1600A series mass and volumetric gas flow meters.

Accuracy	±(0.8% of reading + 0.2% FS)
Repeatability	±0.2%
Turndown Ratio	200:1
Response Time	10 ms typical default response time for 63.2% of a step change.
Operating Temperature	-10 to 50°C (14 to 122°F)
Zero Shift	0.02% FS/°C/atm
Span Shift	0.02% FS/°C/atm
Humidity Range	0 to 100% non-condensing
Pressure (Maximum)	145 psig
Measurable Flow Rate	125% FS
Supply Voltage	7 to 30 V_{dc} (15 to 30 V_{dc} for 4 to 20 mA output)
Supply Current	35 mA typical current draw

Source: [176]

Table 3.4 Specifications of FMA 1800 series mass flowmeters.

Accuracy	±1.5% of full scale, including linearity over 15 to 25°C and 5 to 60 psia (0.35 to 4.2 kg/cm^2); ±3% of full scale, including linearity over 0 to 50°C and 1 to 500 psia (0.07 to 10 kg/cm^2)
Repeatability	±0.5% of full scale and for units ≥100 scm from 0 to 20% of range
Pressure coefficient	0.01% of full scale per psi (0.07 bar)
Temperature coefficient	0.15% of full scale per °C or better
Response time	800 msec time constant; 2 seconds (typical) to within ±2% of set flow rate over 25 to 100% of full scale
Materials in fluid contact	316 Stainless steel and FKM O-rings

Source: [177]

The FMA1700/1800 Series electronic gas mass flowmeters (shown in Fig. 3.8) deliver for monitoring the flow of extensive variety of gases from low flows to 1000 SLM. Using heat transfer over a heated pipe to measure molecular gas flow rate, the flowmeter delivers

measurement of direct gas mass flow rate, without the requirement to recompense for differences in gas temperature or pressure. The structure can be aluminum/brass structure for typical gas streams and a 316 SS structure for uses necessitating more corrosion resistance such as ammonia. Specific ammonia flowmeter is employed in the experiments where the specifications are listed in Table 3.4.

MQ-137 gas sensor for ammonia shown in Fig. 3.9 composes of micro ceramic tube, sensitive layer, measuring electrode and heater are fixed into a crust made by plastic and stainless steel net. The heater delivers essential work circumstances for sensitive mechanisms [178]. They are used in air quality control equipment for buildings/factory, are suitable for detecting of NH_3.

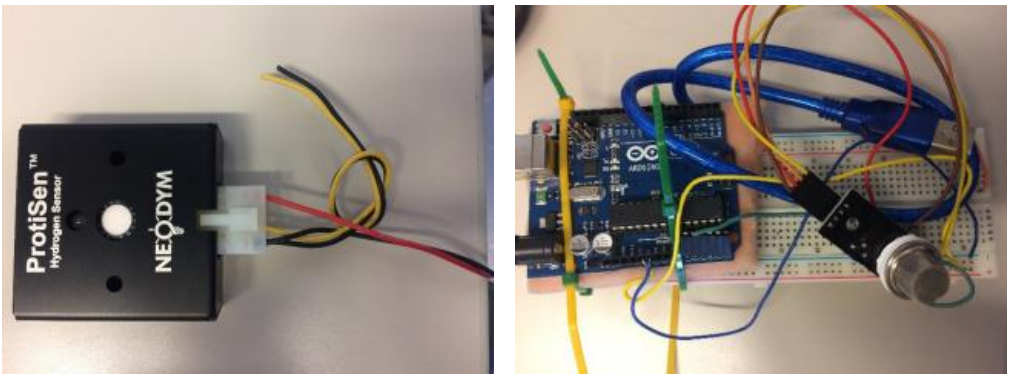

Fig. 3.9 Hydrogen and ammonia concentration sensors.

ProtiSen hydrogen concentration sensor shown in Fig. 3.9 is designed as a compact device for sensitive applications, and structures a catalytic sensor for measuring hydrogen in air up to 40,000 ppm (4% volume) with 200 ppm resolution [179]. The sensor bear VOC filters, decent long term constancy, native linearity, increased tolerance of silicone-based impurities, and are resistant to overexposure damage. The concentration sensors are used in the experiments in addition to mass flow meters in order to increase the accuracy of measurements.

3.1.6 Photovoltaic module

A solar photovoltaic (PV) module is used in the system to provide the necessary power for the hydrogen-producing photoelectrochemical (PEC) reactor as well as any auxiliary components. In order to characterize this module a graph of the relation between voltage and current as well as voltage and power is created. This is compared against the open-circuit voltage (V_{OC}) and short-circuit current (I_{SC}) of the PV and used to calculate additional parameters. The utilized PV module is a 6 W SunWize SC6-12V model with an open circuit voltage of 22.4 V and short circuit current of 0.33 A that is named as larger PV as shown in Figs. 3.10 and 3.11. A smaller scale PV cell named as smaller PV is also utilized to enable measurements in the Gamry potentiostat device since the supply voltage of this device is limited to 11 V. The specifications of the large PV module are listed in Table 3.5.

Table 3.5 Specifications of SunWize PV module.

Overall cell area (m^2)	0.04085
Temperature range (°C)	-20 to 90
V_{oc} (V)	22.4
I_{sc} (A)	0.33
V_m (V)	18.7
I_m (A)	0.3
Power at STC (W)	6
FF (%)	0.759

Fig. 3.10 PV cells used in the experimental setup.

The measurements under artificial light and actual sunlight are recorded in the CERL Laboratory of University of Ontario Institute of Technology (43.9448°N, 78.8917°W). The solar simulator (OAI Trisol TSS-208 Class AAA) with an irradiance of 800-1100 W/m^2 is used in artificial light measurements. The measurements under actual sunlight are taken outside the laboratory. The outputs from the PV module are measured by a Potentiostat/Galvanostat/ZRA (Gamry Instruments Reference 3000).

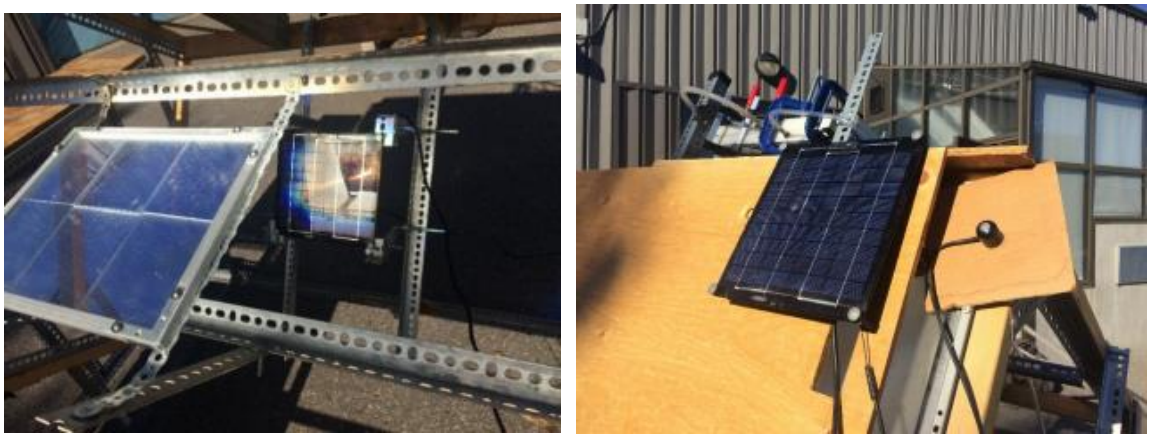

Fig. 3.11 Experimental setup with for PV performance measurements under concentrated light and ambient irradiance.

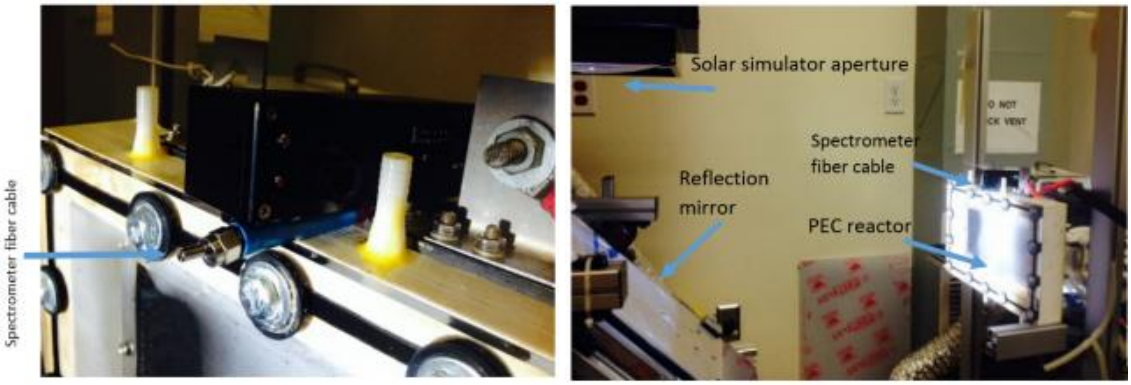

Fig. 3.12 (a) Experimental setup with spectrometer and (b) solar simulator and reflecting mirror.

To examine the spectral irradiance scattering, solar spectra with the wavelength range of 350–1000 nm are recorded by a spectrometer shown in Fig. 3.12. PV surface temperature is measured with surface temperature sensor (Vernier STS-BTA) and ambient temperature is measured with probe temperature sensor (Vernier GO-TEMP) through a data acquisition unit (Vernier LabQuest). A pyranometer (Vernier PYR-BTA) and irradiance meter are mounted with same angle of PV modules to measure total global irradiance as illustrated in Fig. 3.13.

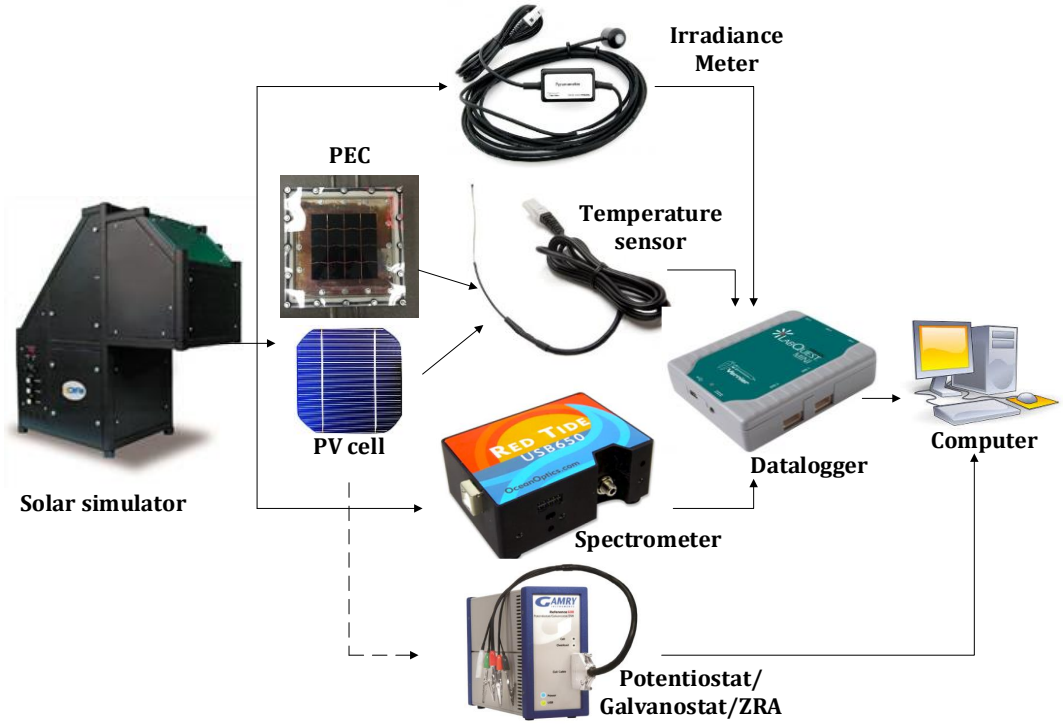

Fig. 3.13 Sketch of experimental setup under artificial light.

In order to characterize the PV cells, a graph of the relation between voltage and current as well as voltage and power is created. This is compared against the open-circuit voltage and short-circuit current of the PV and used to calculate additional parameters. The voltage and current measurements are obtained using high accuracy potentiostat and multimeters. The fiber cable of the spectrometer is fixed in each measurement point using a clamping structure.

Because of the saturation limitation of the spectrometer device under higher solar concentrations, three dimming filters are utilized and through transmission calculations of the intensity filter, actual irradiance data are obtained.

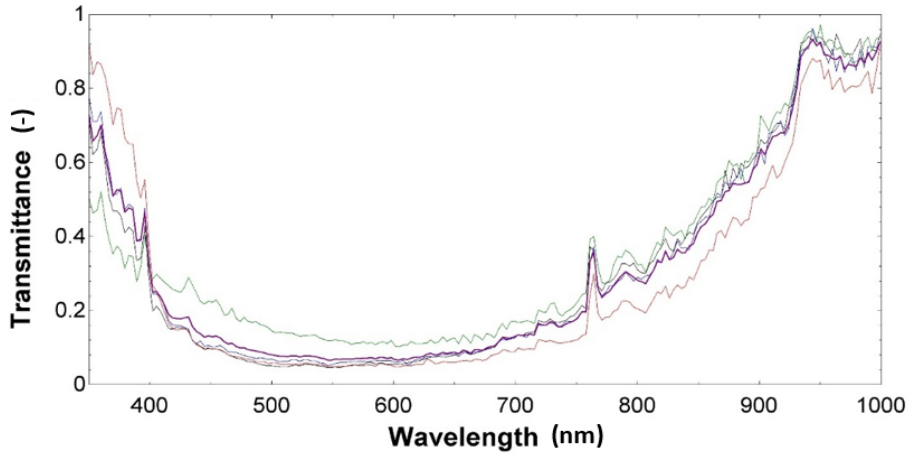

Fig. 3.14 Transmittance of three layers diming filter.

The transmittance factor of three layers of diming filter used to avoid saturation is also measured. In order to accomplish this task, several measurements of the spectrum are captured at different integration times without any filter. After that, three filters are measured several times. Finally, the average value of all the transmittances are obtained. The graph of three layer dimming filter transmittance can be seen in Fig. 3.14. The final result is a transmittance value for every wavelength of the spectrum which is utilized in total irradiance and loss calculations at each state point.

3.1.7 Concentrator (Fresnel lens)

The Fresnel lens is a periodic refractive structure of concentric prisms. The facades of these prisms are constructed to refract light by breaking up the surface curvature of a conventional lens nearly into a plane. By this method, the thickness of the lens is significantly reduced. A Fresnel lens can be combined into a projection lens structure to diminish the number of apparatuses, cost, dimension, and mass cost.

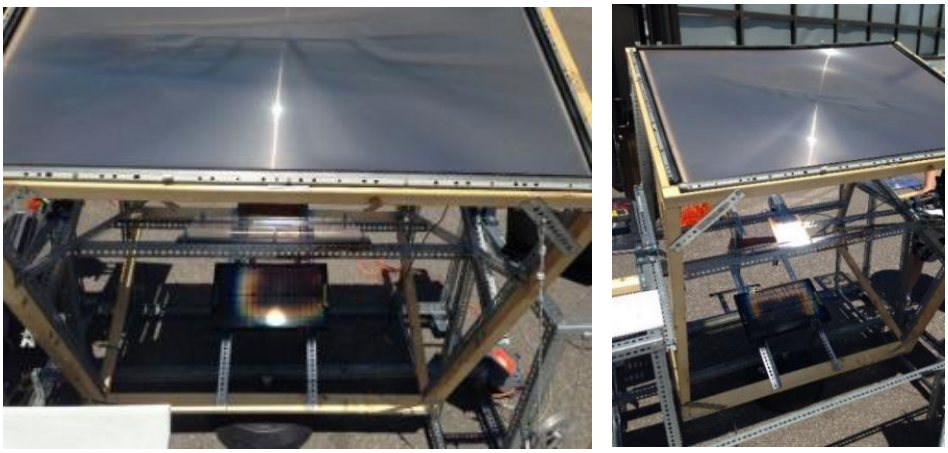

Fig. 3.15 The Fresnel lens used in the experimental setup.

They are used as field and condenser lenses in single panel LCD projectors to more efficiently direct light through the LCD. They are also frequently used as part of the screen system in rear projection monitors. Fresnel lenses consist of a series of concentric grooves imprinted into plastic as shown in Fig. 3.15. Fresnel lens solar concentrators remain to fulfill a market requirement as a system component in high volume cost effective concentrating photovoltaic (CPV) power generation. The Fresnel lens is used as solar light concentrator in the experiments.

3.1.8 Dielectric (cold) mirrors

A cold mirror is an optical device that reflects certain part of the electromagnetic spectrum and transmits a portion of the spectrum. The cold mirrors are made for working at 45º to be able to reflect the spectrum with a wavelength of 400 to 690 nm and transmit the spectrum with a wavelength of 700 to 1200 nm [180].

The high performance cold mirror is manufactured by Edmund Optics and designed to reflect a portion of the visible light and transmit near-infrared (NIR) and infrared (IR) with a dimension of 101 mm × 127 mm. The mirrors are coated with a multi-layer dielectric material and optimized for either 0° or 45° angle of incidence (AOI). The rays incoming at other angles will undergo a shift in spectrum. An anti-reflective (AR) coating has been used that reflects a small portion of the NIR and IR spectrum. The reflectance and transmittance of the cold mirror at 45º can be seen in Fig. 3.16.

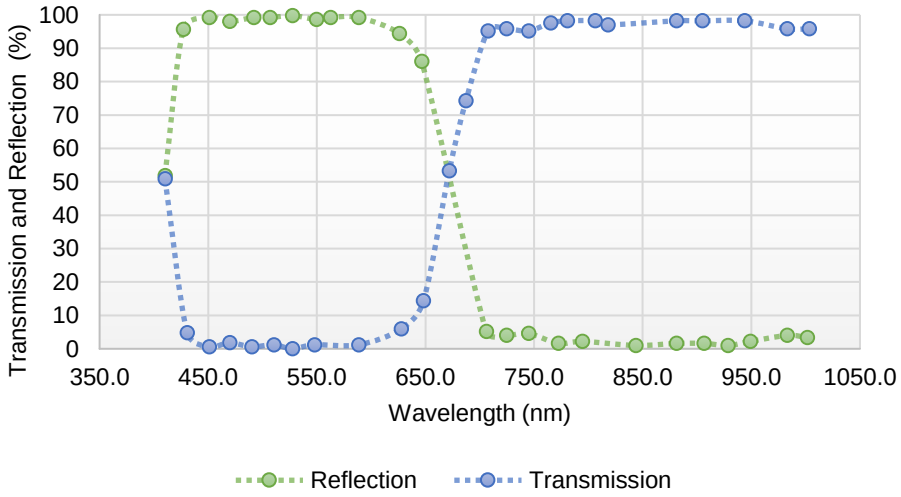

Fig. 3.16 Transmittance and reflectance of cold mirror at 45°.

The manufacturer provides the transmittance and reflectance features for 0° and 45° angle of incidence as mirror reflectance range is 400-690 nm whereas mirror transmittance range is 700-1200 nm. The substrate is borosilicate glass. The surface dimensions of the cold mirror used in the experiments are 101 mm × 127 mm which corresponds to about 128.27 cm^2 surface area for one mirror. In total, six cold mirrors are utilized forming a rectangular area of 769.62 cm^2 in order to increase the illuminated area on the PEC cell as depicted in Fig. 3.17.

Only reflected portion of the spectrum is utilized for the PEC cell since the transmitted portion is used for power production via solar PV module.

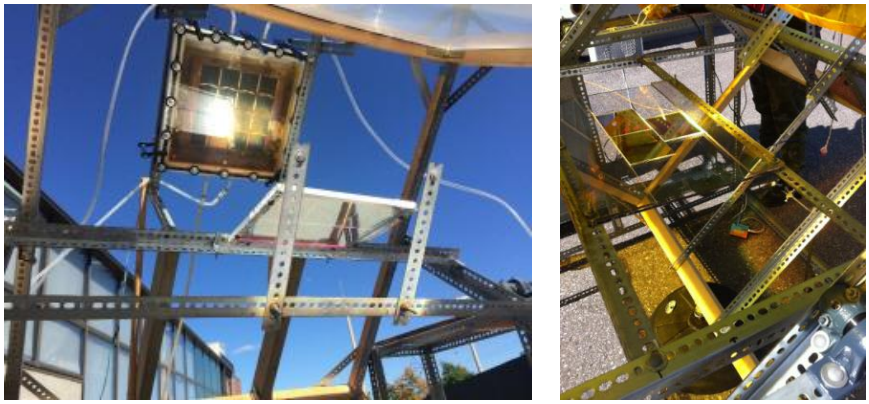

Fig. 3.17 Measurement of cold mirror reflectance and transmittance under sunlight.

3.1.9 Photoelectrochemical reactor

The Nafion membrane is used where the anode surface is iridium ruthenium oxide and the cathode is platinum black (PtB). Both catalysts have a density of 3 mg/cm^2. Iridium-ruthenium oxide ($IrRuO_x$) is the anode electro-catalyst of the membrane which is known for fast kinetics and the electro-catalyst loading. For the selection of the membrane, the critical design parameters are the catalyst loading and thickness. The reactor design is illustrated in Fig. 3.18. A membrane electrode assembly is built with stainless steel anode and cathode plates as shown in Fig. 3.19. The plates are selected as stainless steel due to non-corrosive features in water medium. In addition, the coating could be performed easier in this case.

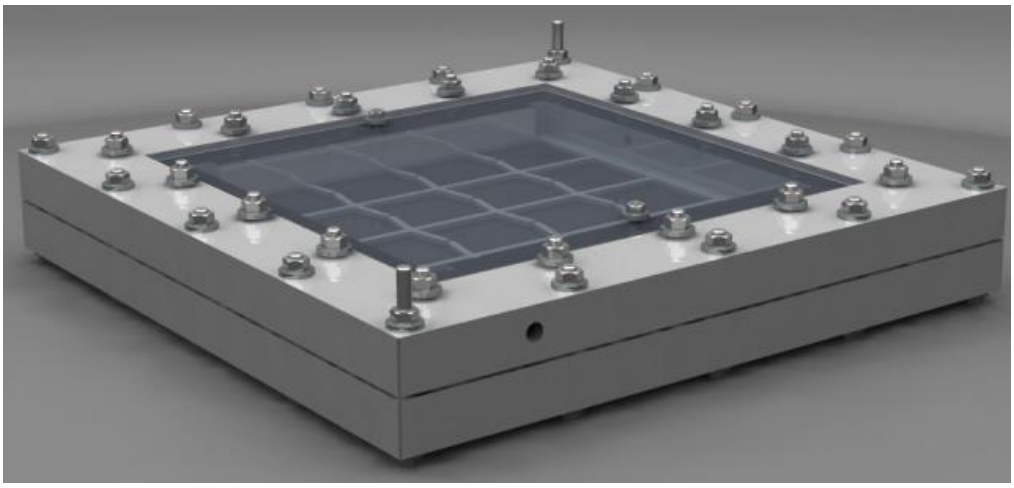

Fig. 3.18 Photoelectrochemical reactor design.

The cathode plate is electrochemically deposited with copper oxide photosensitive material enhancing the hydrogen evolution as photocathode. The specifications of the Nafion 115 membrane are listed in Table 3.6. Most the specifications reported were performed at 50% RH, 23°C by the manufacturer [181] .

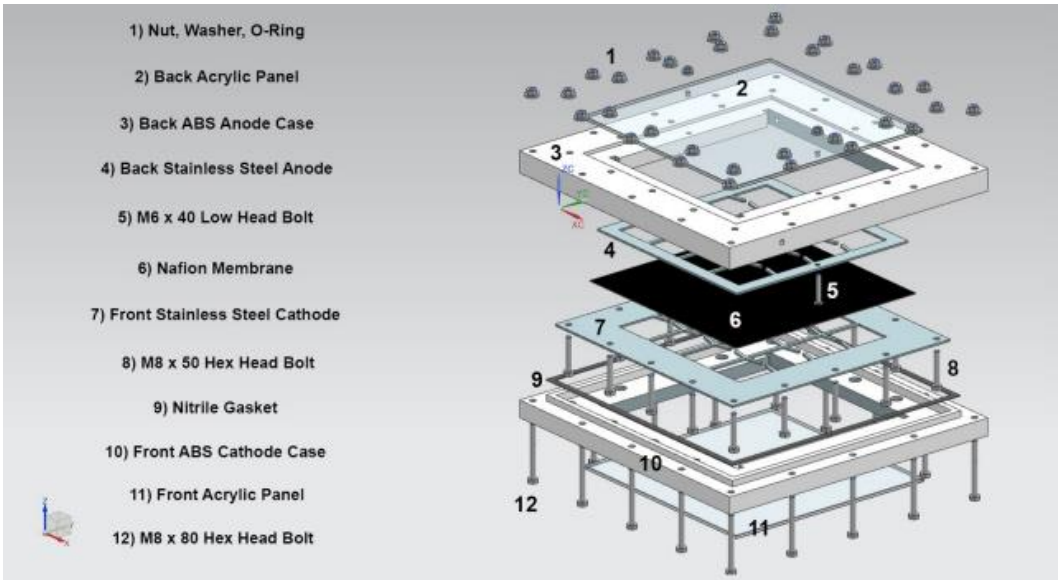

Fig. 3.19 The assembly of the PEC reactor.

Table 3.6 Specifications of the Nafion 115 membrane used in the PEC reactor.

Membrane Type		Nafion 115
Thickness, Micrometer		127
Basis Weight, g/m²		250
Tensile Modulus, MPa		249
Tensile Strength, maximum, MPa	machine direction	43
	transverse direction	32
Elongation at Break, %	machine direction	225
	transverse direction	310
Tear Resistance - Initial, g/mm	machine direction	6000
	transverse direction	6000
Tear Resistance - Propagating, g/mm	machine direction	>100
	transverse direction	>150
Specific Gravity		1.98
Available Acid Capacity, meq/g		0.90 min
Total Acid Capacity, meq/g		0.95 to 1.01
Water Content, % Water		5
Water Uptake, % Water		38
Thickness % Increase (from 50% RH, 23 °C to water soaked, 23°C)		10%
Thickness % Increase (from 50% RH, 23 °C to water soaked, 100°C)		14%
Linear Expansion, % Increase (from 50% RH, 23 °C to water soaked, 23°C)		10%
Linear Expansion, % Increase (from 50% RH, 23 °C to water soaked, 100°C)		15%

Source: [181]

The specification of the viewing panel made of acrylic are given in Table 3.7. This material has high tensile strength, machinable and electrical insulator. The fundamental advantage of the acrylic is to have high transmission in visible light spectrum. The most critical design parameter of viewing panel is having high transmission ratio and high temperature resistance. Since the temperature on the reactor can reach to higher levels, the selected material needs to have high melting temperature.

The reactor casing material is chosen as high density polyethylene (HDPE) as the specifications are given in Table 3.8. It is often used for tank linings and industrial cutting boards, HDPE polyethylene offers the outstanding moisture resistance of LDPE with a higher-density, firmer construction. It also resists most chemicals, such as alcohols and ethers. It is chemically resistant, machinable and flame retardant.

Table 3.7 Specifications of the optically clear acrylic sheet used as viewing panel in the PEC reactor.

Thickness	7/32"
Thickness Tolerance	+0.035", -0.018"
Color	Clear
Temperature Range	-40° to 170° F
Tensile Strength	Excellent
Impact Strength	Poor
Additional Specifications	Sheets

Source: [182]

Table 3.8 Specifications of rigid HDPE Polyethylene reactor case material.

Thickness	1 1/4"
Thickness Tolerance	±0.063"
Color	Semi-clear to opaque white
Maximum Temperature	180° F
Tensile Strength	Poor
Impact Strength	Good

Source:[183]

Table 3.9 Specifications of chemical-resistant polyethylene rubber gasket material.

Thickness	1/8"
Thickness Tolerance	±0.020"
Maximum Length	50 ft.
Color	Black
Temperature Range	-20° to 250° F
Tensile Strength	1,500 psi
Additional Specifications	Sheeting—Smooth Finish

Source:[184]

The gasket material used in the design is polyethylene rubber which is engineered for increased resistance to acids, alkali, oils, greases, and ozone. The specifications of the rubber gasket used in the reactor are listed in Table 3.9. It also resists flex cracking and abrasion from weather and heat. Because of these properties, and the fact that it has low water absorption, it is often used in roofing systems, hose, timing belts, and insulation. The tensile strength and sealing are the fundamental selection criteria for the gasket material.

The final assembled form of the PEC hydrogen production reactor is shown in Fig. 3.20. Here, cathode plate is already electrodeposited with copper oxide as seen in Fig 3.20.

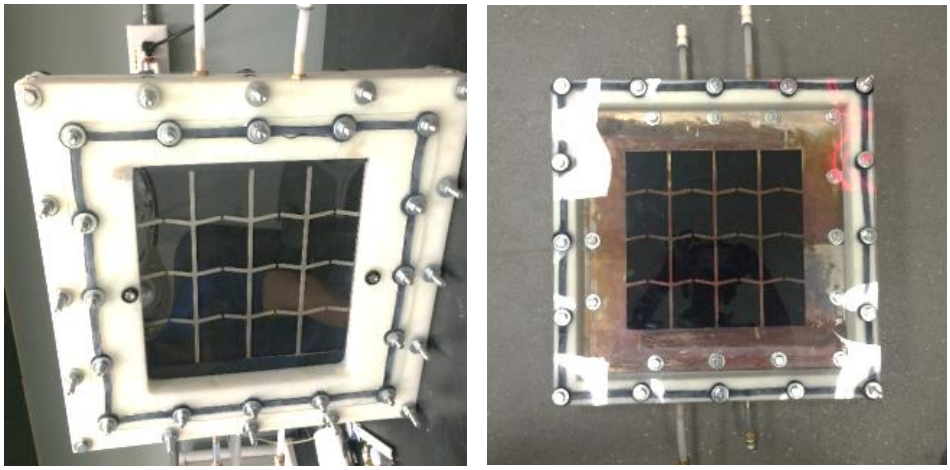

Fig. 3.20 The assembled PEC reactor anode and cathode sides.

The reactor is placed in the experimental setup in an optimum distance from the dielectric mirror to increase the light exposed surface area. On the other hand, if the distance is too far from the dielectric mirror, then the concentration ratio is low hence, hydrogen production rate diminishes. Therefore, the optimum distance is set after multiple arrangements. The pictures of the PEC reactor under concentrated and split light are shown in Fig. 3.21.

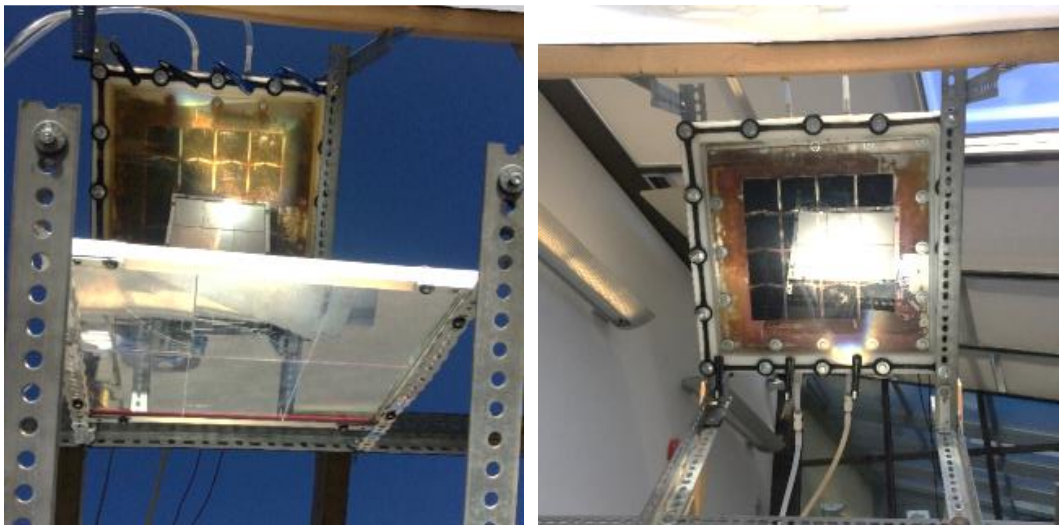

Fig. 3.21 The PEC reactor under concentrated and split spectrum.

The support mechanism allows to relocate the PEC reactor. The reactor inlet and outlet connections are made using quick connect couplings for water and gas. In this way, the reactor is modular meaning that it can be relocated depending on the desired illumination area.

3.1.10 Electrochemical molten salt ammonia reactor

The molten salt eutectic mixture begins to melt at approximately 170°C. High temperatures in the range of 200°C-300°C must be sustained, and a corrosive resistant material should be used. For the reactor design, since the cylinder design seems simplest to implement sealable covers, the shape of the reactor is cylindrical. The dimensions are based on the volume required. The reactor size details are top diameter: 100 mm, bottom diameter: 60 mm, height: 116 mm with 500 mL volume. The molten salt concentration needs to be in a 50/50 ratio of each of its components (NaOH-KOH) with 500 mL being a sufficient amount of space. It is also important to have enough room in the headspace above the molten salt allowing for the product gases to escape for separation and analysis. The reaction takes place at a high temperature and in molten salt therefore various materials are considered for the reactor. The specifications of the materials used in the reactor construction are shown in Fig. 3.22. The key design parameters for the reactor body and electrodes are being suitable for corrosive media and having high resistance at elevated temperatures. Furthermore, the electrodes need to be highly conductive for the electrochemical process which decreases the overpotentials.

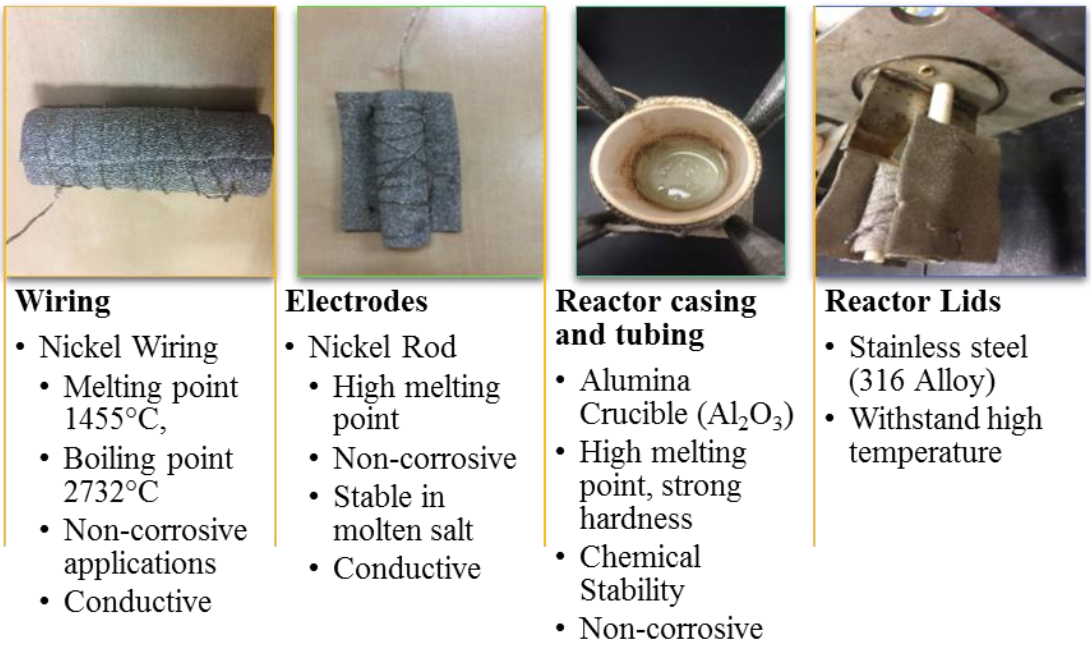

Fig. 3.22 The materials used in the molten salt based ammonia production reactor.

Reactor casing, which is made of alumina (Al_2O_3), is a hard, chemically resistant material and has the capability to endure very high temperature levels in destructive atmospheres. 99.8% Alumina can be utilized at operational temperatures up to 1750°C in both oxidizing and reducing ambient. Tubes are evacuated to 10^{-7} Torr at 1500°C. 99.8% evidences

inert to hydrogen, carbon and refractory metals in many severe circumstances. The bulk density is about 3.91 g/cm^3. The 3D design of the reactor body is given in Fig. 3.23. The developed ammonia reactor which is utilized in the experiments is shown in Fig. 3.24. In order to sustain reaction temperature, a heating tape around the alumina crucible is used.

Fig. 3.23 The 3D design of the ammonia reactor.

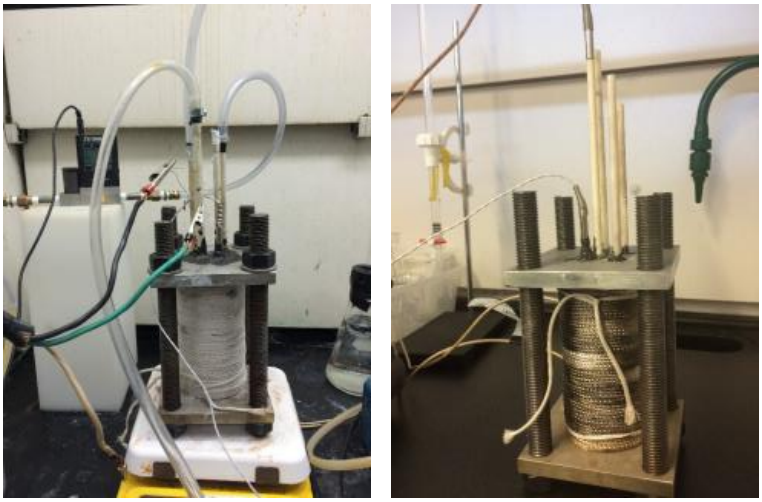

Fig. 3.24 The developed and tested ammonia reactor used in the experimental setup.

3.2 Experimental Setup of Photocatalyst Electrodeposition

The experimental setup consists of solar simulator, electrodeposition chemicals, hydrogen sensor, pH meter, graphite and platinum electrodes, heating plate, stirrer, temperature sensors, cathode and anode plates, concentrating lens and potentiostat. The cathode plate is electrochemically deposited with copper oxide photosensitive material enhancing the hydrogen evolution as photocathode. In this thesis, the electrochemical deposition of Cu_2O onto the stainless steel cathode plate is conducted in an electrolyte solution consisting of 0.4 M $CuSO_4 \cdot 5H_2O$ and 3 M lactic acid which are purchased from Sigma Aldrich. By complexing

with lactate ion, the copper is stabilized and the pH can be raised to alkaline values. The dark blue solution has been prepared and continuously stirred during electrodeposition. Electrodeposition of Cu_2O is carried out in a three-electrode setup consisting of graphite counter electrode with platinum winding, Ag/AgCl reference electrode, and stainless steel substrate as a working electrode [185]. Electrochemical deposition is controlled by Gamry Reference 3000 Potentiostat with a 30 K booster potentiostat. The pH of the solution is adjusted between to be 10 by the addition of sodium hydroxide pellets. The solution temperature is kept constant during deposition by temperature controller where it is set to 55°C. The stainless steel plate having an area of 830 cm^2 requires 4 runs of 20 minutes in order to have full surface deposition coating. The applied voltage for the electrodeposition process is -0.3 V vs. Ag/AgCl. The dark blue solution has been prepared and continuously stirred during electrodeposition. The electrodeposition setup is illustrated in Fig. 3.25 where the green wire is working electrode, which is connected to the stainless steel plate, while the red wire is the counter electrode which is connected to the graphite rod with platinum winding.

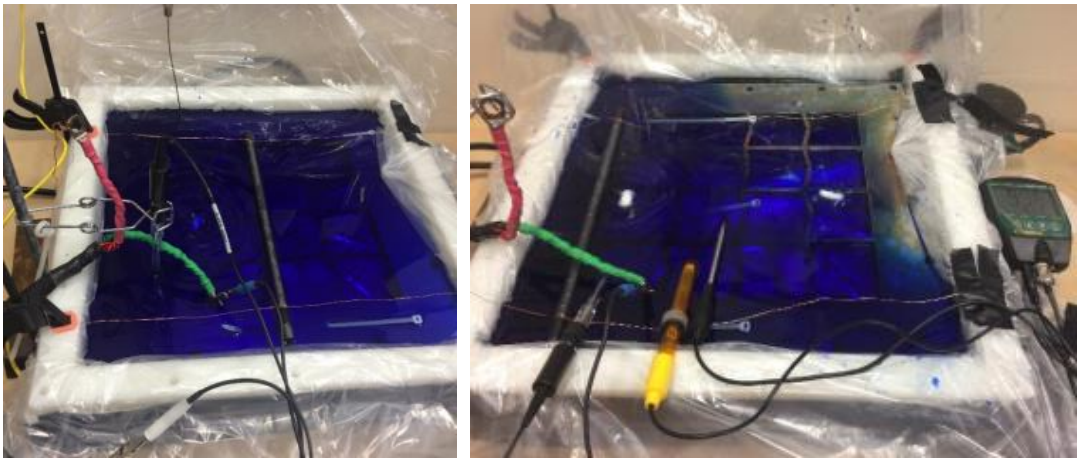

Fig. 3.25 Electrodeposition setup for the stainless steel plate.

Fig. 3.26 Measurement of photo-responsivity of Cu_2O coated cathode plate.

The white wire is connected to the reference electrode which is the Ag/AgCl in this thesis. It is placed in the electrodeposition solution perpendicularly. In the solution for the stainless steel cathode plate, a total of 151.9 g of $CuSO_4 \cdot 5H_2O$ is dissolved in 340 ml of lactic acid to form the copper lactate complex. The amount of added NaOH is about 150 g for the solution. The photo-responses are tested under solar simulator light (OAI Trisol TSS-208 Class AAA) and under actual concentrated light using Fresnel lens in an electrolyte. Initially, the photo-responsivity of the coated photocathode is tested before assembling the reactor as shown in Fig. 3.26. After several tests, by installing the photocathode, the PEC reactor is constructed. The successful electrodeposition of Cu_2O on the cathode plate is shown in Fig. 3.27.

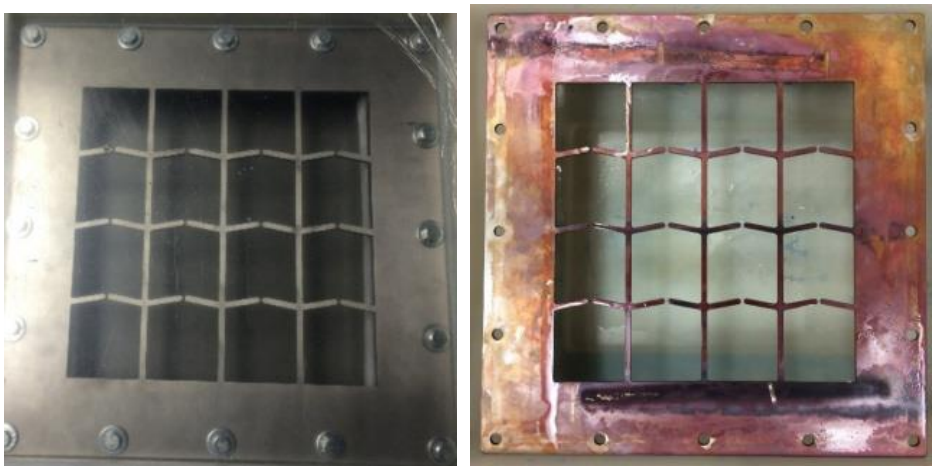

Fig. 3.27 Stainless steel plate before (a) and after (b) the electrodeposition process.

3.3 Experimental Setup of Hydrogen Production

Photoelectrochemical (PEC) hydrogen generation system in this thesis comprises of primarily a photoelectrochemical cell with a membrane electrode assembly, photovoltaic (PV) module, light source (concentrated), electricity supply and optical tools such as Fresnel lens and spectrum splitting mirrors as illustrated in Fig. 3.28. After the Fresnel lens, the light is split using spectrum splitting cold mirrors. The higher wavelength spectrum is used for photovoltaics and lower wavelength spectrum is used for PEC cell to increase the solar energy utilization [186].

The state points in which the amount of energy are determined are shown in Fig. 3.28 where state point 1 is non concentrated light, state point 2 is the concentrated light, state point 3 is the light coming on reactor and state point 4 is the light coming on PV.

The EIS measurements are performed by a Potentiostat/Galvanostat/ZRA (Gamry Instruments Reference 3000). Potentiostatic EIS was the applied method. The spectrum of the impedance is logged in the laboratory for no-light conditions and outside the laboratory for the concentrated light measurements by scanning the frequencies ranging from 20 kHz to 10 mHz with 5 points per decade. The amplitude of the sinusoidal AC voltage signal is 10 mV (RMS). The PEC cell is supplied different DC potentials ranging from 1.3 V to 3 V during the EIS measurements in which the active area of the membrane is 500 cm^2.

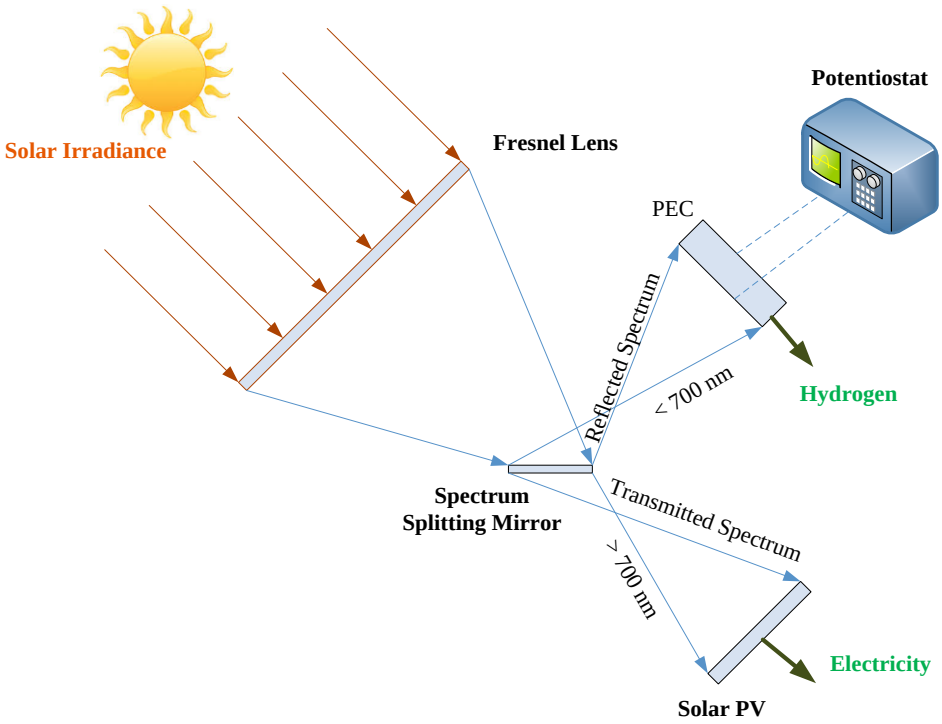

Fig. 3.28 Sketch of the experimental setup under concentrated light measurements.

The photocathode side of the PEC cell is blocked using a non-transparent metal to obtain no-light conditions. A pyranometer (Vernier PYR-BTA) is used to measure total global irradiance irradiating on the PEC cell. In order to filter the incoming light intensity for pyranometer measurements, one layer of dimming filter is utilized with a correction factor of 5.6. The irradiance is measured separately for each EIS cycle. The concentrated light does not cover the full surface of the PEC cell. Hence, the irradiation measurements are individually performed for fully concentrated and non-concentrated part of the PEC cell.

3.4 Experimental Setup of Ammonia Production

The experimental setup for molten salt based ammonia production is illustrated in Fig. 3.29. As the first reactant, nitrogen gas is supplied from nitrogen tank with a flow control valve and pressure gauge. As the second reactant hydrogen is produced initially from an electrolysis in NaOH solution and then form PEC system and transmitted to ammonia reactor through pipes.

Using power source, direct current (DC) is supplied to both electrodes inside the reactor via nickel wires. By adjusting voltage and current values, the rate of change in the reaction can be determined. A potentiometer adjusts the potential and resistance of the circuit. Both reactants enter into the ammonia reactor. Here the two reactants nitrogen and hydrogen mix with a eutectic mixture composed of KOH-NaOH. An electrochemical pathway is created to produce ammonia by the reaction of nitrogen and hydrogen in a molten hydroxide salt solution (with a molar ratio of 0.5 NaOH/0.5 KOH). This eutectic mixture is prepared prior to the start of the experiment and preheated to form the molten salt. The reactor will remain at atmospheric pressure and is leak-free because of a gasket used to maintain the seal.

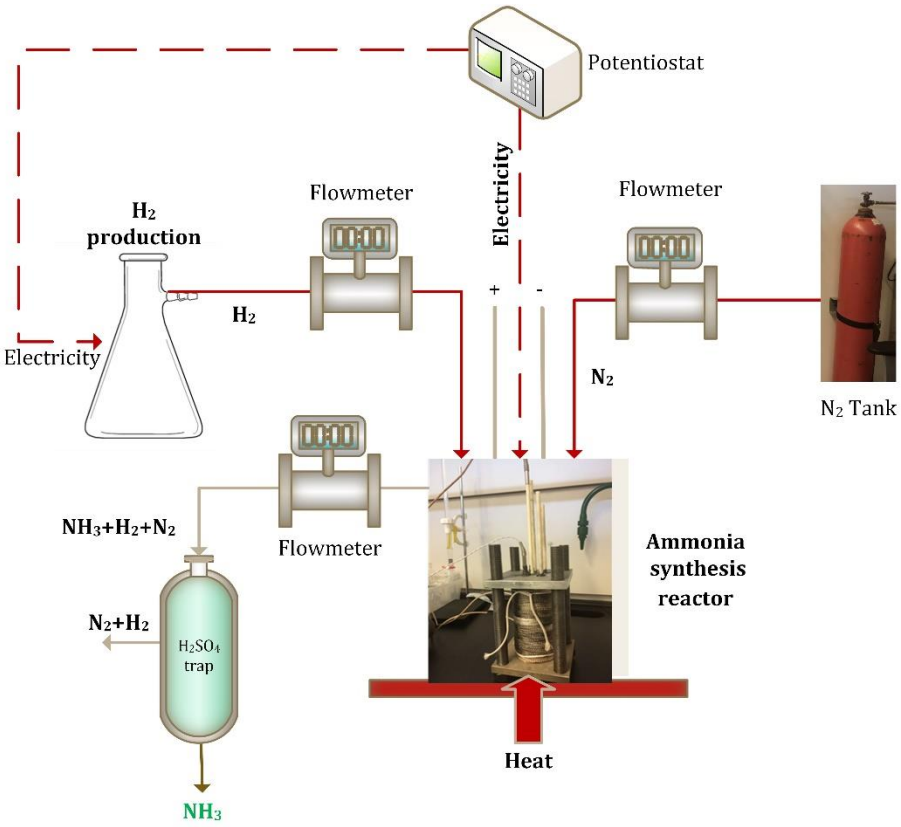

Fig. 3.29 Hydrogen based electrochemical ammonia synthesis in molten salt reactor.

The suspension of nano-Fe_3O_4 within the molten salt acts as a catalyst for the reaction to occur faster. The reactants inside the crucible are separated by a partition to allow the ammonia produced to flow through the output tube and are sprinkled into deionized water. Ammonia test strips with a range of 0 – 6 mg/l and then it is used to identify/give a good estimate of ammonia. The strips work by detecting the change in pH as a result of the added ammonia. The fume hood also acts as a safety device in case there is a leak or problem.

Supplying air instead of nitrogen could also be a modification to the system however in that case, the oxygen needs to be safely removed from the reactor. The reactor is designed to eliminate any leakage from the joints. It is designed to contain a molten salt mixture previously discussed with the catalyst as well as the electrode set up carefully supported by supplying rods with nickel wire. There is also a wall designed into the reactor set up to separate the production gases at the anode and cathode which are oxygen (in case water is used) and ammonia/hydrogen respectively.

The boiling points of the certain salts that are intended to be melted within the crucible is important. The melting point of NaOH is 318°C, and the melting point of KOH is 406°C. Taking these temperature values into account, the mixture is heated up to 450-500°C to ensure that the salts are totally melted. Providing a mass ratio of 0.5 NaOH/0.5 KOH within the reactor is required. The iron oxide is catalyst for the traditional Haber-Bosch synthesis of ammonia. The high surface area of the nano-Fe_3O_4 in the electrochemical synthesis is significant for the amount of ammonia to be produced at higher rates.

The fused iron catalysts have been used in industrialized ammonia synthesis forvery long time. The typical iron catalysts consist of Fe_3O_4 or Fe_2O_3, Al_2O_3, K_2O, CaO, MgO and SiO_2. The fused iron catalysts bear multiple advantages such as sustaining for higher reactant flow rates, being low cost and robust. The service lifetime of the fused iron catalysts can reach up to 14-20 years in modern ammonia production plants [187]. The endeavor of the fused iron catalysts is intensely associated with the operating situations, residual oxygen mixes concentration in the feed gas (if any) and the NH_3 concentration produced from the reaction. If ammonia is produced from steam methane reforming, the obtained hydrogen requires purification from carbon containing gases and oxygen. These oxygen-containing compounds such as H_2O, CO, CO_2, and O_2 are the most common poisons faced in ammonia synthesis. These oxygen composites can origin lasting poisoning problems at lower operation conditions such as electrochemical routes, but can become reversible on some forms of iron catalysts at high temperatures [187]. However, if hydrogen is produced from water electrolysis and used in the ammonia synthesis, then the purity of the hydrogen is already in the desired level and there is no requirement for additional separation process. This lowers the poisoning effect of the catalyst in the molten salt medium.

H_2 and N_2 are directly used for electrochemical synthesis of ammonia at the electrodes. N_2 receives the electrons from external power supply. Hence nitrogen gas sent via the porous nickel cathode is reduced to nitride according to the following equation:

$$N_2 + 6e^- \rightarrow 2N^{3-} \tag{3.1}$$

It becomes N^{3-} then after moves to the other electrode where H_2 is being supplied. Hydrogen ions combine with nitrogen ions and form NH_3 at anode electrode as illustrated in Fig. 3.30 and shown the following equation:

$$2N^{3-} + 3H_2 \rightarrow 2NH_3 + 6e^- \tag{3.2}$$

The anode reaction is also achieved on porous nickel electrode.
The overall reaction is:

$$3H_2 + N_2 \rightarrow 2NH_3 \tag{3.3}$$

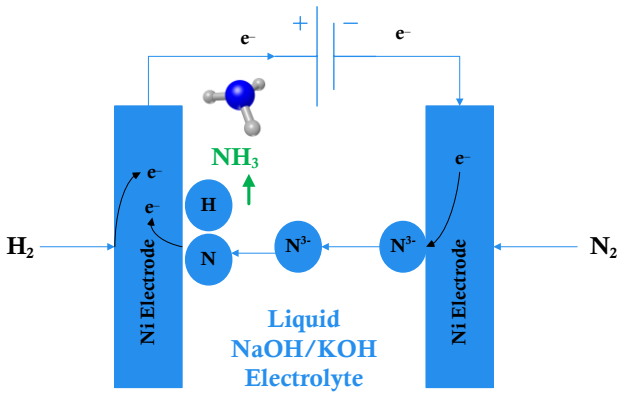

Fig. 3.30 Electrochemical ammonia synthesis reaction in molten salt medium.

Hydrogen and nitrogen are required separately to be produced and supplied to the ammonia synthesis reactor. To conduct the electrochemical reaction for ammonia synthesis, reactant nitrogen is supplied from then nitrogen tank. For the production of hydrogen, a separate electrode-electrolyte assembly was formed consisting of graphite rods and NaOH electrolyte. The volume of the electrolyte is 1 L whereas the molarity of NaOH solution is 1 M.

Nickel mesh is used for both electrodes each having an area of 100 cm^2 as shown in Fig. 3.31. In some experiments, the nickel electrodes are not fully immersed in the electrolyte resulting in less active area. The active area of the electrodes immersed in the electrolyte is used for coulombic efficiency calculations. Nickel meshes have high melting point, non-corrosivity, high conductivity and good stability in molten salt medium. The reactor, 500ml crucible, is made of Alumina (Al_2O_3) being 99.6% pure, having high melting point, strong hardness, chemical stability and non-corrosivity. The cover plates are made of stainless steel (316 alloy) which withstand high temperatures.

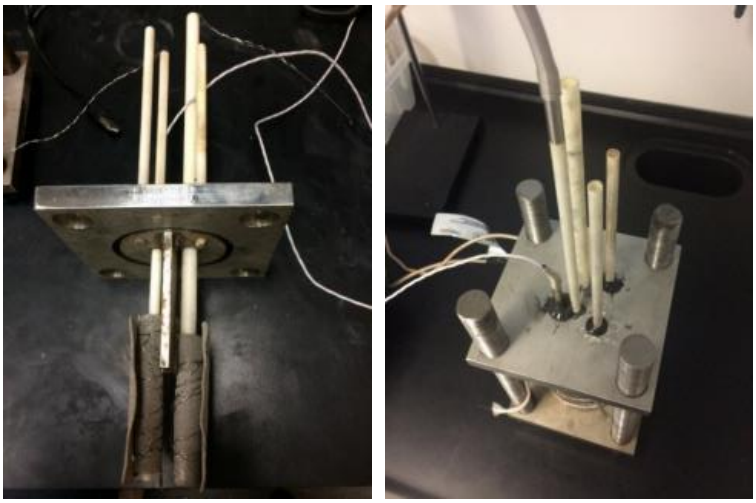

Fig. 3.31 Nickel mesh electrodes in the reactor, reactants and products tubing for the reactor.

The molten salt electrolyte is a mixture of 0.5 M NaOH and 0.5 M KOH. The mass of the NaOH is 221 g whereas KOH mass is 310 g. The total volume of the mixture was about 430 mL at 200°C. The mixture is originally prepared at room temperature, putting the salts into the reactor to melt in the crucible when heated up to 255°C.

Iron oxide (Fe_3O_4) as nano-powder (20-30 nm, 98+%) is used in the experiments as catalyst. The high surface area of the nano-Fe_3O_4 in the electrochemical synthesis is critical for the reaction to occur and to obtain higher ammonia evolution rates. Since ammonia is highly soluble in water, the molten salt electrolyte is not mixed with the water inside the reactor to allow higher ammonia capturing in the H_2SO_4 solution.

As mentioned earlier, the product gases from the reactor is bubbled through an ammonia trap consisting of a dilute 500 ml 0.001 M H_2SO_4 solution, changed every 15 minutes for ammonia analysis. Ammonia concentration is determined using various techniques to confirm the results. The methods utilized are as follows: ammonia test strips, ammonia gas

flowmeters, Arduino ammonia gas sensor and salicylate-based ammonia determination method as the experimental setup is shown in Fig. 3.32.

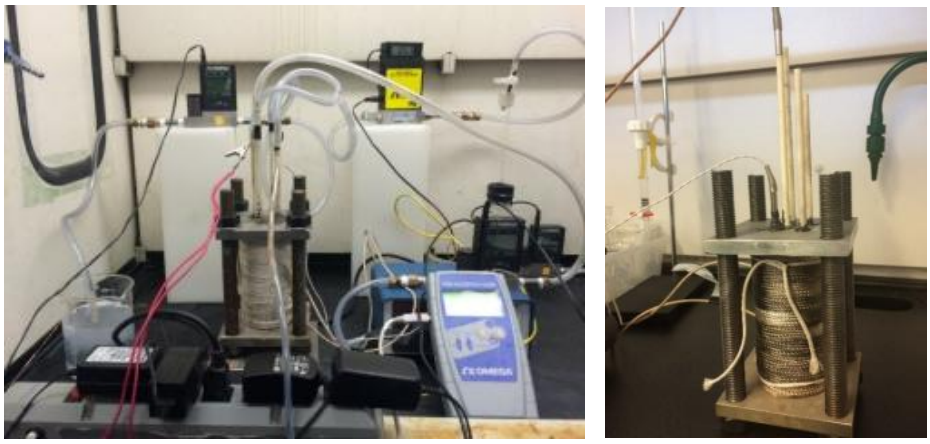

Fig. 3.32 Heating tape used around the alumina crucible and experimental setup with flowmeters, temperature controller and tubing.

For the salicylate-based method, two different solutions are used where one of them contains sodium salicylate and the other one contains sodium hydroxide and sodium hypochlorite. In each case, redundant measurements yield similar ammonia formation values, with the observed reproducibility of methodologies. In addition, the pH level of the dilute H_2SO_4 solutions are recorded before and after NH_3 trapped in the solution in order to observe the dissolved ammonia.

3.5 Experimental Setup of Integrated Ammonia Synthesis Using Photoelectrochemical Hydrogen

Synthesis of NH_3 using water as a source of H_2 in the electrochemical process is also possible in the current setup. However, here hydrogen is separately produced using photoelectrochemical route. Co-generation of H_2 and NH_3 allows cases where NH_3 and H_2 as alternative fuels are required individually. In this thesis, photoelectrochemically generated H_2 is directly used in the formation of electrochemical NH_3. In the integrated system, it is reported the electrochemical synthesis of ammonia using photoelectrochemical H_2 and N_2 at ambient pressure in a molten salt ambient with the catalyst of nano-Fe_3O_4 as the schematic diagram is shown in Fig. 3.33.

The ammonia electro-synthesis chamber comprises a nickel mesh cathode and a nickel mesh anode immersed in molten hydroxide electrolyte containing 10 g suspension of the nano-Fe_3O_4 contained in alumina crucible sealed to allow gas inlet at the cathode and gas outlet from the exit tubes. The reactants, H_2 and N_2, are bubbled through the mesh over the anode and cathode, respectively. The combined gas products (H_2, N_2 and NH_3) exit through two exit tubes in chamber head space. The exiting gases are firstly measured using flowmeters and bubbled through an ammonia water trap then analyzed for ammonia, and subsequently the NH_3 scrubbed-gas is further analyzed for H_2 or N_2 using hydrogen analyzer device (ABB Continuous gas analyzers model AO2020) and hydrogen sensor. In the alumina crucible cell,

the anode consists of a pure Ni mesh and the cathode consisting of same material. These Ni meshes are stable in the molten 200°C-250°C hydroxide. The electrodes are connected externally by spot welded Ni wires. The reactor is kept at constant temperature using on/off temperature controller and the internal temperature of the reactor is continuously measured using a Pt 100 temperature probe inside the reactor body.

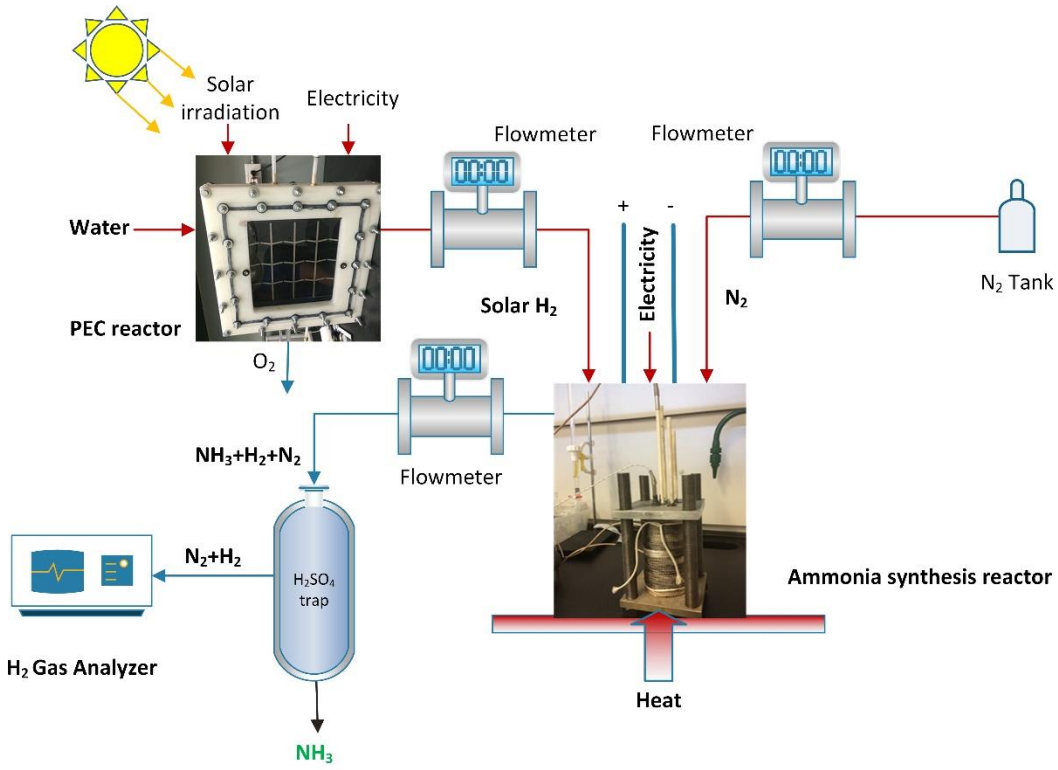

Fig. 3.33 Photoelectrochemical integrated electrochemical ammonia synthesis.

Both hydrogen and nitrogen are required separately to be produced and supplied to the ammonia synthesis reactor. To conduct the electrochemical reaction for ammonia synthesis, reactant nitrogen is supplied from then nitrogen tank. The hydrogen is supplied from photoelectrochemical reactor as depicted in Fig. 3.34.

Fig. 3.34 Integrated system for photoelectrochemical hydrogen and ammonia production unit.

The nickel mesh is used for both electrodes each having an area of 25 cm^2 (immersed in the electrolyte) for the integrated system although it was 100 cm^2 for the individual ammonia production tests. This is because of the electrolyte volume in the ammonia reactor. The area of 25 cm^2 is used for coulombic efficiency calculations. The nickel meshes have high melting point, non-corrosivity, high conductivity and good stability in molten salt medium. The reactor, 500 mL crucible, is made of Alumina (Al_2O_3) being 99.6% pure, having high melting point, strong hardness, chemical stability and non-corrosivity. The cover plates are made of stainless steel (316 alloy) which withstand high temperatures. The molten salt electrolyte is a mixture of 0.5 M NaOH and 0.5 M KOH. The total volume of the mixture is about 215 mL at 200°C. The mixture is originally prepared at room temperature, placing the salts into the reactor to melt in the crucible when heated up to the desired reaction temperature. The reactants, H_2 and N_2, are bubbled through the mesh over the anode and cathode, respectively. The nitrogen gas flow rate is about 80 mL/min on average and hydrogen flow rate is about 10 mL/min on average during the experiments. The combined gas products (H_2, N_2 and NH_3) exit through two exit tubes in chamber head space. The exiting gases are firstly measured using flowmeters and bubbled through an ammonia water trap then analyzed for ammonia, and subsequently the NH_3 scrubbed-gas is analyzed for H_2 or N_2 using hydrogen analyzer device.

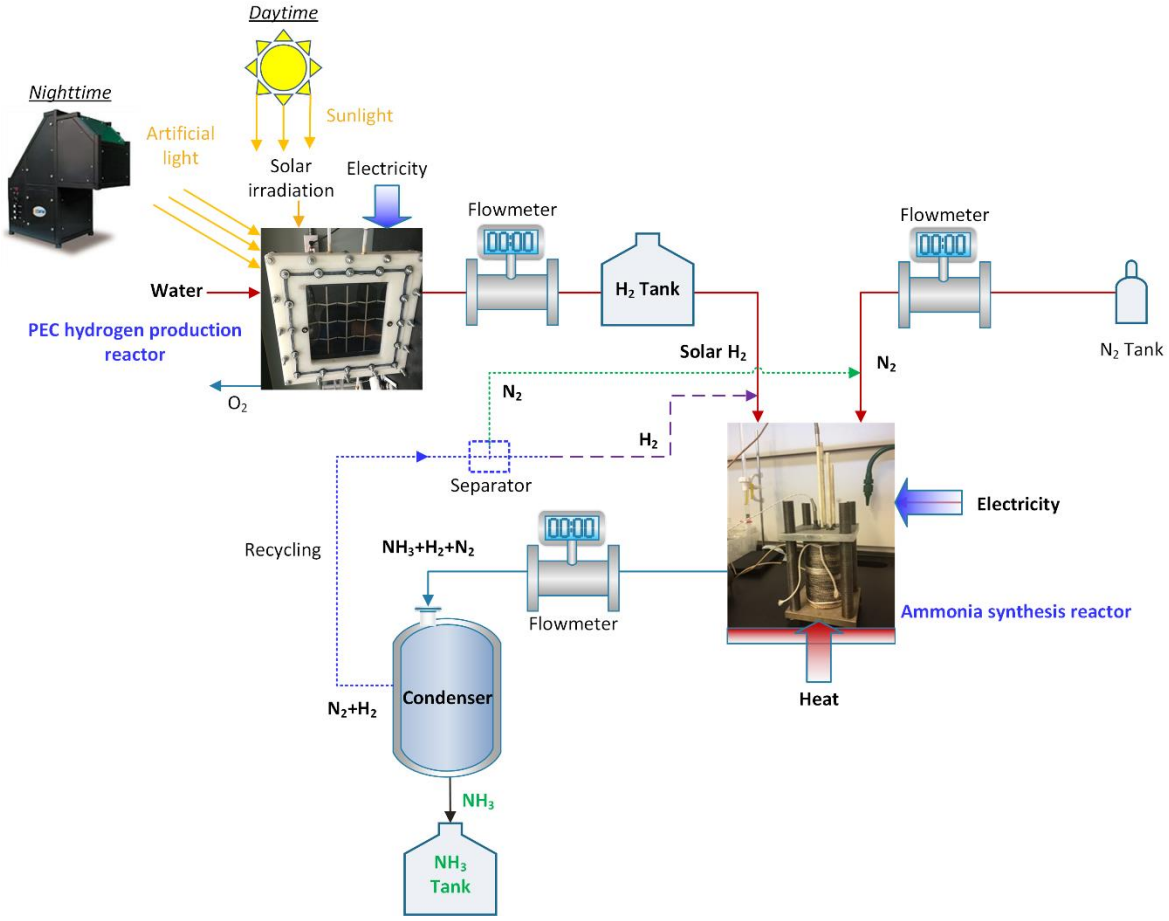

Fig. 3.355 Integrated system for photoelectrochemical hydrogen and ammonia production including storage tanks and back-up artificial light source.

Although the unreacted gases are not recycled in the experiments, the recycling of the unreacted H_2 and N_2 is possible using appropriate arrangements such as gas separators. In addition, the yielded H_2 can be initially stored in a H_2 hydrogen storage tank and then used in the NH_3 production as illustrated in Fig. 3.35. In this way, the changes in the demand can be compensated. Since the boiling temperature of NH_3 is quite higher than H_2 and N_2, a condenser can be used to collect the yielded NH_3 in the tank. When needed, NH_3 can be used for power generation using power generators, fuel cells, etc. Furthermore, as a back-up light source, an artificial light source can be integrated to the system for running the system in the nighttime or to support the system at low-irradiation levels.

CHAPTER 4: ANALYSIS AND MODELING

In this chapter, a detailed explanation of methodology used in the study is presented. The performance of the hydrogen and ammonia production systems and the integrated system are studied by conducting comprehensive energy and exergy analyses. Furthermore, electrochemical models of the systems are developed and assessed comparatively with experimental results. In order to assess the economic aspects of the system, exergoeconomic and scale-up analyses are conducted. Moreover, a multi-objective optimization technique is employed to find the optimal operating conditions and corresponding exergy efficiencies and total cost rates. The main analyses performed in this thesis are explained in the following sections as shown in Fig. 4.1.

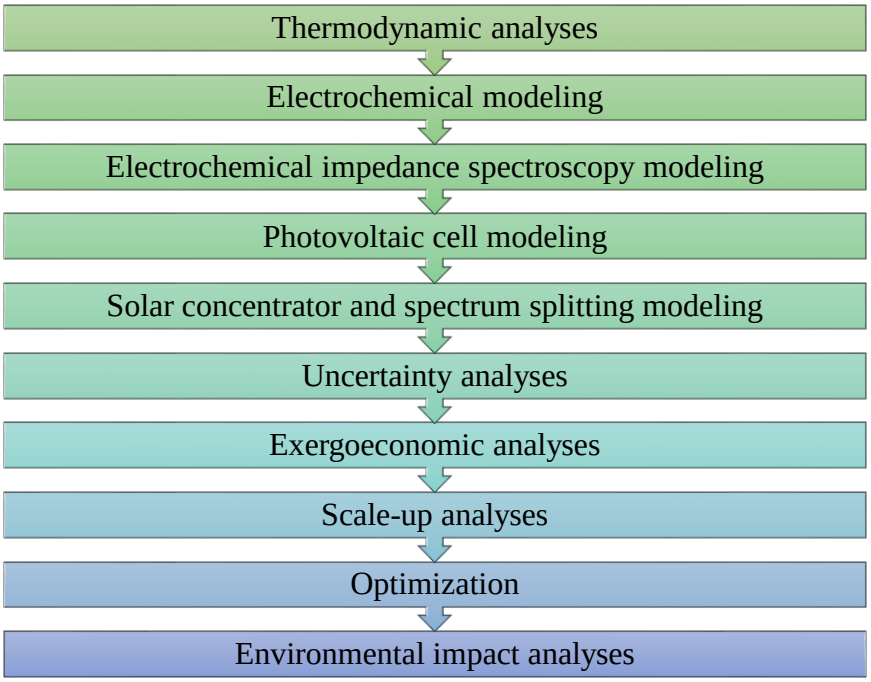

Fig. 4.1 The modeling and analyses performed within this thesis.

4.1 Thermodynamic Analyses

In thermodynamic analyses, overall mass, energy, entropy and exergy balance equations are written for each component of the integrated system.

General conservation of mass in a control volume for any system can be written as follows:

$$\sum \dot{m}_{in} - \sum \dot{m}_{out} = \frac{dm}{dt} \tag{4.1}$$

Here, the terms "in" and "out" specify the control volume and the inlet and outlet of the control volume, respectively. If the operation is considered as steady state, then there is no accumulation or consumption of mass which results in $\dot{m}_{in} = \dot{m}_{out}$.

The common steady state form of the energy balance equation (neglecting the potential and kinetic energy) can be written as

$$\dot{Q} - \dot{W} + \sum \dot{m}_{in} h_{in} - \sum \dot{m}_{out} h_{out} = 0 \quad (4.2)$$

where $\dot{Q}$ and $\dot{W}$ represent the heat transfer and work rate crossing the boundaries and $\dot{m}$ and h represent the mass flow rate and the specific enthalpy of the streams of the system.
The flow exergy terms for streams are expressed using specific enthalpies as follows:

$$ex_i = h_i - h_0 - T_0(s_i - s_0) + ex_{ch} \quad (4.3)$$

where ex_{ch} is specific chemical exergy of flow streams.
Applying the exergy balance at steady state, the exergy destruction rate for each component is calculated using:

$$\dot{E}x_{d_i} = \dot{E}x^{Q_i} - \dot{E}x_{W_i} + \sum \dot{m}_{in} ex_{in} - \sum \dot{m}_{out} ex_{out} \quad (4.4)$$

The exergy transfer due to heat can be expressed as follows:

$$\dot{E}x^{Q_i} = \dot{Q}_i \left(1 - \frac{T_0}{T_{s_i}}\right) \quad (4.5)$$

where T_o is the ambient temperature and T_S is the temperature of source in case there is a heat penetration and temperature of sink in case there is a heat loss.
From energy or exergy perspectives, an indicator of how effectively the input is converted to the product is the ratio of product to input. That is, the energy efficiency η_{en} can be written as

$$\eta_{en} = \frac{\text{Energy output in product}}{\text{Energy input}} = 1 - \frac{\text{Energy loss}}{\text{Energy input}} \quad (4.6)$$

When the useful portion of energy is considered, second law efficiency or exergy efficiency η_{ex} can be defined as

$$\eta_{ex} = \frac{\text{Exergy output in product}}{\text{Exergy input}} = 1 - \frac{\text{Exergy waste emission+Exergy destruction}}{\text{Exergy input}} \quad (4.7)$$

Some of the main assumptions in the thermodynamic analyses are listed as follows:

- The changes in the control volumes are ignored.
- The H_2, O_2, and NH_3 gases are assumed as ideal
- The changes in potential and kinetic energies are negligible.
- The processes take place in steady-state and steady-flow.
- The ambient temperature and pressure are 25°C and 1 atm, respectively.
- The ammonia reaction temperature is constant at set temperature.
- The dielectric mirrors fully divide the spectrum after 700 nm up to 1200 nm.

4.2 Electrochemical Modelling of Photoelectrochemical Hydrogen Production

In the designed membrane electrode assembly for the PEC cell, a membrane is used as a solid electrolyte instead of a liquid electrolyte. The two half-cells are divided by the solid acidic membrane, which is commonly called proton exchange membrane or polymer electrolyte membrane (PEM). The current collectors allow an electric current to flow from the bipolar plates to the electrodes and, concurrently, the supply of reactant water to and the removal of the produced gas bubbles from the electrodes [188]. The bipolar plates enclose the two half-

cells and deliver the electrical contact to the exterior power supply. Commonly, they comprise flow field assemblies to improve the transport of liquid water to the electrodes and oxygen and hydrogen out of the cell. Frames with fastening components or gaskets squeeze the half-cells to avoid gas and water leakage from the inside to the environment. The membrane as the solid electrolyte is very thin, permitting for a shorter proton transport path and thus lesser ohmic loss. Electrocatalysts prepared from the origins of the platinum group metal empower high efficiency and fast kinetics. The electrolyte is restrained in the membrane and cannot be leached out of the membrane or pollute the generated gases. The cell scheme is very dense causing in low thermal masses and fast heat-up and cooling-off times and in grouping with the fast kinetics of the electrocatalysts, in a very fast response time even at ambient circumstances [188].

The general chemical equation of water electrolysis can be expressed by the following equation:

$$\mathrm{H_2O_{(l)}} + \Delta\mathrm{H_R} \rightarrow \mathrm{H_{2_{(g)}}} + \frac{1}{2}\mathrm{O_{2_{(g)}}} \tag{4.8}$$

Here, ΔH_R signifies the change in the reaction enthalpy for this endothermic reaction where electricity is used to decompose water into hydrogen and oxygen. Water is supplied as liquid reactant as the PEC cell is operated below 100°C. The overall electrolysis reaction is the summation of the two electrochemical half reactions, which occurs at the electrodes according to the following equations:

$$\text{Anode: } \mathrm{H_2O_{(l)}} \rightarrow \frac{1}{2}\mathrm{O_{2_{(g)}}} + 2\mathrm{H^+} + 2\mathrm{e^-} \tag{4.9}$$

$$\text{Cathode: } 2\mathrm{H^+} + 2\mathrm{e^-} \rightarrow \mathrm{H_{2_{(g)}}} \tag{4.10}$$

An electrical DC supply is coupled to the electrodes, which are, in the basic case, two plates made from inert metal such as platinum or iridium immersed in the aqueous electrolyte. The decomposition of water begins when a DC voltage greater than the thermodynamic reversible potential, is applied to the electrodes. Nevertheless, the entropy change for the reaction is negative and various activation obstacles have to be overcome. Consequently, a DC voltage higher than the thermoneutral potential is obligatory to drive a PEC hydrogen production cell. At the anode (positively charged electrode) water is oxidized, the electrons pass through the exterior electrical circuit and oxygen evolves as gas. Protons travel through the solid electrolyte from the anode to the cathode (negatively charged electrode) where they are reduced by the electrons from the exterior electrical circuit to hydrogen gas. The amount of hydrogen produced is twice the amount of oxygen generated on the anode side if an ideal faradaic efficiency is presumed.

The splitting of water is determined by electrical and thermal energy input. ΔH_R can be rewritten as the sum of the involvement of these driving forces:

$$\Delta H_R = \Delta G_R + T\,\Delta S_R \tag{4.11}$$

Here, the entropy is a quantity of the disorder for a thermodynamic system. The change in entropy because of the chemical reaction is given by the difference in entropy of the product and the sum of the entropies of the reactants, with the associated stoichiometric factors:

$$\Delta S_R = \sum_p v_p \, \Delta S_{R_p} - \sum_r v_r \, \Delta S_{R_r} \tag{4.12}$$

where p represent products and r represents reactants. Here, $T\,\Delta S_R$ is named as the entropy term and signifies the thermal input desirable for the splitting of water. ΔG_R is another thermodynamic quantity, named the change in Gibbs free energy or free enthalpy of reaction. It can be considered as the maximum work which can be taken out from the thermodynamic system, without the volume work. Most of the PEC systems operate at temperatures lower than 80°C. Therefore, the introduction of thermal energy is considered to be small, which means all the energy required must be applied by electrical energy. If the electrolysis process takes place under reversible conditions, the potential difference at the electrodes is called the reversible cell voltage E_{rev}. It is the minimum electrical work which is required to split up water if the necessary involvement of thermal energy is present. Using the defined ΔG_R at standard state, the Faraday constant F and the quantity of charges n (electrons) transported during the reaction, E_{rev} can be calculated by the following equation:

$$E_{rev} = \frac{\Delta G_R}{n\,F} = 1.229\ V \tag{4.13}$$

As ΔG_R and ΔH_R are not only functions of temperature but of pressure as well, the Nernst equation links the concentration (or activity) of the reactants (which can be replaced by partial pressures) and products to the potential difference of the electrodes. The common representation of the Nernst equation for the reversible cell voltage of the water splitting method is given as follows [186, 187]:

$$E_{rev}\,(T, P_i) = E_r(T, P) + \frac{RT}{nF} \ln\left(\frac{p_{H_2}\, p_{O_2}^{\frac{1}{2}}}{p_{H_2O}}\right) \tag{4.14}$$

where p is the partial pressures of the species and R is the ideal gas constant.

As the cell modules are electrically settled in a series connection, all voltage losses from the anode and the cathode parts can be added up to obtain the total cell overpotentials. The cell voltage E_{actual}, that is a measure of the total quantity of electrical energy demand for water decomposition, then results from the sum of the reversible cell voltage E_{rev} and all irreversible losses within the cell. There are three major mechanisms that lead to kinetics losses in a PEC cell: activation losses due to slow electrode reaction kinetics, ohmic losses, and mass transfer losses. Hence, actual cell voltage can be determined using:

$$E_{actual} = E_{rev} + E_{act} + E_{ohm} + E_{conc} \tag{4.15}$$

Here, “act”, “ohm” and “conc” represent the activation, ohmic and concentration overpotentials, respectively. Once the current is passed through the cell, the actual voltage for water splitting becomes considerably higher than the open circuit voltage (OCV) values, due to irreversible losses within the cell.

The activation losses are so-called faradaic and result from the direct transfer of electrons between redox couples at the boundary between the electrode and the electrolyte of the oxygen generation and the hydrogen generation. This causes irreversibilities on the anode and the cathode called anodic activation overpotential and cathodic activation overpotential which when summed up together forms the total activation overpotential. The ohmic and mass transport losses conversely are because of non-faradaic loss mechanisms [188]. Ohmic losses happen due to resistance to electron flow through the electrodes and cell components as well as resistance to the flow of protons through the membrane. It is directly related to the quantity of current delivered through the cell according to Ohm's law. Activation losses are prevailing at low current densities, while the ohmic overpotential develops to be prevailing at mid current densities. The development of mass transport losses takes two major forms: diffusion and bubbles overpotentials. Diffusion losses happen when gas bubbles partly blocks the pores network of current collectors and thus limiting the supply of reactant water to the active sites, while bubbles overpotential occurs when very large gas bubbles shield the electrochemical active area, reducing catalyst utilization [188].

The activation polarization is given in terms of current density and exchange current density by Butler-Volmer equation [186, 187]:

$$J = J_0 \left\{ \exp\left(\frac{\alpha_a n F E_{act,a}}{RT}\right) - \exp\left(-\frac{\alpha_c n F E_{act,c}}{RT}\right) \right\} \tag{4.16}$$

where J_0 is the exchange current density, α_a and α_c are the electron transfer coefficients for anode and cathode, respectively, n is number of transferred electrons, and $E_{act,a}$ and $E_{act,c}$ are the activation overpotentials related with anode, and cathode respectively.
This equation can be reorganized and written with respect to each electrode as follows:

$$E_{act,a} = \frac{RT}{\alpha_a n F} \ln\left(\frac{J}{J_{0,a}}\right) \tag{4.17}$$

$$E_{act,c} = \frac{RT}{\alpha_c n F} \ln\left(\frac{J}{J_{0,c}}\right) \tag{4.18}$$

Here, number of electrons for cathode electrode is 2 whereas it is 4 for anode electrode. α_c is taken as 2.87 and α_a is taken as 0.64 [190]. The $J_{0,a}$ and $J_{0,c}$ exchange current densities are taken as 3.2×10^{-9} A/cm^2 for anode electrocatalyst which is Ir/Ru-oxide and 1.7×10^{-11} A/cm^2 for cathode electrocatalyst which is Pt for the PEC cell [189, 190].
Therefore, the total activation overpotential is the summation of each electrode:

$$E_{act} = E_{act,c} + E_{act,a} \tag{4.19}$$

Ohmic overpotentials are a form of non-faradaic losses because of the resistance of the movement of electrical currents over the cell mechanisms and the movement of protons over the polymer electrolyte membrane.

The total ohmic overpotential is computed by the employing Ohm's law:

$$E_{ohm} = I\mathcal{R}_{ohm} \tag{4.20}$$

where $\mathcal{R}$ is the sum of all electrical and ionic (ohmic) resistances of the cell modules since they are connected electrically in series.

The chief issues affecting the proton conductivity of a membrane are temperature and the membrane hydration. The membrane conductivity can be calculated based on [188]:

$$\sigma_{mem} = (0.005139 \times \lambda_m - 0.00326) \times \exp(1268 \left(\frac{1}{303} - \frac{1}{T_{cell}}\right) \tag{4.21}$$

where T is the operating cell temperature and λ_m is the degree of membrane hydration expressed as the mole of H_2O per mole of SO_3^- in the Nafion membrane. The λ_m value ranges from 14 to 25, depending on the membrane hydration, with 14 for very poorly hydrated membrane and 25 when it is fully hydrated. Here, we take it as 18 since the membrane is quite fresh [192]. The ohmic resistance can be written as

$$\mathcal{R}_{ohm} = \frac{\delta_{mem}}{\sigma_{mem}} \tag{4.22}$$

where δ_{mem} is the membrane thickness.

When the electrode kinetics is noticeably fast, there is zero buildup of reactants on the electrode surface as it is being quickly used up, and the reaction is mass transport controlled. For the reaction to be continued, reactants are required to be supplied to the reaction interface at an appropriate rate. The rate of reaction can be calculated by the rate of supply of the reactants. Since the half-cell reaction occurs on porous electrode surfaces and since there are no more than two component mixtures for the anode and cathode reaction, Fick's diffusion is assumed to be the dominant mass transport mechanism. The concentration polarizations are derived for each electrode:

$$E_{conc,c} = -\frac{RT}{nF}\ln\left(1 - \frac{J}{J_{L,c}}\right) \tag{4.23}$$

$$E_{conc,a} = -\frac{RT}{nF}\ln\left(1 - \frac{J}{J_{L,a}}\right) \tag{4.24}$$

Here, $J_{L,a}$ and $J_{L,c}$ are the limiting current densities for anode and cathode, respectively.

The limiting current densities are dependent on the diffusion coefficients. The diffusion rate is limited by flow through the porous media diffusion layer and electrode. If we assume one-dimensional flux to the electrode surface in the x direction with no bulk flow velocity, the limiting current density can be calculated based on [189]:

$$J_{L,a} = -n\,F D_{eff} y_i \frac{P}{RT\,\delta} \tag{4.25}$$

Here, δ is the distance to the electrode surface from the flow channel boundary (The Nernst diffusion layer is a thin layer that lies intermediate bounds the electrodes and the bulk), y_i is the molar fraction of the species, P is the pressure in Pascal and D_{eff} is the effective diffusion coefficient of the species. For a typical membrane electrode assembly such as PEC cell, $D_{eff} = \frac{D}{1.5}$ can be used [189].

The diffusion coefficients of the water and hydrogen species can be determined in cm^2/s by:

$$D_{H_2O-H_2} = 10^{-3}\frac{T^{1.75}}{P}\left(\frac{\frac{1}{MW_{H2O}}+\frac{1}{MW_{H2}}}{\sum_i(V_{H2O})^{1/3}+\sum_i(V_{H2})^{1/3}}\right) \quad (4.26)$$

where T and P are in Kelvin and atmospheres, respectively, MW is molecular weight, and molecular diffusion volumes V_{H2O} and V_{H2} are given as 12.7 and 7.07 for water and hydrogen respectively [189].

For oxygen and water diffusion coefficient, we can write the following equation [189]:

$$D_{H_2O-O_2} = \frac{4.19836\times10^{-7}}{P}\times T^{2.334} \quad (4.27)$$

where pressure P is in atmospheres and temperature T is in Kelvin.

The quantity of gas produced by an electrochemical process can be associated to the electrical charge consumed by the cell, which is described by Faraday's law.

$$\dot{m} = \frac{I\,MW_{H_2}}{n\,F} \quad (4.28)$$

where I is the total current in Amps supplied to the PEC cell which can be calculated using $A_{cell}\times J$. The main parameters considered in the electrochemical model are listed in Table 4.1.

Table 4.1 Main input parameters for the electrochemical model and integrated system.

Parameter	Value	Unit
Cathode exchange current density	3.2×10^{-7}	A/m^2
Anode exchange current density	1.70×10^{-9}	A/m^2
Hydrogen pressure	1	atm
Water pressure	1	atm
Oxygen pressure	1	atm
Membrane conductivity	0.102	S/cm
Membrane conductivity under concentrated light	0.1156	S/cm
Membrane thickness	0.0127	cm
Anode - Effective diffusion coefficient	0.1869	cm^2/s
Anode - Effective diffusion coefficient under concentrated light	0.2011	cm^2/s
Cathode - Effective diffusion coefficient	0.4097	cm^2/s
Cathode - Effective diffusion coefficient under concentrated light	0.4329	cm^2/s
PEC cell active area	0.025	m^2
Fresnel lens area	8.76×10^{-1}	m^2
Dielectric mirrors area	7.70×10^{-2}	m^2
PV area	4.09×10^{-2}	m^2
Ambient temperature	298	K
Bandgap temperature of Cu_2O	24364	K
Bandgap temperature of silicone PV	12765	K
PEC cell temperature	313	K
PEC cell temperature under concentrated light	323	K
PV temperature	348.9	K

For an ideal water electrolysis process, the electric charge, flowing over the cell, is a direct measure of the amount of hydrogen and oxygen produced. From this equation, it is probable to measure the efficiency of the real process by associating the charges fed to the system and the amount of hydrogen (or oxygen) being formed.

4.3 Electrochemical Impedance Spectroscopy Modeling

Electrochemical impedance spectroscopy (EIS) is an effective method where a minor voltage sinusoidal perturbation is applied to the system and then amplitude and phase angle of the resultant current reaction are defined. Detailed understanding of the manners happening in the cells is desired to advance their performance. An extensive diversity of physical and chemical approaches were determined to investigate the electrical features of semiconductor electrodes in contact with liquid electrolyte. Amongst, the EIS is an important experimental technique since it delivers information about charge transfer occurrences, double layer features, carrier generation and recombination practices. The explanation of the EIS results needs the usage of appropriate theoretic models. The usage of equivalent electrical correspondents to fit the EIS data is consequently foreseen as an imperative instrument to detect and infer the charge transfer phenomena happening in the PEC cell under characteristic operating circumstances. This method eventually permits defining electrochemical parameters which help evolving the best approach to arrange the photoelectrodes with optimal features [193]. Principally, the non-destructive method of measuring allows EIS, an attractive implement for investigating the photoelectrochemical cell performance without disconcerting from the operation.

In electrochemical impedance spectroscopy, the structure is perturbed with an AC of minor degree and system response is calculated under different conditions. One of the important benefit of using EIS measurements is that the method is non-destructive permitting to be performed during the operation of PEC cell without troubling the system. The degree of the impedance is written with real and imaginary portions as follows:

$$|Z| = \sqrt{{Z_r}^2 + {Z_j}^2} \tag{4.29}$$

and the phase angle can be found as follows:

$$\varphi = \tan^{-1}\frac{Z_j}{Z_r} \tag{4.30}$$

Nyquist and Bode plots are frequently utilized to characterize the impedance measurements [194]. In the Nyquist plot, the real portion of the impedance is denoted in the x-axis and the imaginary portion of the impedance is denoted in the y-axis. Every point in the Nyquist diagram resembles impedance at one specific frequency. A main drawback in the Nyquist diagram is that the frequency is not determined by purely observing at the plot. In contrast, the impedance is figured with the logarithmic frequency shown on the x-axis and mutually the total value of impedance and the phase angle are illustrated on the y-axis in the Bode diagram.

Experimental electrochemical impedance spectroscopy records are regularly examined by fitting into an equivalent electrical circuit model. Numerous circuit components in the

models are general electrical components namely: resistors, capacitors and inductors. The responses of these impedances are written as

$$Z_R = R \tag{4.31}$$

$$Z_L = j\,\omega\,L \tag{4.32}$$

$$Z_C = \frac{1}{j\,\omega\,C} \tag{4.33}$$

The impedance of a perfect resistor is purely real and the electrons over the resistor are generally in phase with the potential through it, while, the impedance of a perfect inductor and capacitor has only imaginary part. For example, the response of an inductor is exactly inverse of a capacitor in terms of impedance. The impedance of an inductor rises as the frequency is elevated while the impedance of capacitor drops with a rise in frequency.

There are couple of processes inside the PEC cells occurring during the operations such as double layer capacitance, charge transfer resistance and diffusion. Double layer capacitance is a splitting of charges or electrical double layer happens at any border in the polarized arrangement like the border between the electrode and the electrolyte, ion exchange membranes, etc. This corresponds to a capacitor in the electrical circuit. Charge transfer resistance is the transfer of electrons from the ionic kinds in the solution to the solid metal that is based on the type of the reaction, temperature, concentration of the entering chemicals and the voltage. Diffusion is one of the significant manners in mass transport processes from the bulk electrolyte via the membranes. The substrates should diffuse passing via the films, become oxidized and the products obtained need to diffuse back to the bulk electrolyte. This type of diffusion is considerable solitary at the low AC frequency, while at an upper AC frequency the impedance because of the surface for the electrochemical reactions.

Consequently the impedance formed by this type of diffusion occurrence necessitates combination of a diffusion component in the equivalent circuit model. The element representative of the semi-infinite linear diffusion is named as Warburg impedance [193, 194]. Diffusion can generate an impedance called as Warburg impedance. Warburg impedance is based on the frequency of the voltage perturbation. At higher frequencies the Warburg impedance is minor since, diffusing reactants do not necessitate to travel very distant. At lower frequencies the reactants need to diffuse farther, thus causing an increase in the Warburg impedance. The equation for the infinite Warburg impedance can be written as [196]

$$Z = \frac{\frac{1}{Y_0}}{\sqrt{(j\omega)}} \tag{4.34}$$

where $Y_0 = \frac{1}{\sqrt{2}\,\sigma}$

This type of the Warburg impedance is solitary useable if the diffusion sheet has an infinite thickness. However, in practical applications, it not generally infinite. If the diffusion layer is bounded, the impedance at low frequencies does not follow Eq. 6. As a substitute, we get the following form [196]:

$$Z = \frac{\frac{1}{Y_0}}{\sqrt{(j\omega)}} tanh(B\sqrt{j\omega}) \quad (4.35)$$

where $B = \frac{\delta}{\sqrt{D}}$.

Here, δ is Nernst diffusion layer thickness in cm and D is mean value of the diffusion coefficients of the diffusing species (cm²/s). The parameters used for fitting this element in model are Y_0 (W-M in this thesis) in siemens-$s^{0.5}$, and B in $s^{0.5}$.

Another variation of the Warburg is the Bounded Warburg which is defined as follows [196]:

$$Z = \frac{1/Y_0}{\sqrt{(j\omega)}} \quad (4.36)$$

The Bounded Warburg describes a diffusion process totally within a thin slice of solution or a thin slice of material. Common examples are a conducting polymer membranes or supercapacitors. A Warburg component delivers data about the charge diffusion procedures in a PEC cell. Therefore, the mass transportation/diffusion practice perceived at low frequencies can be modeled by means of the Warburg element [197]. Since a finite diffusion is perceived in PEC cell, the impedance of a general finite Warburg component can be written as follows [196]:

$$Z_W = R \frac{tanh(j\, T_W\, \omega)^{\varphi}}{(j\, T_W\, \omega)^{\varphi}} \quad (4.37)$$

where R denotes the Warburg resistance, T_W is a Warburg time constant, φ is the Warburg phase constant, and ω is the angular frequency. The Warburg impedance acts as a diagonal line with an angle of 45° on the Nyquist plot and occurs with a shift in phase corresponding to 45° on the Bode plot.

The capacitors in EIS experiments often do not behave ideally. The double layer capacitor on real cells often behaves like a CPE instead of like a capacitor as defined below:

$$Z = \frac{1/Y_0}{(j\omega)^a} \quad (4.38)$$

When this equation defines a capacitor, the constant Y_0 = C (the capacitance) and the exponent a = 1. For a CPE component, the exponent a is lower than one.

Numerous reasonable series and parallel arrangement of Warburg element, CPE, resistance and inductor are tried to fit the experimental impedance diagrams. Because several equivalent circuit models can yield similar impedance behavior, the combinations are carefully selected when modeling the circuits as close as possible to actual PEC cell processes. Finally, the equivalent circuit model having a bounded Warburg element shown in Fig. 4.2 is considered for fitting purposes.

A nonlinear numerical least-square fitting method is utilized to get precise numbers for the equivalent circuit elements. Simplex method is utilized to fit the impedance of circuit model to the experimental EIS data using Gamry Echem Analyst software. The Simplex method minimizes x^2 to fit the impedance data to the selected equivalent circuit model. Each model includes a number of adjustable parameters. The fitting routine searches for the parameter values that cause the model's impedance spectrum to most closely match the experimental

spectrum. The minimization algorithm makes a number of estimates for the values of the adjustable parameters. After each estimate, a goodness of fit value is determined and evaluated. New estimates for the parameter values are then made, using the Simplex algorithm. The process is repeated until the fit stops improving, or until a preset number of iterations have been made. The goodness of fit values are accepted which were under the 10^{-4} criterion implying a good fit. After fitting the model to the experimental data, the fit guesses numbers for the model parameters, such as the resistance, the double-layer capacitance and Warburg element.

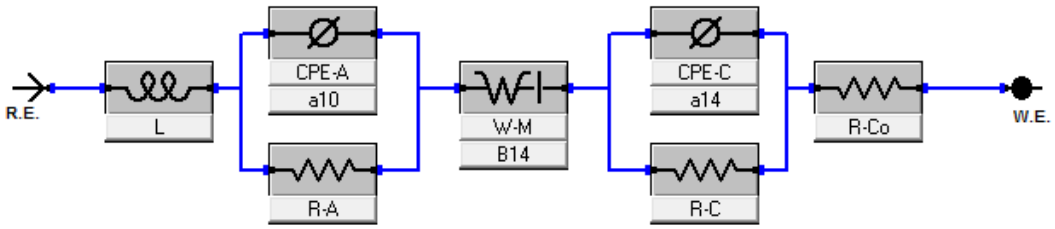

Fig. 4.2 Equivalent circuit model of photoelectrochemical cell in this thesis.

4.4 Photocurrent Generation Process

In this section, the analyses for photocurrent generation process from the PV cell and PEC cell are described in detail by considering the complete process starting from photonic radiation to photodiode.

4.4.1 Photonic radiation

The spectral irradiance of the blackbody radiation at temperature T signifies the power conceded by monochromatic photons flux per unit of normal surface and wavelength (W/m^2nm). The irradiance of the blackbody (W/m^2) consequences from the integral of $I_{\lambda,b}$ for the complete range of wavelengths. It is noted that entropy of a monochromatic radiation is an broad property independent of wavelength [198].

A universal quanta of entropy could be related to a quanta of light. Since entropy is extensive meaning that entropy is additive. Moreover, as all photons of the monochromatic radiation have completely the same features meaning that they have same wavelength, same speed, same energy, they should yield perfectly the same vibrionic dissipation at interaction with matter. Therefore,

$$\dot{S}_{\lambda}'' = \dot{N}_{\lambda}'' \mathcal{S}_{\lambda} \tag{4.39}$$

where $\dot{N}_{\lambda}''$ is the spectral photon distribution, that is photon rate per unit of normal surface and wavelength ($photons/m^2nm$), $\mathcal{S}_{\lambda}$ is the entropy of light quanta (here the subscript λ signifies light – or wavelength; noting that $\mathcal{S}_{\lambda}$ is independent on wavelength), $\dot{S}_{\lambda}''$ is the entropy flux of the monochromatic radiation (W/m^2nm). The parameter $\mathcal{S}_{\lambda}$ is signified entropy constant of a photon and it is a universal constant [38, 196, 197].

The entropy constant of a photon results as follows:

$$\mathcal{S}_\lambda = \frac{hc}{T}\,\frac{\int_0^\infty I_{\lambda,\mathrm{b}}\mathrm{d}\lambda}{\int_0^\infty \lambda I_{\lambda,\mathrm{b}}\mathrm{d}\lambda} \tag{4.40}$$

where T is the temperature of blackbody radiation.

The entropy flux of the blackbody radiation becomes

$$\dot{S}''_\mathrm{b} = \frac{1}{T}\int_0^\infty I_{\lambda,\mathrm{b}}\mathrm{d}\lambda \tag{4.41}$$

At the same time, $\dot{S}''_\mathrm{b} = \mathcal{S}_\lambda \int_0^\infty \dot{N}''_{\lambda,\mathrm{b}}\mathrm{d}\lambda$, where one has $I_{\lambda,\mathrm{b}} = \dot{N}''_{\lambda,\mathrm{b}}(hc/\lambda)$

$$\dot{N}''_{\lambda,\mathrm{b}} = \frac{\lambda}{hc} I_{\lambda,\mathrm{b}} \tag{4.42}$$

Therefore,

$$\dot{S}''_\mathrm{b} = \frac{\mathcal{S}_\lambda}{hc}\int_0^\infty \lambda I_{\lambda,\mathrm{b}}\mathrm{d}\lambda \tag{4.43}$$

The equality of $\dot{S}''_\mathrm{b}$ given by the above two statements written as follows:

$$\frac{1}{T}\int_0^\infty I_{\lambda,\mathrm{b}}\mathrm{d}\lambda = \frac{\mathcal{S}_\lambda}{hc}\int_0^\infty \lambda I_{\lambda,\mathrm{b}}\mathrm{d}\lambda \tag{4.44}$$

that proves the preceding expression. Moreover, as solved by Chen et al. [198], the entropy constant of the photon yields

$$\mathcal{S}_\lambda = 2.69952 k_\mathrm{B} = 3.7268 \times 10^{-23}\,\frac{\mathrm{J}}{\mathrm{K}} \tag{4.45}$$

The entropy flux of any polychromatic radiation of spectral photon distribution given by $\dot{N}''_\lambda$ (photon/s m^{2}nm) or the spectral irradiance given by I_λ (W/m^{2}nm) is specified by

$$\dot{S}'' = \mathcal{S}_\lambda \int_0^\infty \dot{N}''_\lambda \mathrm{d}\lambda = \frac{\mathcal{S}_\lambda}{hc}\int_0^\infty \lambda I_\lambda \mathrm{d}\lambda \tag{4.46}$$

for that the proof is straightforward.

The temperature of any polychromatic radiation of spectral photon scattering given by $\dot{N}''_\lambda$ (photon/s m^{2}nm) or the spectral irradiance given by I_λ (W/m^{2}nm) is considered by

$$T_\mathrm{rad} = \frac{hc}{\mathcal{S}_\lambda}\,\frac{\int_0^\infty I_\lambda \mathrm{d}\lambda}{\int_0^\infty \lambda I_\lambda \mathrm{d}\lambda} \tag{4.47}$$

The entropy flux the preceding expression must be equivalent to the irradiance $\int_0^\infty I_\lambda \mathrm{d}\lambda$ divided to the temperature of the radiation. This equation is solved for T_rad.

A temperature T_λ of a photon (or of a monochromatic radiation) could be described as follows:

$$\lambda T_\lambda = \frac{hc}{\mathcal{S}_\lambda} = \text{constant} \tag{4.48}$$

In the above equation, hc/λ is the energy of a photon. When this energy is divided to the entropy, a parameter with units of temperature results as follows:

$$T_\lambda = \frac{hc}{\lambda s_\lambda} = \text{constant} \tag{4.49}$$

Therefore, using Chen et al. [198] results, the effective temperature and photon's entropy constant of a single photon are, respectively:

$$\mathrm{T}_\lambda = \frac{\mathrm{c}_\lambda}{\lambda} \tag{4.50}$$

$$\mathrm{S}_{\mathrm{ph}} = \frac{\mathrm{hc}}{\mathrm{c}_\lambda} \tag{4.51}$$

with $\mathrm{c}_\lambda = 0.00533016\ \mathrm{mK}$

Moreover, the temperature equation of a polychromatic radiation given formerly can be reorganized as follows:

$$\frac{1}{T_{\mathrm{rad}}}\int_0^\infty I_\lambda \mathrm{d}\lambda = \frac{hc}{s_\lambda}\int_0^\infty \lambda I_\lambda \mathrm{d}\lambda = \int_0^\infty \frac{1}{\left(\frac{hc}{\lambda s_\lambda}\right)} I_\lambda \mathrm{d}\lambda = \int_0^\infty \frac{I_\lambda}{T_\lambda}\mathrm{d}\lambda \tag{4.52}$$

The first and last expressions of the equalities above show that T_{rad} signify a weighted average of T_λ assistances for which the weighting factors are the spectral irradiances.

When a closed thermodynamic system interrelates with a reference environment at T_0 through a photonic radiation at temperature $T_{\mathrm{rad}} \geq T_0$, then the exergy of the system, denoted also the exergy of the radiation is shown as follows:

$$\dot{E}x'' = \left(1 - \frac{T_0}{T_{\mathrm{rad}}}\right)\int_0^\infty I_\lambda \mathrm{d}\lambda = \left(1 - \frac{T_0}{T_{\mathrm{rad}}}\right) I \tag{4.53}$$

where $I = \int_0^\infty I_\lambda \mathrm{d}\lambda$ represents the normal irradiance ($\mathrm{W/m^2}$).

The solar radiation is polychromatic consisting of a broad spectrum of wavelengths that usually is approximated with a blackbody radiation. Therefore the interaction of solar light with the matter must happen at numerous wavelengths. The photons may excite electrons by transporting work, though most of this work is transformed to heat over numerous forms of dissipative process. Here, in order to attain the exergy and entropy contents of solar radiation, a reference spectrum is presumed for AM 1.5 solar spectrum given in standard ASTM G 173-03 [200].

The photocurrent generation process is modeled using photodiode approach. The photoactive surface is the semiconductor Cu_2O that is deposited on the photocathode electrochemically. The dark current density J_{dark} represents the current across the p-n junction that is enthused by the background radiation. The background radiation is a blackbody radiation at the temperature of the cell. As the photons radiated by the blackbody cover the entire spectrum of wavelengths (0, ∞), there should be photons with energy greater than the bandgap energy. At saturation, the holes and electrons concentration across the junction is such that the current in both directions is identical. Even though the energetic photons impose the electrons from n to p, the formed electric field encourages a reverse electrons current, that is from p to n.

The dark saturation current density J_0 must be equivalent to the elementary charge multiplied to the rate of photons of blackbody radiation per unit of cell surface area that have energy higher than the bandgap energy. The bandgap energy is represented with $E_{\mathrm{g}} = eV_{\mathrm{g}}$,

where V_{g} is the potential across the junction at saturation. One can describe an effective temperature of the bandgap by associating $E_{\mathrm{g}} = k_{\mathrm{B}}T_{\mathrm{g}} = h\frac{c}{\lambda_g}$. Here, λ_g is taken as 590 nm for copper oxide where the bandgap energy is 2.1 eV [58, 62, 65, 199]. The calculation of the bandgap energy is given elsewhere [202]. Providing that the cell emits blackbody radiation at temperature T_{cell} from both faces, the rate of energetic photons per unit of cell surface can be written as follows:

$$\dot{N}''_{\mathrm{g,b}} = f\,\frac{2\pi k_{\mathrm{B}}T_{\mathrm{c}}^3}{h^3 c}\int_{T_{\mathrm{g}}/T_{\mathrm{c}}}^{\infty}\frac{\chi^2}{e^{\chi}-1}\,\mathrm{d}\chi \tag{4.54}$$

where χ denotes dummy variable and $\dot{N}''_{\mathrm{g,b}}$ is a measured in photons/m^2 of exposed surface.

Subsequently, the dark saturation current density is considered as $J_0 = e\dot{N}''_{\mathrm{g,b}}$, or it can be computed with the estimated formula where the unit is A/m^2 [111]:

$$J_0 = 1.5 \times 10^9 \exp\left(-T_{\mathrm{g}}/T_{\mathrm{c}}\right) \tag{4.55}$$

If the junction is polarized by any means (e.g., connection of a load) then the potential across becomes V_{D} (where D stands for diode; or p-n junction). Accordingly, the direct polarization current upsurges proportionately with activation energy eV_{D}, thus, the net current expresses the dark current according to the Shockley equation for diode, namely:

$$J_{\mathrm{dark}} = J_0\left(\exp\left(\frac{eV_{\mathrm{D}}}{n_{\mathrm{i}}k_{\mathrm{B}}T_{\mathrm{c}}}\right) - 1\right) \tag{4.56}$$

where $n_{\mathrm{i}} = 1 \ldots 2.5$ represents the p-n junction non-ideality factor that is taken as 1 for the analyses.

If no load is coupled to the PV/PEC cell, then the load potential takes the value of the so-called open circuit potential, V_{oc}. Additionally, the open circuit potential in dark condition (non-illuminated cell) can be attained if one sets $J_{\mathrm{Load}} = 0$ and $J_{\mathrm{ph}} = 0$. In practical PEC cells it is stated that the open circuit potential for the non-illuminated cell is insignificant with respect to the open circuit potential of the illuminated cell. This means that for the purpose of estimating the open circuit potential one can presume that shunt resistance $R_{\mathrm{sh}} \to \infty$. This gives the following approximate solution acquired when the photocurrent equation of the PV/PEC cell is solved:

$$V_{\mathrm{oc}} \cong \frac{n_{\mathrm{i}}k_{\mathrm{B}}T_{\mathrm{c}}}{e}\ln\left(1 + \frac{J_{\mathrm{ph}}}{J_0}\right) \tag{4.57}$$

If the load is in short circuit, then it is reasonable to assume that $J_{\mathrm{dark}} + J_{\mathrm{sh}}$ is negligible with respect to J_{ph}. Thus, the short circuit current will be given by:

$$J_{\mathrm{sc}} \cong J_{\mathrm{ph}} = \left(\frac{e}{hc}\right)\int_0^{\infty}\lambda\Phi_{\mathrm{e},\lambda}I_{\mathrm{ph},\lambda}\,\mathrm{d}\lambda \tag{4.58}$$

The internal spectral quantum efficiency $\Phi_{\mathrm{i},\lambda}$ of a PEC cell is described as the rate of electrons displaced by photons from valence to conduction band of the p-n junctions and the rate of photons absorbed. Not all the absorbed photons are useful: some photons have energy smaller than band gap and their absorption (if any) results in heat dissipation. The spectral

internal quantum efficiency (IQE) is an important aspect that is defined as the ratio of electrons displaced across the semiconductor junction ($\dot{N}_{e,\lambda}$) and the rate of photons absorbed at a certain wavelength ($\dot{N}_{ph,abs,\lambda}$):

$$\Phi_{i,\lambda} = \frac{\dot{N}_{e,\lambda}}{\dot{N}_{ph,abs,\lambda}} = \frac{I_\lambda}{e} \times \frac{h \times c}{\lambda \times I_{abs,\lambda}(\lambda)} \tag{4.59}$$

where I_λ in A/m^2 is the electric current density generated by the absorbed photons and $I_{abs,\lambda}(\lambda)$ W/m^2 nm is the spectral irradiance at wavelength λ of the absorbed photons in a normal direction to PEC surface.

Since there are losses, another quantum efficiency called as external spectral quantum efficiency (EQE) is defined. The external spectral quantum efficiency $\Phi_{e,\lambda}$ of a photoactive surface is defined as the rate of electrons displaced by photons from valence to conduction band of the p-n junctions and the rate of photons incident on the cell surface.

$$\Phi_{e,\lambda} = (1 - \mathcal{R}_\lambda - \mathcal{T}_\lambda)\Phi_{i,\lambda} \tag{4.60}$$

where $\mathcal{R}_\lambda$ represent the spectral reflectance of transparent coatings applied to the PEC cell protective materials and $\mathcal{T}_\lambda$ is the spectral transmittance. It can be stated as:

$$\Phi_{e,\lambda} = \frac{\dot{N}_{e,\lambda}}{\dot{N}_{ph,\lambda}} = \Phi_{i,\lambda}\,(1 - \mathcal{R}_\lambda - \mathcal{T}_\lambda) = \frac{I_\lambda}{e} \times \frac{h \times c}{\lambda \times I_\lambda(\lambda)} \tag{4.61}$$

where $\dot{N}_{ph,\lambda}$ is the rate of incident photons on the surface of PEC cell, and $I_\lambda(\lambda)$ is the spectral irradiance at the wavelength λ of the incident photons.

The spectral photonic current density $J_{ph,\lambda}$ in A/m^2 is described as the electric current in A per unit of area (m^2) persuaded by the photons of wavelength λ, incident on the photoactive surface according with the spectral irradiance $I_{ph,\lambda}$. Based on the spectral quantum efficiencies definitions, the photonic current density becomes:

$$J_{ph} = \left(\frac{e}{hc}\right) \int_0^\infty \lambda \Phi_{e,\lambda} I_{ph,\lambda} d\lambda = \left(\frac{e}{hc}\right) \int_0^\infty \lambda (1 - \mathcal{R}_\lambda - \mathcal{T}_\lambda) \Phi_{i,\lambda} I_{ph,\lambda} d\lambda \tag{4.62}$$

where e represents the elementary charge.

The fill factor is given by the following empirical correlation from [203]:

$$FF \cong \frac{v_{oc} - \ln(v_{oc} - 0.72)}{v_{oc} + 1} \left(1 - \frac{R_s J_{sc} A_c}{V_{oc}}\right) \tag{4.63}$$

where $v_{oc} = (eV_{oc})/(k_B T_c)$ signifies a dimensionless open-circuit potential.

4.5 Photovoltaic Cell Modeling

There are various practices and their relations inside a PV cell. These are mainly (i) photonic processes: photons transmission, reflection and spectral absorption, background (blackbody) radiation emission at cell temperature, (ii) electrical processes: electron excitation to create a photocurrent, electron-hole recombination, electrical power transmission to an external load, (iii) thermal processes: internal heat generation by shunt and series resistances, heat dissipation by conduction-convection as shown in Fig. 4.3. A physical model considering the highly complex collaboration and interdependence among these procedures is elaborated based on

energy and exergy balances accomplished with numerous constitutive calculations, counting relationships for the convective heat transfer coefficient and for the photocurrent dependency of the spectral distribution of the quantum efficiency. The irreversibilities caused by the practices are evaluated concerning their relative magnitudes of the exergy destructions.

The steps of energy and exergy analysis of a PV cell under imposed operating circumstances are exemplified in this division. The goal of the exergy study is to evaluate the system (PV cell) with respect to a totally reversible power cycle operating under the same energy source (photonic radiation) and the atmosphere.

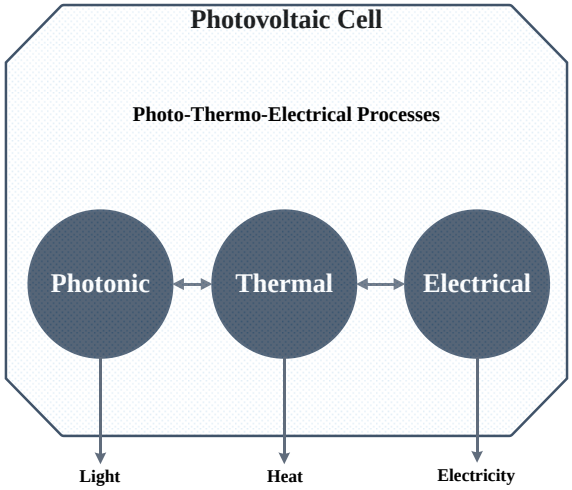

Fig. 4.3 Interactions of sub-processes in a PV cell.

Table 4.2 The defined processes within the PV cell.

State	Description
1	Light radiation involvement
2	Light radiation reflected by the wafer
3	Light absorbed by the wafer
4	Light radiation transmitted through the wafer
5	Heat dissipation due to vibrionic collaboration of the photons
6	Electric power transmitted to the shunt resistance
7	Dissipated heat by the shunt resistance
8	Electrical power transported to the p-n junction
9	Dissipated heat by the p-n junction
10	Blackbody radiation at cell temperature T_c
11	Electric power transferred to the internal series resistance
12	Dissipated heat by the series resistance
13	Heat flux dissipated by the casing into the environment at T_0
14	Useful power output provided to the load

The exergy examination and assessment defines the exergy efficiency and exergy destruction of the overall system and of the sub-processes, namely; photonic, thermal and

electrical where they are listed in Table 4.2. The interactions of these processes are schematically illustrated in Fig. 4.4 where the equivalent electrical circuit diagram of a PV cell is shown in Fig. 4.5.

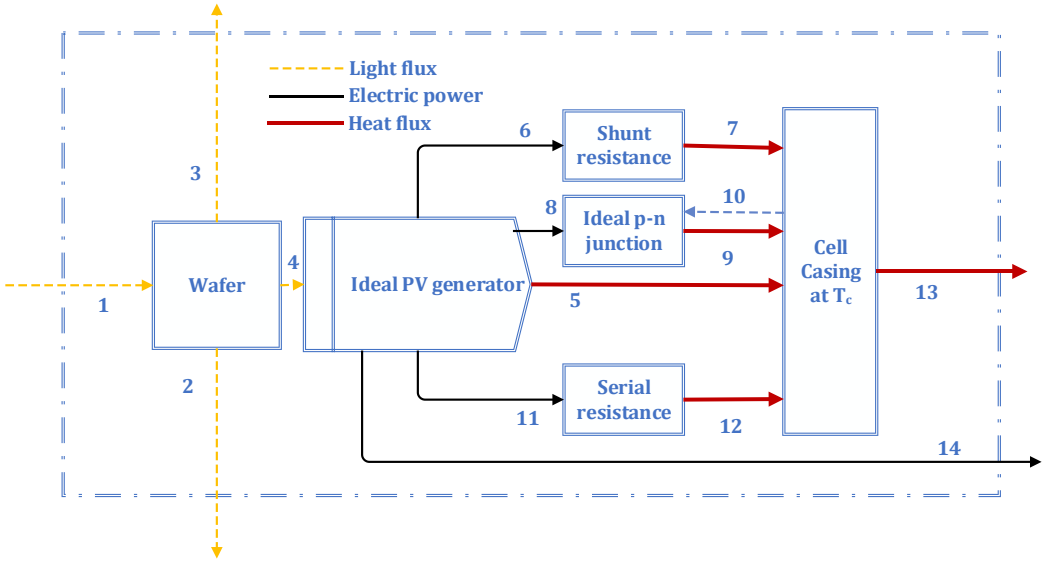

Fig. 4.4 Schematic diagram of PV cell as a holistic approach including photo-thermo-electrical processes.

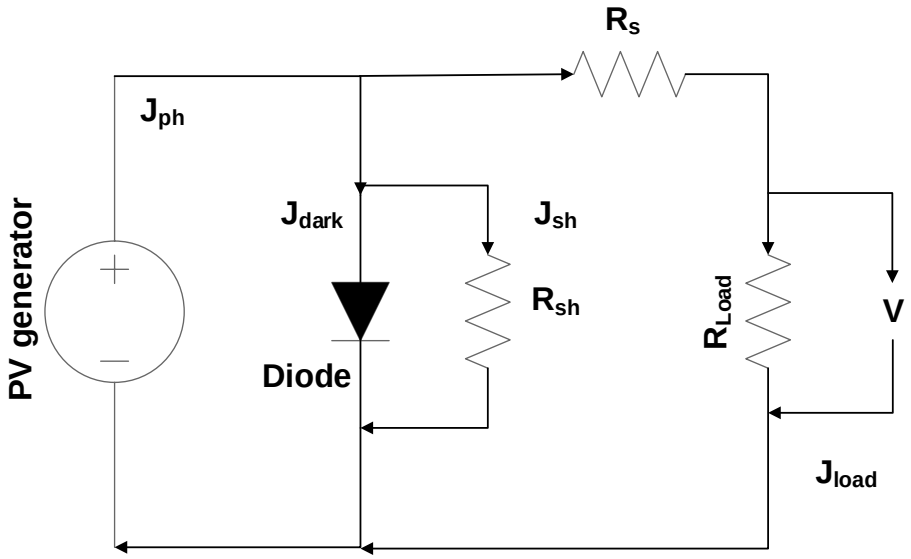

Fig. 4.5 Equivalent electric circuit diagram of PV cell.

In the second analysis step, the streams and the state points are designated in detail to examine the internal processes mentioned in Table 4.3. The state points defined in the PV cell are described as given in Table 4.3 below.

Table 4.3 Descriptions and definitions of state points within the system.

State	Description
1	Light radiation involvement at temperature $T_1 = T_{\mathrm{rad}}$ and with spectral irradiance $I_{\lambda,1}$
2	Light radiation reflected by the wafer conferring to spectral reflectance $\mathcal{R}_\lambda$
3	Light transmitted by the wafer conferring to spectral transmittance T_λ
4	Light radiation absorbed through the wafer according to spectral absorbance A_λ and ultimately contributing to photocurrent generation
5	Heat dissipation due to vibrionic interaction of the absorbed photons with the wafer
6	Electric power transported to the shunt resistance, $\dot{W}_6'' = J_{\mathrm{sh}} V_{\mathrm{D}}$
7	Dissipated heat by the shunt resistance, transported to the casing at T_{c}, $\dot{Q}_6'' = \dot{W}_5''$
8	Electrical power transferred to the p-n junction, $\dot{W}_8'' = J_{\mathrm{dark}} V_{\mathrm{D}}$
9	Dissipated heat by the p-n junction transferred to the cell casing at T_{c}
10	Blackbody radiation at cell temperature T_{c} absorbed by the p-n junction, $I_{10} = \dot{Q}_9''$
11	Electric power transferred to the internal series resistance, $\dot{W}_{11}'' = J_{\mathrm{Load}} V_{\mathrm{s}}$
12	Dissipated heat by the series resistance, transferred to the casing at T_{c}, $\dot{Q}_{12}'' = \dot{W}_{11}''$
13	Heat flux dissipated by the casing into the environment at T_0
14	Useful power output delivered to the load, $\dot{W}_{14}'' = J_{\mathrm{Load}} V_{\mathrm{Load}}$

Only a share (4) of the instance photons (1) are transferred by the wafer (photovoltaic generator). Plentiful of the energy of the absorbed photons is dissipated as heat (5) because of vibrionic interaction. The formed photovoltaic power is transported to the shunt resistance (6), to the p-n junction for its polarization (8), to the load (14) and to the internal series resistance (11).

In the present study, an optical model so called OPAL 2 is utilized. It is an optical simulator for the front surface of a photovoltaic solar cell [204]. In the stated model, the assembly of a solar cell is designated and OPAL 2 computes the reflection from its front surface, the absorption in its thin-film coatings, and the diffusion into its substrate over a series of wavelengths. OPAL 2 at the same time estimates the photocurrent that is formed within the cell for a specified instance spectrum.

Table 4.4 Parameters for PV equivalent circuit analyses.

Parameter	Value
V_{load} (V)	18.7
J_{load} (A/m^2)	7.344
A_{cell} (m^2)	0.04085
R_s (Ω)	0.0364
R_{sh} (Ω)	60.2409
J_{dark} (A/m^2)	6.45×10^{-10}
J_0 (A/m^2)	2.057×10^{-10}
V_{oc} (V)	22.67
J_{sc} (A/m^2)	8.078

Source: [203, 204]

The generation pattern is projected. The assumptions in the model are as follows: (i) all transmitted light moves perpendicularly to the plane of the substrate, and (ii) secondary-pass light is absorbed evenly in the substrate. Thus, the net generation should be accurate for a given set of inputs, but the scattering of that generation within substrate is projected. Substrate width of wafer is presumed to be 180 mm in the present study. It is made of crystalline at 300 K [204]. In the current study, a monocrystalline silicon (m-Si) type PV cell is used for the analyses. Corresponding circuit parameters of PV cell such as saturation current, series resistance etc. are used as shown in Table 4.4.

In the analyses unit, steady-state energy balance equations (EBE) are inscribed for each process. A code to solve the scheme is built in Engineering Equation Solver (EES). The energy and exergy balance equations of the procedures are given in Table 4.5.

Table 4.5 Energy and exergy balance equations of the processes inside the PV cell.

Process	**Energy Balance Equation**	**Exergy Balance Equation**
Wafer - light absorption	$\dot{E}_1 = \dot{E}_2 + \dot{E}_3 + \dot{E}_4$	$\dot{E}x_1 = \dot{E}x_2 + \dot{E}x_3 + \dot{E}x_4 + \dot{E}x_{d,waf}$
PV generator - photocurrent generation	$\dot{E}_4 = \dot{E}_5 + \dot{E}_6 + \dot{E}_8 + \dot{E}_{11} + \dot{E}_{14}$	$\dot{E}x_4 = \dot{E}x_5 + \dot{E}x_6 + \dot{E}x_8 + \dot{E}x_{11} + \dot{E}x_{14} + \dot{E}x_{d,ph}$
Shunt resistance - dissipation	$\dot{E}_6 = \dot{E}_7$	$\dot{E}x_6 = \dot{E}x_7 + \dot{E}x_{d,sh}$
Ideal p-n junction - dissipation	$\dot{E}_8 + \dot{E}_{10} = \dot{E}_9$	$\dot{E}x_8 + \dot{E}x_{10} = \dot{E}x_9 + \dot{E}x_{d,dark}$
Series resistance - dissipation	$\dot{E}_{11} = \dot{E}_{12}$	$\dot{E}x_{11} = \dot{E}x_{12} + \dot{E}x_{d,s}$
Cell casing - heat transfer	$\dot{E}_5 + \dot{E}_7 + \dot{E}_9 + \dot{E}_{12} = \dot{E}_{10} + \dot{E}_{13}$	$\dot{E}x_5 + \dot{E}x_7 + \dot{E}x_9 + \dot{E}x_{12} = \dot{E}x_{10} + \dot{E}x_{13} + \dot{E}x_{d,cas}$
Overall	$\dot{E}_1 = \dot{E}_2 + \dot{E}_3 + \dot{E}_{13} + \dot{E}_{14}$	$\dot{E}x_1 = \dot{E}x_2 + \dot{E}x_3 + \dot{E}x_{13} + \dot{E}x_{14} + \dot{E}x_{d,cell}$

In order to govern the maximum quantity of work from solar radiation instance on the Earth, ideal conversion efficiency of solar radiation (η_{carnot}) may be written:

$$\eta_{carnot} = 1 - \frac{T_o}{T_s} \tag{4.64}$$

Furthermore, the maximum work utilized from solar radiation (exergy) can be acquired by the following equation:

$$\dot{E}x_{max} = \eta_{carnot}\, S_{T_o} \tag{4.65}$$

where $S_{T_o} = \frac{S_T}{\cos\theta}$ is the total amount of normal irradiance.

The spectral reflectance is obtained based on the extinction coefficient of the material (k) and the refraction index n according to [207].

$$R_\lambda = \frac{(n(\lambda)-1)^2 + k(\lambda)^2}{(n(\lambda)+1)^2 + k(\lambda)^2} \tag{4.66}$$

The refractive index (n) and extinction coefficient (k) are associated to the interaction between a material and incident light and are related with refraction and absorption, respectively. Both refractive index (n) and extinction coefficient (k) depend on the wavelength.
A part of the incoming energy is lost because of transmittance as $\dot{E}_3$:

$$\dot{E}_3 = A_c \int_0^{\infty} T_\lambda I_\lambda d\lambda \tag{4.67}$$

where T_λ is the spectral transmittance of wafer.
Combining above expressions, energy captured by PV generator is defined as follows:

$$\dot{E}_4 = A_c \int_0^{\infty} (1 - \mathcal{R}_\lambda - T_\lambda) I_\lambda d\lambda \tag{4.68}$$

The exergy rate of state points from 1 to 4 can be calculated as follows:

$$\dot{E}x_i = \dot{E}_i (1 - T_0/T_i) \tag{4.69}$$

where i represents the stream number.

The exergy destruction rate occurred in wafer – light absorption process is defined as

$$\dot{E}x_{d,tot,waf} = \dot{E}x_1 - \dot{E}x_4 \tag{4.70}$$

Here, temperatures of state points can be considered from following formulas [208]:

$$T_1 = \frac{hc}{\mathcal{S}_\lambda} \frac{\int_0^{\infty} I_\lambda d\lambda}{\int_0^{\infty} \lambda I_\lambda d\lambda}, T_2 = \frac{hc}{\mathcal{S}_\lambda} \frac{\int_0^{\infty} \mathcal{R}_\lambda I_\lambda d\lambda}{\int_0^{\infty} \lambda \mathcal{R}_\lambda I_\lambda d\lambda}, T_3 = \frac{hc}{\mathcal{S}_\lambda} \frac{\int_0^{\infty} \mathcal{T}_\lambda I_\lambda d\lambda}{\int_0^{\infty} \lambda \mathcal{T}_\lambda I_\lambda d\lambda}, T_4 = \frac{hc}{\mathcal{S}_\lambda} \frac{\int_0^{\infty} (1-\mathcal{R}_\lambda-\mathcal{T}_\lambda) I_\lambda d\lambda}{\int_0^{\infty} \lambda (1-\mathcal{R}_\lambda-\mathcal{T}_\lambda) I_\lambda d\lambda} \tag{4.71}$$

As discussed in Chen et al. [208], the series of constants such as constant speed and wavelength can be extended with the temperature constant of a photon T_λ and the entropy constant of a photon $\mathcal{S}_\lambda$. Consequently, when the photon interacts with a reference environment of temperature T_o the energy conversion into work corresponds to a Carnot factor in accordance to T_λ and T_o. This quantifies an exergy destruction by the individual photon. Thus, when a multi-chromatic photon radiation interrelates with matter at a reference temperature T_o, the exergy destruction can be projected provided that the spectral distribution of the radiation is identified.

4.5.1 PV generator-photocurrent generation process

This process could be named as ideal as there are no ohmic dissipations, etc., nonetheless there is only vibrionic dissipation because of quantum efficiency $\Phi_{i,\lambda} < 1$.
The dissipated heat by the photocurrent generator is defined as follows:

$$\dot{E}_5 = \dot{Q}_{ph} = SF\ k\ (T_{ph} - T_c) \tag{4.72}$$

where SF is in use as the shape factor for conduction through the plane wall where it is a PV cell area here, k is the thermal conductivity of silicon and T_{ph} is the final temperature of the surface.
The energy rate in the shunt resistance is well-defined as the total potential over the resistance divided by shunt resistance based on Ohm's law:

$$\dot{E}_6 = \dot{W}_{sh} = (V_{Load} + J_{Load} A_c R_s)^2 / R_{sh} \tag{4.73}$$

The energy rate in the ideal p-n junction is expressed as follows:

$$\dot{E}_8 = \dot{W}_{dark} = (V_{Load} + J_{Load} A_c R_s) A_c J_{dark} \quad (4.74)$$

where J_{dark} is the current density over diode.
The energy rate on series resistance is calculated based on Ohm's law:

$$\dot{E}_{11} = \dot{W}_s = R_s (J_{Load} A_c)^2 \quad (4.75)$$

Finally, the energy utilized by the load is determined as follows:

$$\dot{E}_{14} = \dot{W}_{Load} = J_{Load} V_{Load} = \dot{W}_{max} = FF\, J_{sc} V_{oc} \quad (4.76)$$

since the cell generates maximum power.
The exergy of heat dissipation at state point 5 is determined as follows:

$$\dot{E}x_5 = \dot{Q}_{ph}(1 - T_0/T_c) \quad (4.77)$$

The exergy rate definitions of state points in Fig. 4.4 at 6,8,11 and 14 is equal to electrical work:

$$\dot{E}x_6 = \dot{W}_{sh}\ ,\ \dot{E}x_8 = \dot{W}_{dark}\ ,\ \dot{E}x_{11} = \dot{W}_s\ ,\ \dot{E}x_{14} = \dot{W}_{Load}. \quad (4.78)$$

The exergy balance for the ideal PV generator can be written as follows and be solved to determine the exergy destruction by the photocurrent generation process ($\dot{E}x_{d,tot,ph}$):

$$\dot{E}x_{d,tot,ph} = \dot{E}x_4 - \dot{E}x_6 + \dot{E}x_8 + \dot{E}x_{11} + \dot{E}x_{14} \quad (4.79)$$

4.5.2 Shunt resistance-dissipation process

The shunt resistance acts as heat source because of shunting of the generated photocurrent and can be written as follows:

$$\dot{E}_7 = \dot{Q}_{sh} = \frac{V_{sh}}{{R_{sh}}^2} \quad (4.80)$$

The exergy rate at state point 7 is written:

$$\dot{E}x_7 = \dot{Q}_{sh}(1 - T_0/T_c) \quad (4.81)$$

The exergy destruction in shunt resistance – dissipation process is stated:

$$\dot{E}x_{d,tot,sh} = \dot{E}x_6 \quad (4.82)$$

4.5.3 Ideal p-n junction-dissipation process

Ideal p-n junction also dissipates heat for the reason that of dark current over the diode that can be calculated as per following formula:

$$\dot{E}_9 = \dot{Q}_{dark} \text{ where } \dot{Q}_{dark} \text{ is equal to } A_c\, J_{dark} V_D. \quad (4.83)$$

The blackbody radiation emitted from the p-n junction at state point 10 can be found for the wavelengths between 280 nm and 4000 nm as

$$\dot{E}_{10} = A_c \sigma {T_c}^4 \quad (4.84)$$

The exergy rates at state points 9 and 10 are calculated:

$$\dot{E}x_9 = \dot{Q}_{dark}(1 - T_0/T_c) \tag{4.85}$$

$$\dot{E}x_{10} = \dot{E}_{10}(1 - T_0/T_{10}) \tag{4.86}$$

where $T_{10} = \frac{hc}{\delta_\lambda} \frac{\int_{\lambda_g}^{\infty} I_{\lambda,b}(T_c)d\lambda}{\int_{\lambda_g}^{\infty} \lambda I_{\lambda,b}(T_c)d\lambda}$ [208] and $\lambda_g = \frac{hc}{E_g}$. (4.87)

The overall exergy destruction rate in ideal p-n junction – dissipation process is determined as follows:

$$\dot{E}x_{d,tot,dark} = \dot{E}x_8 + \dot{E}x_{10} \tag{4.88}$$

4.5.4 Series resistance-dissipation process

Due to the potential drop over the series resistance, heat is generated:

$$\dot{E}_{12} = \dot{Q}_s = I_s V_s \tag{4.89}$$

The exergy rate at state point 12 is stated:

$$\dot{E}x_{12} = \dot{Q}_s(1 - T_0/T_c) \tag{4.90}$$

The exergy destruction rate in series resistance – dissipation process is determined:

$$\dot{E}x_{d,tot,s} = \dot{E}x_{11} \tag{4.91}$$

4.5.5 Cell casing-heat transfer process

There is a temperature difference between cell surface T_c and ambient T_0. Therefore a heat loss or heat penetration can happen depending on the temperature values. It can be determined as follows:

$$\dot{E}_{13} = \dot{Q}_{cell} = h_c A_c (T_c - T_o) \tag{4.92}$$

The exergy rate at state point 13 is stated as follows based on T_c and T_0.

$$\dot{E}x_{13} = \dot{Q}_{cell}(1 - T_0/T_c) \tag{4.93}$$

The total exergy destruction rate in cell casing – heat transfer process is stated as follows:

$$\dot{E}x_{d,tot,cas} = \dot{E}x_5 + \dot{E}x_7 + \dot{E}x_9 + \dot{E}x_{12} - \dot{E}x_{10} \tag{4.94}$$

4.5.6 System performance

The overall energy balance can be computed:

$$\dot{E}_1 = \dot{E}_2 + \dot{E}_3 + \dot{E}_{13} + \dot{E}_{14} \tag{4.95}$$

The overall exergy balance can be written:

$$\dot{E}x_{d,tot,cell} = \dot{E}x_1 - \dot{E}x_{14} \tag{4.96}$$

The energy efficiency of the overall system is stated as follows:

$$\eta_{en} = \dot{E}_{14}/\dot{E}_1 \tag{4.97}$$

The exergy efficiency of the overall system is stated as follows:

$$\eta_{ex} = \frac{\dot{E}x_{14}}{\dot{E}x_1} = \frac{\dot{W}_{act}}{\dot{W}_{tot,rev}} \tag{4.98}$$

where $\dot{W}_{act} = \dot{W}_{max} = \dot{E}x_{14}$ is the power generated by the actual cell and $\dot{W}_{tot,rev}$ is the power produced by a totally reversible generator connected to the source of radiation 1 with radiation temperature T_1 and to the reference environment at T_0.

4.6 Spectrum Modeling

The solar spectra and air mass can be foreseen conferring to the procedure adopted by NREL (National Renewable Energy Laboratory) that is based on the study of Gueymard [209] and can be computed using the software SMARTS described in Gueymard [210]. Alongside the air mass, the solar spectrum depends on the water content and ozone in the atmosphere, also on turbidity, aerosol types and concentration, cloudiness and haziness and optical thickness of the atmosphere. The most significant factor that affects both the intensity of solar radiation at earth surface and the spectrum is the air mass. The air mass is described as the ratio between the path length of sunrays through the atmosphere and the effective atmosphere thickness at local zenith. Air mass relies on the zenith angle, the day of the year and the geographical latitude. At sea level when sun is at zenith then air mass is AM=1, while if sun is at horizon then AM = 38.2 whereas AM1.5 is the most widely accepted case (zenith angle = 48.2°). The complete solar wavelength range is presumed to be between 280 nm and 4000 nm, and the solar constant is 1367 W/m^2. However since the spectrum is split using dielectric mirrors, the portion received by the PEC reactor is limited to 280 nm to 700 nm in that Cu_2O is more active. Upper spectrum is used for PV module for power generation. The solar constant is described as the amount of solar energy (W/m²) at normal incidence outside the atmosphere (extraterrestrial) at the mean sun-earth distance. Nevertheless, the standard spectrum at the Earth's surface is called AM1.5. The air mass values and irradiances for the specific location are computed based on the coordinates and date of the year via SMARTS software. It is considered that sun is being tracked by the setup, hence solar position and experimental system positions are equal in terms of azimuth and zenith angle perpendicular to sun rays. The time of the day is taken to be as 1.00 pm local standard time in Oshawa, Canada.

Environmental circumstances such as vegetation, soil type and geographic irregularity change the PV performance for the reason that Albedo effect. The Albedo is the fraction of incoming radiation reflected off a surface which add to total irradiation on the PV module. The U.S. Standard Atmosphere is an atmospheric model in which pressure, temperature, density, and viscosity of the Earth's atmosphere alternate over an extensive collection of altitudes or elevations. The model that is built over an existing international standard, was first dispersed in 1958 by the U.S. Committee on Extension to the Standard Atmosphere. It was then updated in 1962, 1966, and 1976. It is essentially reliable in procedure with the International Standard Atmosphere, opposing mostly in the assumed temperature distribution at higher altitudes. MLS and MLW denote the middle latitude summer and middle latitude winter, respectively. The middle latitudes are between 23°26'22" North and 66°33'39" North, and between 23°26'22" South and 66°33'39" South latitude, or, the Earth's temperate zones between the tropics and the

Arctic and Antarctic polar regions. The aerosol type is set to S&F RURAL or S&F URBAN where it is based on Shettle and Fenn [211] and SRA CONTL or SRA URBAN where it is based on IAMAP preliminary standard atmosphere [212].

4.7 Concentrator and Spectrum Splitting Mirrors

The energy of photons is associated to their wavelength as stated in this equation:

$$E = \frac{hc}{\lambda} \tag{4.99}$$

where h is Planck's constant, c is the speed of light and λ is the wavelength in m. Also, the amount of Joules in every wavelength is calculated. In order to obtain the spectral irradiance, the following formula is used:

$$I_\lambda = E\dot{N}''_{ph,\lambda} \tag{4.100}$$

where $\dot{N}''_{\mathrm{ph},\lambda}$ is the amount of photons per unit area, for every second. In this way, it is possible to find the irradiance of the photons for each wavelength, and then:

$$I = \int I_\lambda d\lambda \tag{4.101}$$

This value provides the complete irradiance in terms of W/m^2 according to the photons that the system receives at each stage.

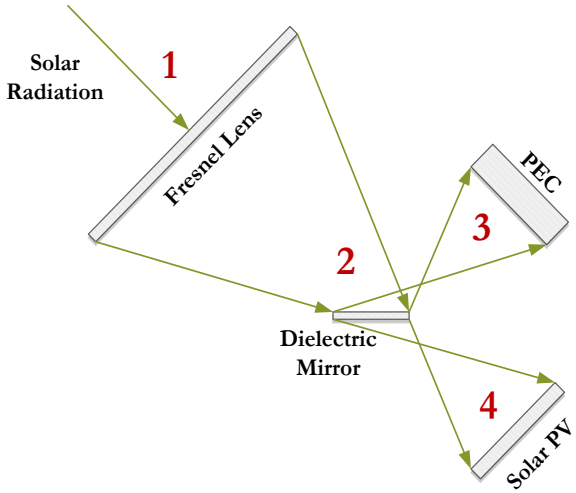

Fig. 4.6 Solar concentrator and spectrum splitting mirrors including the state points.

The Fresnel lens is utilized for concentration that is a periodic refractive structure of concentric prisms. After the Fresnel lens, the light is split using dielectric mirrors. The higher energy spectrum is used for PV and lower energy spectrum is used for PEC reactor. In the integrated system, the point before the Fresnel lens is named state point 1, after the Fresnel lens on the mirror level: state point 2, on the surface of the reactor: state point 3 and on the PV module: state point 4 as illustrated in Fig.4.6. In order to determine the total power that actually reaches to each component in the system shown in Fig. 4.6, the following equations are utilized.

The total energy and exergy with respect to area and irradiance values can be generally written:

$$\dot{E} = A \int I_\lambda d\lambda \tag{4.102}$$

$$\dot{Ex} = \eta_{carnot}\, A \int I_\lambda d\lambda \tag{4.103}$$

where A is illuminated area and η_{carnot} is the Carnot efficiency calculated based on the incoming photon temperatures at each state.

The incoming energy and exergy rates on the Fresnel lens are written for the wavelength range 280 nm to 4000 nm as follows:

$$\dot{E}_1 = A_{lens} \int_{280}^{4000} I_{\lambda,1}\, d\lambda \tag{4.104}$$

$$\dot{Ex}_1 = \eta_{carnot,1}\, A_{lens} \int_{280}^{4000} I_{\lambda,1}\, d\lambda \tag{4.105}$$

where A_{lens} is the Fresnel lens area corresponding to 0.8761 m^2

The energy and exergy rates equation at state point 2 after the Fresnel lens on the dielectric mirrors can be written as follows:

$$\dot{E}_2 = C_{ratio}\, A_{mirror} \int_{280}^{4000} I_{\lambda,2}\, d\lambda \tag{4.106}$$

$$\dot{Ex}_2 = \eta_{carnot,2}\, C_{ratio}\, A_{mirror} \int_{280}^{4000} I_{\lambda,2}\, d\lambda \tag{4.107}$$

where A_{mirror} is the focal area of the dielectric mirrors at specific distance from Fresnel lens and C_{ratio} is the concentration ratio of Fresnel lens that is measured experimentally at the specific position. Here, depending on the Fresnel lens light transmission characteristics, the upper wavelength of the integral can be changed.

The surface dimensions of the cold mirror used in the system are 101.0 mm x 127.0 mm that corresponds to about 128.27 cm^2 surface area for one mirror. In total, six cold mirrors are utilized forming a rectangular area of 769.62 cm^2 in order to increase the illuminated area on the PEC cell.

The energy and exergy light conversion efficiencies from sunlight to dielectric mirror can be written as

$$\eta_{en_{1-2}} = \frac{\dot{E}_2}{\dot{E}_1} \tag{4.108}$$

$$\eta_{ex_{1-2}} = \frac{\dot{Ex}_2}{\dot{Ex}_1} \tag{4.109}$$

The dielectric mirror reflects lower spectrum (<700 nm) to the PEC reactor where the amount of energy and exergy can be stated as follows:

$$\dot{E}_3 = A_{PEC} \int_{280}^{700} I_{\lambda,2} R_\lambda\, d\lambda \tag{4.110}$$

$$\dot{Ex}_3 = \eta_{carnot,3}\, A_{PEC} \int_{280}^{700} I_{\lambda,2} R_\lambda\, d\lambda \tag{4.111}$$

where A_{PEC} is the total light exposed area of PEC reactor and R_λ is the reflectance of the mirrors which is given by the manufacturer and additionally measured by the photo spectrometer taken as 95%.

In this case, the energy and exergy efficiency from concentrated light to reactor input can be defined:

$$\eta_{en,2-3} = \frac{\dot{E}_3}{\dot{E}_2} \tag{4.112}$$

$$\eta_{ex,2-3} = \frac{\dot{E}x_3}{\dot{E}x_2} \tag{4.113}$$

The dielectric mirrors transmits the higher wavelength (>700 nm) spectrum to the PV module up to 1200 nm. Therefore, the energy and exergy rate at state point 4 can be stated as follows:

$$\dot{E}_4 = A_{PV} \int_{700}^{1200} I_{\lambda,2} T_\lambda \, d\lambda \tag{4.114}$$

$$\dot{E}x_4 = \eta_{carnot,4} \, A_{PV} \int_{700}^{1200} I_{\lambda,2} T_\lambda \, d\lambda \tag{4.115}$$

where A_{PV} is the area of the PV cell and T_λ is the transmittance of the mirrors which is given by the manufacturer and additionally measured by the photo spectrometer taken as 95%.

The energy and exergy efficiency from concentrated light to PV can be defined as follows:

$$\eta_{en,2-4} = \frac{\dot{E}_4}{\dot{E}_2} \tag{4.116}$$

$$\eta_{ex,2-4} = \frac{\dot{E}x_4}{\dot{E}x_2} \tag{4.117}$$

4.8 Ammonia Production

Ammonia synthesis process in a reversible reaction as shown below:

$$N_2 + 3H_2 \leftrightarrows 2\,NH_3 \tag{4.118}$$

H_2 and N_2 are directly used for electrochemical synthesis of ammonia at the electrodes. N_2 receives the electrons from external power supply. Hence nitrogen gas sent via the porous nickel cathode is reduced to nitride according to the following equation:

$$\mathrm{N_2 + 6e^- \rightarrow 2N^{3-}} \tag{4.119}$$

It becomes N^{3-} then after moves to the other electrode where H_2 is being supplied. Hydrogen ions combine with nitrogen ions and form NH_3 at anode electrode shown in the following equation:

$$\mathrm{2N^{3-} + 3H_2 \rightarrow 2NH_3 + 6e^-} \tag{4.120}$$

The anode reaction is also achieved on porous nickel electrode.
The overall reaction is:

$$\mathrm{3H_2 + N_2 \rightarrow 2NH_3} \tag{4.121}$$

Besides the temperature, the pressure effects the value of the enthalpy of reaction. Though this influence is insignificant in the case of reactions in the liquid phase, substantial impacts are detected for gas-phase reactions at high pressures. The deviances from ideal gas behavior can directly be considered using residual enthalpies $(h - h_{ideal})_{T,P,i}$, which describe

the enthalpy difference between the real state and the ideal gas state at a given temperature and pressure. Using residual enthalpies of the reactants and products, the enthalpy of reaction in the real state at given temperature and pressure can be determined if the standard enthalpy of reaction in the ideal gas state at this temperature is known. A representation for the calculation of the enthalpy of reaction for a given pressure and temperature can be derived from the following equation:

$$\Delta h_R\,(T,P) = \Delta h_R^0\,(T,P^0) + \sum v_i (h - h_{ideal})_{T,P,i} \tag{4.122}$$

In the ammonia synthesis, the enthalpy of ammonia decreases since attractive forces dominate whereas for both highly supercritical compounds N_2 and H_2, the forces are mainly of repulsive nature. Using this equation, the enthalpy of reaction for the ammonia synthesis is calculated:

$$\Delta h_R\,(T,P) = \mathrm{h}^0_{\mathrm{NH_3}} - \frac{1}{2}\mathrm{h}^0_{\mathrm{N_2}} - \frac{3}{2}\mathrm{h}^0_{\mathrm{H_2}} \tag{4.123}$$

Similarly, entropy change is determined for specific temperature and pressure as follows:

$$\Delta s_R\,(T,P) = \mathrm{s}^0_{\mathrm{NH_3}} - \frac{1}{2}\mathrm{s}^0_{\mathrm{N_2}} - \frac{3}{2}\mathrm{s}^0_{\mathrm{H_2}} \tag{4.124}$$

At constant temperature and pressure, chemical equilibrium is satisfied when the Gibbs energy reaches a minimum. To describe the change of the Gibbs energy with temperature, pressure, the following fundamental equation can be applied:

$$\Delta g_R = \Delta h_R - T\Delta s_R \tag{4.125}$$

The values are calculated using Engineering Equation Solver (EES) considering the ideal gas behavior and correction with real state behavior.

In addition to the calculation of enthalpies of reaction as a function of temperature and pressure, thermodynamics permits to calculate the equilibrium conversion for reversible reaction of ammonia at given conditions.

The difference of the Gibbs energies of formation at 25°C in the different states is only initiated by the different fugacities in the standard state. The standard fugacities of pure liquids and solids resemble almost to the vapor respectively sublimation pressure at 25°C. The standard fugacity of the hypothetical ideal gas is 1 atm.

The chemical equilibrium constant K and can be calculated from the standard Gibbs energy of reaction [213]:

$$\Delta g_R^0 = -R\,T\,\sum \ln\left(\frac{f_i}{f_{i_0}}\right)^{v_i} = -R\,T\ln K \tag{4.126}$$

Here, the fugacities are given in the real state f_i and in the standard state f_{i_0}.

If the standard enthalpy of reaction Δh_R can be deliberated as constant in the temperature range covered, the following equation can be used to obtain the equilibrium constant at the desired temperature [213]:

$$\ln K_{@\,T} = \ln K_{@T_0} - \frac{\Delta h_R^0}{R}\left(\frac{1}{T} - \frac{1}{T_0}\right) \tag{4.127}$$

In case that the standard enthalpy of reaction Δh_R^0 is not constant in the temperature range considered, the temperature dependence can be described using Kirchhoffs law taking into account the temperature-dependent heat capacities of the compounds involved.
Since there is an exothermic reaction of ammonia synthesis, the equilibrium constant decreases with increasing temperature. This means that also the maximum conversion rate is less at higher temperatures. The equilibrium conversion can be determined by a material balance. The equilibrium conversion is the maximum conversion X_{max} which can be reached for the number of moles present at the beginning. The conversion rate X_i can be defined as follows:

$$X_i = \frac{n_{i_0} - n_{i_{eq}}}{n_{i_0}} \tag{4.128}$$

where n_{i_0} is the initial number of moles of component i and $n_{i_{eq}}$ is the number of moles of component i in chemical equilibrium.
For the case that the conversion is related to nitrogen, the number of moles of all other components can be defined as follows:

$$n_{N_2} = n_{N_{2_0}}(1 - X_{N_2}) \tag{4.129}$$

$$n_{H_2} = 3\, n_{N_{2_0}}(1 - X_{N_2}) \tag{4.130}$$

$$n_{NH_3} = 2\, n_{N_{2_0}}\, X_{N_2} \tag{4.131}$$

The total number of moles can be expressed as

$$n_{Total} = n_{N_{2_0}}\,(4 - 2\, X_{N_2}) \tag{4.132}$$

Using the moles of the species at specific temperature, pressure and equilibrium constant, the mass flow rates can be determined in case one of the flow rates are given.
Hence, all mole fractions, $y_i = \frac{n_i}{n_{total}}$, can be expressed by initial number of moles of nitrogen.
Using the conversion X_{N_2} and pressure, the equilibrium constant can be written as follows [213]:

$$K = \frac{2\, X_{N_2}\,(4 - 2\, X_{N_2})}{3^{1.5}\left(1 - X_{N_2}\right)^2\, P} \tag{4.133}$$

Here, pressure P is given in atm.
Another quantity can be defined to describe equilibrium constant based on temperature and pressure only:

$$K' = \frac{3^{1.5} P\, K}{4} \tag{4.134}$$

The conversion X_{N_2} can be determined for every temperature and every pressure using the following relation [213]:

$$X_{N_2} = 1 - \frac{1}{\sqrt{1 + K'}} \tag{4.135}$$

It is noted that low temperatures and high pressures are advantageous for the ammonia synthesis. Nevertheless, temperatures of 450°C levels are commonly used in chemical industry

for Haber-Bosch process. The reason is that despite enriched catalysts, the reaction rate is too slow at low temperatures, so that the conversion is much lower than the equilibrium conversion for a limited residence time. Only at higher temperatures, the reaction rate is fast enough to attain a conversion close to chemical equilibrium.

At low pressures, the differences between the calculation assuming ideal gas behavior and taking into account the deviation from ideal gas behavior can be neglected. For a consideration of the real behavior, a reliable representation of the $P\ v\ T$ behavior of the reacting compounds is required. By definition, the fugacity in the gas phase can be described with the help of fugacity coefficients:

$$f_i = p_i\,\beta_i = y_i\,\beta_i\,P \tag{4.136}$$

Using this relation, the equilibrium constant K can be written in the following form (standard fugacity f_0 = 1 atm) [213]:

$$K = K_p\,K_\beta\,1\left(\frac{1}{1\ atm}\right)^{\sum v_i} = \pi_{{p_i}^{v_i}}\,\pi_{{\beta_i}^{v_i}}\left(\frac{1}{1\ atm}\right)^{\sum v_i} \tag{4.137}$$

This also states that the equilibrium constant for the reversible reaction shown before where $\sum v_i$ is equal to zero, can also be described as follows [213]:

$$K = \frac{p_C^2}{p_A\,p_B}\frac{\beta_C^2}{\beta_A\,\beta_B} \tag{4.138}$$

For reactions where the number of moles changes, it is significant that the same unit is used for the partial pressures as for the standard fugacities (atm). Depending on the values of K_β, the equilibrium conversion increases or decreases. For K_β values smaller than 1, the real behavior leads to an equilibrium conversion higher than that in the case of ideal behavior for the ammonia synthesis. If K_β values higher than 1, a lower conversion than that in the ideal case is obtained.

For electrochemical ammonia synthesis, a certain potential or current is applied to the electrodes located in the molten salt electrolyte. In either case, both potential and current characteristics are recorded and known. Therefore, total electrical power input to the system can be defined as

$$W_{in} = V\,I \tag{4.139}$$

Here, I is the total current in Amps flowing between the electrodes and given as

$$I = J\,A_{electrode} \tag{4.140}$$

where $A_{electrode}$ represents the total electrode surface area immersed in the electrolyte.

4.8.1 Electrochemical modeling

In the ammonia synthesis reactor, there are couple of processes occurring during the operations such as double layer capacitance, charge transfer resistance and diffusion. Double layer capacitance is a splitting of charges or electrical double layer happens at any border in the polarized arrangement like the border between the nickel electrode and the liquid electrolyte. This corresponds to a capacitor in the electrical circuit. Charge transfer resistance is the transfer

of electrons from the ionic kinds in the solution to the solid metal that is based on the type of the reaction, temperature, concentration of the entering chemicals and the potential. In the ammonia reactor, liquid state molten salt is present. Hence, diffusion is one of the significant manners in mass transport processes from the electrolyte. The substrates should diffuse passing via through the electrolyte. In order to quantify these processes, an electrochemical impedance spectroscopy model is developed.

The degree of the impedance is written with real and imaginary portions as follows:

$$|Z| = \sqrt{{Z_r}^2 + {Z_j}^2} \tag{4.141}$$

and the phase angle can be found as follows:

$$\varphi = \tan^{-1}\frac{Z_j}{Z_r} \tag{4.142}$$

Nyquist and Bode plots are frequently utilized to characterize the impedance measurements. resistors, capacitors and inductors. The responses of these impedances are written as

$$Z_R = R \tag{4.143}$$

$$Z_L = j\,\omega\,L \tag{4.144}$$

$$Z_C = \frac{1}{j\,\omega\,C} \tag{4.145}$$

Diffusion can generate an impedance called as Warburg impedance. Warburg impedance is based on the frequency of the potential perturbation. At higher frequencies the Warburg impedance is minor since, diffusing reactants do not necessitate to travel very distant. At lower frequencies the reactants need to diffuse farther, thus causing an increase in the Warburg impedance. The equation for the infinite Warburg impedance can be written as

$$Z = \frac{\frac{1}{Y_0}}{\sqrt{(j\omega)}} \tag{4.146}$$

$$Y_0 = \frac{1}{\sqrt{2}\,\sigma} \tag{4.147}$$

A nonlinear numerical least-square fitting method is utilized to get precise numbers for the equivalent circuit elements. Simplex method is utilized to fit the impedance of circuit model to the experimental EIS data using Gamry Echem Analyst software. The Simplex method minimizes x^2 to fit the impedance data to the selected equivalent circuit model. The goodness of fit values are accepted which were under the 10^{-4} criterion implying a good fit. After fitting the model to the experimental data, the fit guesses numbers for the model parameters, such as the resistance, the double-layer capacitance and Warburg element.

There are three major loss mechanisms in the ammonia reactor which are activation losses because of slow electrode reaction kinetics, ohmic losses, and mass transfer losses. Counting all these losses, the required applied voltage can be calculated by summing the overpotentials.

$$E_{actual} = E_{rev} + E_{act} + E_{ohm} + E_{conc} \tag{4.148}$$

Here, act, ohm and conc represent the activation, ohmic and concentration overpotentials, respectively. Note that, at given conditions, the reversible voltage would be negligible for ammonia reaction because of the nature of the reaction which is dependent on Gibbs free energy. However the overpotentials are quite significant and dominant because of the electrodes and electrolyte. Using the electrochemical impedance spectroscopy data, the ohmic, activation resistances and concentration resistances are quantified by solving the complex number equations. Real part of the complex impedances are calculated and used by employing Ohm's law for the actual required potential.

4.9 Efficiency Evaluation

The efficiency of the electrolysis process in the PEC cell can be defined as the reversible voltage divided by the actual cell voltage counting the overpotentials:

$$\eta_{en,PEC,voltage} = \frac{\mathrm{E_{rev}}}{E_{actual}} \tag{4.149}$$

This efficiency mainly represents the electrolyzer effectiveness which does not reflect the photonic conversion.

The energy and exergy efficiency of electrolyzer without light can also be defined using the lower heating value of the produced hydrogen.

$$\eta_{en,electrolyzer} = \frac{\dot{\mathrm{m}}_{\mathrm{H2}}\, LHV_{H2}}{\dot{W_{in}}} \tag{4.150}$$

$$\eta_{ex,electrolyzer} = 1 - \frac{\dot{E}x_{d,electrolyzer}}{\dot{W_{in}}} \tag{4.151}$$

Here, $\dot{\mathrm{m}}_{\mathrm{H2}}$ is the mass flow rate of produced hydrogen and $\dot{W_{in}}$ is the total work input to the electrolyzer which can be found using $\dot{W_{in}} = J\, A_{cell}\, E_{actual}$.

When the concentrated solar input is taken into account for the PEC hydrogen production system, the energy and exergy efficiencies are defined as follows:

$$\eta_{en,PEC,electrolyzer,concentrated} = \frac{\dot{\mathrm{m}}_{\mathrm{H2}}\, LHV_{H2}}{\dot{W_{in}} + I_{r_3}\, A_{cell}} \tag{4.152}$$

$$\eta_{ex,PEC,electrolyzer,concentrated} = 1 - \frac{\dot{E}x_{d,PEC,electrolyzer,concentrated}}{\dot{W_{in}} + I_{r_3}\, A_{cell}} \tag{4.153}$$

Here, I_{r_3} is the concentrated light irradiance on the PEC cell.

The exergy balance equation to find the total exergy destruction can be written as follows:

$$\dot{m}_{H_2O}\, ex_{H_2O} + \dot{W}_{in} + \dot{E}x_{I_{r_3}}\, A_{cell} = \dot{m}_{H_2}\, ex_{H_2} + \dot{m}_{O_2}\, ex_{O_2} + \dot{E}x_{d,PEC,electrolyzer,concentrated} \tag{4.154}$$

where ex is the total exergy of the species including the chemical and physical exergy contents. The work input here includes photoelectrochemical process which produces photocurrent and contributes to hydrogen production.

In sole PEC process, the total input to the system is considered as solar energy input whereas the useful output is considered as power output from the cell calculated based on PEC cell voltage, photocurrent and fill factor. As defined earlier, fill factor (FF) is introduced as a

useful tool to determine the maximum power output from the PEC cells. The overall conversion efficiency of the PEC cell is determined by the photocurrent density measured at short circuit (j_{ph}), the open-circuit photo-voltage (V_{oc}), the fill factor of the PEC cell (FF) and the intensity of the incident light (I_r):

$$\eta_{en,PEC} = \frac{J_{ph}\, V_{OC}\, FF}{I_r} \tag{4.155}$$

where the unit of J_{ph} is mA/cm^2, I_r is mW/cm^2 and V_{OC} is V.
Similarly, exergy efficiency of the PEC cell based on generated photocurrent can be defined as follows:

$$\eta_{ex,PEC} = \frac{J_{ph}\, V_{OC}\, FF}{Ex_{I_r}} \tag{4.156}$$

where Ex_{I_r} is the exergy of the incoming light on the system which is the ambient irradiance.

The system employs both photoelectrochemical and electrolysis processes. Therefore, the overall energy and exergy efficiency of the PEC system -which is named as solar-to-hydrogen efficiency- can be defined as follows:

$$\eta_{en,ov,PEC} = \frac{\dot{m}_{H2}\, LHV_{H_2}}{I_{r_3}\, A_{cell}} \tag{4.157}$$

$$\eta_{ex,ov,PEC} = \frac{\dot{m}_{H2}\, ex_{H_2}}{Ex_{I_{r_3}}\, A_{cell}} \tag{4.158}$$

Here, ex_{H_2} is the total exergy of hydrogen including physical and chemical exergy terms. There is no external power input to the system because PV cell produces the required electricity for PEC electrolysis process. Here, the input irradiance is taken as the concentrated irradiance on the PEC cell after the dielectric mirror.

The conversion efficiencies of PEC cells can also be calculated by solar conversion efficiency based on the photocurrent generation which is the ratio of the power used for water splitting to the input light power [76, 212]:

$$\eta_{PEC} = \frac{j\,(E^0_{rev} - V_{bias})}{I_o} \tag{4.159}$$

where j is photocurrent density (mA/cm^2) at a certain applied voltage, E^0_{rev} is the standard water splitting reaction potential given reference to NHE at pH=0, I_o is the light intensity (mW/cm^2), and V_{bias} is the applied external potential given reference to RHE. This efficiency considers only photocurrent generation rather than hydrogen production.

In order to convert Ag/AgCl reference electrode to the reversible hydrogen electrode (RHE) [215], the applied external potential and the effect of pH of electrolyte can be converted into the potential vs. RHE as follows:

$$E_{RHE} = E_{AgCl} + E^0_{AgCl} + 0.059\ pH \tag{4.160}$$

Here, E^0_{AgCl} is 0.197 at 25°C and the pH of the electrolyte is 9.

The method to evaluate the efficiency of a PV module is to compare the total solar power input and produced power. The PV efficiency is the ratio of maximum power output to incident solar energy and is written as follows:

$$\eta_{en,PV} = \frac{I_M V_M}{I_{r_1} A_{PV}} \tag{4.161}$$

$$\eta_{ex,PV} = \frac{I_M V_M}{Ex_{I_{r_1}} A_{PV}} \tag{4.162}$$

In this equation V_M and I_M are the voltage and current of the module at maximum power output, respectively. A_{PV} is the PV cell area. I_{r_1} and $Ex_{I_{r_1}}$ are irradiance on the Fresnel lens surface before concentration.

The efficiency of the module under concentrated sunlight can also be found by replacing the power input with the incoming energy on the PV cell surface:

$$\eta_{en,CPV} = \frac{I_{MP} V_{MP}}{I_{r_4} A_{PV}} \tag{4.163}$$

$$\eta_{ex,CPV} = \frac{I_{MP} V_{MP}}{Ex_{I_{r_4}} A_{PV}} \tag{4.164}$$

Here, I_{r_4} and $Ex_{I_{r_4}}$ irradiance on the PV surface after the dielectic mirror.

In the integrated system, the light inputs are defined for each component and summed to find the total energy on the components. PV generates electricity and some portion of the generated electricity is supplied to photoelectrochemical hydrogen production reactor. Therefore, the overall integrated system efficiencies for hydrogen production system can be calculated as follows:

$$\eta_{en,integrated\ system,H_2} = \frac{(\dot{m}_{H2}\, LHV_{H_2} + \dot{W}_{PV} - \dot{W}_{in,PEC})}{I_{r_4} A_{PV} + I_{r_3} A_{PEC,cell}} \tag{4.165}$$

$$\eta_{ex,integrated\ system,H_2} = \frac{(\dot{m}_{H2}\, ex_{H_2} + \dot{W}_{PV} - \dot{W}_{in,PEC})}{Ex_{I_{r_4}} A_{PV} + Ex_{I_{r_3}} A_{PEC,cell}} \tag{4.166}$$

where A_{PV} and $A_{PEC,cell}$ are the areas of the PV and PEC cell, respectively, $\dot{W}_{PV}$ is the generated electricity by PV, $\dot{W}_{in}$ is the electricity input to the PEC reactor and I_r is the irradiances on the components.

When the hydrogen production system is integrated to ammonia synthesis, overall integrated system efficiencies for ammonia production system can be calculated as follows:

$$\eta_{en,integrated\ system.NH_3} = \frac{\dot{m}_{NH3}\, LHV_{NH_3} + \dot{W}_{PV} - \dot{W}_{in,PEC} - \dot{W}_{in,NH_3}}{I_{r_4} A_{PV} + I_{r_3} A_{PEC,cell} + \dot{m}_{N_2} h_{N_2}} \tag{4.167}$$

$$\eta_{ex,integrated\ system,NH_3} = \frac{\dot{m}_{NH3}\, ex_{NH_3} + \dot{W}_{PV} - \dot{W}_{in,PEC} - \dot{W}_{in,NH_3}}{Ex_{I_{r_4}} A_{PV} + Ex_{I_{r_3}} A_{PEC,cell} + \dot{m}_{N_2} ex_{N_2}} \tag{4.168}$$

Here, hydrogen is considered to fully react with nitrogen to form ammonia, therefore it is not included as useful output.

For the sole ammonia production process, three different efficiencies are defined namely; energy, exergy and coulombic efficiencies. Hydrogen and nitrogen react in the

chamber and form ammonia. Not all of the reactants are converted to products because of equilibrium. Therefore, only reacted amounts are considered in the energy and exergy efficiencies.

The coulombic efficiency is calculated based on the moles of electrons consumed compared to the $3e^-/NH_3$ equivalents produced. Thus, the coulombic efficiency of ammonia generation process is defined as follows:

$$\eta_{\text{Coulombic}} = \frac{\dot{n}_{NH_3} F n}{j} \tag{4.169}$$

where F is Faraday constant, n is number of electrons involved, and j is the current density (A/cm^2).

The energy efficiency of the ammonia production process is also calculated based on lower heating values of reacted hydrogen and ammonia, nitrogen enthalpy and electrical power input as follows:

$$\eta_{en,NH_3} = \frac{\dot{m}_{NH_3} LHV_{NH_3}}{(\dot{m}_{H_2} LHV_{H_2} + \dot{m}_{N_2} h_{N_2} + \dot{W}_{in,NH_3})} \tag{4.170}$$

where $\dot{W}_{in,NH_3}$ is the total electricity input calculated using the total voltage and current, LHV is the lower heating value and h is the enthalpy.

Similarly, the exergy efficiency of the ammonia synthesis process can be defined as follows:

$$\eta_{ex,NH_3} = \frac{\dot{m}_{NH_3} HHV_{NH_3}}{(\dot{m}_{H_2} ex_{H_2} + \dot{m}_{N_2} ex_{N_2} + \dot{W}_{in,NH_3})} \tag{4.171}$$

where HHV is the higher heating value and ex is the exergy of the flows.

4.10 Experimental Uncertainty Analysis

Quantifying the uncertainties in the experiments is significant to confirm the accuracy of the results. In many cases, the measured variables have a random variability which is referred to its uncertainty. In this section, the devices used in the experiments are listed with related accuracies to find the total uncertainty for each variable.

Assuming the individual measurements are uncorrelated and random, the uncertainty in the calculated quantity can be determined as

$$U_y = \sqrt{\sum_i \left(\frac{\partial y}{\partial x}\right)^2 U_x^2} \tag{4.172}$$

where U represents the uncertainty of the variable.

In Table 4.6, the measurement range and accuracy of all devices used in the experiments are listed based on the manufacturer datasheets [170, 172–177, 216, 217]. Since there are more than one device for some of the measurement parameters, they are individually listed in the table and considered in the total uncertainty calculations.

The calculation of the experimental uncertainty is based on the systematic (S_i) and random errors (R_i) of the measurement process and it is defined as follows:

$$U_i = \sqrt{S_i^2 + R_i^2} \tag{4.173}$$

Table 4.6 The measurement range and accuracies of the measurement devices.

Device	Measurement Parameter	Measurement Range	Accuracy
Gamry Reference 30k Booster	Voltage	± 32 Volts	±0.2% of scale ±0.2% of reading
Gamry Reference 3000	Voltage	±11 V	± 1 mV ±0.3% of reading
Gamry Reference 30k Booster	Current	±30 A	±0.2% of scale ±0.2% of reading
Gamry Reference 3000	Current	±3 A	± 10 pA ±0.3% of range
OM-DAQPRO-5300 Thermocouple K (for ammonia reactor)	Temperature	-250 to 1200°C	±0.5%
Vernier surface temperature sensor STS-BTA (for PV)	Temperature	–25 to 125°C	±0.5°C
OAI Trisol TSS-208 Class AAA	Irradiance	800-1100 W/m^2	± 20.28 W/m^2
Vernier pyranometer PYR-BTA	Irradiance	0-2200 W/m^2	± 5 %
Ocean Optics Red Tide USB 650 Spectrometer	Spectrum	350-1000 nm	<0.05%
Omega FMA-1600A Flowmeter (for hydrogen)	Volume flow rate	0-100 SCCM	±(0.8% of reading + 0.2% FS)
Omega FMA1700/1800 Flowmeter (for ammonia)	Volume flow rate	0-500 SCCM	±1.5% of full scale, ±3% of full scale
Omega FMA-1600A Flowmeter (for nitrogen)	Volume flow rate	0-100 SCCM	±(0.8% of reading + 0.2% FS)
Omega PHH103A PH Meter	pH	0-14 pH	0.02 pH

Source: [170, 172–177, 216, 217]

The partial derivatives of the variables are calculated using Engineering Equation Solver (EES) from the experimental results which is a function of measured variables. The method for determining this uncertainty propagation in EES is described in NIST Technical Note 1297 [218] . There are two main kinds of uncertainties, systematic (or bias) and random (or precision) uncertainties. Systematic uncertainties are those due to faults in the measuring instrument or in the techniques used in the experiment. Random uncertainties are related with irregular variations in the experimental conditions under which the experiment is being accomplished, or are due to a deficiency in defining the quantity being measured. Random uncertainty reduces the precision of an experiment whereas systematic uncertainty decreases the accuracy of an experiment.

Table 4.7 Calculated bias, precision error and total uncertainty values.

Device	Measurement Parameter	Ref. Value	Absolute Bias Error	Relative Bias Error (%)	Relative Precision Error (%)	U (%)
Gamry Reference 30k Booster	Voltage	2 V	0.004 V	0.2000	2.19002	2.1991
Gamry Reference 3000	Voltage	2 V	0.006 V	0.3000	2.19002	2.2105
Gamry Reference 30k Booster	Current	4 A	0.008 A	0.2000	1.32795	1.3429
Gamry Reference 3000	Current	4 A	0.012 A	0.3000	1.32795	1.3614
OM-DAQPRO-5300 Thermocouple K (for ammonia reactor)	Temperature	200°C	1°C	0.5000	0.79057	0.9354
Vernier surface temperature sensor STS-BTA (for PV)	Temperature	60°C	0.5°C	0.8333	2.63523	2.7639
OAI Trisol TSS-208 Class AAA	Irradiance	1000 W/m^2	20.28 W/m^2	2.0280	0.23476	2.0415
Vernier pyranometer PYR-BTA	Irradiance	1000 W/m^2	50 W/m^2	5.0000	2.59362	5.6327
Ocean Optics Red Tide USB 650 Spectrometer	Spectrum	700 nm	0.350 nm	0.0500	0.52054	0.5229
Omega FMA-1600A Flowmeter (for hydrogen)	Volume flow rate	15 SCCM	0.12 SCCM	0.8000	3.10970	3.2110
Omega FMA1700/1800 Flowmeter (for ammonia)	Volume flow rate	30 SCCM	0.45 SCCM	1.5000	3.13934	3.4793
Omega FMA-1600A Flowmeter (for nitrogen)	Volume flow rate	45 SCCM	0.36 SCCM	0.8000	3.04290	3.1463
Omega PHH103A PH Meter	pH	10 pH	0.02 pH	0.2000	1.58114	1.5937

The complete statement of a measured value is required to contain an estimate of the level of confidence associated with the value. There are some common complications initiating the error in the experiments such as instrument resolution, calibration, zero offset, instrument drift, physical variations and personal errors. In order to find the random (precision) errors, the relative standard deviation (RSD) term is defined which is useful for comparing the uncertainty between different measurements of varying absolute magnitude. The relative standard deviation is calculated from the standard deviation, s, as per following formula:

$$RSD = \frac{s}{\bar{x}} 100\% \tag{4.174}$$

where $\bar{x}$ is the mean of the results. The experiments are performed at least 3 times and obtained average and standard deviation values are calculated to be used in the combined uncertainty results. The relative standard deviation can also be named as coefficient of variance.

The individual uncertainty of the components are combined using the law of propagation of uncertainties, commonly called the root-sum-of-squares method. In this case, the combined standard uncertainty is equal to the standard deviation of the result which satisfies a 68% confidence interval level. If 95% confidence interval is desired, a k factor of 2 is multiplied by the combined uncertainty value. The calculated total uncertainties are shown in Table 4.7

Some of the parameters are measured using different devices for various processes. For example, the temperature of the PV cell is measures by a surface temperature sensor whereas the ammonia reactor temperature is measured by a thermocouple. Therefore, the individual uncertainty for each measurement parameter is calculated separately and listed in the table. In order specify the uncertainty associated with the measured variables in EES software, the obtained absolute or relative (fraction of the measured value) uncertainties for each selected measured variable are specified. The values and uncertainty for the calculated variable and each measured variable are listed as a table after the calculations are completed. The calculated variables are plotted with error bars and given in the tables representing the propagated uncertainty.

4.11 Exergoeconomic Analyses

In this chapter, the equipment cost of experimental systems are first introduced. Secondly, exergoeconomic analyses of the experimental system are performed. Thirdly, scale-up analysis is performed to investigate the cost of hydrogen and ammonia in larger scale applications. A scale-up analysis for the cost of hydrogen in a 1000 kg/day production capacity plan is performed.

The purchased costs of the experimental systems in this thesis are presented in the following tables. The experimental systems are divided into three main sub-systems;

- Photoelectrochemical hydrogen production reactor
- Electrochemical ammonia production reactor
- Integrated system comprising of solar light concentrator and splitter, PV cell and support mechanism.

The purchased costs of the materials used in the PEC reactor are listed in Table 4.8.

Table 4.8 The cost of materials used in the PEC hydrogen production reactor.

Material	Quantity	Unit Price ($)	Total Price ($)
Reactor casing (HDPE)	2	$130	$260
Stainless steel electrodes	2	$200	$400
Nafion membrane	1	$2,000	$2,000
Chemicals for electrodeposition	3	$150	$450
Washers, bolt nuts	50	$1	$50
Acrylic or polycarbonate reactor window	1	$100	$100
Piping (plastic)	4	$25	$100
Rubber gasket	6	$10	$60
Machining (for casing and electrodes)	1	$450	$450
Others (adhesive, silicon etc.)	1	$120	$120
TOTAL			$3,990

The reactor casing is chosen as HDPE for the reactor because of the advantages explained in the experimental apparatus. The machining is easier and requires low cost. For higher solar concentration ratios, the temperature levels on the PEC reactor body may rise more than material specification. It is similar for the viewing panel of the reactor which is made of acrylic. Therefore, the temperature levels on the PEC reactor surface need to be checked before deciding the materials selection. In total, the cost of the PEC reactor in the experimental setup is calculated to be 3990$. The purchased costs of the materials used in the electrochemical ammonia production reactor are listed in Table 4.9.

Table 4.9 The cost of materials used in the electrochemical ammonia production reactor.

Material	Price ($)
Nickel wiring	$40
Nickel electrodes	$160
Reactor casing alumina crucible (Alumina Al_2O_3)	$140
Reactor lids (Stainless steel 316 Alloy)	$120
Bolt Nuts and Washers	$55
Reactor tubes (Alumina Al_2O_3)	$160
Piping (plastic)	$50
Heating tape	$110
Gaskets	$25
Others (adhesive, insulation etc.)	$65
TOTAL	$925

The ammonia reactor casing has 500 mL capacity. The tubes for the gas inlet and outlet the reactor are also made of Alumina (Al_2O_3) which is non-corrosive. After the gasses exit the reactor, plastic pipes are used. The heating tape used in the experiments are for sustaining the

reaction temperature. That is an additional equipment to the reactor construction. The total cost of ammonia reactor is found to be 925$.

The PEC hydrogen production reactor is used under concentrated and split spectrum. Therefore, the solar concentrator, dielectric mirrors and PVs are included in the integrated system costs as shown in Table 4.10. These two sub-systems for hydrogen and ammonia production are integrated in the experimental setup which yield the total system capital cost.

Table 4.10 The cost of materials used in the integrated system for PEC hydrogen based electrochemical ammonia production system.

Material	Price ($)
Photovoltaic cell, multicrystalline silicon	$80
Fresnel lens	$75
Dielectric mirrors (6 in total) (Borosilicate glass)	$672
PEC hydrogen production reactor	$3,990
Ammonia production reactor	$925
Support structure (wood)	$45
Metal support mechanism including nuts and bolts	$75
TOTAL	$5,862

The support mechanism used in the integrated system consists of wood and metal parts. The highest cost is for the PEC hydrogen production reactor which corresponds to about 68% of total cost as show in Fig. 4.7.

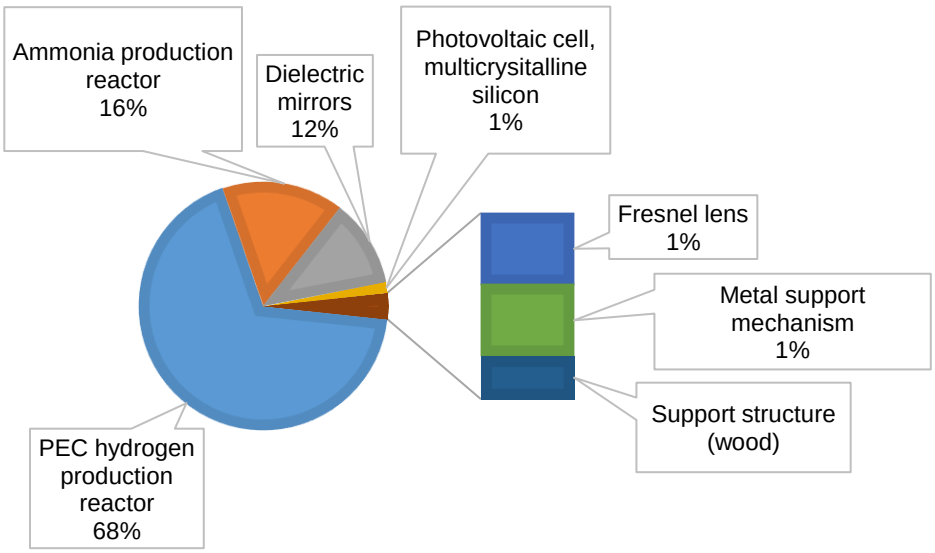

Fig. 4.7 Cost breakdown of the integrated system for hydrogen and ammonia production.

The exergoeconomic analysis requires that a specific cost is put on the exergy streams in an exergy balance on a component. On top of putting costs on the exergy streams, capital and running costs are taken into account in order to get a complete cost analysis. The

exergoeconomic analyses are performed for the experimental integrated system. The capital costs are taken from the experimental setup costs as listed above. Exergy cost for the streams in any cost rate balance is given as [219]

$$\dot{C} = c\,\dot{Ex} \tag{4.175}$$

Here, c is in given in \$/kWh and $\dot{Ex}$ is given in W. The capital costs of the components is given as $\dot{Z}$ in \$/h.
Typical cost rate balance for a component is given below [215, 216]:

$$\sum \dot{C}_{in} + \dot{W}\,c_{in} + \dot{Z} = \sum \dot{C}_{out} + \dot{W}\,c_{out} \tag{4.176}$$

CRF refers to capital recovery factor and depends on the interest rate and equipment life time, and is determined here as follows:

$$CRF = \frac{i\,(1+i)^n}{(1+i)^n - 1} \tag{4.177}$$

Here, i denotes the interest rate and n the total operating period of the system in years. Total costs for each of the components in the system are needed in \$/h in order to use them in cost rate balance equations. The capital cost and the operating and maintenance costs are added. The total costs are then divided by the number of hours in a year to get a cost in \$/h. Operating and maintenance costs are assumed to be a ratio of the capital costs as

$$OM = CC\ \ OM_{ratio} \tag{4.178}$$

where OM_{ratio} depends on the type of application and material.
The capital costs of the equipment are calculated based on the experimental setup costs as explained in the previous tables. The total cost balance is written as follows:

$$TCC = CRF\ (CC + OM) \tag{4.179}$$

The annual investment cost rate of any component, $\dot{Z}$ is calculated for the components of the experimental integrated system. It is the summation of the annual capital investment cost rate and the annual O&M cost rate and defined as follows:

$$\dot{Z} = \frac{TCC}{t_{operation}} \tag{4.180}$$

where $t_{operation}$ is the total operational hours in a year.
The cost rate of exergy destruction for each component is expressed as [215, 216]

$$\dot{C}_D = c\,\dot{E}x_d \tag{4.181}$$

Summation of additional cost caused by exergy destruction, $\dot{C}_D$ and final capital and operating cost rate $\dot{Z}$ gives a critical parameter named as total cost rate $\dot{C}_D + \dot{Z}$:

$$\dot{C}_{total} = \dot{C}_D + \dot{Z} \tag{4.182}$$

Total cost rates of the system consists of the total investment cost and cost of exergy destruction. In general, the smaller the sum of this parameter, it means that the component is

more cost effective. Therefore, this parameters is taken as optimization function in the optimization analyses.

The exergoeconomic factor, which is a measure of system effectiveness in terms of cost, obtained through exergoeconomic analysis is given as

$$f = \frac{\dot{Z}}{\dot{Z}+\dot{C}_D} \tag{4.183}$$

The exergoeconomic variables $\dot{Z}$ and $\dot{C}_D$ provide the significance of component in the system optimization, whereas the variable f exergoeconomic factor is a relative measure of the component cost effectiveness.

The obtained results in the exergoeconomic analysis of the streams for each of the sub-systems in the experimental setup are presented in results and discussion chapter. The following financial parameters shown in Table 4.11 are used in the exergoeconomic analysis.

Table 4.11 The financial and operational cost parameters used in the exergoeconomic analyses.

Parameter	Value
Interest rate	7%
Lifetime of all components	10 years
Calculated capital recovery factor	0.1424
Calculated hydrogen cost	3.24 $/kg
Calculated ammonia cost	0.84 $/kg
Cost of electricity	0.06 $/kWh
Cost of thermal energy	0.02 $/kWh
O&M percentage of capital cost	2.2%
System annual operation hours	2500 hours

The exergy cost rates balance of the components in the integrated system are written below:

- Fresnel lens:

$$\dot{Ex}_1\, c_1 + \dot{Z}_{FRESNEL} = \dot{Ex}_2\, c_2 + \dot{Ex}_{d_{FRESNEL}}\, c_{Ex_{d_{FRESNEL}}} \tag{4.184}$$

The inlet and outlet streams of the Fresnel lens are sunlight. Therefore, the cost of light is taken as zero for c_1 and c_2. The final capital and operating cost rate of the components are calculated using the purchased equipment costs and O&M, ratios.

- Dielectric mirror:

$$\dot{Ex}_2\, c_2 + \dot{Z}_{MIRROR} = \dot{Ex}_3\, c_3 + \dot{Ex}_4\, c_4 + \dot{Ex}_{d_{MIRROR}}\, c_{Ex_{d_{MIRROR}}} \tag{4.185}$$

The inlet and outlet streams of the dielectric mirror are sunlight. Therefore, the cost of light is taken zero for c_2, c_3 and c_4.

- PV:

$$\dot{Ex}_3\, c_3 + \dot{Z}_{PV} = \dot{Ex}_{Electricity}\, c_{Electricity} + \dot{Ex}_{Heat}\, c_{Heat} + \dot{Ex}_{d_{PV}}\, c_{Ex_{d_{PV}}} \tag{4.186}$$

The inlet and outlet streams of the dielectric mirror are sunlight. Therefore, the cost of light is taken zero for c_3. $\dot{E}x_{Heat}$ is the exergy rate of calculated heat dissipation from the PV. Here, it is a waste heat which could be further utilized iv PV/T modules are used.

- PEC:

$$\dot{E}x_{H_2O}\, c_{H_2O} + \dot{E}x_{Electricity}\, c_{Electricity} + \dot{E}x_4\, c_4 + \dot{Z}_{PEC} = \dot{E}x_{O_2}\, c_{O_2} + \dot{E}x_{H_2}\, c_{H_2} + \dot{E}x_{d_{PEC}}\, c_{Ex_{d_{PEC}}} \quad (4.187)$$

One of the inlet stream of the PEC reactor are sunlight. Therefore, the cost of light is taken zero for c_4.

- Ammonia Reactor (AR):

$$\dot{E}x_{H_2} c_{H_2} + \dot{E}x_{N_2} c_{N_2} + \dot{E}x_{Electricity} c_{Electricity} + \dot{Z}_{AR} = \dot{E}x_{NH_3} c_{NH_3} + \dot{E}x_{d_{AR}} c_{Ex_{d_{AR}}} \quad (4.188)$$

The cost rate of water and nitrogen are taken as zero in the calculations.

4.11.1 Scale-up analyses

In case of larger production scales, the mass manufacturing of these equipment will be considerably lower. In order to analyze the cost of hydrogen and ammonia at larger production capacities such as 1000 kg/day, the scale up analyses are conducted as explained in the following paragraphs.

PEC systems use solar photons to generate a voltage in an electrolysis cell sufficient to electrolyze water, producing H_2 and O_2 gases. For the economic analyses of the photoelectrochemical hydrogen production system, the Hydrogen Analysis (H2A) production model [221] is used which is developed by U.S. DOE Hydrogen & Fuel Cells Program. The H2A Production Model analyzes the technical and economic aspects of central and forecourt hydrogen production systems. Using a standard discounted cash flow rate of return methodology, it determines the minimum hydrogen levelized cost, including a specified after-tax internal rate of return from the production technology.

The employed scenario models a PEC solar concentrator system using reflectors to focus the solar flux with a concentration ratio of 10 intensity ratio onto multi-junction PEC cell receivers immersed in an electrolyte reservoir and pressurized to 300 psi. The PEC cells are in electrical contact with a small electrolyte reservoir and produce oxygen gas on the anode side and hydrogen gas on the cathode side. The start-up year of the plant is taken as 2020.

The Chemical Engineering Plant Cost Index (CEPCI) is used to adjust the capital cost of the H_2 Production facility from the basis year to the current year. The Consumer Price Inflator (CPI) is used to deflate all dollars from the current year to the Reference Year. The available model is quite similar to the designed and tested concentrated PEC system except for the solar light splitting part. Hence, the solar spectrum splitting mechanism is not considered in the scaled-up cost assessment. A solar tracking system is employed to make best use of direct radiation capture. Solar concentrators, which can use reflectors or lenses to concentrate the solar energy, considerably lessen the cost influence of the PV component of the system, but add the costs of the concentrators and directing systems. For the concentrator PEC system, the water reservoir and the H_2 and O_2 collected are pressurized by the inlet water pump at

relatively low added cost. Pressurization to 300 psi avoids the need for a separate compressor, minimizes water vapor loss by the reactor, and reduces O_2 gas bubble size, which minimizes potential bubble scattering of incident photons at the anode face.

The H2A Costing Model [221] delivers an organized layout to enter factors which impact cash inflows and outflows associated with the construction and operation of a hydrogen production plant. The system practices a solar concentrator reflector to focus solar direct radiation onto the PEC cell. A PEC concentrator system can possibly use a concentration ratio of 10-50 suns; nonetheless, since the experimentally tested system uses about a concentration ratio of 6 to 10, the scale-up analyses are considered for 10 suns. Plant control arrangements perform many duties including local and remote monitoring, alarming and controlling of plant equipment and functions. The model comprises the control and instrumentation mechanisms including the functionality and safety. In the scaled up analyses for hydrogen production, the capacity factor and plant outputs are listed in Table 4.12.

The main financial parameters used in the cost analyses are shown in Table 4.13. Industrial electricity prices are taken in the calculations as \$0.06/kWh [222]. The overall solar-to-hydrogen conversion efficiency of the concentrated PEC hydrogen production system is taken as 16% which is the expected efficiency by 2020 as mentioned in the literature review section. It is assumed that the average solar irradiance is 6.55 kWh/m^2/day.

Table 4.12 The capacity and hydrogen production plant output.

Operating Capacity Factor (%)	85.0%
Plant Design Capacity (kg of H_2/day)	1,000
Plant Output (kg/day)	850
Plant Output (kg/year)	310,250

Table 4.13 The financial input parameters used to calculate the unit hydrogen production cost.

Reference year	2009
Assumed start-up year	2020
Basis year	2009
Length of Construction Period (years)	2
% of Capital Spent in 1st Year of Construction	20%
% of Capital Spent in 2nd Year of Construction	80%
Start-up Time (years)	0.4
Plant life (years)	40
Analysis period (years)	40
Depreciation Schedule Length (years)	20
Decommissioning costs (% of depreciable capital investment)	10%
Salvage value (% of total capital investment)	5%
Inflation rate (%)	1.1%

Source: [221]

Engineering & design and up-front permitting costs are assumed to be 7.5% of the direct capital cost whereas process contingency cost is assumed to be 10% of direct capital

cost. Furthermore, the land cost in Ontario, Canada is taken as $6,500 per acre for rural area. The costs are expressed in U.S dollar. The total required land area is calculated based on the solar-to-hydrogen efficiency and light absorption efficiencies. The basis year costs (2009) are inflated to 2017 dollars using inflation tool [223].

The cost of production for the ammonia facility is of principal importance: a great portion of the complete costs will come from acquiring electricity, presumed to be the utility cost. The cost of production is the summation of waste disposal, labor costs, utilities, general expenses, raw materials, taxes, maintenance expenses as well as other minor costs. Cryogenic air separation methods are frequently used in medium to large scale facilities to yield nitrogen, oxygen, and argon as gases or liquid products. Cryogenic air separation is generally favored technology for generating very high purity oxygen and nitrogen. The plants producing only nitrogen are less complex and need less power to function than an oxygen-only plant making the same amount of product. Producing these products in liquid form necessitates additional apparatus and more power required per unit of delivered product.

The average cost of ammonia production from the electrolysis-based systems are approximately 20% to 40% of hydrogen production cost as previously given in [8] for various ammonia production methods such as PV electrolysis. On a mass basis, 17.8% of ammonia is hydrogen, and approximately 3% of ammonia production cost comes from air separation based nitrogen production [224]. The schematic diagram of the large scale electrochemical ammonia production plant using photoelectrochemical hydrogen is depicted in Fig 4.8.

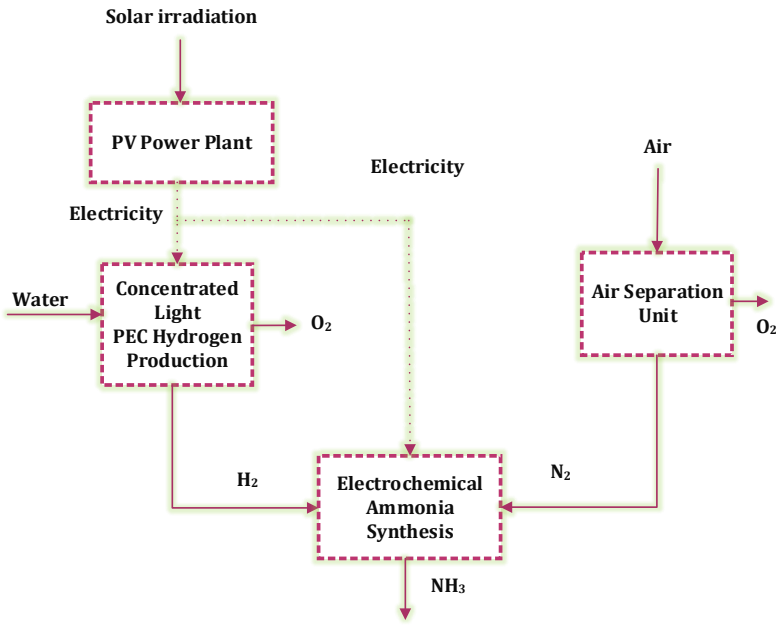

Fig. 4.8 Illustration of large scale electrochemical ammonia production plant using concentrated light based photoelectrochemical hydrogen.

In Haber-Bosch ammonia synthesis plants, there are two main compressors to compress the feed gases into the Haber-Bosch reactor. These compressors consume most of the electricity in the synthesis loop. The synthesis loop requires about 5.5% of the total power

requirements in an electrolyzer based Haber-Bosch plant [224]. On the other hand, in the tested electrochemical ammonia synthesis, the gases are in atmospheric pressure in the reaction. Hence, compression costs are eliminated. However, currently electrochemical ammonia synthesis requires more electricity than Haber-Bosch process per unit kg of product because of the strong chemical bonds. Considering these conditions, a conversion factor is calculated for ammonia cost determination based on the hydrogen cost. Therefore, ammonia production costs are calculated as the 26% of hydrogen production cost. The prices are production prices for hydrogen and ammonia which means that the transportation to the final end user or storage processes are not included. In addition, the start-up year of the plant is assumed to be 2020.

4.12 Optimization Study

An optimization of any process, system and application is critical to improve the process by increasing the efficiency and quality, reducing the cost of the system. In this thesis, the systems are analyzed both thermodynamically and exergoeconomically. Therefore, the objective functions are the combinations of exergy efficiency (to be maximized) and the total cost rate of the system (to be minimized).

There are various methods used to perform multi-objective optimization problems. There is not a unique method suitable for any type of problem. In this thesis, a generic algorithm method is employed since it requires no initial conditions, works with multiple design variables, finds global optima (as opposed to local optima), utilizes populations (as opposed to individuals) and uses objective function formation (as opposed to derivatives). This genetic technique is one of the most robust method since global optimum can be found even though there are local optima. Though, the optimization process takes very long time. The genetic method aims to mimic the procedures happening in biological evolution. For instance, a population of individuals is firstly selected randomly from the given data range which is defined based on the limitations of independent variables. The individuals in this population are measured to define their fitness either for minimization of maximization. After that, a new generation of individuals is formed in a stochastic manner by 'breeding' designated members of the current population. The properties of an individual that are passed on to the next generation are categorized by encoded values of its independent variables. The likelihood that an individual in the current population chooses for breeding the next generation is a cumulative function of its fitness. The 'breeding' combines the characteristics of two parents in a stochastic manner. Additional random variations are introduced by the possibility of 'mutations' for which the offspring may have features that vary distinctly from those of the parents. In the current implementation, the number of individuals in the population remains constant for each generation.

Engineering Equation Solver (EES) is used for optimization purposes. EES requires finite lower and upper bounds to be set for each independent variable. Careful selection of the bounds and the guess value(s) of the independent variables improves the likelihood of finding an optimum. The decision parameters need to comprise all significant variables that could affect the performance and cost effectiveness of the system. Also, the variables with minor importance could be neglected. The constraints in a given design problem occur because of

limitations on the ranges of the physical variables, basic conservation principles which must be satisfied and other limitations. Especially, in the genetic algorithm, the lower and upper bounds on the independent parameters are very important since the initial population and subsequent stochastic selections are chosen from this data range within the bounds.

The main performance influencing parameters in the integrated system including the constraints are given in Table 4.14. The constraints of the decision variables in this thesis are selected as listed in Table 4.14.

Table 4.14 The selected decision variables and constraints in the integrated system.

Variable	Lower	Upper	Unit
A_{PV}	0.03	0.05	m^2
$A_{cell,PEC}$	0.025	0.093	m^2
i (interest rate)	1	10	%
I_3	1500	3000	W/m^2
I_4	1500	3000	W/m^2
$Lifetime$	5	40	years
T_o	290	310	K

Most of the constraints are defined based on the experimental measurements and component specifications. Interest rate and lifetime of the system are defined within actual limits observed in the practice.

Three objective functions are considered here for optimization: exergy efficiency of hydrogen and ammonia production (to be maximized) and total cost rate of the system (to be minimized). Both hydrogen production and ammonia production exergy efficiencies are maximized individually as follows:

- Exergy efficiency (Hydrogen production):

$$\eta_{ex,integrated\ system,H_2} = \frac{(\dot{m}_{H2}\ ex_{H_2} + \dot{W}_{PV} - \dot{W}_{in,PEC})}{Ex_{I_{r_3}}\ A_{PV} + Ex_{I_{r_4}}\ A_{PEC,cell}} \tag{4.189}$$

- Exergy efficiency (Ammonia production):

$$\eta_{ex,integrated\ system,NH_3} = \frac{\dot{m}_{NH3}\ ex_{NH_3} + \dot{W}_{PV} - \dot{W}_{in,PEC} - \dot{W}_{in,NH_3}}{Ex_{I_{r_3}}\ A_{PV} + Ex_{I_{r_4}}\ A_{PEC,cell} + \dot{m}_{N_2}\ ex_{N_2}} \tag{4.190}$$

The total cost rate of the system is minimized using the following cost function obtained from the exergoeconomic analysis.

- Total cost flow rate:

$$\dot{C}_{total} = \dot{C}_{D,total} + \dot{Z}_{\text{total}} = \dot{C}_{D.FRESNEL} + \dot{C}_{D,MIRROR} + \dot{C}_{D,PEC} + \dot{C}_{D,PV} + \dot{C}_{D,AR} + \dot{Z}_{FRESNEL} + \dot{Z}_{MIRROR} + \dot{Z}_{PEC} + \dot{Z}_{PV} + \dot{Z}_{AR} \tag{4.191}$$

Optimum values are obtained for minimized cost and maximized exergy efficiency. The objective functions are initially optimized with single-objective and then combined for multi-objective optimization purposes by giving equal weighting factors.

4.13 Environmental Impact Assessment

Life cycle assessment (LCA) is mainly a cradle to grave analysis technique to inspect environmental effects of a system or process or product. LCA designates a systematic set of procedures for accumulating and examining the inputs and outputs of materials and energy, and the related environmental effects, directly transferrable to the product or service during the course of its life cycle. A life cycle is the set of stages of a product or service system, from the removal of natural resources to last removal. LCA is an instrument which helps engineers, scientists and policy makers to assess and compare energy and material use, emissions and wastes, and environmental influences for various products or processes. Overall environmental impact of any process is not comprehensive if only operation is considered, all the life stages from resource extraction to disposal throughout the lifetime of a product or process should be deliberated. Mass and energy streams and environmental effects related to plant construction, utilization, and dismantling stages are taken into account in LCA analysis [221, 222]. LCA is a four-step process namely; goal and scope definition, inventory analysis, impact assessment, improvement potential as shown in Fig. 4.9.

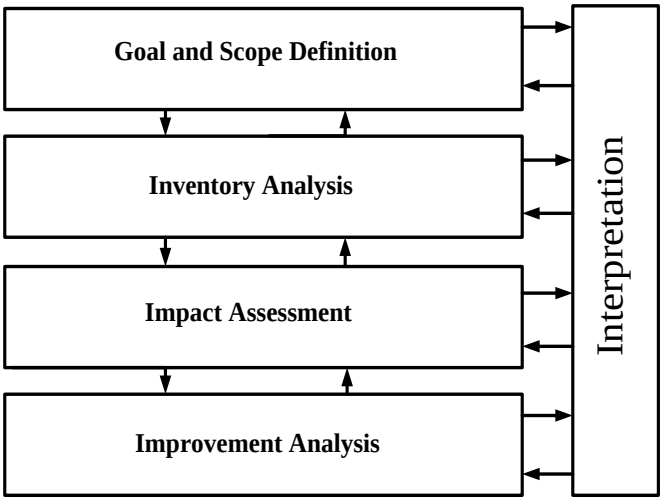

Fig. 4.9 The framework of LCA analysis.

Goal definition and scoping defines the product, process or activity. It classifies the boundaries and environmental effects to be considered for the assessment. Inventory section categorizes and computes energy, water and materials usage and environmental discharges. Impact assessment step assesses the human and ecological effects of energy, water, and material usage and the environmental releases recognized in the inventory analysis. Interpretation step assesses the results of the inventory analysis and impact assessment to select the chosen product, process or service. The techniques for performing of an LCA have been defined by such International Organization for Standardization (ISO) based on ISO 14040-Environmental management - Life cycle assessment - Principles and framework and ISO 14044:2006 - Environmental management - Life cycle assessment - Requirements and guidelines [221, 222].

4.13.1 LCA analysis methodology

The four steps followed throughout the life cycle assessment study are explained as follows:

4.13.1.1 Goal and scope definition

This is the first step of an LCA study. This step describes the aims of study and also the range of activities under investigation. The utmost care and detail is required to define the goals and scope of study. The LCA is an iterative process, therefore the feedback consideration should be kept in definition of systems. Normally drawing boundary and the energy indicates the scope and materials are considered for the processes falls within these boundary limits.

4.13.1.2 Inventory analysis

In this step, raw material and energy, the emissions and waste data is composed. This data is used to compute the total emissions from the system. The mass and energy balances are used at each step to compute the life cycle inventory of the system. The life cycle inventory needs to comprise every possible energy and material input and all probable emissions to establish credible results. Data quality is significant feature of LCA. During inventory analysis, the standards are followed for preserving the data quality.

4.13.1.3 Impact assessment

The third step of LCA is life cycle impact assessment. This step evaluates the influences of activities under examination. The LCI data is used to find out the affected areas. The LCI data is essentially analyzed in a two-step process:

Classification: The impact classes are established and LCI data is analyzed to mark the data and compute the values of emissions conforming to each group. The impact categories are based on the evaluation method utilized. As example, some of the categories are global warming potential, acidification, human toxicity etc.

Characterization: It is the second step of impact assessment. Classification step group the data in respective impact categories. Characterization step is used to assess the relative contribution of each type of emission to these impact classes.

Normalization and Weighting: This step is not obligatory according to the standards. The emissions are normalized conforming to a standard and converted into a score system. The total score is used to ascertain the methods and processes of concern.

4.13.1.4 Interpretation of results and improvement

The last step is interpretation of results and feedback for improvement of system. The gray areas of system are recognized and extremely contaminating processes can be removed with cleaner alternatives. LCA can detect critical stages where process variations could considerably decline effects [227]. Performing an LCA brings following advantages:

- Assessing systematically the environmental concerns related with a given product or process
- Evaluating the human and environmental properties of material and energy consumption and environmental emissions to the local community, region, and world
- Ascertaining effects related to precise environmental zones of concern

- Supporting in identifying important changes in environmental effects between life cycle stages and environmental media
- Comparing the health and environmental effects of substitute products and processes
- Computing environmental releases to air, water, and land in relation to each life cycle stage and major contributing process

4.13.2 Assessment methods

There are numerous assessment approaches advanced over the time to classify and characterize the environmental effects of system such as Eco-indicator 99, EDIP 2003, CML 2001, IMPACT 2002+, ReCiPe Endpoint, CML 2 baseline 2000, BEES, TRACI 2, EDIP 2. The two methods used for the current analysis are CML 2001 and Eco-indicator 99.

4.13.3 CML 2001 method

It is a technique developed by a group of scientists under the lead of CML (Center of Environmental Science of Leiden University) counting a set of impact categories and characterization methods for the impact assessment step in 2001 [228]. Normalization is provided but there is neither weighting nor addition. Some of the baseline indicators of this method which are employed in this thesis are clarified as follows [228]:

Depletion of Abiotic Resources

The key concern of this group is the human and ecosystem health that is affected by the extraction of minerals and fossil as inputs to the system. For each extraction of minerals and fossil fuels, the Abiotic Depletion Factor (ADF) is determined. This indicator has globe scale where it is based on concentration reserves and rate of de-accumulation.

Human Toxicity

Toxic substances on the human environment are the key concerns for this category. The health risks in the working environment are not included in this category. Characterization factors, Human Toxicity Potentials (HTP) are computed with USES-LCA, describing fate, exposure and effects of toxic substances for an infinite time horizon. 1,4-dichlorobenzene equivalents/kg emissions is used to express each toxic substance.

Fresh Water Aquatic Eco-Toxicity

This indicator deliberates the influence of the emissions of toxic substances to air, water, and soil on fresh water and ecosystems. USES-LCA is used to calculate the Eco-toxicity Potential by describing fate, exposure and effects of toxic substances. 1,4-dichlorobenzene equivalents/kg emissions is used to express infinite time horizon. The scale of this indicator can be applied to global/continental/ regional and local scale.

Acidification potential

Acidifying substances origins a wide range of effects on soil, groundwater, surface water, organisms, ecosystems and materials. RAINS 10 model is used to calculate the Acidification Potential (AP) for emissions to air, describing the fate and deposition of acidifying substances. SO_2 equivalents/kg emission is used to expresses the AP.

Global Warming

The GHG to air are related with the climate change. Adversative impatcs upon ecosystem

health, human health and material welfare can result from climate change. The Intergovernmental Panel on Climate Change (IPCC) developed the characterization model which is elected for the development of characterization factors. A kg carbon dioxide/kg emission is used to express the Global Warming Potential for time horizon 500 years (GWP500). This indicator has a global scale.

Eutrophication

This category deliberates the effects of to excessive levels of macro-nutrients in the environment triggered by emissions of nutrients to air, water and soil. The stoichiometric procedure of Heijungs is the base of the Nutrification potential (NP) which is expressed as kg PO_4 equivalents per kg emission and the geographical scale varies between local and continental scale, time span is infinity. Fate and exposure are not included.

Land use

Land use which is the extraction of raw materials, production processes, agricultural land, area of industrial territory, landfill sites, incineration plant area, transport, use processes and given in terms of m^2a. The land use refers to the total arrangements, activities and inputs undertaken in a certain land cover type. The term land use is also used in the sense of the social and economic purposes for which land is managed. In the CML2001 the life cycle impact assessment method, competition is measured as occupied area*time (m^2a) where a represents the annual (year).

4.13.4 Eco-indicator 99 method

The Eco-indicator technique states the environmental impact in terms of numbers or scores. It simplifies the interpretation of LCA by including a weighting method. After weighting, it supports to give single score for each of the product or process which is calculated based on the relative environmental impact. The score is signified on a point scale (Pt), where a point (Pt) means the yearly environmental load (i.e. whole production/consumption undertakings in the economy) of an average citizen. Eco-Indicator 99 (E) uses load of average European [229]. The Eco-indicator 99 describes the environmental damage in three comprehensive categories [228]:

Human Health

It comprises the number and duration of diseases and loss of life years because of stable deceases produced by environmental degradation. The effects are included mainly by: climate change, ozone layer depletion, carcinogenic effects, respiratory effects and ionization.

Ecosystem Quality

This category comprises the impact of species diversity, acidification, ecotoxicity, eutrophication and land-use.

Resources

This category resembles to the depletion of raw materials and energy resources. It is measured in terms of the surplus energy essential in future for the extraction of lower quality of energy and minerals. The agricultural resource depletion is studied under the category of land use.

Some of the assumptions made for the LCA analysis of the systems are listed below:

- The nitrogen is considered as gas from cryogenic air separation unit.
- The inputs used in calculations are feedstock, energy or electricity and emissions.
- The processes for ammonia production contains production of hydrogen and nitrogen separately.
- The mass balance is used to identify the amount of hydrogen and nitrogen required for unit ammonia production.
- The fugitive emissions are considered negligible.
- The selected location of ammonia plants are U.S since US electricity values are used.
- The functional unit is one kg ammonia production.
- The LCA is performed until plant gate since storage and further transportation of the product is not considered.

4.13.5 Selected ammonia production methods

In the scope of this thesis, twenty five different ammonia production techniques are nominated for comparative assessment purposes based on conventional and renewable resources. As most common ammonia production technique is Haber-Bosch and one of the most developed hydrogen production method is electrolysis, electrolysis and Haber-Bosch based ammonia production methods are utilized using various resources. In addition, typically employed ammonia production methods such as SMR, coal and biomass gasification are investigated here. For nitrogen production step, cryogenic air separation is frequently used technique for huge amount of nitrogen production. In the life cycle assessment of nitrogen production, electricity for process, cooling water, waste heat and infrastructure for air separation plant are included. Except for the experimental system, photoelectrochemical hydrogen based electrochemical ammonia production, all of the systems uses Haber-Bosch method for ammonia synthesis. In order to analyze electrolysis and Haber-Bosch based ammonia production processes, following diagrams are used as illustrated in Figs. 4.10 and 4.11.

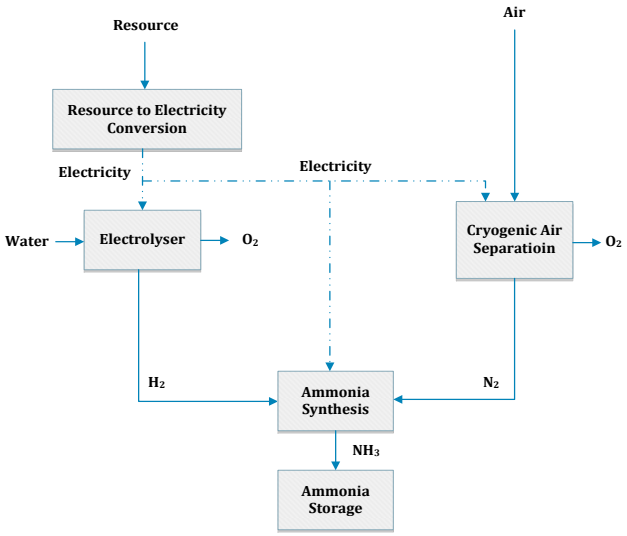

Fig. 4.10 Ammonia production based on electrolysis and Haber-Bosch process from various resources.

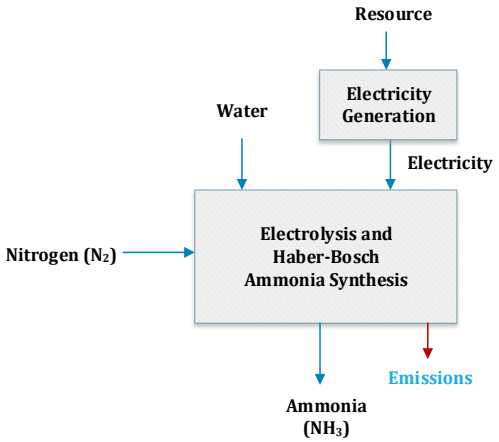

Fig. 4.11 Energy and material flows of electrolysis and Haber-Bosch based ammonia production methods.

Steam methane reforming (SMR) based ammonia production

It is a mature production process in which high-temperature steam is used to produce hydrogen from a methane source, such as natural gas. In steam-methane reforming, methane reacts with steam under 3–25 bar pressure in the presence of a catalyst to produce hydrogen, carbon monoxide, and a relatively small amount of carbon dioxide [230]. Steam reforming is endothermic. In the steam reforming processes process steam is taken from the plant steam system, usually from an extraction turbine. Combining the produced hydrogen with nitrogen in a Haber-Bosch plant yields ammonia which is the commonly used method so far. The system schematics are given in Figs. 4.12 and 4.13.

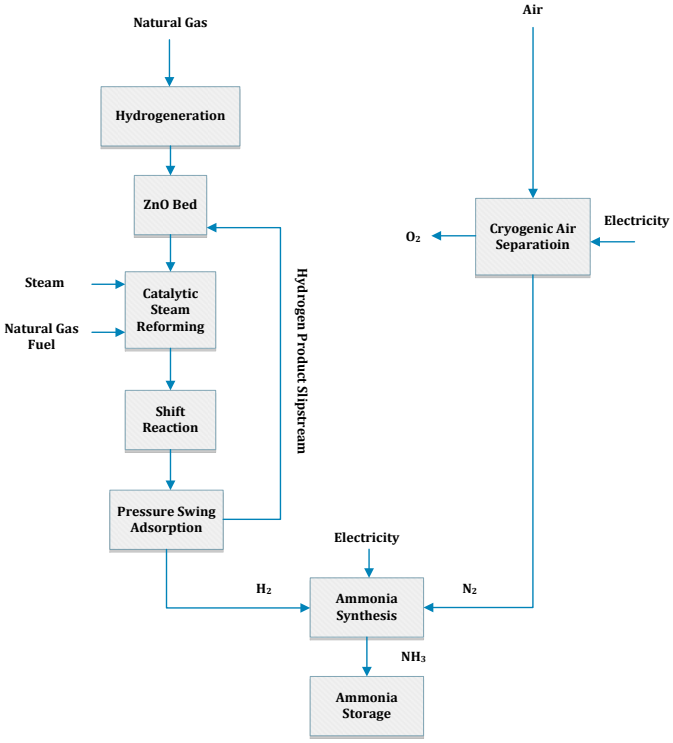

Fig. 4.12 Ammonia production via steam methane reforming.

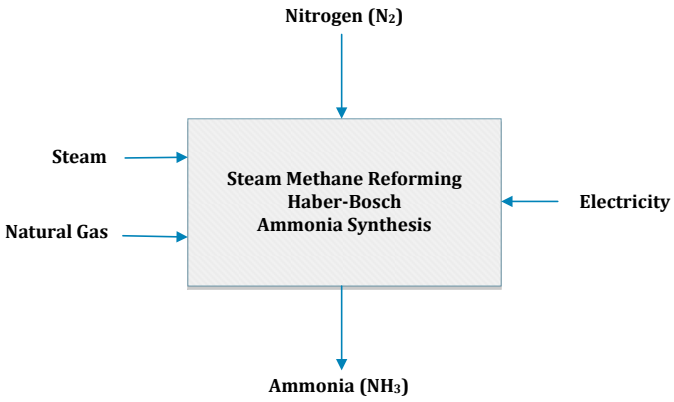

Fig. 4.13 Energy and material flows in SMR based ammonia production.

Wind electrolysis based ammonia production

The system considered for manufacturing hydrogen from wind energy includes two chief systems: a wind turbine which generates electricity, which in turn drives a water electrolysis unit for production of hydrogen. Wind energy is converted to mechanical work by wind turbines and then transformed by an alternator to alternating current (AC) electricity, which is transmitted to the power grid. The efficiency of wind turbines depends on location. This affects the stability of power generation. Wind to ammonia systems uses the electricity produced by the generator coupled with wind turbine. The type of the turbines are generally large horizontal-axis wind turbines mounted on a tower. The fundamental ammonia synthesis structure uses an electrolyzer to produce hydrogen from water electrolysis and an air separation unit to get nitrogen from air [231]. The produced hydrogen and nitrogen are reacted in a Haber Bosch plant for ammonia production.

Solar electrolysis based ammonia production

Solar power is probably, along with wind power, the most readily available solution to clean energy alternatives. Solar cells produce direct current electricity from light, which can be used to power any process. The produced electricity from photovoltaic modules supply the required electricity for electrolyzer to produce hydrogen from water and an air separation unit to obtain nitrogen from air [48]. Then using a Haber-Bosch plant, ammonia is produced. In the LCA analysis for the PEC based electrochemical ammonia production, multicrystalline silicon solar cells are used since they are the types utilized in the experiments. In the PV electrolysis option, a mixture of PV power plants in US grid is employed.

Coal gasification and UCG with carbon capture based ammonia production

There are mainly two type of coal gasification. The one is called as underground coal gasification which take place below earth level and the other one is coal gasification which takes place above earth level.

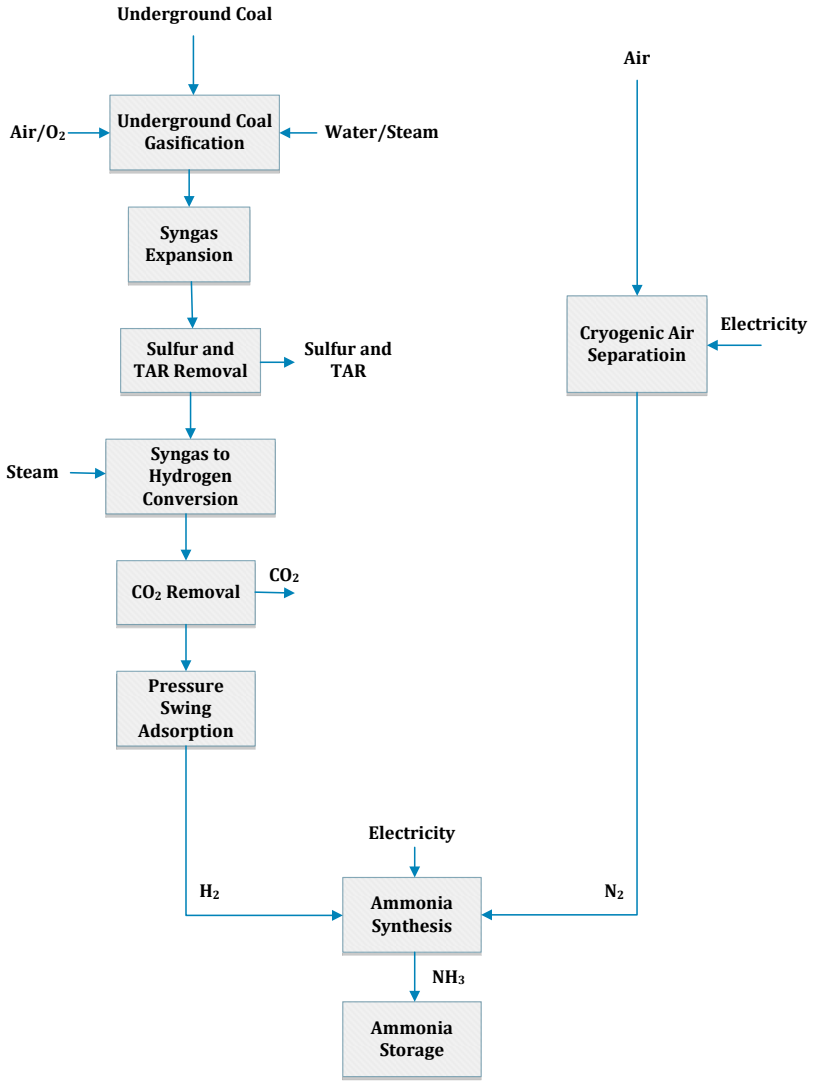

Fig. 4.14 Ammonia production via UCG process.

Underground coal gasification (UCG) is an encouraging option for the future use of un-worked coal. Instead of mining coal reserves, UCG may ultimately make unreached coal reserves accessible. Carbon capture and storage of carbon dioxide technology are treated as two effective technologies. The syngas produced through the gasification process consists mainly of hydrogen (H_2) and carbon monoxide (CO). The values of LCA analysis for UCG process are based on [95]. In this method, since CO_2 is captured, it is evaluated as useful output as seen in Fig. 4.14. Coal gasification is the second most commonly used process for ammonia production. The process of ammonia production from underground coal gasification can be seen in Figs. 4.14 and 4.15. Coal is gasified underground and obtained syngas is sent to surface to be processed in syngas cleaning units. After hydrogen is yielded, it is combined with nitrogen to produce ammonia. The electricity requirements of the processes in the cycle are supplied from coal fired power plant.

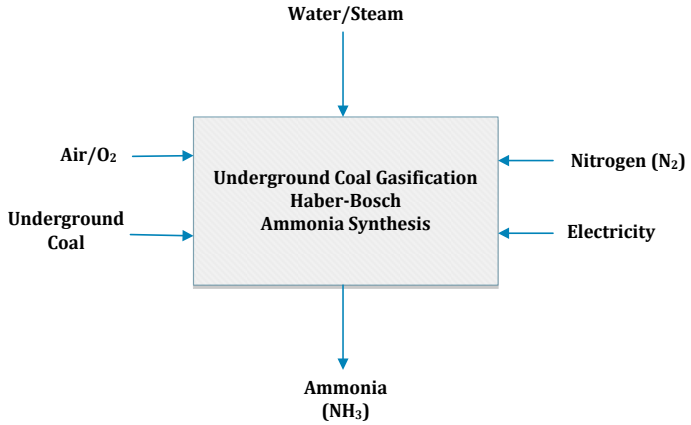

Fig. 4.15 Energy and material flows in UCG based ammonia production.

Hydrocarbon cracking based ammonia production

In this method, all processes from raw material extraction until delivery at plant are included. The data are from European plastics industry. The amount of sulphur (bonded) is assumed to be included into the amount of raw oil. The process is the naphtha cracking for hydrogen production. After hydrogen is produced from hydrocarbon cracking, it is combined with nitrogen from air separation unit to form ammonia [232–235]. In this method, electricity required for the processes are assumed to be from US grid mix.

Biomass downdraft gasifier based ammonia production

As an energy source, biomass can either be used directly via combustion to produce heat, or indirectly after converting it to various forms of biofuel.

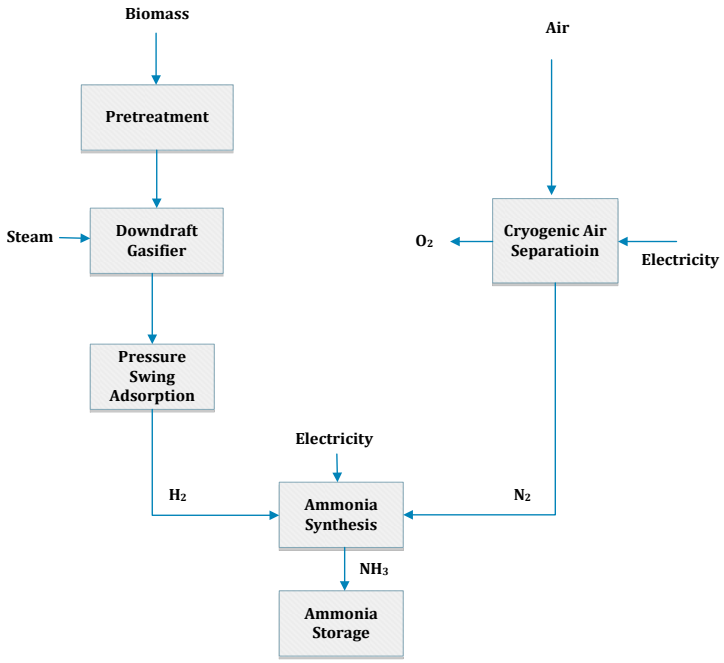

Fig. 4.16 Ammonia production via biomass DG.

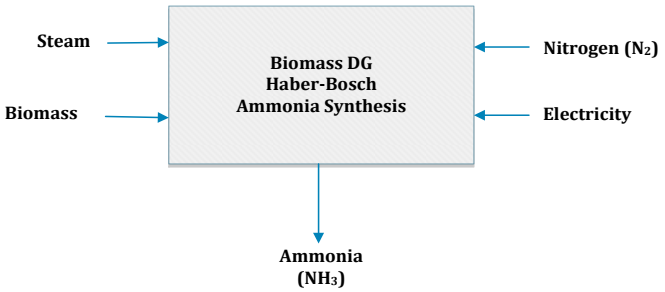

Fig. 4.17 Energy and material flows in biomass DG based ammonia production.

Conversion of biomass to biofuel can be achieved by different methods can be categorized into: thermal, chemical, and biochemical methods. In this method, as seen in Figs. 4.16 and 4.17, biomass is gasified using downdraft gasifier (DG) to obtain hydrogen and combine with nitrogen [129]. The electricity requirement for the Haber-Bosch process is supplied from biomass fired power plant.

Biomass circulating fluidized bed gasifier based ammonia production

Circulating Fluidized Bed Gasifier (CFBG) offers a prospective technology for biomass gasification with steam [129]. The only difference is the type of gasifier as seen in Figs. 4.18 and 4.19. The electricity requirement for the Haber-Bosch process is supplied from biomass fired power plant.

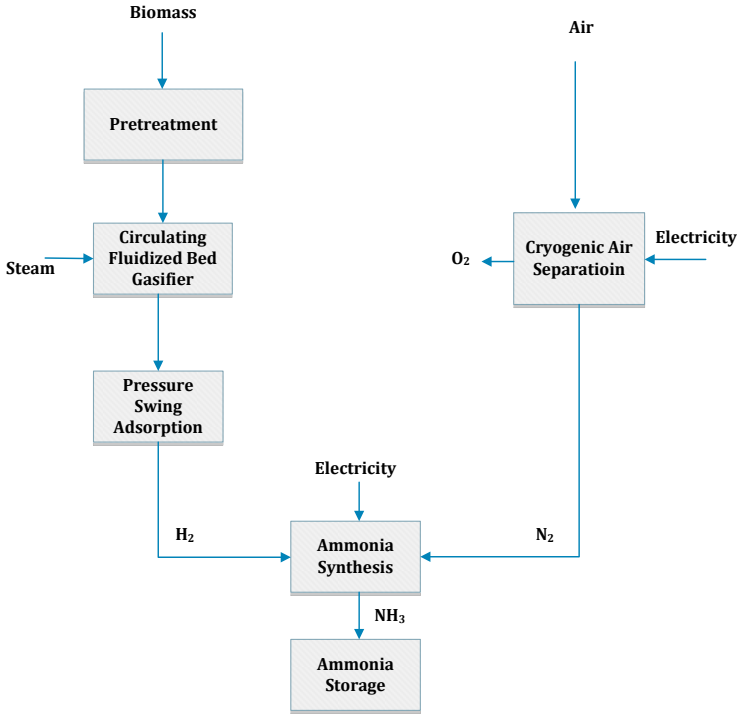

Fig. 4.18 Ammonia production via biomass CFBG.

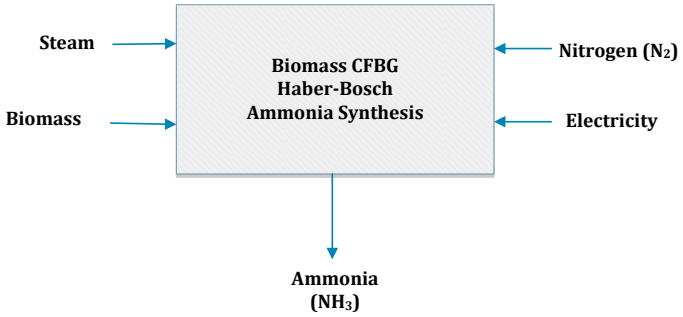

Fig. 4.19 Energy and material flows in biomass CFBG based ammonia production.

Hydroelectric (pumped storage) electrolysis based ammonia production

In Canada, approximately 475 hydropower facilities generate 70,000 MW of hydropower [236]. Total hydro based utility generation appeared at 527,689,407 MWh which is 60% share of electricity generation in Canada. Quebec represents the majority of hydropower based electricity generation in Canada. It supplies nearly 94% of its electricity from hydropower [237]. On the other hand, the province of British Columbia represents the second biggest producer with an installed capacity of above 11,000 MW. These features of hydropower plants make ammonia production from hydropower based methods more attractive and reasonable in which the cost could be substantially decreased. In the LCA analysis, three different hydropower types are used namely; run-of-river, reservoir and pumped storage. In this method, pumped hydro storage, the process includes the conversion of electricity from domestic high voltage grid to potential energy by pumping water up to the reservoir and generation of peak-load power when water flows back down to the turbine (reverse mode).

Nuclear electrolysis based ammonia production

Nuclear based ammonia production methods can also be a promising source for ammonia production. Nuclear based electricity yields lower cost and reliable supply. Combining nuclear power plant with ammonia production plant is a promising method [131, 137]. In nuclear electrolysis based option, electricity is produced in nuclear power plant and directly utilized in electrolysis coupled with Haber-Bosch ammonia synthesis loop. There is no heat assisting in this method. Hence, more electrical energy is required to split water into hydrogen and oxygen compared to nuclear high temperature electrolysis. The main inputs of nuclear electrolysis based hydrogen production option are listed in Table 4.15.

Table 4.15 Main elements for nuclear electrolysis based hydrogen production method.

Parameter	Value	Unit
Hydrogen from Nuclear Electrolysis (product)	1	kg
Water	9	kg
Electricity, nuclear, at power plant	53.5	kWh

Partial oxidation of heavy oil based ammonia production

Heavy fuel oil is the residue of crude oil distillation that still flows. Waste oil from other industries are often added. The partial oxidation process is used for the gasification of heavy

feedstocks such as residual oils and coal. Exceedingly viscous hydrocarbons and plastic wastes may also be used as fractions of the feed. HFO may have a composition of 88% wt. C, 10 % wt. H, 1 % wt. S, 0.5 % wt. H_2O, 0.1 % wt. ash, and may contain dispersed solid or semi-solid particles (asphaltenes, minerals and other leftovers from the oil source, metallic particles from the refinery equipment, and some dumped chemical wastes), plus some 0.5% water. As shown in Figs. 4.20 and 4.21, heavy oil is gasified and then cleaned. After CO_2 removal, it is combined with nitrogen and compressed for the ammonia reaction. The electricity is supplied from oil fired power plant. Partial oxidation of heavy oil method includes manufacturing process starting with heavy fuel oil, air and electricity [234, 235]. Auxiliaries, energy, transportation, infrastructure and land use, as well as wastes and emissions into air and water are all considered. Transportation of the raw materials, auxiliaries and wastes is involved but transportation and storing of the product are not involved. Carbon dioxide is the byproduct produced. Transient or unbalanced processes are not considered. Emissions to air are measured as creating in a high population density area. Emissions into water are assumed to be emitted into rivers.

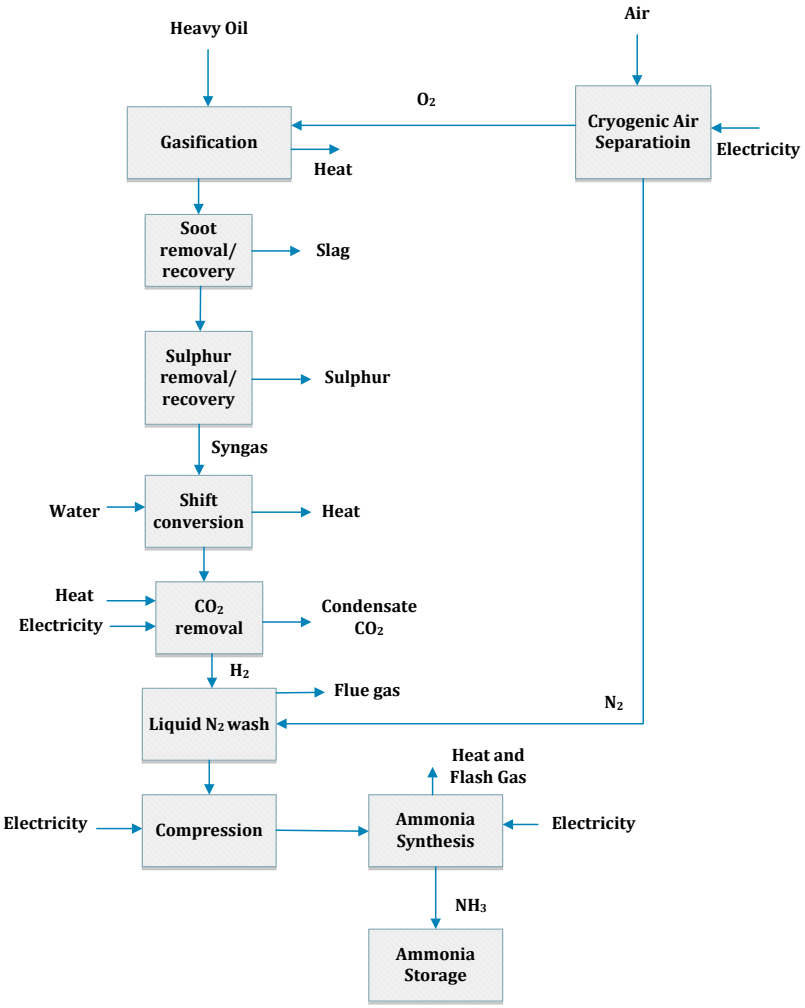

Fig. 4.20 Ammonia production via partial oxidation of heavy oil.

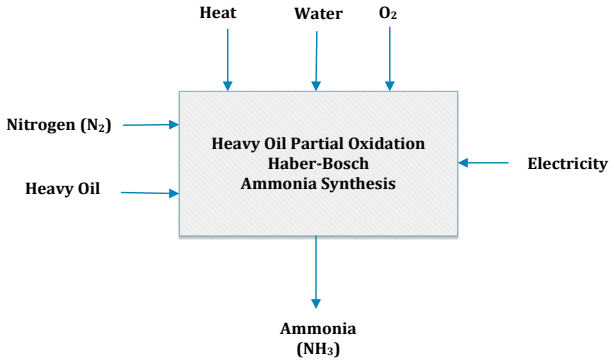

Fig. 4.21 Energy and material flows of partial oxidation of heavy oil based ammonia production.

Nuclear high temperature electrolysis based ammonia production

In nuclear-based high-temperature ammonia production, the system consists of a nuclear power plant, high temperature electrolyzer, cryogenic air separation unit and a Haber-Bosch synthesis plant as shown in Fig. 4.22. The required electricity is utilized from nuclear power plant and the required heat for high temperature electrolysis is supplied from nuclear waste heat [131, 236]. The main parameters of the nuclear high temperature electrolysis method are listed in Table 4.16.

Table 4.16 Main elements for nuclear high temperature electrolysis hydrogen production method.

Parameter	Value	Unit
Hydrogen from Nuclear High Temperature Electrolysis (product)	1	kg
Water	9	kg
Electricity, nuclear	28.9	kWh
Nuclear heat	6.67	kWh

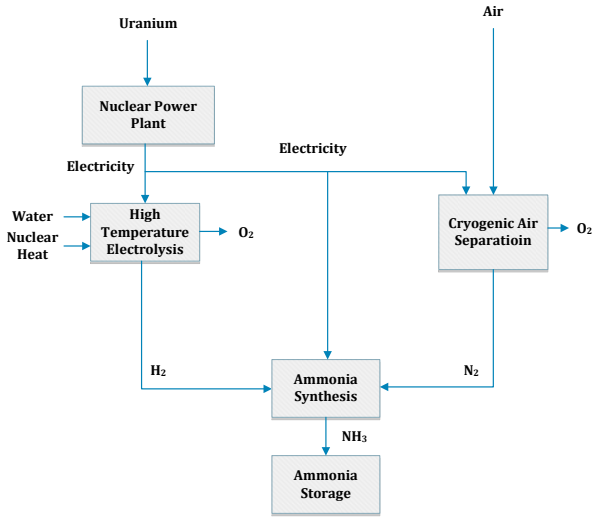

Fig. 4.22 Ammonia production via nuclear high temperature electrolysis.

Nuclear power plant electricity is assumed as a mixture of 66.5% from pressure water reactor (PWR) and 33.5% from boiling water reactor (BWR) type reactors [228], since the

SimaPro software database does not contain CANDU type reactors. In high temperature electrolysis, the excess heat in the nuclear power plant is utilized to decrease the required amount of electricity for electrolysis as seen in Fig. 4.22. In high temperature electrolysis, the excess heat in the nuclear power plant is utilized to decrease the required amount of electricity for electrolysis as seen in Figs. 4.22 and 4.23.

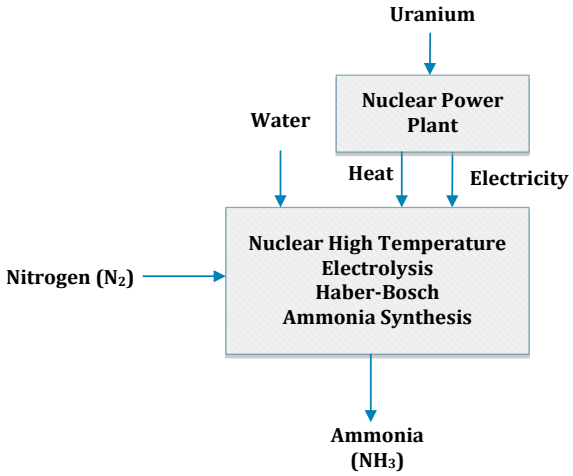

Fig. 4.23 Energy and material flows of nuclear high temperature electrolysis based ammonia production.

Biomass electrolysis based ammonia production

Biomass can be used to produce electricity directly. The biomass based electricity generation cycle is the conventional Rankine cycle with biomass being burned in a high pressure boiler to produce steam. The biomass power cycle efficiencies can range between 23% - 34%. The exit of the steam turbine can be fully condensed to produce power as much as possible or the excess heat can be utilized for various useful heating activity.

In this system, by gasifying the biomass, electricity is generated through a gas turbine [237, 238]. Biomass is produced within the boundaries of this system and is thus not shown as a fuel input. Fuel and material extraction, biomass gasification power plant, biomass production, transportation are all included in the life cycle assessment. Infrastructure requirements for biomass production, biomass gasification, and biomass electricity generation are also included. For the specific biomass fired power plant, the energy efficiency is taken as 33%. The generated electricity is used in the electrolyzer for hydrogen production and reacted with nitrogen for ammonia production in Haber-Bosch plant.

Bituminous coal electrolysis based ammonia production

Bituminous coal is one of the primary coal types utilized in power generation. Therefore it is also called as steam coal. Nearly 50% of the coal used in the coal fired power plants in the world are this grade of coal. It includes 50-86% carbon. The energy content is approximately 6,400 kcal/kg. In Canada, Alberta, Saskatchewan and Nova Scotia have rich coal deposits and they produce most of their electricity from coal. The electricity from bituminous coal fired power plant is used in the electrolyzer and Haber-Bosch plant for ammonia production [15].

Coal electrolysis based ammonia production

In this method, hard coal is utilized for electricity generation in coal fired power plant. Final degree of carbonization leads to anthracite, "hard coal". With any carbon content greater than 86%, hard coal is the least common and therefore it is considered the most expensive grade of coal. Electrolysis is the method for hydrogen production which is then combined with nitrogen for ammonia synthesis [15].

Heavy oil electrolysis based ammonia production

Oil can be used for electricity generation like the other fossil fuels. The process is the same as coal or natural gas power plants. The fuel is burned, heats water that turns into steam and spins a turbine. The required electricity is supplied from oil fired power plant for electrolyzer and ammonia production plant [15].

Hydropower (reservoir type) electrolysis based ammonia production

In hydropower systems, there is no fuel burning hence there is insignificant pollution. Water to run the power plant is provided by nature which makes it renewable. Hydropower plays a major role in reducing greenhouse gas emissions globally. The technology is reliable and proven over time. For this type of method, lifetime is assumed to be 150 years for the structural part and 80 years for the turbines in LCA. A representative sample of dams with a height of more than 30 meters is taken into account for calculating the input. The net average efficiency, including pipe losses, is 78%. Ammonia production plant and electrolyzer consume the electricity from the dams.

Hydropower (on river) electrolysis based ammonia production

The kinetic energy of flowing water is the primary mover for hydropower plants. Using the turbines and generators, kinetic energy is converted into electricity. Run-of-river plants utilize the natural flow and altitude drop of rivers. A structure at the inlet powers water via an underwater pipeline and sends it to a turbine. The turbine drives a generator, which then generates alternating current. Lifetime is assumed to be 80 years and net average efficiency is taken as 82% for LCA.

Municipal waste electrolysis based ammonia production

Electricity can be generated by combusting municipal solid waste as a fuel in the conventional plants. Consequently in this system, the compulsory electricity is attained from a municipal waste incineration power plant. Waste-specific air and water emissions from incineration, auxiliary material consumption for flue gas cleaning are encompassed in the life cycle assessment. In the LCA analysis, the short term reliefs to river water, long term releases to ground water from slag section and remaining material landfill and demands for process energy for municipal waste incineration plant are taken into account. Share of carbon in waste, which is biogenic, is about 60.4%. Share of iron in waste, which is metallic/recyclable, is about 60%.

The waste used in the calculations comprises 21% paper, 8% mixed cardboard, 15% plastics, 3% laminated materials, 2% laminated packaging, e.g. tetra bricks, 3% combined goods: diapers; 3% glass, 2% textiles, 8% minerals, 9% natural products, 22% compostable

material, 2.65% inert metals, 1% volatile metals, 0.0065% batteries, 0.34% electronic goods. The lower heating value of the solid waste fuel is 11.74 MJ/kg and thermal efficiency is taken as 25%. The produced electricity is sent to power electrolyzer, cryogenic air separation plant and Haber-Bosch process. Using commercial electrolyzer and cryogenic air separation, ammonia is manufactured in Haber-Bosch plant [242].

Natural gas electrolysis based ammonia production

Approximately 5% of total electricity generated in Canada can be attributed to the combustion of natural gas. Therefore, natural gas fired power plants are an important source of power generation. The generated electricity is utilized in electrolyzer and Haber-Bosch plant for ammonia production [15]. The values represent the average of installed power plants in US which operate only with 100% natural gas firing.

Nuclear 3 step CuCl cycle based ammonia production

The copper-chlorine (CuCl) cycle is a multiple step thermochemical cycle for the production of hydrogen. The CuCl cycle is an integrated process that engages both thermochemical and electrolysis steps. The CuCl cycle involves four chemical reactions for water splitting, whose net reaction decomposes water into hydrogen and oxygen. Input of water and energy for the generation of steam are included but other infrastructure is not included, as the heating infrastructure is already a part of the respective heating modules used in the plant. Electricity generation from nuclear energy plant is presumed as 66.5% from PWR and 33.5% from BWR kind reactors. The LCA of nuclear based methods include chemicals, and diesel necessities as well as the fuel elements and applicable transportation necessities. Water usage for chilling is accounted for too.

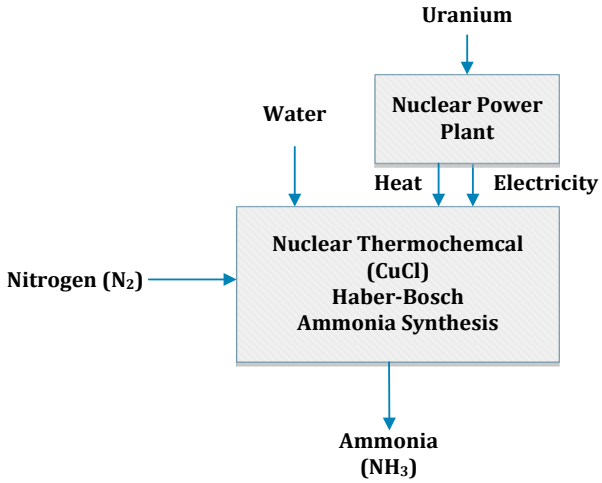

Fig. 4.24 Energy and material flows of nuclear 3-4-5 step CuCl cycle based ammonia production.

Deliberated radioactive waste streams are: spent fuel to reusing and preparing; operative low active waste for preparing in the middle repository; and, accumulated waste from disassembling. Non-radioactive wastes are accounted for. The mean burnup resembles an average enhancement of 3.8% U235 for fresh uranium fuel elements in BWR kind reactor. The

transportation necessities are considered with the standard locations for chemical and diesel necessities and particular distances for fuel recharge and radioactive waste. The average burnup corresponds to an average enhancement of 4.2% U235 for fresh uranium fuel elements in PWR kind reactor. The diesel necessities for the annual check of diesel emergency generators are accounted for. As shown in Fig. 4.24, both heat and electricity are supplied at the same time for hydrogen production and then hydrogen reacts with nitrogen to produce ammonia [133, 239, 240]. The main streams of the nuclear 3 step thermochemical cycle based hydrogen production process are listed in Table 4.17.

Table 4.17 Main elements for nuclear 3 Step Cu-Cl cycle based hydrogen production method.

Parameter	Value	Unit
Hydrogen from Nuclear 3 Step Cu-Cl Cycle (product)	1	kg
Water	9	kg
Electricity, nuclear	67.15	MJ
Nuclear heat	325	MJ

Nuclear 4 step CuCl cycle based ammonia production

Thermochemical cycles are a promising selection for large-scale hydrogen production which can be realized at nuclear reactor facilities. Therefore, Cu-Cl based nuclear thermochemical cycles with multiple steps are considered in this thesis. The CuCl process can be linked with nuclear plants or other heat sources such as solar and industrial waste heat to potentially achieve higher efficiencies, lower environmental impact and lower costs of hydrogen production than any other conventional technology. In this method, 4 step CuCl cycle is utilized for hydrogen production and then it is reacted in a Haber-Bosch plant for ammonia production [133, 239, 240]. The main streams of the nuclear 4 step thermochemical cycle based ammonia production process are listed in Tables 4.18.

Table 4.18 Main elements for nuclear 4 Step Cu-Cl cycle based hydrogen production.

Parameter	Value	Unit
Hydrogen from Nuclear 4 Step Cu-Cl Cycle (product)	1	kg
Water	9	kg
Electricity, nuclear	67.15	MJ
Nuclear heat	289.89	MJ

Nuclear 5 step CuCl cycle based ammonia production

Thermochemical water-splitting cycles denote technical processes which decompose the water molecule while the separate streams of hydrogen and oxygen gases are released via a closed system of chemical reactions. In addition to the chemical elements constituting the water molecule, the chemical composites in multi-step thermochemical water-splitting cycles include other components. For example, the copper–chlorine thermochemical cycle includes compounds of Cu and Cl whereas the sulfur–iodine thermochemical cycle includes chemical composites of S and I. In a thermochemical cycle, water is only consumed; the only products generated are hydrogen and oxygen as separated streams; and all other chemicals involved in

particular reaction steps are completely recycled. The thermochemical plants are supplied only with heat and water to operate. In the 5 step cycle, copper is produced electrolytically, moved to an exothermic thermo-chemical hydrogen reactor and then reacted with HCl gas to produce hydrogen gas and molten CuCl. The overall efficiency of the CuCl cycle is theoretically much higher than conventional water electrolysis via thermal power plants because heat is directly utilized to generate hydrogen. The generated hydrogen is combined with nitrogen and ammonia is produced [133, 239, 240]. In this method, 50.3 MJ of nuclear electricity is used whereas 352.26 MJ nuclear heat is utilized for 1 kg hydrogen production. These parameters are for 1 kg hydrogen production which is then combined in ammonia production plants as the quantities are given in Table 4.19 for all nuclear cases.

Table 4.19 Main elements for all selected nuclear ammonia production processes.

Parameter	Value	Unit
Ammonia	1	kg
Nitrogen	0.823	kg
Hydrogen	0.177	kg
Electricity, nuclear	2	kWh

Photoelectrochemical hydrogen based ammonia production

In this thesis, experimental process of photoelectrochemical based ammonia production is carried out. Using the practical data taken from the experiments, an LCA is implemented.
In this respect, firstly photoelectrochemical hydrogen production process is built in the LCA software. The material list required for the PEC reactor design is listed in Table 4.20.

Table 4.20 The type and quantity of the materials used in the PEC reactor.

Material	Value	Unit
HDPE	2	kg
Stainless steel electrodes	2	kg
Nafion Membrane	930	cm^2
Copper oxide	2.7	g
Platinum black	2.7	g
Washers	0.125	kg
Bolt Nuts	0.125	kg
Acrylic or polycarbonate reactor window	0.4	kg
Piping (plastic)	100	g
Rubber gasket	0.2	kg

The amount of listed materials are employed in LCA software. The boundary of the LCA study for PEC hydrogen production is shown in Fig. 4.25. The main energy and material requirements of this PEC hydrogen production system are summarized in Table 4.21 as follows.

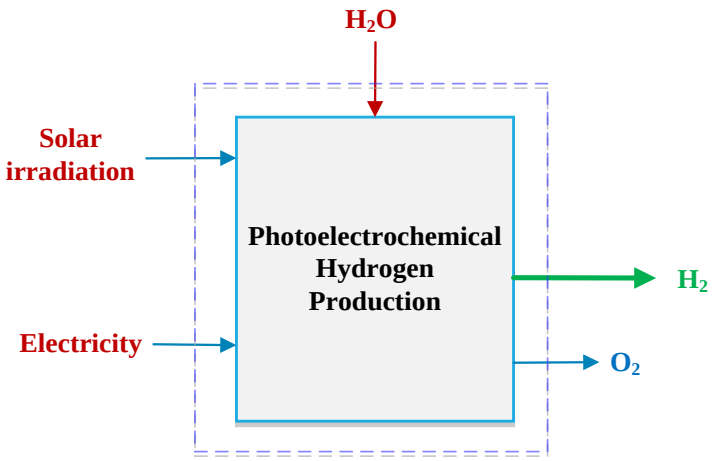

Fig. 4.25 The boundaries of the conducted LCA for PEC hydrogen production.

Table 4.21 Main energy and material flows in PEC hydrogen production system.

Parameter	Value	Unit
Hydrogen (product)	0.000004669	g
Electricity, production from photovoltaic	0.698	J
Water, deionized	0.000042021	g
Solar energy	9.418948327	J

Since the system uses concentrated light with a set of other structures such as Fresnel lens, support mechanism, dielectric mirrors and other equipment, the complete setup is also considered in the LCA analysis as listed in Table 4.22. This step includes only PEC hydrogen production. In this table, ammonia reactor is not taken into account, since it is already included in the ammonia production step. In the second step, electrochemical ammonia synthesis process is simulated as shown in Fig 4.26.

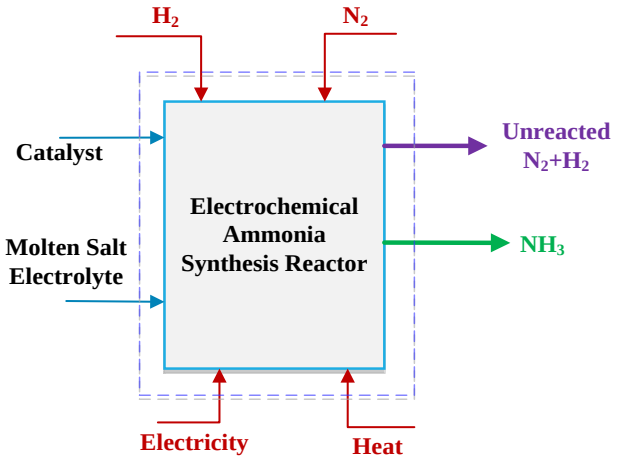

Fig. 4.26 The boundaries of the conducted LCA for electrochemical ammonia synthesis process.

The ammonia production reactor consists of the following materials listed in Table 4.23. The quantities are entered in the LCA software.

Table 4.22 The materials and quantities used in the integrated system for concentrated light PEC hydrogen production.

Material	Value	Unit
Plastic pipes for gases	300	g
Photovoltaic cell, multi-Si	625	cm^2
Fresnel lens (Polycarbonate)	1	kg
Dielectric mirrors (6 in total) (Borosilicate glass)	0.5	kg
PEC hydrogen production reactor	1	item
Support structure (wood)	50000	cm^3
Support mechanism (Aluminum alloy)	2	kg

Table 4.23 The quantities of the materials used in the ammonia reactor.

Material	Value	Unit
Nickel Wiring	2	m
Nickel Electrodes	200	cm^2
Reactor casing Alumina Crucible (Al_2O_3)	500	mL
Reactor Lids (Stainless steel 316 Alloy)	2	kg
Washers	0.125	kg
Bolt Nuts	0.125	kg
Reactor tubes (Ceramic Round Single Bore Tubes Alumina 99.8%)	50	g
Piping (plastic)	2	m

Nitrogen production is the same method employed in the previous methods which is cryogenic air separation. The heat, electricity and material inputs required for the life cycle assessment are derived from the experimental results. The main energy and material requirements of this electrochemical ammonia synthesis which uses PEC hydrogen are summarized in Table 4.24. Here, the amounts of catalysts and electrolyte are calculated based on service time since they are not in fact consumed in the reaction. Furthermore, the heat is not taken as input in the LCA analysis since it is assumed that the synthesis reaction occurs at constant set temperature.

Table 4.24 Main energy and material flows in electrochemical ammonia synthesis using PEC hydrogen.

Parameter	Value	Unit
Ammonia (product)	1.875	mg
Hydrogen from PEC integrated system	0.331	mg
Nitrogen, gas, at plant, US Grid	1.543	mg
Iron oxide, catalyst	2.7778×10^{-9}	g
Sodium hydroxide (electrolyte)	2.7778×10^{-9}	g
Potassium hydroxide (electrolyte)	2.7778×10^{-9}	g
Electricity production from PV	105	J

4.13.6 Life cycle assessment uncertainty analyses

All data in life cycle models have some uncertainty because of three main issues: (i) the spectrum of data, (ii) representativeness of the model and (iii) incompleteness of the model. Since the reliability of data is critical in the LCA studies, various uncertainty analyses are performed using the SimaPro LCA software. The uncertainty of the inventory data are mostly given in the software library.

In the absence of an uncertainty analysis in LCA, the assessment results is questionable and non-satisfactory for interpretation phase. In fact, an uncertainty evaluation combined with the sensitivity analysis leads to a transparent growth in confidence in the LCA findings. Therefore, in order to capture the characteristic variability of data in the process or production systems, Monte Carlo analysis can be used embedded in SimaPro software.

In this regard, the Monte Carlo uncertainty analyses are implemented for particular ammonia production techniques with respect to CML 2001 method. In Monte Carlo analysis for the take-back system, the absolute uncertainty can be calculated. In this method, the computer receives a random variable for each value within the uncertainty collection stated and recalculates the outcomes. The result is kept and the calculation is repetitive by taking diverse examples within the uncertainty range, and also this result is kept. After repeating the method for example 1000 times, 1000 different solutions are acquired and the solutions for an uncertainty distribution. Mean is the average score of all results. It is one of the beneficial factor to use when the best guess value is anticipated to be stated. Median value is the middle value which is beneficial if outliers are considerably manipulating the mean value. Standard error of mean is in fact the stop criterion that is the amount by which the last calculation affected the mean. Coefficient of variation (CV) is the ratio between the standard deviation and the mean and it is a beneficial factor if sorting of data in a table by the relative magnitude of the uncertainty is needed.

CHAPTER 5: RESULTS AND DISCUSSION

In this chapter, the results obtained through system modeling and experimental results are presented and evaluated comparatively. In order to present the results in a more trackable way, the chapter is divided into five main sub-systems as illustrated in Fig. 5.1.

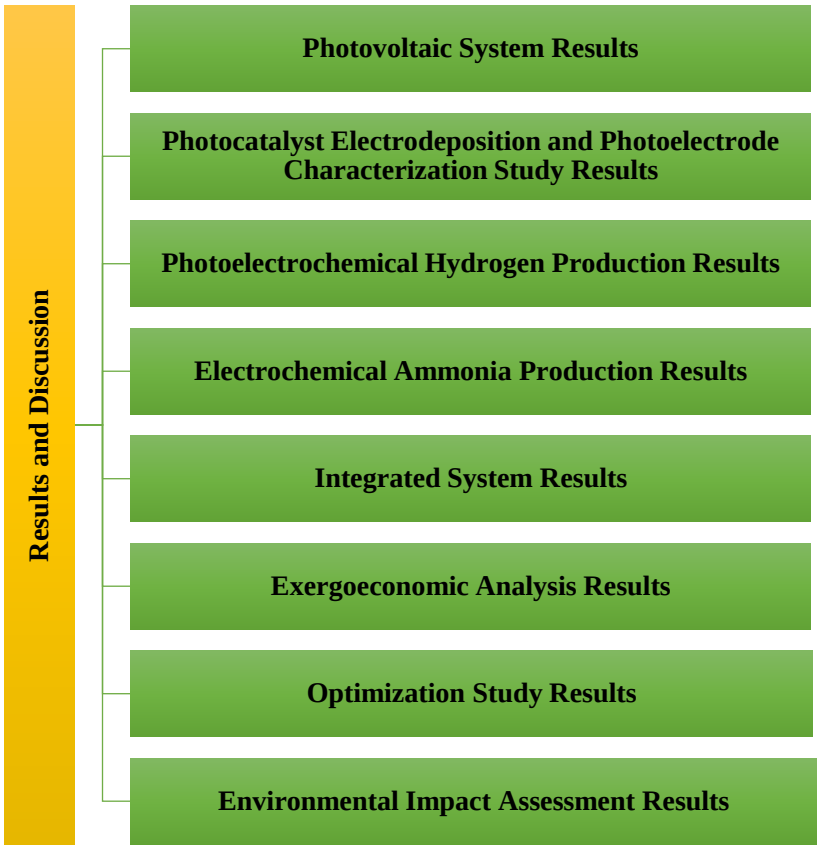

Fig. 5.1 Classification of the results in the thesis.

The results of the exergoeconomic and optimization analyses of the integrated system are also presented in this chapter. Furthermore, the calculated uncertainty results are given under each sub-system individually.

5.1 Photovoltaic System Results

Various parametric studies are conducted for developed the PV model. Wind speed is taken as 4.1 m/s and ambient temperature is taken to be 25°C in the analyses. In Fig. 5.2, the effect of varying ambient temperature on PV cell fill factor and open circuit voltage are illustrated. The ambient temperature affects the cell performance and causes a slight decrease in open circuit voltage of PV cell. Hence, the fill factor (FF) increases from 74.5% to 76.1% when the ambient temperature is varied from 295 K to 305 K as shown in Fig. 5.2.

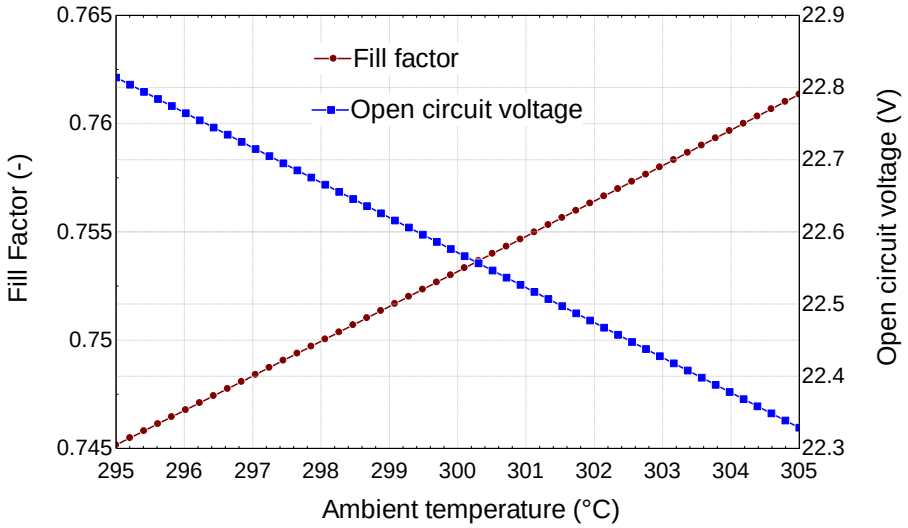

Fig. 5.2 The effects of changing ambient temperature on the open circuit voltage and fill factor of the PV.

Table 5.1 The calculated results at T_o=298 K including the uncertainties.

Parameter	Value	Uncertainty range	Unit
Energy efficiency	10.37	±0.064	%
Exergy efficiency	10.93	±0.0594	%
Exergy destruction rate of cell casing - heat transfer	0.9575	±0.05116	W
Exergy destruction rate of total cell	72.56	±4.853	W
Exergy destruction rate of ideal p-n junction - dissipation	0.047	±0.005924	W
Exergy destruction rate of PV generator - photocurrent generation	65.13	±4.853	W
Exergy destruction rate of series resistance - dissipation	0.003276	±0.00021	W
Exergy destruction rate of shunt resistance - dissipation	5.812	±0.02337	W
Exergy destruction rate of shunt of wafer - light absorption	1.616	±0.0004606	W
Fill factor of PV	76.14	±0.4943	%
Short circuit current of PV	8.078	±0.01	A/m^2
Open circuit voltage of PV	22.33	±0.1416	V
Total heat dissipation from PV	75.27	±4.843	W

The surface temperature of the PV cell is about 349 K when the ambient temperature is 298 K under modeled atmospheric conditions. The energy and exergy efficiencies of the PV cell decreases down to 9% at 350 K as shown in Fig. 5.3. Here, it is important to note that the spectral model (including the day of the year, irradiance, ambient temperature etc.) is built based on a specific day and time of the year in SMARTS software. Therefore, the conditions

such as ambient temperature and irradiance are constant in the model but can be slightly varied since variations are possible to happen. Hence, the range of the parametric studies are taken very close to the real scenario in the specific day. The main results obtained from the developed PV model at ambient temperature of 298 K are tabulated in Table 5.1.

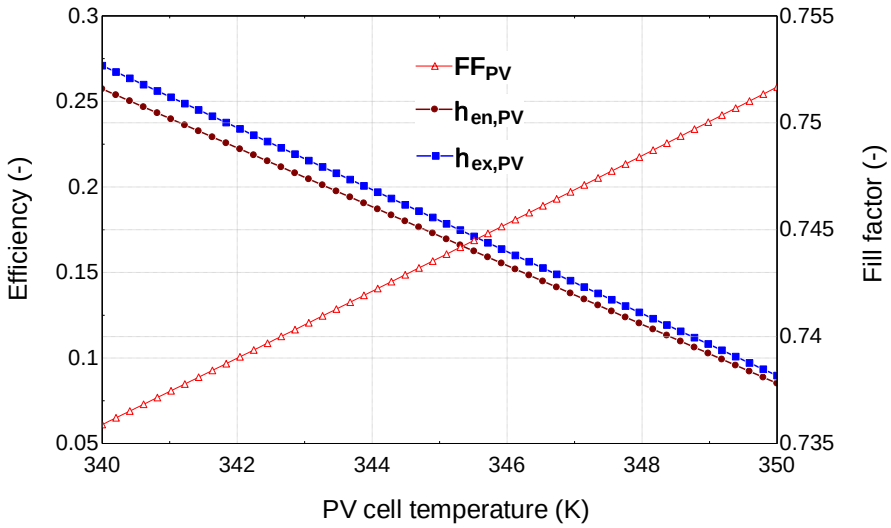

Fig. 5.3 The effects of PV cell temperature on the efficiencies and fill factor.

An increase in the PV cell temperature has negative effect on the PV cell efficiency as shown in Fig. 5.3. Although the efficiency at 349 K (which is the calculated PV cell temperature based on the ambient temperature and wind speed) is about 10%, it is about 20% at 344 K in case the temperature can be lowered.

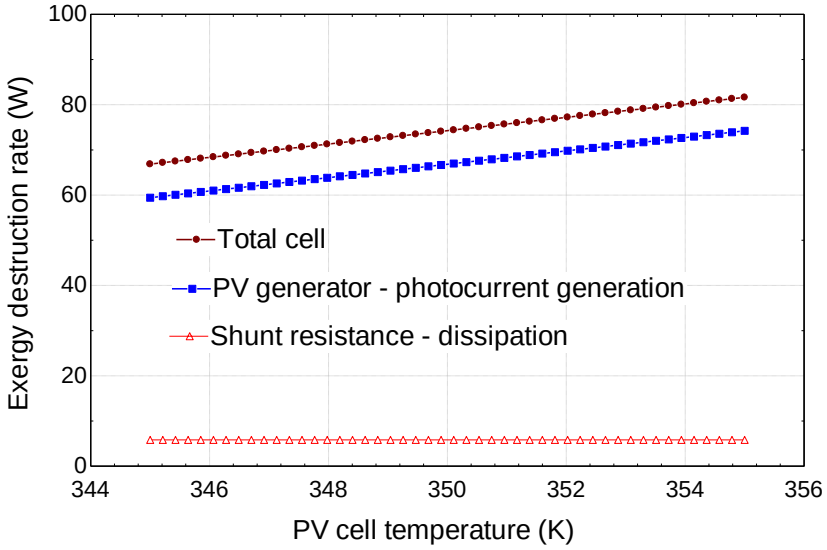

Fig. 5.4 The changes of exergy destruction rates in the PV cell by rising PV cell temperature.

The exergy destruction rate of photo current generation process increases from 60 W to about 78 W when the PV cell surface temperature increases from 345 K to 355 K. The

overall exergy destruction in the cell also upsurges to 82 W at 355 K as illustrated in Fig. 5.4. The shunt resistance is not affected since it is mainly related with the current passing over the resistance.

Moreover, the main results calculated for the PV cell temperature of 350 K are listed in Table 5.2. Here, the efficiencies are slightly lower as the exergy destruction rates increase. The average irradiation on the PV cell under concentrated and split spectrum may vary between ambient irradiance and 10,000 W/m^2 depending on the concentration ratio in the Fresnel lens.

Table 5.2 The calculated results at T_{PV}=350 K including the uncertainties.

Parameter	Value	Uncertainty range	Unit
Energy efficiency	8.518	±0.05639	%
Exergy efficiency	8.969	±0.05938	%
Exergy destruction of cell casing - heat transfer	1.007	±0.05116	W
Exergy destruction of total cell	74.25	±4.853	W
Exergy destruction of ideal p-n junction - dissipation	0.04023	±0.005924	W
Exergy destruction of PV generator - photocurrent generation	66.82	±4.853	W
Exergy destruction of shunt resistance - dissipation	5.812	±0.02337	W
Exergy destruction of shunt of wafer - light absorption	1.618	±0.0004606	W
Fill factor of PV	75.17	±0.4943	%
Total heat dissipation from PV	76.86	±4.843	W
Ambient temperature	298	±1.49	K
PV temperature	350	±2.918	K
Load voltage	18.7	±0.03762	V
Open circuit voltage of PV	22.62	±0.1416	V

When the total concentrated irradiance on the PV cell surface increases from 900 W/m^2 to 5000 W/m^2, the energy and exergy efficiencies enhance to about 11.8% and 11.9%, respectively although the total exergy destruction rate within the PV cell increases up to 175 W as shown in Fig. 5.5. After a certain point of irradiance, the efficiency does not increase proportionally because of the limitation in photocurrent generation. At concentrated light of 5000 W/m^2, the energy and exergy efficiencies including the exergy destruction rate are presented in Table 5.3.

Table 5.3 The calculated results at I_r=5000 W/m^2 including the uncertainties.

Parameter	Value	Uncertainty range	Unit
Energy efficiency	11.52	±0.04188	%
Exergy efficiency	11.77	±0.03011	%
Exergy destruction of total cell	176.4	±8.951	W

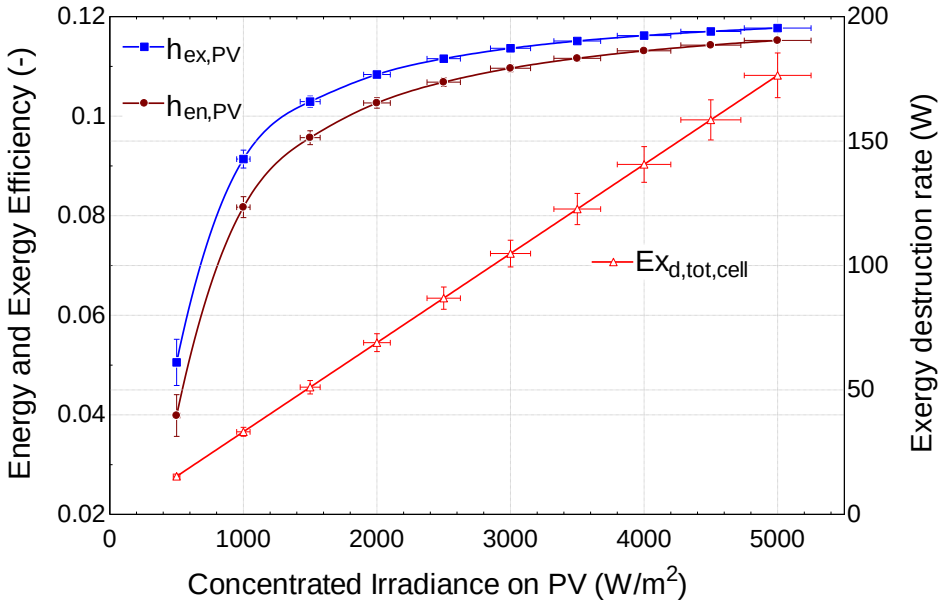

Fig. 5.5 The effects of concentrated light on the PV cell performance and total exergy destruction rate.

PV cells have silicon wafer materials which absorb the light. The reflection and transmission characteristics of silicon wafer are shown in Fig. 5.6 for the entire wavelength received by PV from 280 nm to 1200 nm (because of the dielectric mirror transmission range). The UV portion of the spectrum is partially absorbed and reflected although this section has higher energy.

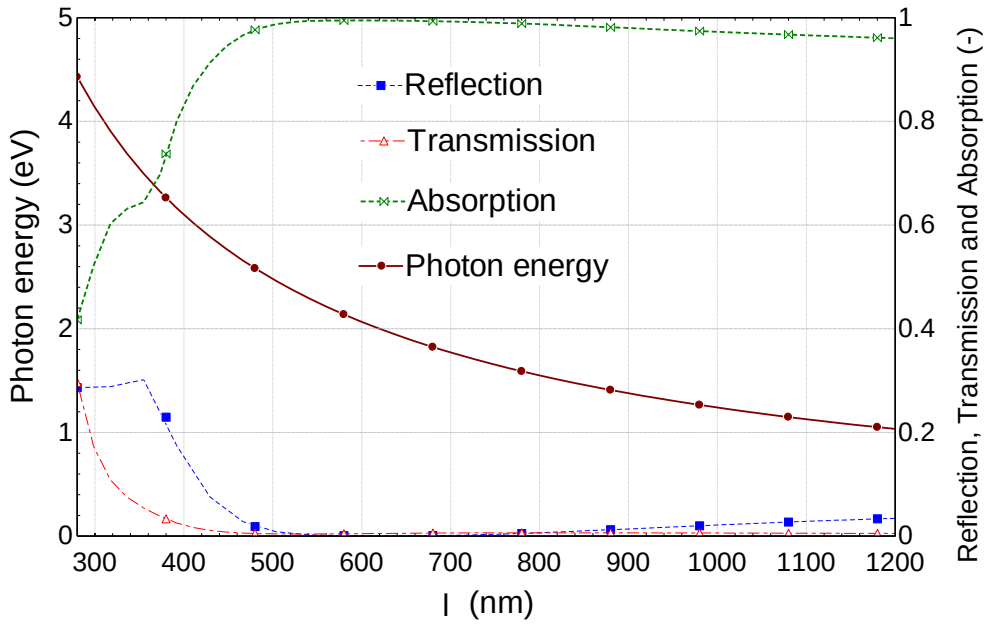

Fig. 5.6 The transmission, reflection and absorption values of the PV cell wafer including the energy of photon at each wavelength.

The average absorption value of the wafer is about 93% where this part contributes to power generation meaning that the remaining is lost either as heat dissipation or reflected light. Under concentrated light conditions shown in Fig. 5.7, the maximum absorbed irradiance value is seen at about 500 nm with a value of about 7.6 W/m^2/nm. Between 400 nm and 500 nm, a portion of the solar light corresponding to a maximum of about 0.4 W/m^2/nm is reflected and a lower portion of solar light is transmitted with a maximum value of 0.05126 W/m^2/nm. After 2600 nm, the solar irradiance is quite low.

In the light absorption process of PV cell, the wafer is the critical part which absorbs the light. There are also some reflection and transmission losses which do not contribute to photocurrent generation process. In Table 5.4, the energy, entropy and exergy values on the PV cell and in the wafer are comparatively shown. At this light intensity, the exergy rate on the PV cell surface is about 81.6 W whereas transmitted and reflected exergy rates are about 0.5 W and 1.12 W, respectively. The remaining part corresponding to about 80 W is absorbed by the wafer contributing to photocurrent generation.

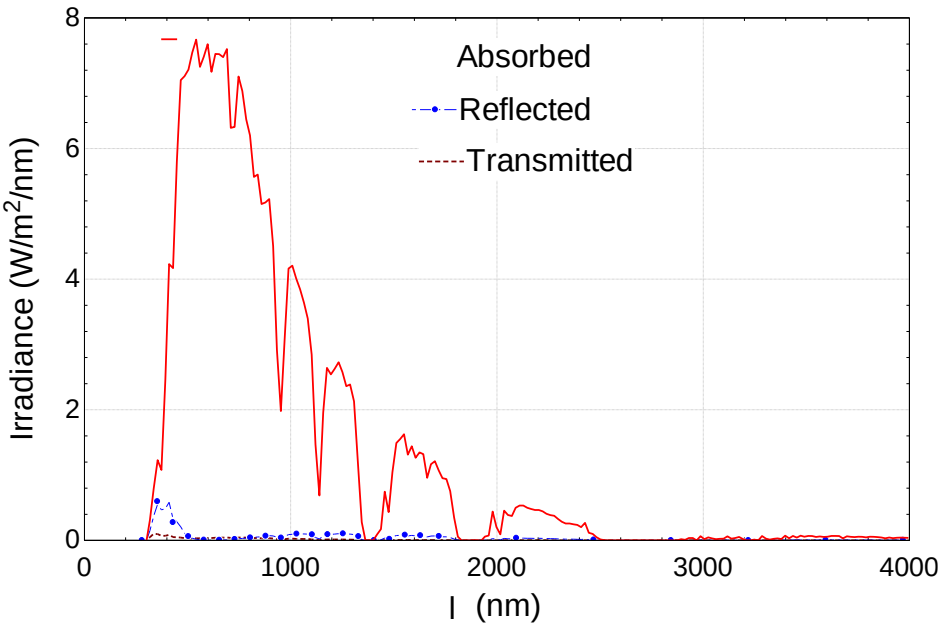

Fig. 5.7 The transmitted, reflected and absorbed portions of the full solar spectrum by the PV wafer under concentrated light.

Table 5.4 Energy, entropy, exergy rates on PV surface and wafer of PV.

	E (W)	**I (W/m^2)**	**Ex (W)**	**S (kW/K)**	**T (K)**
PV Surface	85.89	2102	81.57	0.01448	5931
Wafer Transmitted	0.5176	12.67	0.4918	8.67E-05	5972
Wafer Reflected	1.192	29.19	1.126	0.000222	5360
Wafer Absorbed	84.18	2061	79.95	0.01417	5940

The sub-processes inside the PV cell bear some irreversibilities as comparatively shown in Fig 5.8. The total exergy destruction rates for all processes are shown in Fig. 5.8. The

highest exergy destruction occurs in the PV generator with a corresponding value of 65.23 W whereas the total exergy destruction in the PV cell is about 72 W. It is followed by the exergy destruction in shunt resistance – dissipation process (5.821 W). Ideal p-n junction, serial resistance and casing heat transfer processes have minor exergy destruction rates compared to other processes.

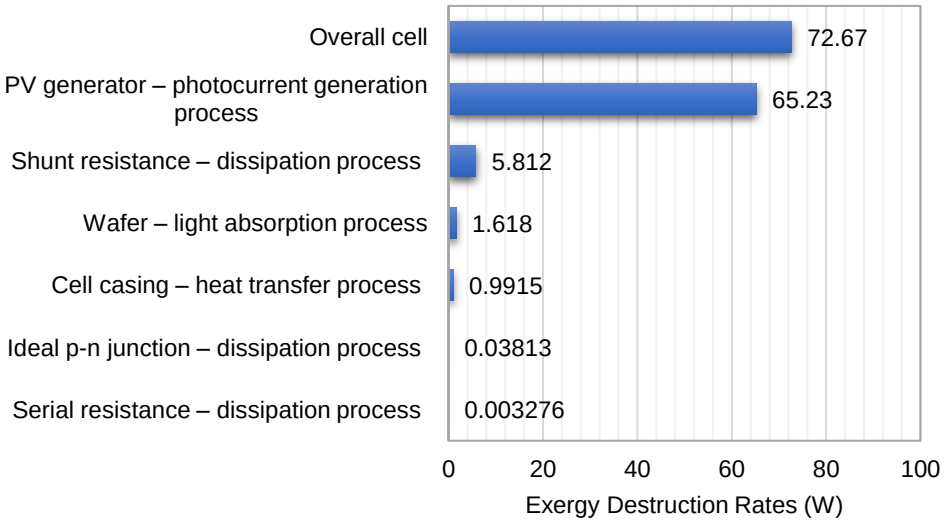

Fig. 5.8 Exergy destruction rates of various processes inside the PV module.

The generation of heat internally plays an important role in PV cell performance as comparatively illustrated in Fig. 5.9. The cell casing heat dissipation process is the major contributor corresponding to 75 W whereas the other processes are lower than 6 W. The second highest heat dissipation occurs in PV generator where it corresponds to 5.8 W. The PV generator heat dissipation rate is calculated to be 1.24 W.

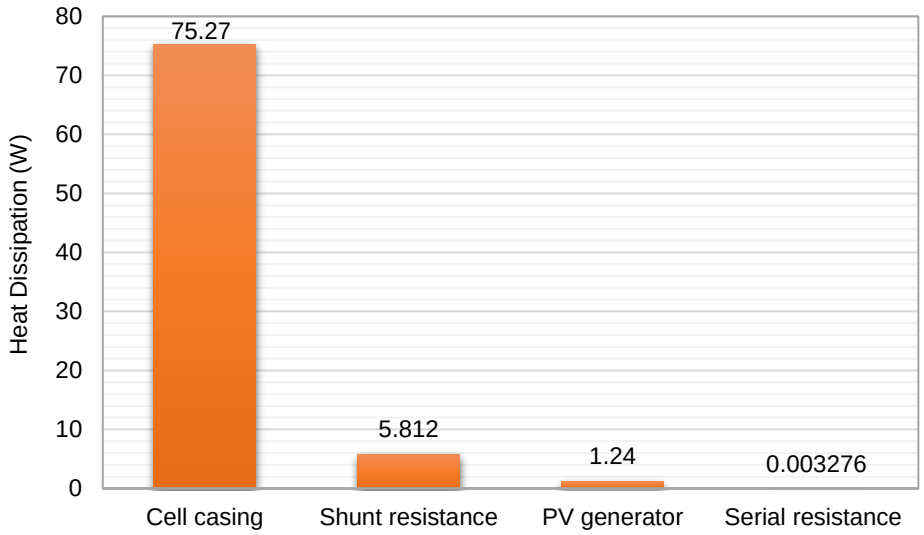

Fig. 5.9 Heat transfer rates for the internal and external processes inside the PV cell.

Little shunt resistance reasons power losses in the PV cells by providing an alternative current way for the light created current. Such an alteration reductions the amount of current passing over the solar cell junction and reduces the potential of the PV cell. The effect of a shunt resistance is mostly serious at low intensity stages. Since there will be less current which is created by light. Additionally, at slight voltages in which the actual resistance of the PV cell is great, the result of a resistance in parallel is greater.

In overall, the energy and exergy efficiencies are calculated based on the given conditions and presented in Fig. 5.10. The energy and exergy efficiencies of the PV cell are calculated to be about 10.4% and 11%, respectively whereas the fill factor is found to be 75%. Carnot efficiencies in the light absorption processes are also illustrated in Fig. 5.10. They are calculated based on the previously given temperature levels of each state point.

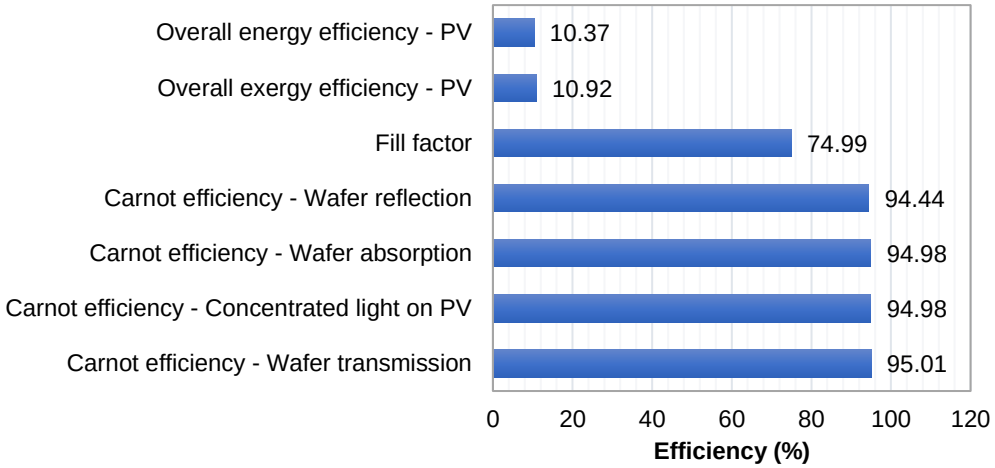

Fig. 5.10 Overall energy and exergy efficiency and fill factor values of the PV cell.

The first PV cell experiments are performed outside of the Clean Energy Research Laboratory (CERL) solarium at the University of Ontario Institute of Technology (UOIT). The conditions are mostly clear sky with winds speed up to 9.0 km/h. The ambient temperatures are measured using a Vernier temperature probe mounted under the base workstation and the module temperature was measured by attaching the surface temperature sensor to the back of the PV cells. Both temperature datasets are recorded using a Vernier LabQuest Mini Data Logger and Logger Pro 3.8.4 software. The set of voltage and current measurements are obtained by the usage of two digital multimeters. The Ohmite rheostat is varied from 0 Ω to 5 kΩ with readings taken at appropriate intervals.

PV cells are evaluated based on some data, such as the short-circuit current (I_{sc}), the open-circuit voltage (V_{oc}), maximum power and the solar-to-electrical efficiency, all which could be determined experimentally or foreseen in modelling from some parameters to plot the I-V curve. In order to acquire the irradiance for concentrated solar beams, a single layer diming filter is used to cover the pyranometer, which protected it from receiving excess of heat and saturate. Nonetheless, since the irradiance measurement in this case is not the real one, it is necessary to quantify the coefficient factor (CF), which is determined and confirmed by multiple experimental tests with and without the filter, to obtain the true irradiance.

In order to fulfill these procedures and to endure the global irradiance, two different PV cells are tested. Due to the difference between the surface areas, the PV modules are named as small PV and large PV.

The results are explained separately here for concentrated and non-concentrated light. The atmospheric conditions used for obtaining the specified spectrum are listed in Table 5.5.

Table 5.5 Atmospheric conditions at the time of the experiment obtained using SMARTS software.

Pressure (mb)	1013.25
Altitude (km)	0.100
Relative Humidity (%)	45.67
Precipitable Water (cm)	1.3590
Ozone (atm-cm)	0.3438 or 343.8 Dobson Units
Aerosols	
Optical depth	at 550 nm = 0.0752 at 500 nm = 0.0840
Angstrom's Beta	0.0375
Schuepp's Beta	0.0365
Visual Range (km)	128.0
Visibility (km)	98.0
Temperatures	
Ground Level	287.6 K
Sea Level	288.2 K

The solar position and PV cell positions adapted in the experiments are as follows:

- Zenith angle (apparent): 60.514°
- Azimuth angle (from North): 225.00°.

The obtained irradiance values are as follows:

- Direct beam: 818.28 W/m^2.
- Sky diffuse irradiance: 62.44 W/m^2.
- Ground reflected irradiance: 55.86 W/m^2.
- Global irradiance (sum of the all): 936.59 W/m^2.

In this section, the experimental results are given as well as the model results. The model simulate the same atmospheric conditions (irradiance, temperature etc.) as the experiments.

5.1.1 Small PV under non-concentrated light

For non-concentrated light, the backward surface temperature is measured at maximum 30°C while the average ambient irradiance is 595 W/m^2. In this case, the irradiance is low because of shadowing at the time of the experiments, but it is quite constant which supports the confidence level of the measurements.

As shown in Fig. 5.11, the maximum power and current as well as the short-circuit current of the model match the ones obtained experimentally. Furthermore, Table 5.6 tabulates the experimental and model efficiency results in which they are about 14%.

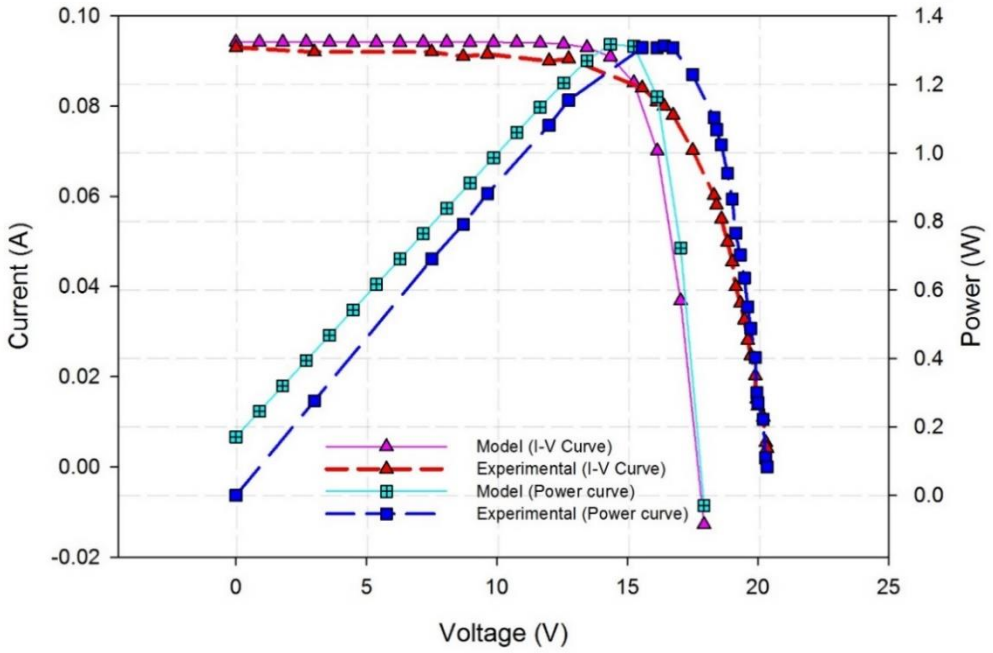

Fig. 5.11 Model and experiment comparison of voltage-current and voltage-power curves of small PV at ambient measurements without concentration and spectrum splitting.

However, the maximum voltage values are a little different than the values predicted by the model. There are two possible causes for this divergence: one of the assumptions is not accurate in the iterative process to calculate vector voltage or the dark saturation current used in the model has small variation. This variation affects the open-circuit voltage more according to the Shockley equations for electrical current and tension.

Table 5.6 Model and experimental results for small PV at ambient conditions without concentration and spectrum splitting.

Model		
V_{max} (V)	**I_{max} (A)**	**P_{max} (W)**
14.70	0.08	1.31
V_{oc} (V)	**I_{ph} (A)**	**Efficiency (%)**
17.93	0.09	14.71
Experiment		
V_{max} (V)	**I_{max} (A)**	**P_{max} (W)**
16.40	0.08	1.31
V_{oc} (V)	**I_{ph} (A)**	**Efficiency (%)**
20.35	0.09	14.70

5.1.2 Small PV under concentrated light

The ambient temperature is measured to be 23.38°C. At the beginning of the measurement, the backward surface temperature of the PV is measured as 54°C whereas it reaches a maximum

value of 68°C for concentrated light in which the measured average ambient irradiance is 850 W/m^2.

In Fig. 5.12, it is visualized that the maximum power and maximum current obtained experimentally match the ones predicted by the model. Moreover, the efficiencies are quite similar because the physical quantities are almost the same.

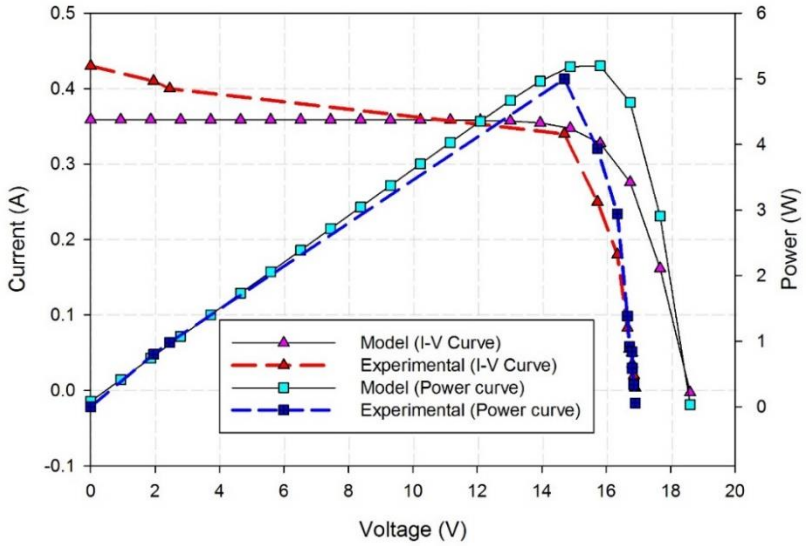

Fig. 5.12 Model and experiment comparison of voltage-current and voltage-power curves of small PV under concentrated light with spectrum splitting.

Nevertheless, the experimental I-V curve deviates in the low voltages because of possibly an instability such as a defect in the load, a non-noticed shade on the solar panel or a small cloud which covered the sun for sufficient time to diverge the results, interfered when the experiment is taken. The values for the important physical quantities can be found in Table 5.7. The efficiency is found to be 15.37% with a maximum power output of about 5 W.

Table 5.7 Model and experimental results for small PV under concentrated light with spectrum splitting.

Model		
V_{max} (V)	**I_{max} (A)**	**P_{max} (W)**
15.44	0.33	5.22
V_{oc} (V)	**I_{ph} (A)**	**Efficiency (%)**
18.60	0.35	15.35
Experiment		
V_{max} (V)	**I_{max} (A)**	**P_{max} (W)**
14.70	0.34	4.99
V_{oc} (V)	**I_{ph} (A)**	**Efficiency (%)**
16.90	0.43	15.37

5.1.3 Large PV module under concentrated and non-concentrated light

A larger area PV module is used in these experiments. In this section, the related results are presented for concentrated and non-concentrated light conditions. As seen in Fig. 5.13, it can be visualized how the irradiance changes outside and inside different positions of the structure composed by the Fresnel lenses, the dielectric mirror and the photovoltaic module. Through the measures at the mirror level, it is possible to confirm that dimming filter's fill factor is 5.6, i.e., the measured irradiance is reduced by the filter 5.6 times. This filtering process is necessary not to damage the pyranometer when the measurements are taken in the PV level in addition to the measurement limitation of pyranometer (about 2300 W/m2). Because of the explained procedure, a value close to 2100 W/m^2 is measured, which means a real irradiance about 11,760 W/m^2, that is more than twelve times the ambient irradiance, in other words, the sun rays are concentrated more than twelve times by the constructed structure. In addition, the average large PV cell's back surface temperature and the average ambient irradiance are, respectively, about 122°C and 912 W/m^2 for concentrated light measurements with spectrum splitting as shown in Fig. 5.14.

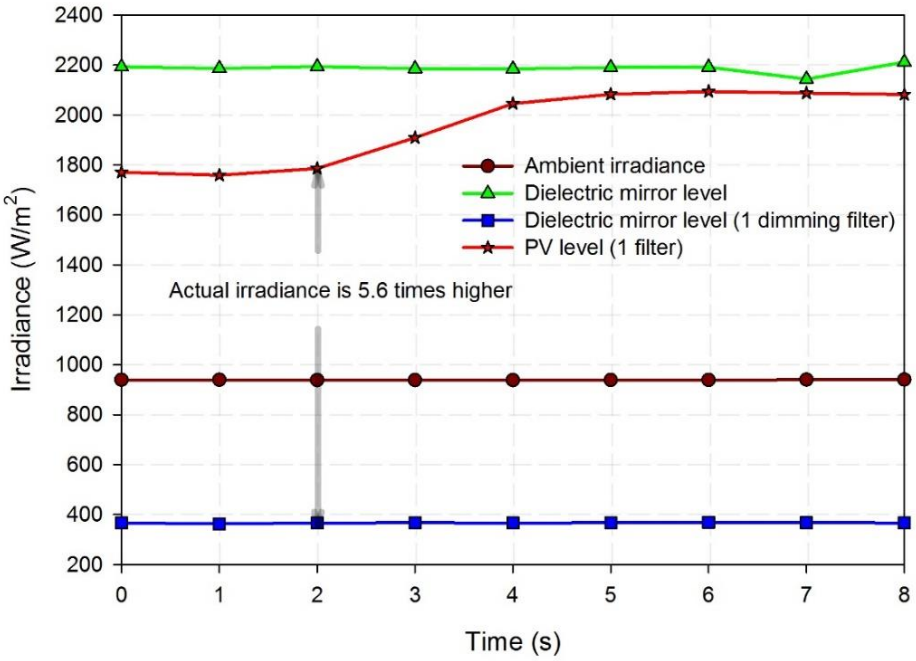

Fig. 5.13 Irradiance values at dielectric mirror level, PV module level and ambient during large PV concentrated light measurements with spectrum splitting.

The temperature levels of the PV cell play an important role on the total performance. Hence, temperature measurements on the back surface of the PV are performed. From Fig. 5.15, it can be visualized that the maximum power and the short-circuit current of the model match the ones obtained experimentally. Furthermore, since the first physical quantities are quite similar, the calculated efficiency values are very close.

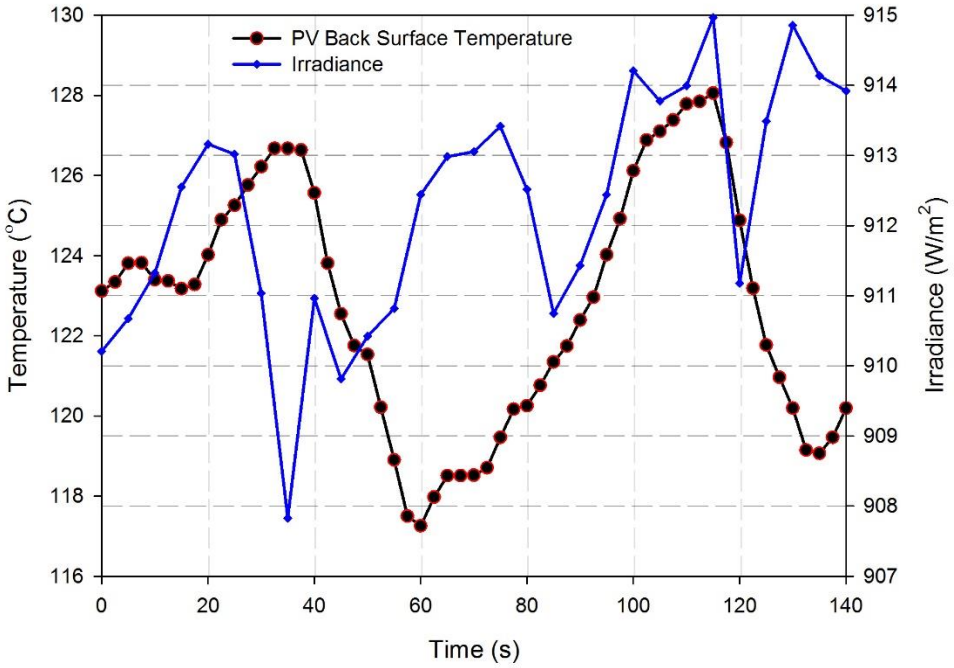

Fig. 5.14 Temperature and ambient irradiance values during large PV module under concentrated light measurements with spectrum splitting.

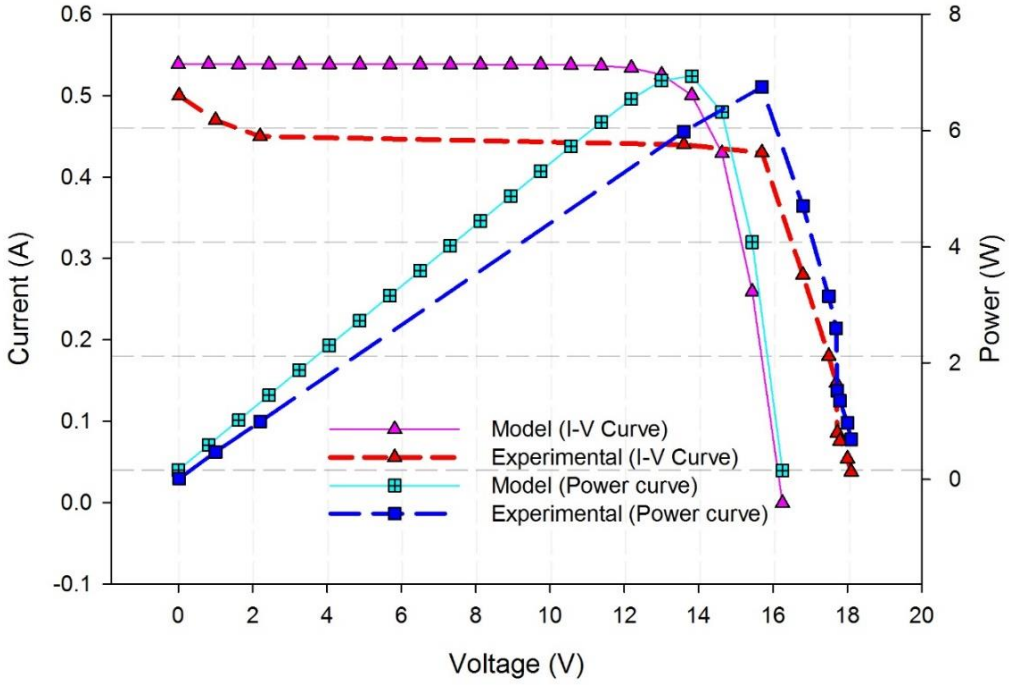

Fig. 5.15 Model and experiment comparison of voltage-current and voltage-power curves of large PV module under concentrated light with spectrum splitting.

Moreover, the experimental I-V curve presents lower values of current for most of the voltages than the model. This includes the maximum current, which deviates 15% from the model, same deviation of the maximum electrical tension. The detailed data related to Fig. 15 are tabulated in Table 5.8.

Furthermore, the comparison of voltage-power and voltage-current curves between the concentrated light with solar spectrum splitting and non-concentrated light without solar light splitting is illustrated in Fig. 5.16 and Table 5.9.

Table 5.8 Experimental results for large PV under concentrated light with spectrum splitting and non-concentrated light without spectrum splitting.

	V_{max} (V)	I_{max} (A)	P_{max} (W)	V_{oc} (V)	I_{ph} (A)	Efficiency (%)
Concentrated light	15.70	0.43	6.75	18.10	0.50	13.22
Non-concentrated light	17.50	0.20	3.50	20.30	0.30	6.68

Table 5.9 Model and experimental results for large PV under concentrated light with spectrum splitting.

Model		
V_{max} (V)	I_{max} (A)	P_{max} (W)
13.65	0.50	6.93
V_{oc} (V)	I_{ph} (A)	Efficiency (%)
16.25	0.53	13.59
Experiment		
V_{max} (V)	I_{max} (A)	P_{max} (W)
15.70	0.43	6.75
V_{oc} (V)	I_{ph} (A)	Efficiency (%)
18.10	0.50	13.22

The concentrated light increases the irradiance over the panel and the temperature around it. Thus, more power is generated in a lower voltage as shown in Fig. 5.16. However, the open-circuit voltage decreases, because the increase in the irradiance is not strong enough to compensate the higher temperature in the concentration of light case compared to the without concentration one. Yet, despite of the rise of the irradiance in twelve times, the current did not rise proportionally to it as expected by the model whereas it increases about 1.67 times in the experiment. This disproportionality occurs because of the irregular distribution of rays over the panel in the way the center received more light than the borders and shading in the lower region of the module. Similar problems and similar arguments were presented in the literature [114] in addition to the slight opacity of the silicon cells used in the tests.

At last, for the values recorded in the non-concentrated light measurements, it is noted that the average large PV cell back surface temperature is 66°C. Further data about this experiment are shown in Fig. 5.17 and Table 5.10.

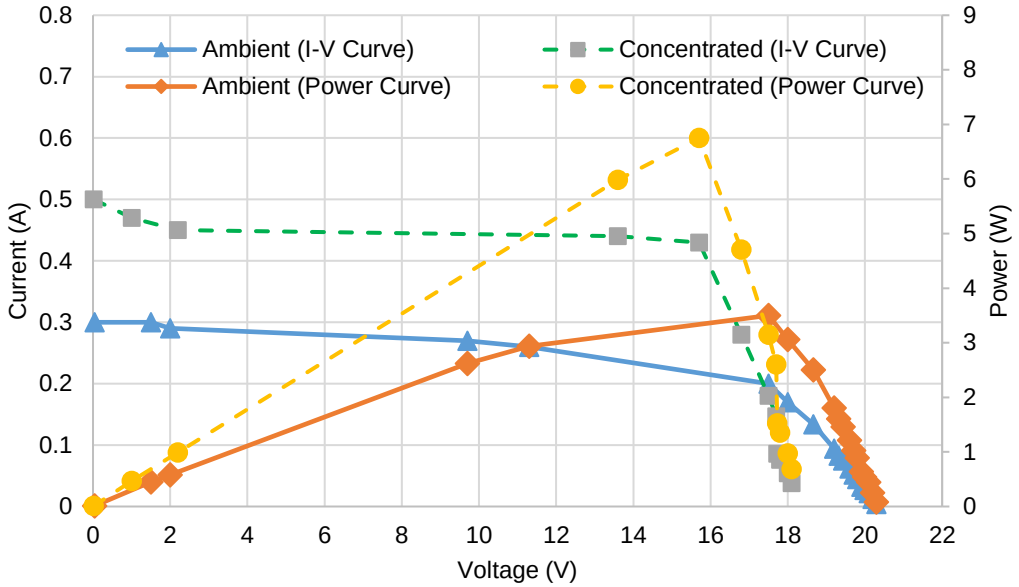

Fig. 5.16 Experimental voltage-current and voltage-power curves for large PV under concentrated light with spectrum splitting and non-concentrated light without spectrum splitting.

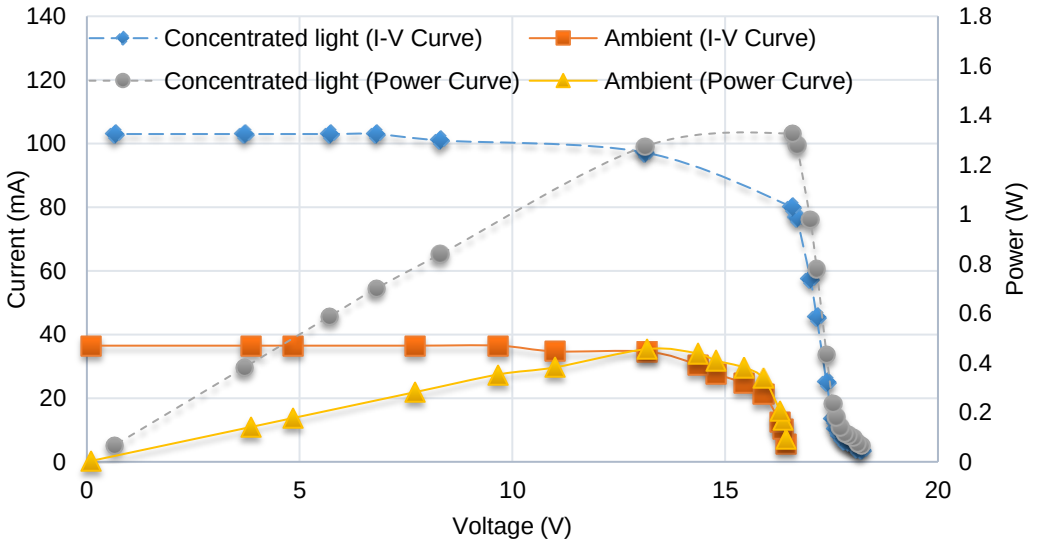

Fig. 5.17 Experimental voltage-current and voltage-power curves at lower irradiance values for large PV under concentrated light spectrum splitting and non-concentrated light without spectrum splitting.

Table 5.10 Irradiance values for the experiments at lower irradiances under concentrated light and non-concentrated light.

Concentrated light		**Non-concentrated light**
Filtered Irradiance (W/m^2)	**Actual Irradiance (W/m^2)**	**Actual Irradiance (W/m^2)**
1870	10,472	515

5.1.4 Photovoltaic cell under solar simulator light

The performance of the small PV cell is also evaluated under artificial light using the solar simulator under different optic filters. In order to quantify the solar spectrum of solar simulator,

lowermost solar irradiation in solar simulator and lowermost integration time in spectrometer are selected since spectrometer system is made to measure typically lower intensity lights and saturates at high intensities. Moreover, a 400 µm core diameter UV-VIS type fiber cable is employed to decline the concentration of incoming light. Fig. 5.18 displays the spectrum of solar simulator light coming to PV cell.

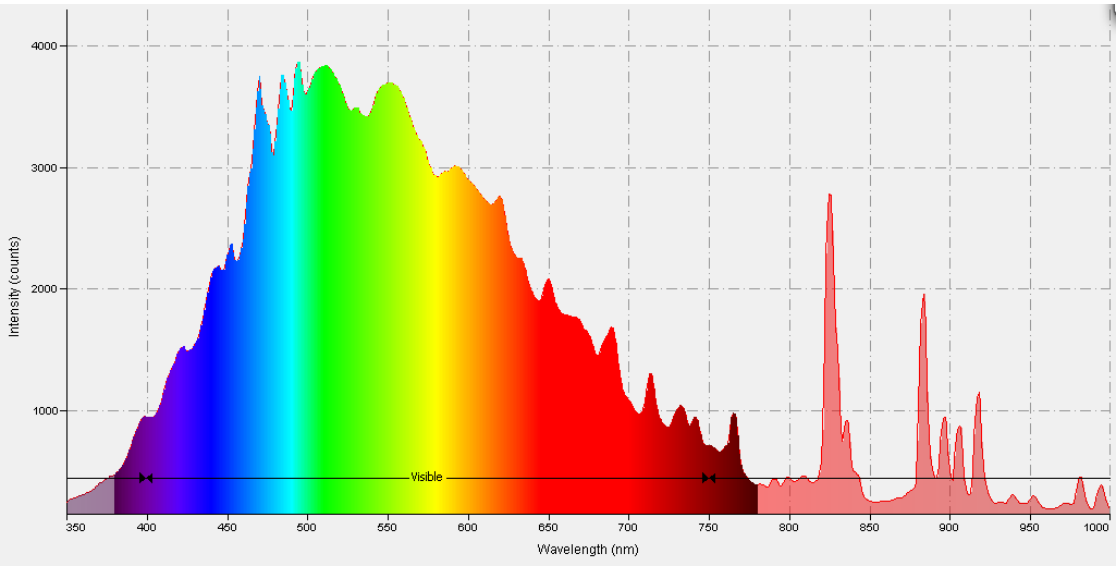

Fig. 5.18 The spectrum measured by spectrometer under artificial light with lowest integration time.

After obtaining the artificial light spectrum, the consequence of numerous kind of optic filters is examined on solar spectra scattering. In the measurements, the filters are located just before the fiber cable of spectrometer for purpose of getting solar spectra.

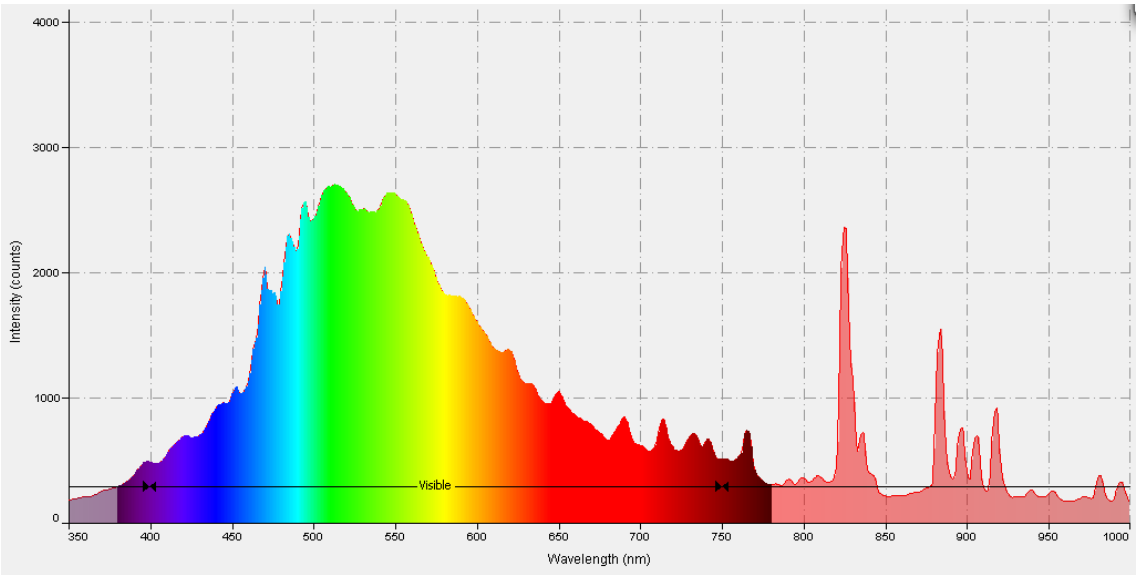

Fig. 5.19 The spectrum measured by spectrometer under artificial light with green color filter.

In Fig. 5.19, it is evident that with a green filter, the number of photons between 500 nm – 550 nm are more than any other wavelength range. After attaining solar simulator spectrum, the outcome of altered type of filters is examined on solar spectra distribution.

Fig. 5.20 displays the spectrum of solar simulator after red color filter in which primarily red color wavelengths are conveyed. As revealed in Fig. 5.21, if a dimming (intensity) filter with greater UV absorbance is employed, overall concentration drops, and wavelengths below 400 nm are absorbed by the filter.

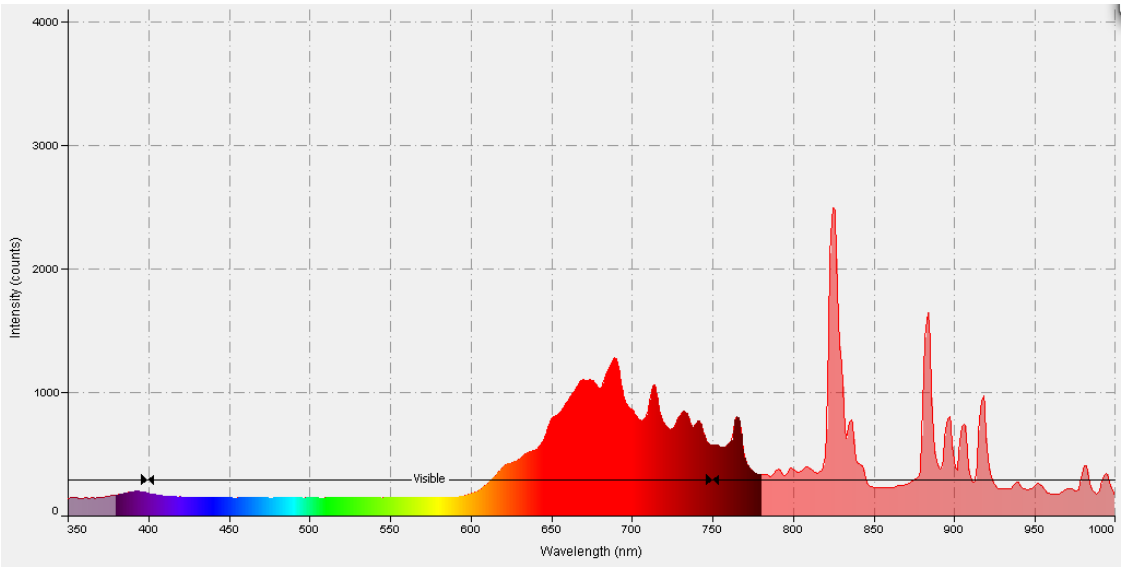

Fig. 5.20 The spectrum measured by spectrometer under artificial light with red color filter.

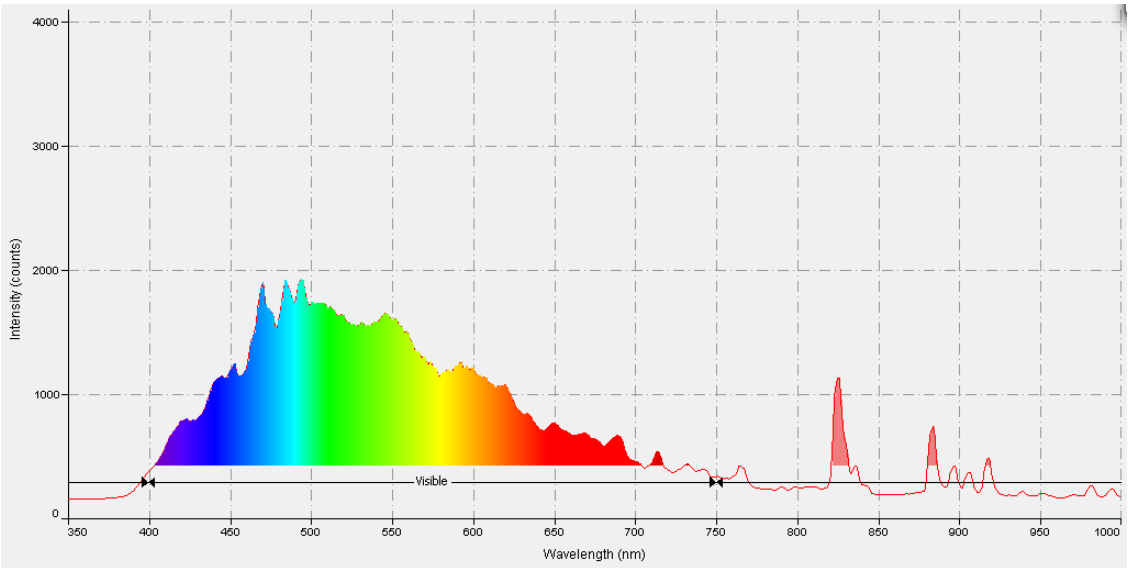

Fig. 5.21 The spectrum measured by spectrometer under artificial light with intensity dimming filter having high UV absorbance.

Fig. 5.22 designates the spectra scattering when blue color filter is used. Here, the blue portion of the light in typically conveyed counting the green portion.

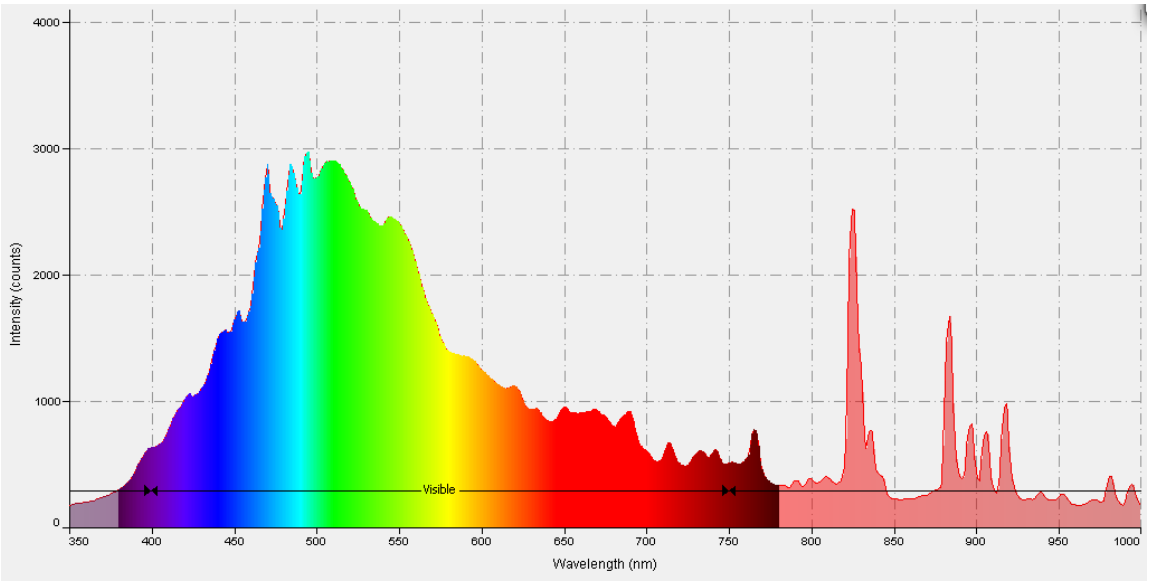

Fig. 5.22 The spectrum measured by spectrometer under artificial light with blue color filter.

The PV measurements are taken with Gamry Potentiostat device in Linear Sweep Voltammetry mode. This method allows programmed sketch of current-potential curve in that it is very easy to determine maximum power point. As potentiostat device's linear sweep voltammetry mode is restricted to 11 V, the half of the smaller PV whose open circuit potential V_{oc}=9.85 V and short circuit current I_{sc}=0.13 A is used. The area of this PV cell in this case is 75 cm^2 since only half of the module is used. Fig. 5.23 exemplifies the I-V curve of PV cell under artificial light without any filters.

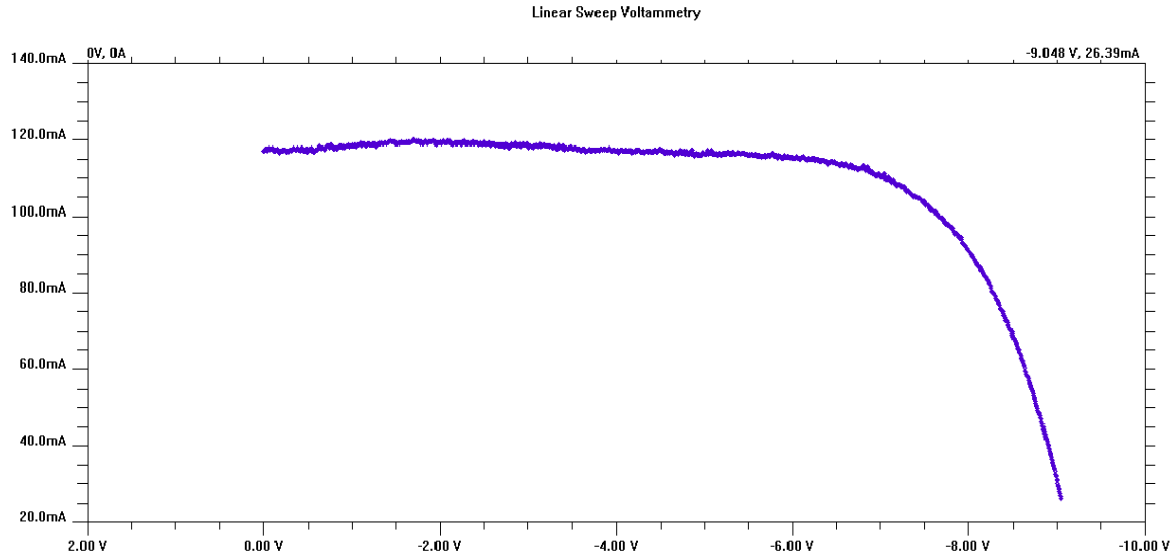

Fig. 5.23 Current-potential curve characterization of PV cell measured by potentiostat under artificial light without any filter.

Fig. 5.24 displays that when dimming filter is utilized, there is a significant reduction in current as concentration of light coming to PV cell from artificial light declines significantly.

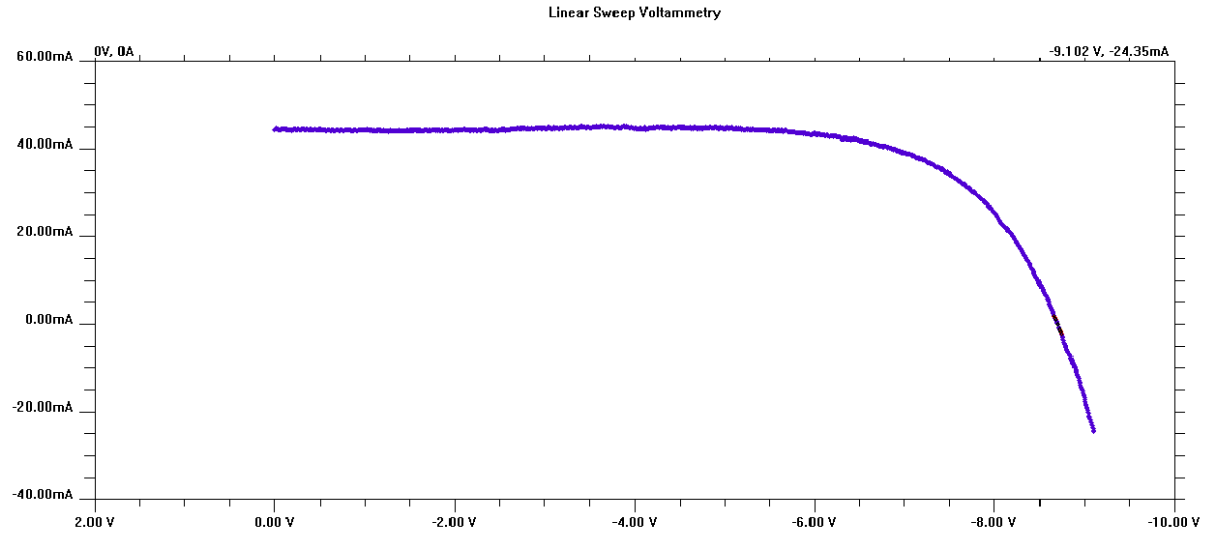

Fig. 5.24 Current-potential curve characterization of PV cell measured by potentiostat under artificial light with intensity dimming filter.

In the green filter spectrum, since we have higher energy light coming to the PV surface compared to the red filter spectrum, current output of PV cell is greater than the red filter current output as comprehended in Fig. 5.25 and Fig. 5.26.

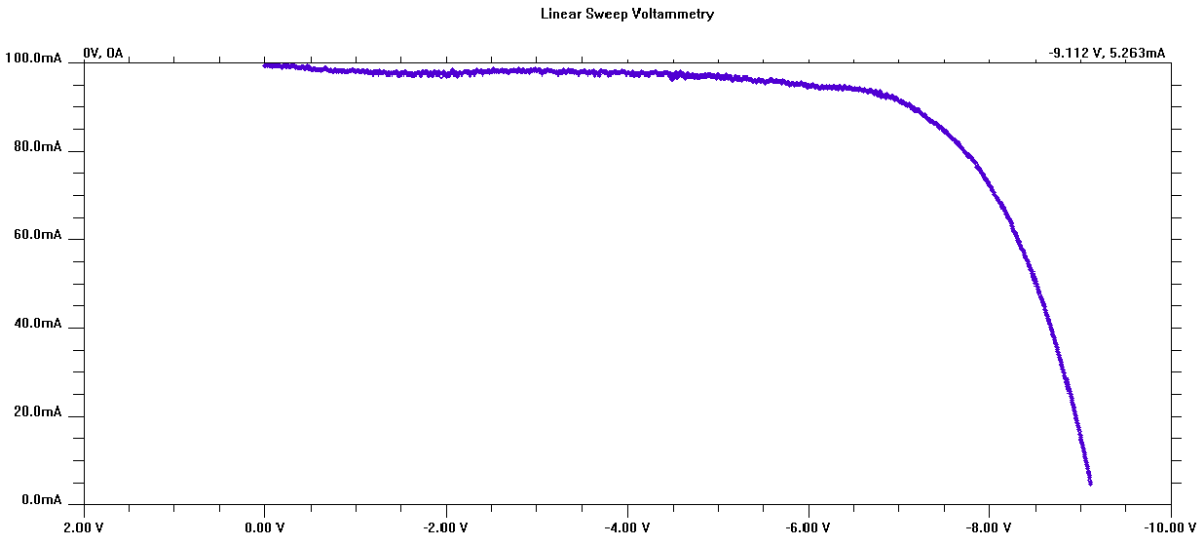

Fig. 5.25 Current-potential curve characterization of PV cell measured by potentiostat under artificial light with green filter.

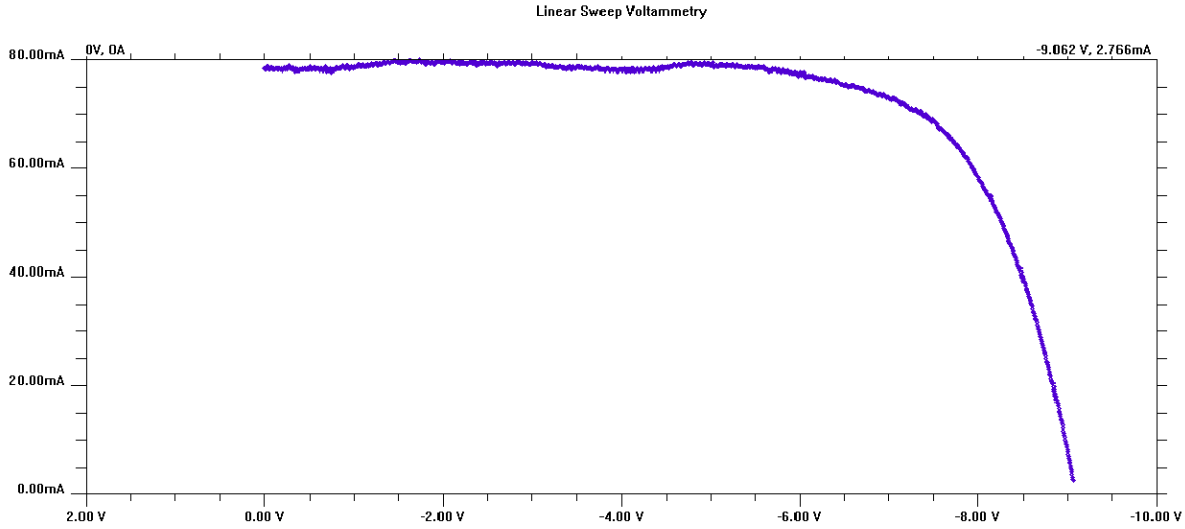

Fig. 5.26 Current-potential curve characterization of PV cell measured by potentiostat under artificial light with red filter.

The current and potential curve of the PV cell is seen in Fig. 5.27 when blue filter is used on the solar simulator aperture. The short circuit current is about 96 mA and open circuit potential is about 9.1 V. A summary of PV cell characterizations including the open circuit potential and short circuit current under different type of filters is shown in Table 5.11.

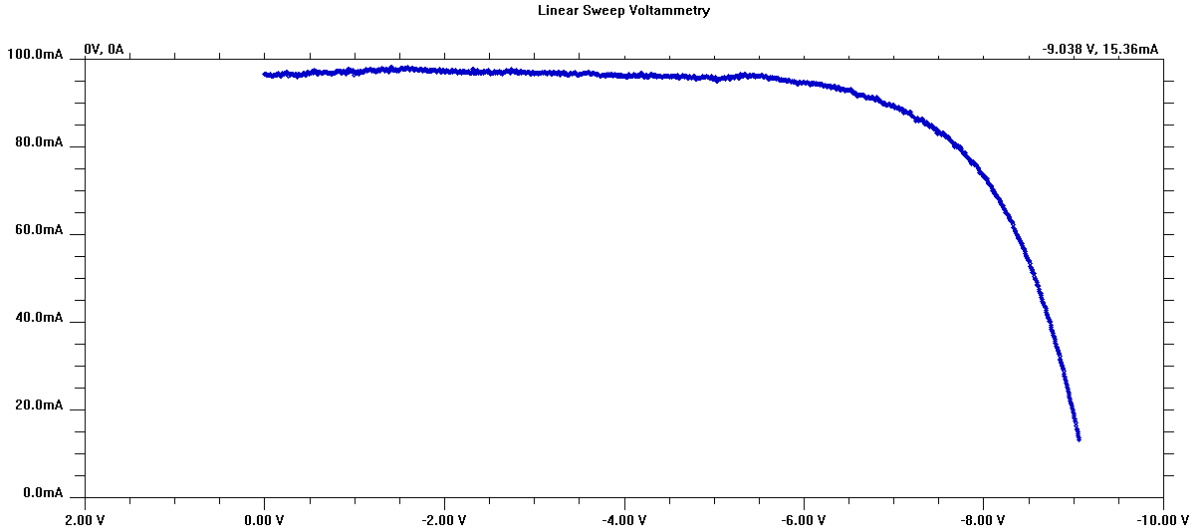

Fig. 5.27 Current-potential curve characterization of the PV cell measured by potentiostat device under artificial light with blue filter.

As designated in Table 5.12, the maximum power output of PV cell is measured in green filter after the one without filter. Then, the PV cell maximum power output under red filter has about 0.53 W. As dimming filter decreases the quantity of light on PV cell and absorbs high energy

spectra, the quantity of power produced by PV cell is lowermost. Using the equations of fill factor, maximum power and efficiencies are computed as stated in Table 5.12.

Table 5.11 Measurement results of PV cell current and potential with different filters.

Parameter	No Filter	Dimming (Intensity) Filter	Green Filter	Red Filter	Blue Filter
$\mathbf{I_{sc}}$ **(A)**	0.12	0.05	0.1	0.08	0.09
$\mathbf{V_{oc}}$ **(V)**	9.0	9.1	9.1	9	9.1
$\mathbf{I_m}$ **(A)**	0.10	0.04	0.09	0.07	0.085
$\mathbf{V_m}$ **(V)**	7.7	7.0	7.5	7.5	7

The energy and exergy efficiencies of PV cell are computed as 10.27% and 10.83% respectively with no filter. The lowermost energy and exergy efficiency are perceived when dimming filter is employed. The maximum current produced by PV cell decreases 60% when an intensity filter is used while exergy efficiency declines about 63%.

Table 5.12 Analysis results of different filters effect on PV cell efficiency.

Parameter	No Filter	Dimming (Intensity) Filter	Green Filter	Red Filter	Blue Filter
$\mathbf{Power_{Max}}$**(W)**	0.77	0.28	0.68	0.53	0.6
$\mathbf{I_{sc} \times V_{sc}}$	1.08	0.41	0.91	0.72	0.82
Fill Factor (%)	71.30	68.40	74.20	72.90	72.60
$\boldsymbol{\eta_{en}}$ **(%)**	10.27	3.73	9.00	7.00	7.93
$\boldsymbol{\eta_{ex}}$ **(%)**	10.83	3.94	9.49	7.38	8.37

5.2 Photocatalyst Electrodeposition and Photoelectrode Characterization Study Results

The procedure of electrodeposition is explained in the experimental apparatus chapter. After electrodeposition, the photoelectrochemical cell is tested and characterized. Photoelectrochemical (PEC) hydrogen production setups are constructed using Cu_2O coated metals as photo cathodes, graphite rod and an Ag/AgCl reference electrode as counter and reference electrodes, respectively. The area of the stainless steel photocathode is 820 cm^2. The Cu_2O coated plates are tested for photoelectrochemical characterization in solutions of $NaHCO_3$ and NaOH with a graphite rod or stainless steel as the counter electrodes.

Initially, the coated stainless steel plate is tested under solar simulator light with an irradiance of 1000 W/m^2 in the solution of NaOH. Most of the relevant studies in the open literature regarding copper oxide coating and photoelectrochemical hydrogen production use dark and light characterizations [79, 81, 213]. In addition, the potential range is between -0.7 V to 0 V in the literature [79, 81, 213]. As being consistent with the literature, the characterization of the electrodeposited stainless steel is presented in Fig. 5.28 for the applied potentials between -0.6 V to 0 V. Furthermore, light and dark measurements are carried out by chopping the light under solar simulator light and actual concentrated light conditions. Note

that the measured currents are negative since there is p-type Cu_2O semiconductor as the photocathode.

Fig. 5.29 illustrates the linear sweep voltagram of the coated stainless steel plate under chopped light. The scan rate is 0.1 mV/s and the electrolyte is 0.05 M NaOH solution. The illuminated area is about 255 cm^2 and the maximum obtained photocurrent is about 0.012 mA/cm^2.

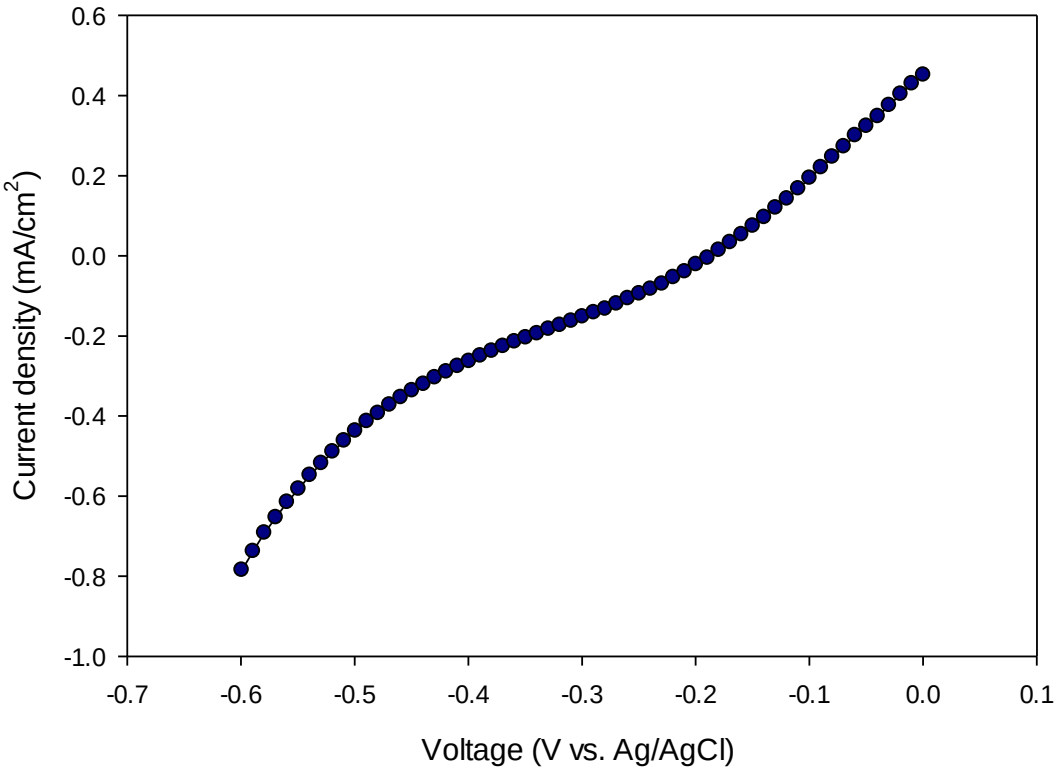

Fig. 5.28 Current density-voltage (J-V) characteristics of Cu_2O deposited stainless steel photocathode under solar simulator light illumination at 1000 W/m^2.

After the solar simulator tests, the concentrated light is applied on the photocathode. For the Cu_2O coated stainless steel electrode (electrodeposited at 55°C at the applied voltage of -0.3 V vs. Ag/AgCl) in $NaHCO_3$ solution, the maximum photocurrent is found to be 0.19 mA/cm^2 as shown in Fig. 5.30. The measured average ambient irradiance is 452 W/m^2 and concentrated irradiance is 1420 W/m^2. The illuminated active area is about 172.5 cm^2. The measurements are based on the average of the several experimental results with high reproducibility. The counter electrode for larger area stainless steel plate experiments is non-coated stainless steel anode plate with one side surface area of 737 cm^2 whereas the full surface is not immersed in the electrolyte.

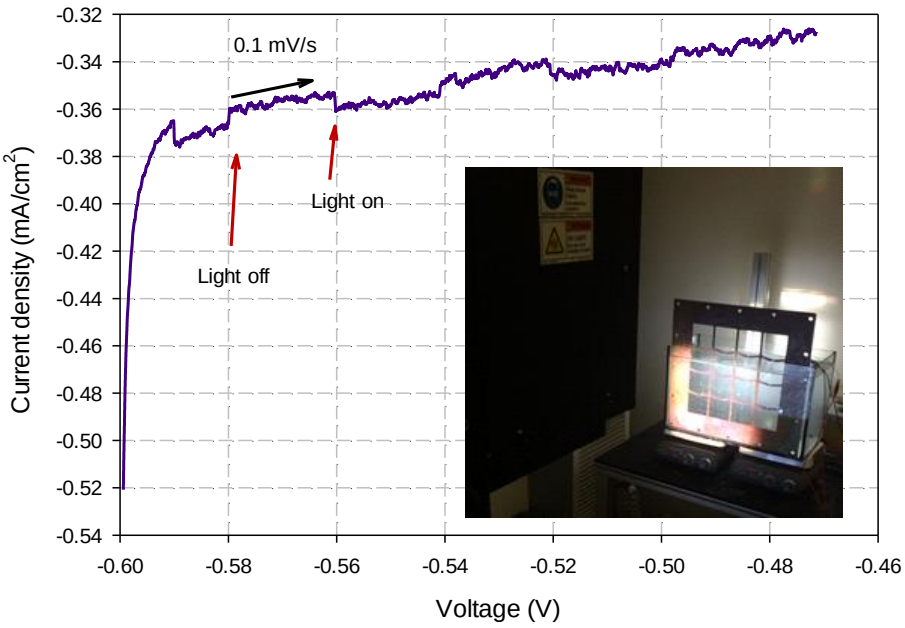

Fig. 5.29 Linear sweep voltammetry results of Cu_2O deposited at -0.30 V and 55°C (vs. Ag/AgCl reference electrode) on a stainless steel plate electrode under solar simulator chopped light of 1000 W/m^2.

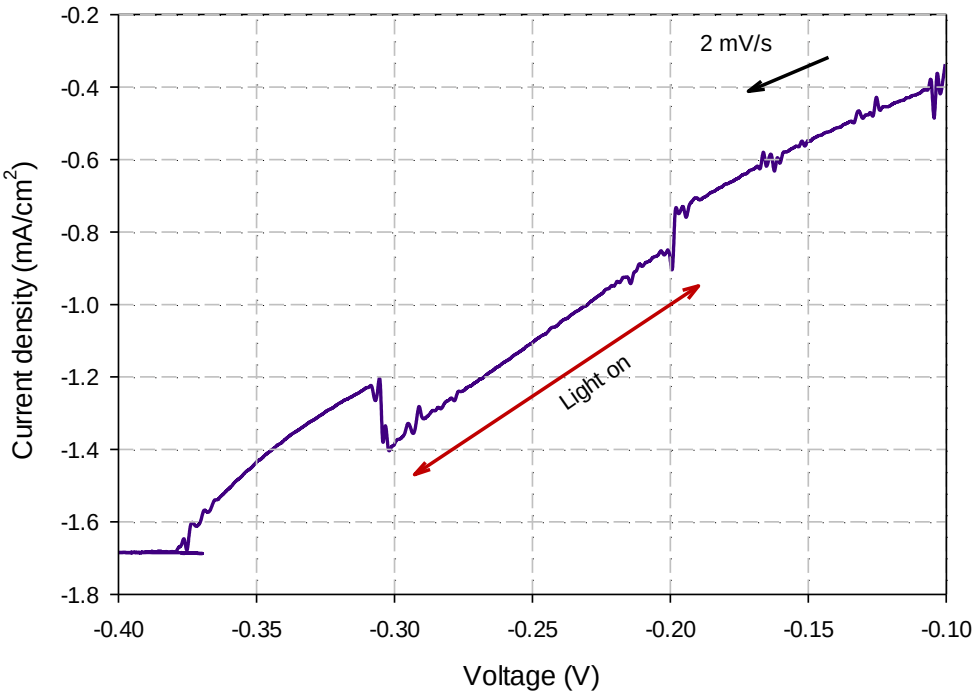

Fig. 5.30 Linear sweep voltammetry results (2 mV/s scan rate) of Cu_2O deposited at -0.30 V (vs. Ag/AgCl reference electrode) and 55°C on a stainless steel cathode electrode under chopped concentrated light (1420 W/m^2).

Fig. 5.31 shows the current–potential responses of the coated stainless steel plate to a linear potentiodynamic scan at 1 mV/s under chopped concentrated light illumination. The measured average ambient irradiance is 425 W/m^2 and concentrated light is about 1335 W/m^2. In the course of the cathodic scan the cathodic photocurrent showed a continuous increase with the negative potential bias, indicating a p-type signal of the coated metal which implies that there is a sufficient over potential for the reduction of water on illuminated Cu_2O. The active area which is illuminated is about 172.5 cm^2. This shows that maximum photocurrent density is about 0.53 mA/cm^2.

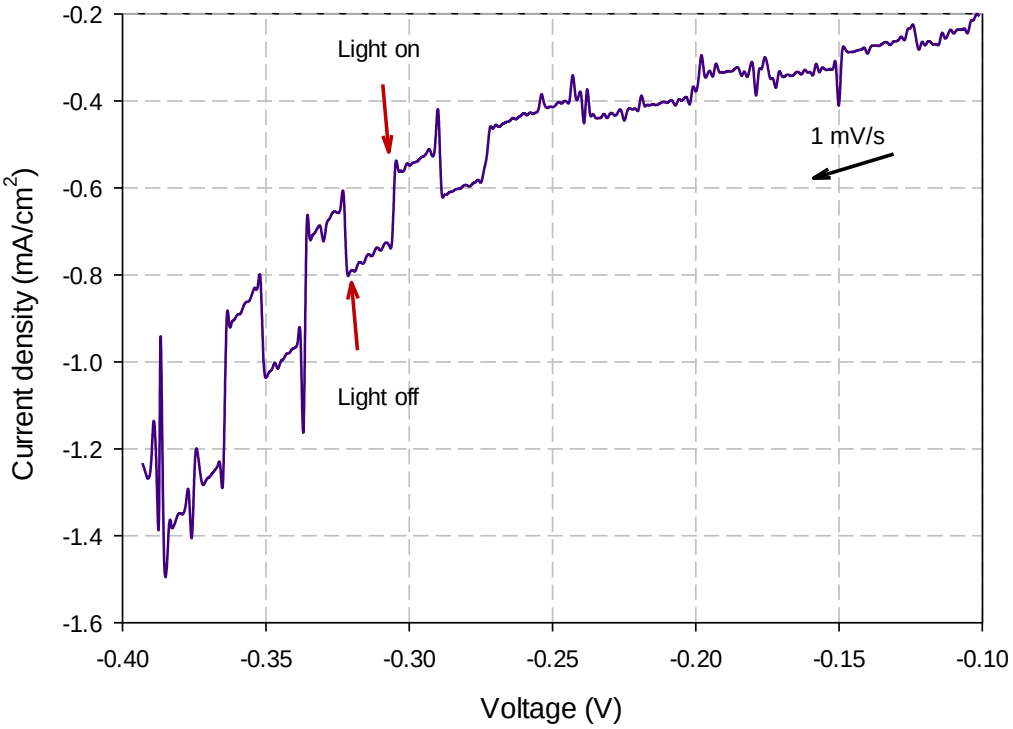

Fig. 5.31 Linear sweep voltammetry results (1 mV/s scan rate) of Cu_2O deposited at -0.30 V (vs. Ag/AgCl reference electrode) and 55°C on a stainless steel cathode electrode under chopped concentrated light (1335 W/m^2).

Fig. 5.32 shows the current–voltage diagram of the Cu_2O coated stainless steel plate to a linear potentiodynamic scan with a rate of 1 mV/s. In order to observe the photo response, a lower scanning rate is used. The test is conducted in concentrated light where the ambient irradiance is 420 W/m^2 and concentrated light is 1320 W/m^2. The approximate illuminated area is about 172.5 cm^2 and the maximum photocurrent density is measured as 0.31 mA/cm^2. The variations in the current density values are attributed to changing conditions of concentrated light since copper oxide is sensitive to changes in solar intensity and the experimental setup is manually adjusted for the azimuth and zenith angles to face the sun.

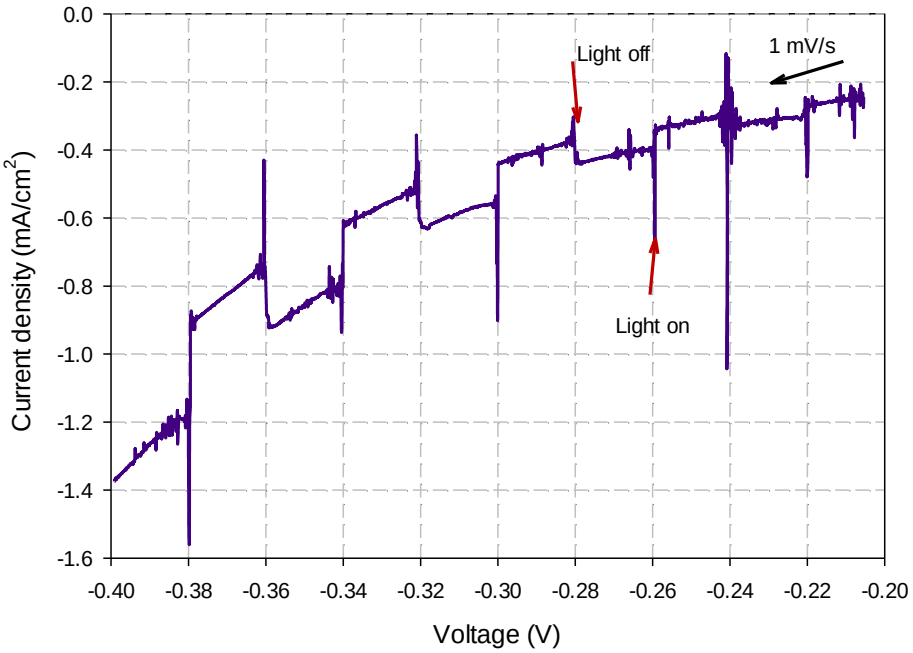

Fig. 5.32 Linear sweep voltammetry results (1 mV/s scan rate) of Cu_2O deposited at -0.30 V (vs. Ag/AgCl reference electrode) and 55°C on a stainless steel cathode electrode under chopped concentrated light (1320 W/m^2).

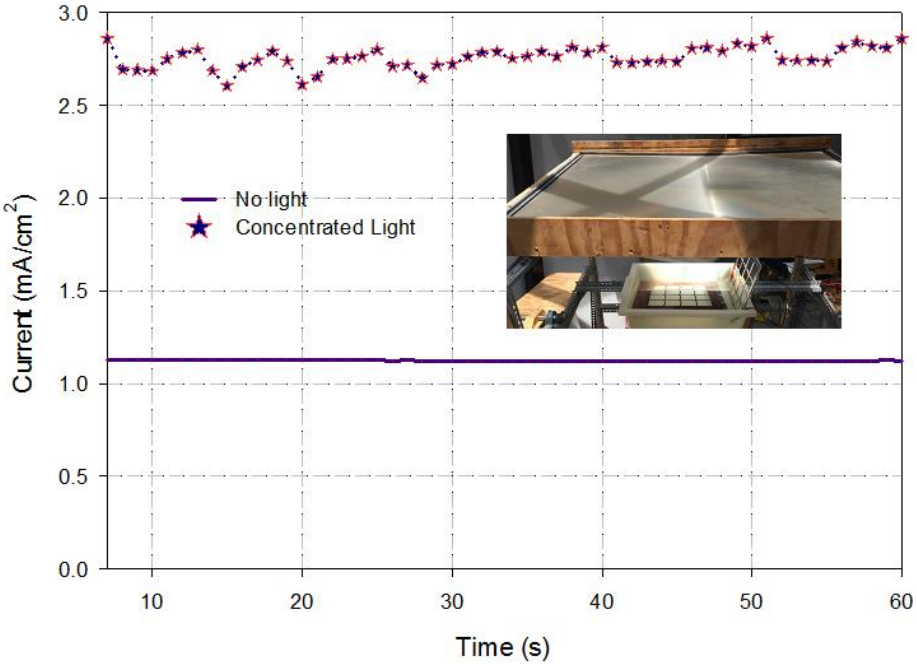

Fig. 5.33 Current density comparison of Cu_2O deposited stainless steel photocathode plate under concentrated light and no-light conditions in $NaHCO_3$ electrolyte solution at 5 V.

At the applied voltage of -0.6 V vs. Ag/AgCl in $NaHCO_3$ electrolyte which yielded the maximum photocurrent of 0.8 mA/cm^2 whereas the solar conversion efficiency (based on

photocurrent generation) is calculated to be 0.86%. Similarly, at the applied voltage of -0.4 V vs. Ag/AgCl in $NaHCO_3$ electrolyte, the conversion efficiency is calculated to be 0.24% having about 0.27 mA/cm^2.

Fig. 5.33 shows the total current as a function of time for the coated stainless steel plate under no-light and concentrated light conditions. The ambient irradiance is 605 W/m^2 and the concentrated irradiance is measured as 1900 W/m^2. There are oscillations in the concentrated light measurements because of the changing sunlight conditions and sensitivity of Cu_2O. The average current is 313.5 mA and 689.8 mA for the no-light and concentrated light conditions, respectively. In addition, the total accumulated charge is 18.44 C and 40.71 C for no-light and concentrated light conditions, respectively. The illuminated area is about 250 cm^2 of the Cu_2O coated metal plate. Hence, this indicates an average photocurrent density of about 1.5 mA/cm^2 as shown in Fig. 5.33. The generated photocurrent is maximum in this experiment with the impact of higher concentrated irradiation. This shows that concentrated light conditions may increase the overall performance of the photoelectrochemical hydrogen production.

The evolution rates of hydrogen are determined for the concentrated light and no-light conditions as seen in Fig. 5.34.

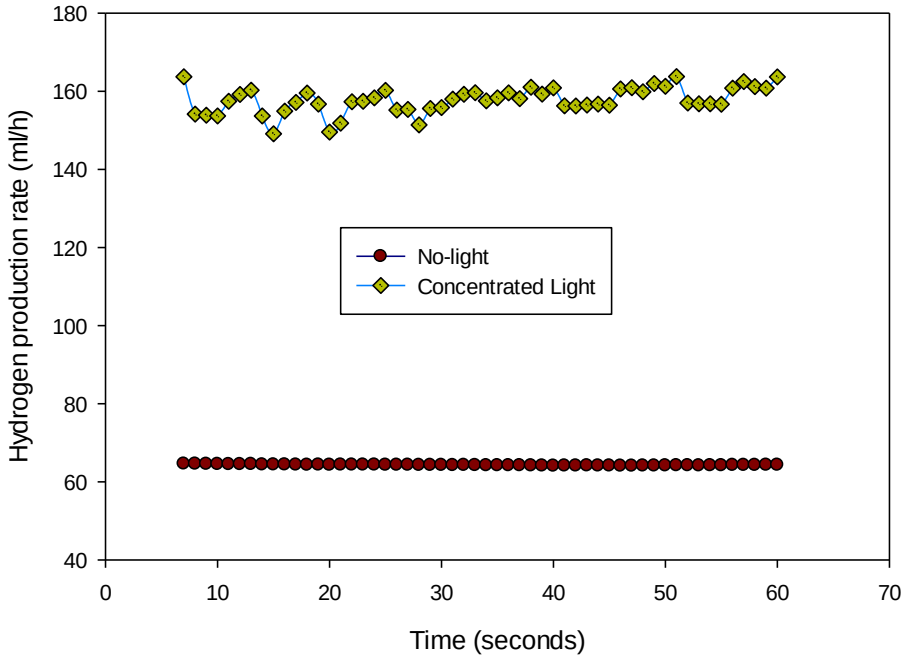

Fig. 5.34 Hydrogen production rate of Cu_2O deposited stainless steel photocathode plate under concentrated light and no-light conditions in $NaHCO_3$ electrolyte solution at 5 V.

The produced hydrogen is at ambient pressure and temperature hence corresponding to about 160 mL/h hydrogen production rate under concentrated illumination. However, in dark measurements, hydrogen production rate decreases to about 65 mL/h as a consequence of lower current. The related open literature has been reviewed for a comparison purpose and the obtained results are tabulated in Table 5.13 including the electrodeposition conditions. The

obtained photocurrent densities and solar conversion efficiency values are quite similar to the literature results.

The impact of changing current density in the electrolyzer assembly on hydrogen evolution rate is shown in Fig. 5.35 for the concentrated light measurements.

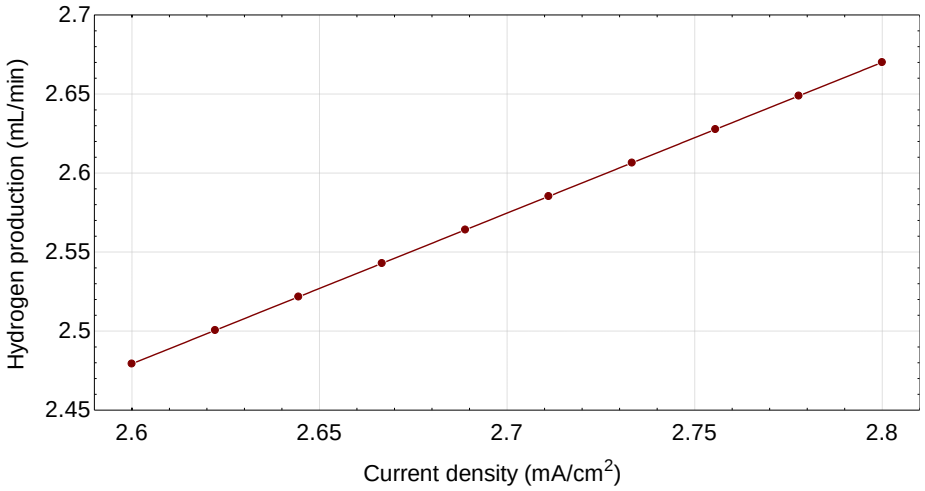

Fig. 5.35 Change of hydrogen evolution rate with rising current density under concentrated light conditions using Cu_2O deposited stainless steel photocathode plate.

Table 5.13 Brief review of electrodeposition literature and comparison with the current study.

Ref.	**Year**	**Max photocurrent density (mA/cm^2)**	**Efficiency (photocurrent) (%)**	**ED Temperature (°C)**	**ED pH**	**ED Potential (V)**
[74]	2011	0.061	0.01%	20	Slightly acidic	-0.2 vs SCE
[75]	2014	0.1	-	90	5	-0.5 vs. Ag/AgCl
[76]	2002	0.57	0.0234	60	9	-
[245]	2008	0.75	0.41	50	12	-0.26 vs Ag/AgCl
[77]	2012	1.4	-	50	9	−0.1 and −0.2 V
[78]	2012	1.20	0.91	60	14	-0.55 vs. Ag/AgCl
[79]	2012	-	0.3	60	12.5	−0.9 vs. MSE
[80]	2016	-	-	55	-	-0.25 vs Ag/AgCl
This study	2017	1.5	0.86	55	10	-0.30 vs Ag/AgCl

5.3 Photoelectrochemical Hydrogen Production

The model described in the analyses section is employed and calculated results are presented in this section. Firstly, the generated photocurrent is calculated based on the external quantum efficiency (EQE) shown in Fig. 5.36 and irradiance on the PEC reactor surface. The EQE of the copper oxide is given in various resources [65, 66].

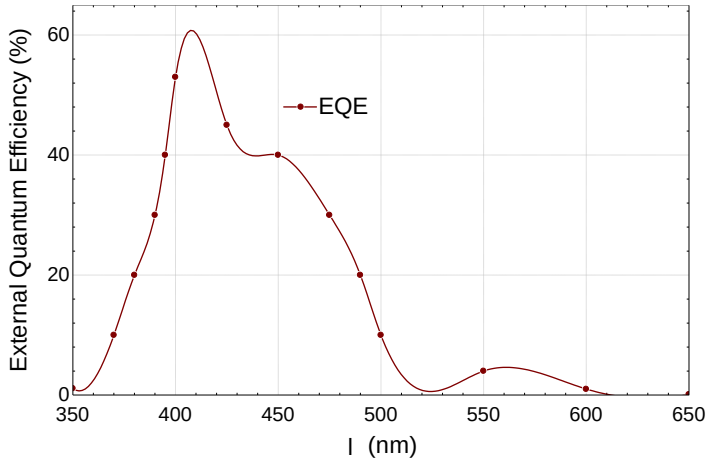

Fig. 5.36 External quantum efficiency of the Cu_2O on the photocathode surface.

Table 5.14 Model input parameters for PEC hydrogen production.

Cathode exchange current density	3.20×10^{-7}	A/m^2
Anode exchange current density	1.70×10^{-9}	A/m^2
Hydrogen pressure	1	atm
Water pressure	1	atm
Oxygen pressure	1	atm
Membrane conductivity	0.102	S/cm
Membrane conductivity under concentrated light	0.1156	S/cm
Membrane thickness	0.0127	cm
Anode - Effective diffusion coefficient	0.1869	cm^2/s
Anode - Effective diffusion coefficient under concentrated light	0.2011	cm^2/s
Cathode - Effective diffusion coefficient	0.4097	cm^2/s
Cathode - Effective diffusion coefficient under concentrated light	0.4329	cm^2/s
PEC cell active area	0.025	m^2
Fresnel lens area	8.76×10^{-1}	m^2
Dielectric mirrors area	7.70×10^{-2}	m^2
PV area	4.09×10^{-2}	m^2
Ambient temperature	298	K
Bandgap temperature of Cu_2O	24364	K
Bandgap temperature of silicon PV	12765	K
PEC cell temperature	313	K
PEC cell temperature under concentrated light	323	K
PV temperature	348.9	K

The developed electrochemical model calculates the reversible voltage and actual cell voltage which accounts for the overpotentials. The calculation of the overpotentials require some PEC cell parameters such as diffusion coefficient, exchange current density etc. which are given in Table 5.14. As mentioned in the analyses chapter, electrochemical impedance spectroscopy of the system can reveal some of these parameters. In this section, both theoretical and experimental parameters are used to compare the obtained results.

In the PEC cell, the concentration and ohmic losses are minor as shown in Fig. 5.37. However, the activation overpotentials are more dominant corresponding to about 0.25-0.30 V. At higher temperatures, the actual cell voltage slightly decrease from 1.67 V to 1.628 V for experimentally calculated one. The reversible cell voltage is calculated to be 1.244 V at 280 K which decreases to 1.202 V at 330 K. Concentration overpotentials are more dominant in higher current densities. The blue lines in Fig. 5.37 shows the actual cell voltage which is calculated using EIS data (shown as Exp). On average, it is about 0.1 V higher than the cell voltage which is calculated using assumed parameters.

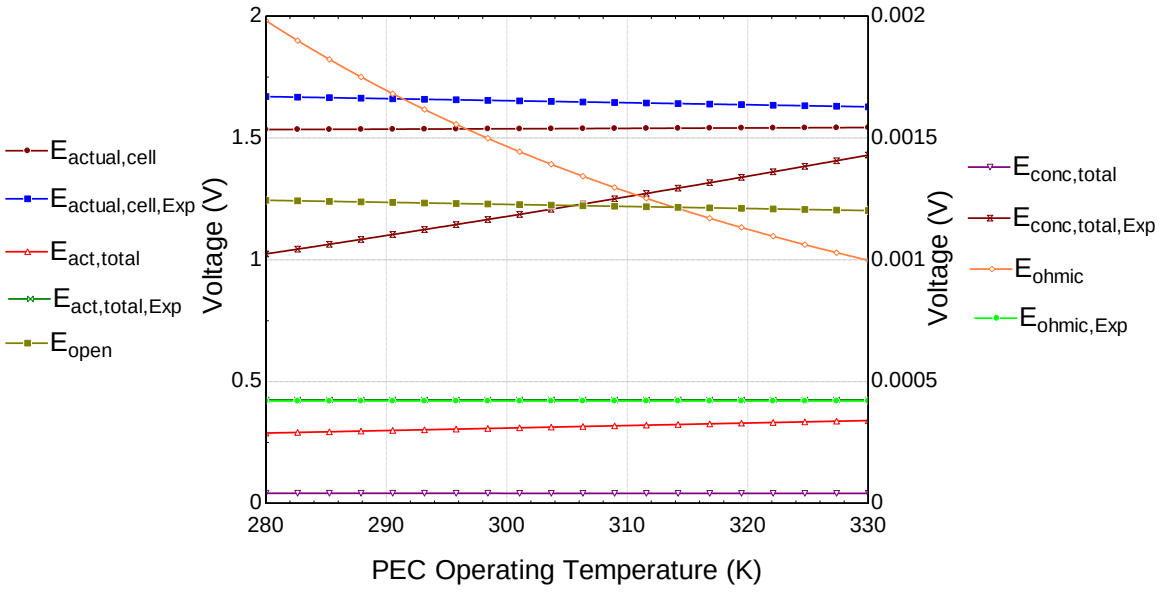

Fig. 5.37 The effect of changing PEC operating temperature on open, actual voltage and overpotentials.

The changes of different efficiencies defined in the analyses section are shown in Fig. 5.38 with respect to varying current density. The electrolyzer voltage efficiencies decrease by rising current density because, the overpotentials increase by rising current density. The overall PEC efficiencies are calculated based on the total irradiance input and produced hydrogen. In case the current density increases, the amount of generated hydrogen upsurges leading higher efficiencies. The overall PEC energy and exergy efficiencies rise to about 10%. This efficiency is calculated based on total hydrogen production amount. Increasing current density causes higher actual cell voltages in the electrolyzer, hence lowering the efficiency. In the PEC process, when there is higher applied current, the hydrogen production rate increases hence the efficiencies rise by rising current density.

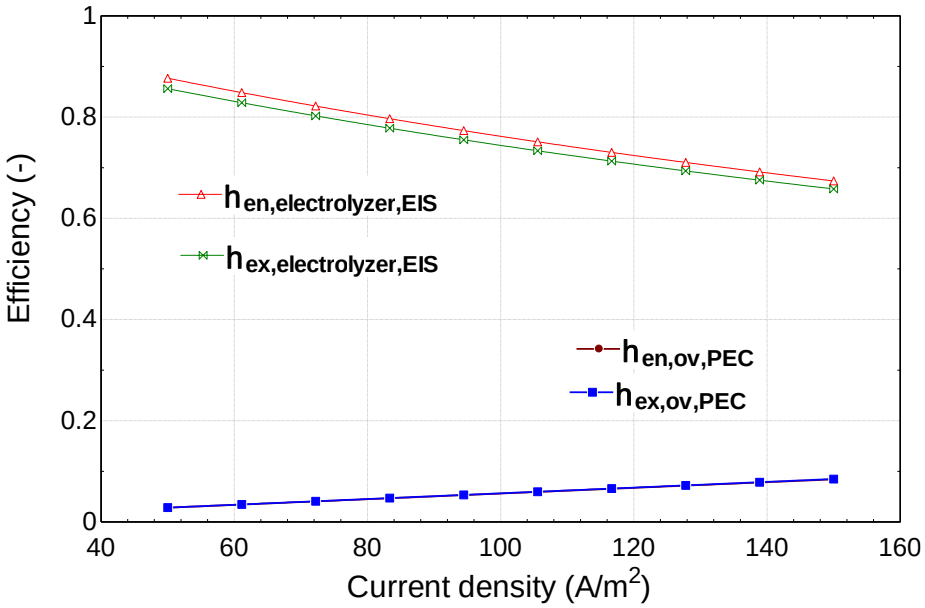

Fig. 5.38 The changes of the electrolyzer and PEC efficiencies by varying current densities.

The change of the actual cell voltage with respect to increasing current density is comparatively given with the manufacturer data in Fig. 5.39. The manufacturer gives a J-V curve based on the entered parameters under ideal conditions [246] which has a deviation from the developed model.

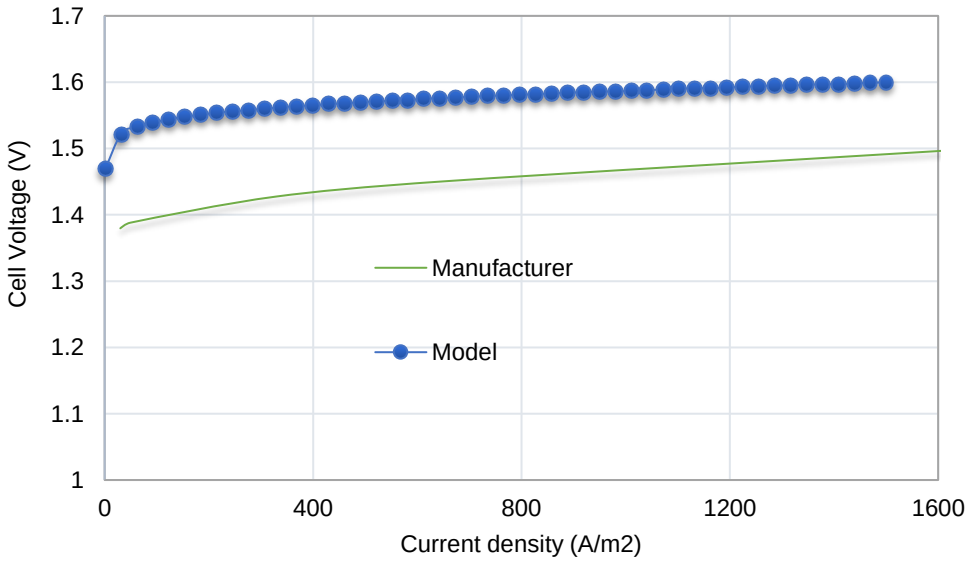

Fig. 5.39 The comparison of model and manufacturer PEC cell voltages by changing current density (data from [246]).

Theoretical open cell voltage of the PEC cell is calculated to be 1.208 and 1.216 under concentrated light and no-light condition, respectively. This is mostly due to higher operating cell temperatures which is about 10°C more under concentrated light. As explained before, the higher temperatures yield lower overpotentials.

In Table 5.15, the resistances calculated based on EIS experiments are tabulated. The equivalent circuit is given in the analyses section. The resistances of the constant phase elements are calculated using real part of the complex number whereas the membrane resistance is found using Warburg element equation. Furthermore, the resistances are comparatively shown for concentrated light and no-light condition. The membrane resistance and anode/cathode activation resistances slightly decrease under concentrated light.

Table 5.15 Calculated impedances of the PEC cell equivalent circuit model.

Resistance	**Value**	**Unit**
R_{co}	86.65	ohm cm^2
$R_{co_{Conc}}$	79.63	ohm cm^2
R_{CPE_A}	20.51	ohm cm^2
$R_{CPE_{AConc}}$	18.6	ohm cm^2
R_{CPE_C}	22.45	ohm cm^2
$R_{CPE_{CConc}}$	8.321	ohm cm^2
R_{mem}	0.1245	ohm cm^2
$R_{mem_{Conc}}$	0.1098	ohm cm^2
R_{mem}	0.04258	ohm cm^2
$R_{mem_{Conc}}$	2.331	ohm cm^2
$R_{mem_{ohm}}$	0.000498	ohm cm^2
$R_{mem_{ohm_{Conc}}}$	0.0004393	ohm cm^2

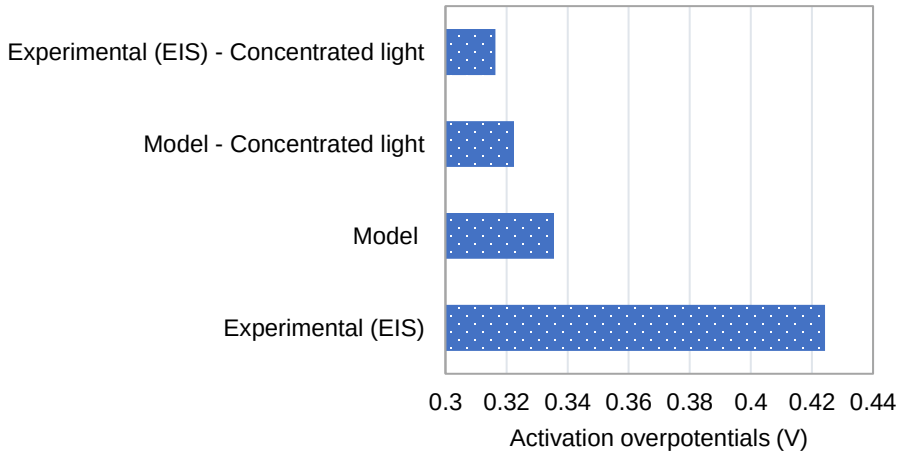

Fig. 5.40 The calculated activation overpotentials under different conditions.

As shown in Fig. 5.40, the activation overpotentials range between 0.3 V to 0.42 V based on the model and experimental results where the minimum activation voltage is calculated as 0.31 V for concentrated light experimental one. These overpotentials are the sum of anode and cathode overpotentials. As the resistance parameters in Table 5.15 imply,

resistances decrease under concentrated light causing lower activation overpotentials. In the no-light measurements, the total activation overpotential is calculated to be 0.42 V.

The experimental and theoretical values of the concentration and ohmic overpotentials in the PEC cell are comparatively shown in Tables 5.16 and 5.17. The concentration overpotentials are not much affected because the current density rises very minor because of photocurrent generation under concentrated light. This increase causes minor upsurges in concentration overpotential both in the model and experimentally calculated ones as shown in Table 5.16.

Table 5.16 Experimental and theoretical concentration overpotentials in the PEC cell.

Calculation method	Value	Unit
Model	0.000041	V
Model - Concentrated light	0.000049	V
Experimental (EIS)	0.001284	V
Experimental (EIS) - Concentrated light	0.028900	V

Similarly, the ohmic overpotentials present slight increases under concentrated light since it is mainly the multiplication of the resistance and current density. Although the resistance of the membrane decreases very little, the photocurrent production is much more compensating the ohmic overpotential and causing an increase as shown in Table 5.17.

Table 5.17 Experimental and theoretical ohmic overpotentials in the PEC cell.

Calculation method	Value	Unit
Experimental (EIS)	0.000421	V
Model	0.00123	V
Model - Concentrated light	0.001291	V
Experimental (EIS) - Concentrated light	0.02739	V

The ambient temperature is 298±2.485 K, T_{cell} is 313±2.61 K and $T_{cell,Conc}$ is 323 ±2.693 K here. The measured concentration ratio is C_{ratio}=6.2±0.31. The calculated EIS results are tabulated in Table 5.18 with the uncertainties considered. The results are given comparatively for no-light and concentrated light conditions. The uncertainties in the EIS measurements mainly derive from the potentiostat device as well as the irradiance and temperature measurements especially for concentrated light condition.

Using these calculated parameters, the actual cell voltages are calculated as shown in Fig. 5.41. The actual cell voltages which are calculated based on experimental EIS data are higher than model results. This shows that in practice, the actual values may differ from model results. Hence, validation of the model results by experimental methods are preferred and suggested.

The uncertainties in the experimental EIS measurements are higher than model results due to measurement devices. The minor uncertainties in the model derive from the pre-set values such as ambient temperature which is also a measurement results and has an uncertainty.

Table 5.18 The calculated results of the PEC cell parameters including the uncertainties.

Parameter	Value	Uncertainty	Unit
$E_{actual_{cell}}$	1.54	±0.008345	V
$E_{actual_{cell_{Conc}}}$	1.545	±0.008416	V
$E_{actual_{cell_{EIS}}}$	1.642	±0.006131	V
$E_{actual_{cell_{EIS_{Conc}}}}$	1.589	±0.006613	V
E_{act_a}	0.206	±0.005415	V
$E_{act_{a_{Conc}}}$	0.2144	±0.005463	V
$E_{act_{a_{EIS}}}$	0.2025	±0.003493	V
$E_{act_{a_{EIS_{Conc}}}}$	0.2186	±0.003543	V
E_{act_c}	0.1165	±0.003062	V
$E_{act_{c_{Conc}}}$	0.121	±0.003083	V
$E_{act_{c_{EIS}}}$	0.2217	±0.003823	V
$E_{act_{c_{EIS_{Conc}}}}$	0.09778	±0.001585	V
$E_{act_{total}}$	0.3224	±0.008476	V
$E_{act_{total_{Conc}}}$	0.3355	±0.008545	V
$E_{act_{total_{EIS}}}$	0.4243	±0.006116	V
$E_{act_{total_{EIS_{Conc}}}}$	0.3164	±0.004316	V
E_{conc_a}	0.00002138	±2.99E-07	V
$E_{conc_{a_{Conc}}}$	0.00002518	±3.15E-07	V
$E_{conc_{a_{EIS}}}$	0.000428	±0.00003039	V
$E_{conc_{a_{EIS_{Conc}}}}$	0.003765	±0.0003192	V
E_{conc_c}	0.00001948	±2.47E-07	V
$E_{conc_{c_{Conc}}}$	0.00002337	±2.60E-07	V
$E_{conc_{c_{EIS}}}$	0.000856	±0.00006077	V
$E_{conc_{c_{EIS_{Conc}}}}$	0.02513	±0.004057	V
$E_{conc_{total}}$	0.00004086	±4.48E-07	V
$E_{conc_{total_{Conc}}}$	0.00004855	±4.49E-07	V
$E_{conc_{total_{EIS}}}$	0.001284	±0.00009116	V
$E_{conc_{total_{EIS_{Conc}}}}$	0.0289	±0.004374	V
E_{ohmic}	0.00123	±0.0001317	V
$E_{ohmic_{Conc}}$	0.001291	±0.0001297	V
$E_{ohmic_{EIS}}$	0.0004205	±0.000007252	V
$E_{ohmic_{EIS_{Conc}}}$	0.02739	±0.000444	V

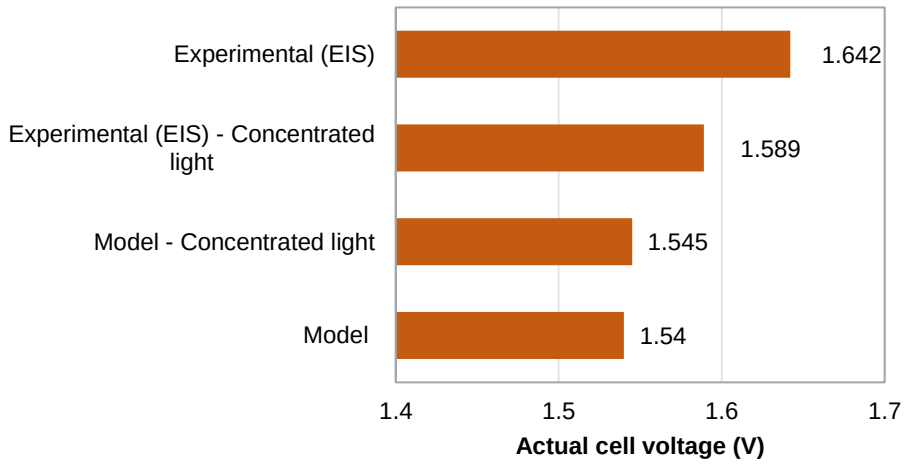

Fig. 5.41 Experimental and theoretical actual cell voltages of the PEC cell.

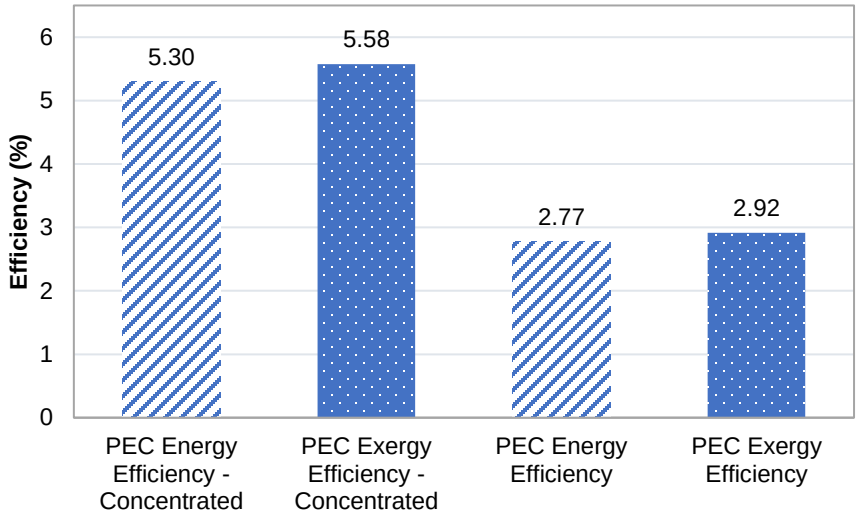

Fig. 5.42 The photocurrent energy and exergy efficiencies of the PEC process.

In the photoelectrochemical process, illumination of light on the photosensitive surface (which is a semiconductor) generates photocurrent. Hence, using open cell voltage, generated photocurrent and fill factor (similar to the PV cells); the energy and exergy efficiencies of the PEC process can be calculated by incoming light irradiance. As shown in Fig. 5.42, the PEC photocurrent energy and exergy efficiencies found to be 2.8% and 2.9%, respectively. Here, the input to the system is the ambient irradiance in both normal and concentrated light operation.

Concentrating the light almost doubles the efficiencies due to higher photocurrent production. One can also calculate the PEC process efficiency based on the concentrated light irradiance on the PEC cell, however, in order to have a common base and comparison, ambient irradiance is taken as the input. In other words, the experimental setup receives the ambient irradiance as the only input to the system (except water inlet) and generates the other useful

commodities. Under these conditions, the photocurrent is calculated to be 1.876 mA/cm^2 in ambient irradiance whereas it is calculated to be 3.7 mA/cm^2 under concentrated light. The hydrogen production rates are 19.8 mL/min and 24.3 mL/min for ambient and concentrated light conditions, respectively. The electrical work input to the PEC cell can be calculated based on the area of the cell, current density and actual PEC cell voltage as explained in the analyses. In theoretical calculations, the electrical work inputs to the PEC cell are found to be 3.8 W and 4.5 W, respectively for ambient and concentrated light conditions. On the other hand, using the experimental EIS data, the electrical work is calculated to be 4.05 W and 4.67 W, respectively for ambient and concentrated light conditions.

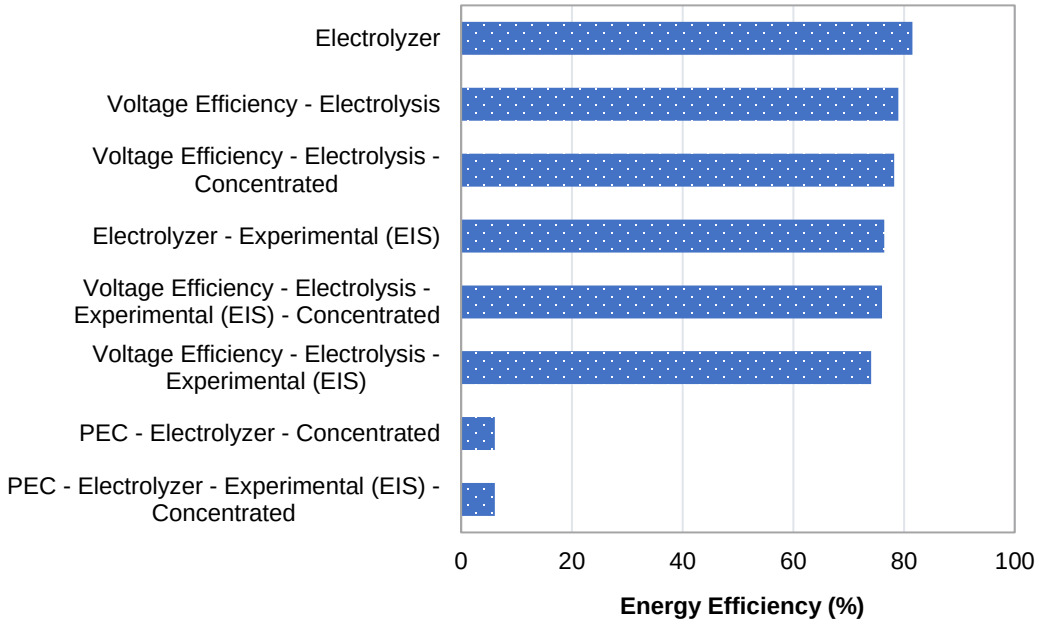

Fig. 5.43 The energy efficiencies in the PEC hydrogen production system based on different efficiency definitions.

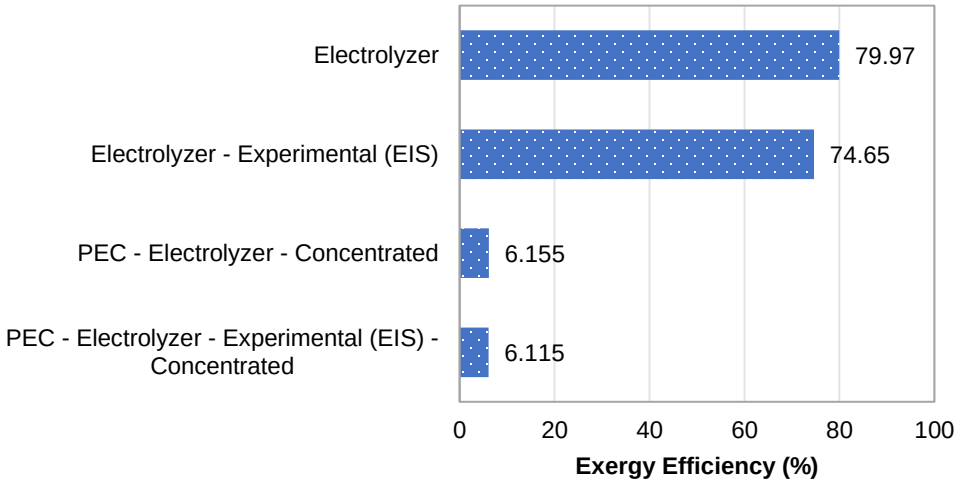

Fig. 5.44 The exergy efficiencies in the PEC hydrogen production system and electrolyzer based on different efficiency definitions.

In Figs. 5.43 and 5.44, the electrolysis process efficiencies are comparatively shown based on various efficiency definitions defined in the analyses section. Both theoretical and experimental efficiencies are presented. The voltage efficiency is based on the actual and reversible cell voltage, hence there is no exergy efficiency definition. Practically, the energy and exergy efficiencies are lower in the experimental results. However, the variations are not much which range between 74% and 81% for all cases in the sole electrolyzer mode.

On the other hand, as shown in Fig. 5.44, the exergy efficiency of the PEC hydrogen production under concentrated light is calculated to be 6.11% in the experiments whereas it is 6.16% in the model.

In Table 5.19, all efficiencies related to PEC hydrogen production system are presented together with the uncertainty ranges. The results are given for experimental, theoretical, ambient and concentrated light conditions. Here, there is overall PEC efficiency which is calculated based on the hydrogen production rate and total solar energy input to the system that is the irradiance before the Fresnel lens. It can also be named as solar-to-hydrogen, efficiency. The overall PEC efficiency under concentrated light ($\eta_{en_{ov_{PEC,Conc}}}$) and exergy efficiency ($\eta_{ex_{ov_{PEC,Conc}}}$) are calculated to be 6.5% and 6.6%, respectively. The corresponding energy and exergy efficiency under ambient irradiance are calculated as 5.5%.

The internal processes of the PEC cell are defined using electrochemical impedance spectroscopy measurements. Numerous experiments are conducted to investigate the concentrated light conditions on the cell performance and obtained results are compared with dark conditions. The EIS measurements are performed by a Potentiostat/Galvanostat/ZRA (Gamry Instruments Reference 3000). Potentiostatic EIS is the applied measurement technique. The spectrum of the impedance is logged in the laboratory for no-light conditions and outside the laboratory for the concentrated light measurements by scanning the frequencies ranging from 20 kHz to 10 mHz with 5 points per decade. The amplitude of the sinusoidal AC voltage signal is 10 mV (RMS). The PEC cell is supplied different DC potentials ranging from 1.3 V to 3 V during the EIS measurements. The resistances are normalized to the area of 500 cm^2. The PEC cell is continuously supplied deionized water. In this way, formed hydrogen is collected in a glass container and excess water is discharged to the water tank which includes a submersible pump. The flowrate of the water for measurements is on average 4 mL/min. The temperature of the water is measured continuously using a temperature probe and data logger. On average, during no-light experiments, the water temperature is measured as 29.5°C whereas it is 39.5°C for concentrated light experiments. The tests are performed at least three times to assure the reproducibility of the results.

The solar light intensity hitting on the PEC cell is one of the critical parameters affecting the overall performance. Hence, the irradiance values are recorded for each individual EIS cycle as shown in Table 5.20. The ambient irradiance is between 960 to 990 W/m^2 during the applied potentials of 1.3 V to 2.5 V. It is slightly lower for 3 V measurements because of the time of the experiment which is around 4:30 pm afternoon. As mentioned earlier, only a portion of the PEC reactor is illuminated. The irradiance on the concentrated part of the PEC cell (quarter of the whole surface) is between 4300 and 6500 W/m^2, although non-concentrated section is between 160 W/m^2 and 250 W/m^2 because of the restricted cold mirror area.

Table 5.19 The calculated efficiencies of the PEC hydrogen production system including the uncertainties.

Efficiency	Value (%)	Uncertainty (%)
$\eta_{en_{ov_{PEC}}}$	5.541	±0.3398
$\eta_{en_{ov_{PEC_{Conc}}}}$	6.594	±0.3082
$\eta_{en_{PEC}}$	2.771	±0.006209
$\eta_{en_{PEC_{Conc}}}$	5.296	±0.103
$\eta_{en_{electrolyzer}}$	81.53	±0.02647
$\eta_{en_{PEC_{electrolyzer_{Conc}}}}$	6.099	±0.02776
$\eta_{en_{electrolyzer_{EIS}}}$	7.645	±0.3005
$\eta_{en_{PEC_{electrolyzer_{EIS_{Conc}}}}}$	6.086	±0.2596
$\eta_{ex_{ov_{PEC}}}$	5.581	±0.4143
$\eta_{ex_{ov_{PEC_{Conc}}}}$	6.641	±0.3757
$\eta_{ex_{PEC}}$	2.917	±0.00665
$\eta_{ex_{PEC_{Conc}}}$	5.576	±0.1062
$\eta_{ex_{electrolyzer}}$	7.997	±0.0272
$\eta_{ex_{PEC_{electrolyzer_{Conc}}}}$	6.155	±0.02936
$\eta_{ex_{electrolyzer_{EIS}}}$	7.465	±0.2938
$\eta_{ex_{PEC_{electrolyzer_{EIS_{Conc}}}}}$	6.115	±0.2534
$\eta_{voltage_{electrolysis}}$	78.98	±0.1663
$\eta_{voltage_{electrolysis_{Conc}}}$	78.2	±0.1719
$\eta_{voltage_{electrolysis_{EIS}}}$	74.06	±0.2763
$\eta_{voltage_{electrolysis_{EIS_{Conc}}}}$	76.02	±0.2936

Table 5.20 Irradiance measurements on the PEC cell and ambient during EIS experiments.

Parameter	Irradiance (W/m^2)						
Applied Voltage	1.3 V	1.5 V	1.7 V	1.9 V	2.1 V	2.5 V	3 V
Ambient	987	989	979	980	981	961	866
PEC Reactor (Concentrated area: 351 cm^2)	6518	5628	4681	5656	5829	5684	4312
PEC Reactor (Non-concentrated area:1054 cm^2)	246	210	203	205	220	210	163
Solar Power on PEC Reactor (W)	255	220	186	220	228	222	168

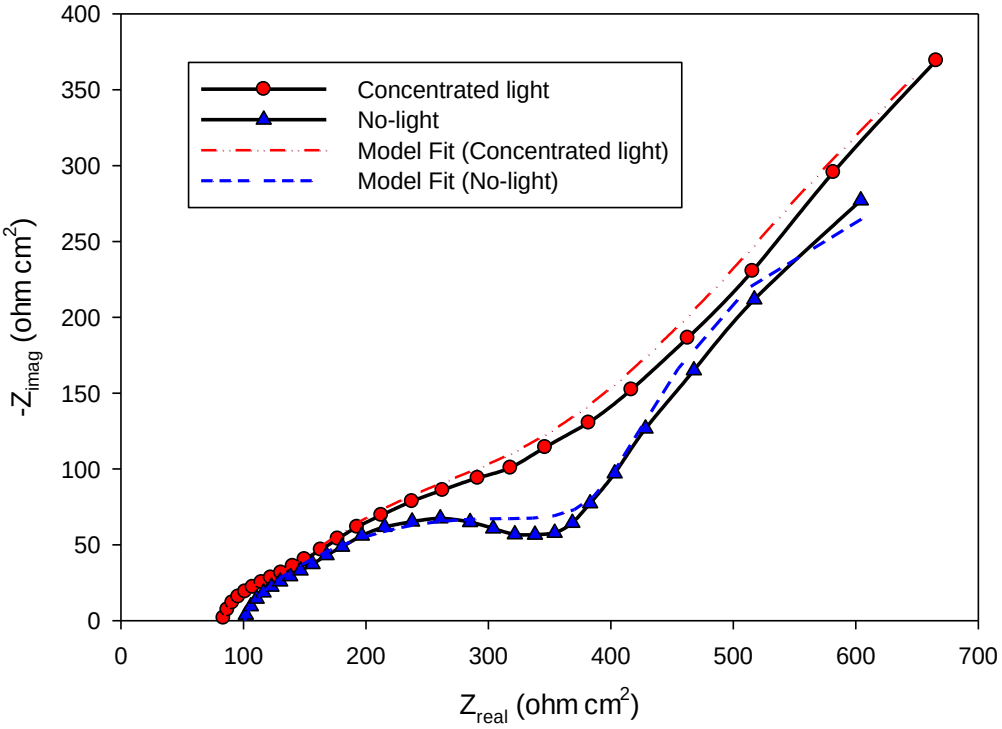

Fig. 5.45 Nyquist plot of concentrated light and no-light measurements with equivalent circuit fit curves at 1.3 V applied potential.

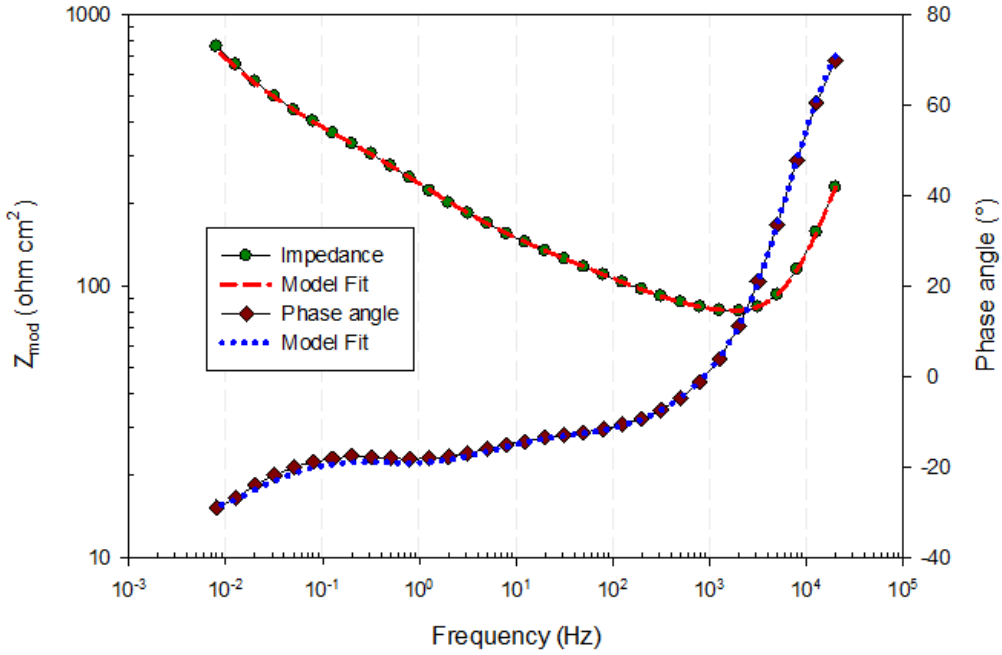

Fig. 5.46 Bode plot of concentrated light measurements with equivalent circuit fit curves at 1.3 V applied potential.

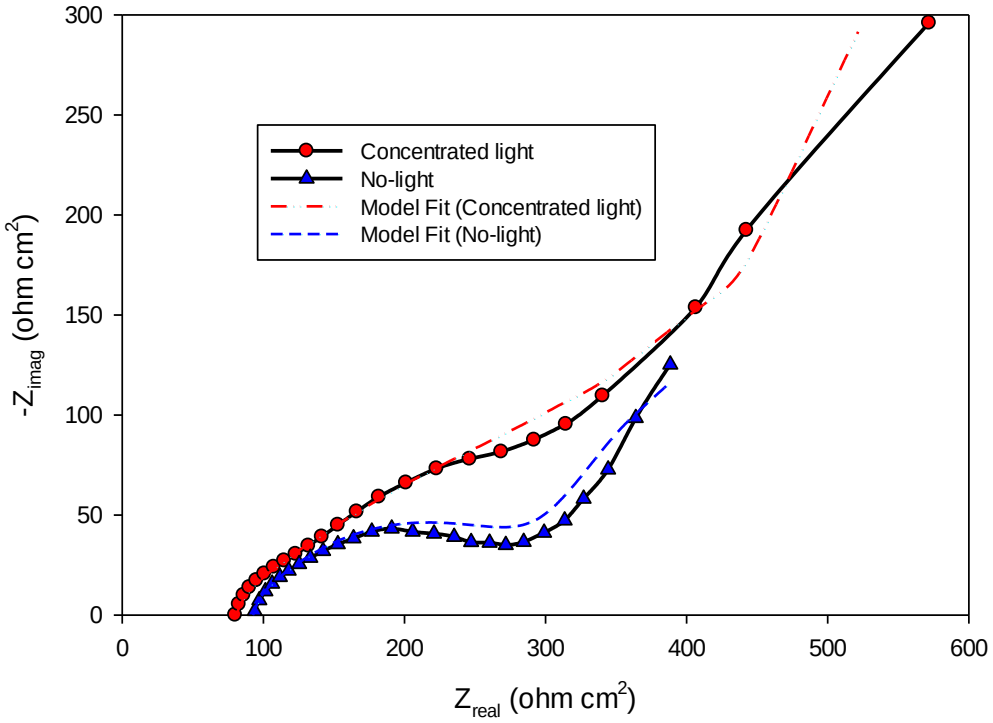

Fig. 5.47 Nyquist plot of concentrated light and no-light measurements with equivalent circuit fit curves at 1.5 V applied potential.

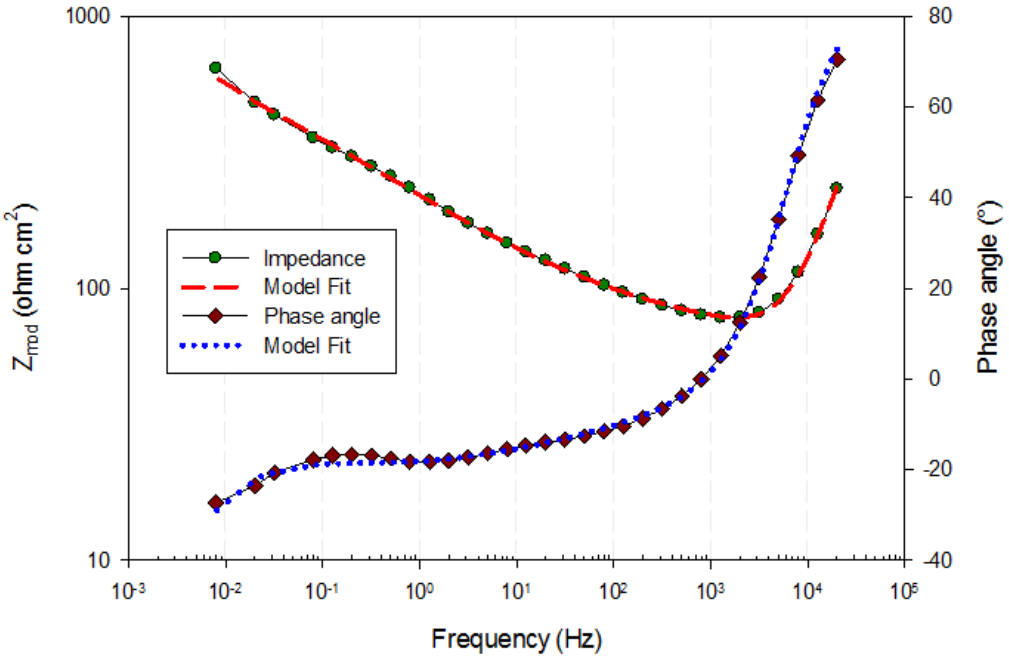

Fig. 5.48 Bode plot of concentrated light measurements with equivalent circuit fit curves at 1.5 V applied potential.

The reported irradiances are the average values. Based on the illuminated areas, the total energy rates on the PEC cell are calculated which ranged between 160 W and 255 W. Both Nyquist and Bode diagrams are provided to better evaluate the results. The no-light results are not illustrated in Bode diagrams because of complexity of the lines. The overall processes occurring in the PEC cell, namely, in the semiconductor, in the electrolyte and at the working and counter-electrode side, are evaluated in the no-light and under concentrated sunlight conditions as depicted in Figs. 5.45 to 5.62. The fitted equivalent circuit parameters for each voltage level are listed in Tables 5.21 to 5.26.

The hydrogen evolution reaction occurs at the photocathode. This reaction is faster than the oxygen evolution reaction which occurs at the anode. The semicircles seen in Figs. 5.45 to 5.62 for no-light conditions is due to the cathode and anode activation resistance. The diameter of the semicircles represent the activation losses which includes the membrane, gas diffusion layer, bipolar plate and contact resistances. A change in this value during different current densities is related to be membrane hydration and kinetics of the reactions at the anode and cathode. For concentrated light measurements, the semicircles are not visible too much because of lesser activation losses.

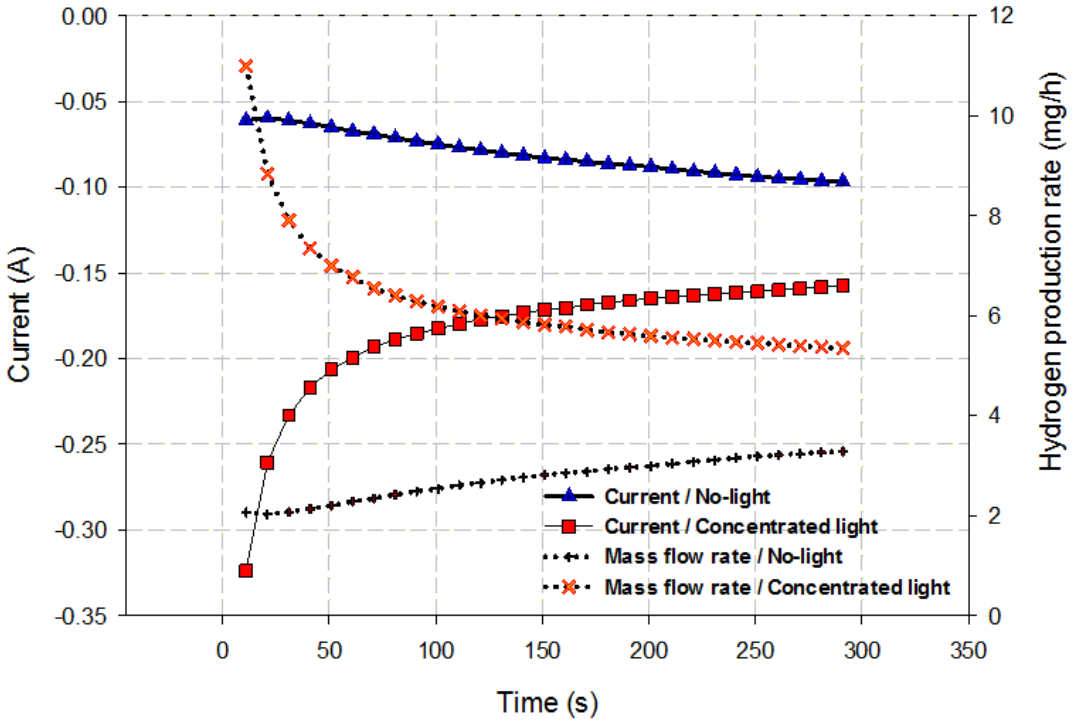

Fig. 5.49 Comparison of hydrogen production rate and current in the PEC reactor at 1.5 V applied potential under concentrated light and no-light.

The total current through the PEC cell and generated hydrogen mass flow rates at 1.5 V applied voltage are comparatively shown in Fig. 5.49. It is seen that there is significant photocurrent generation. Since there is photocathode for hydrogen production, negative potential is applied yielding a negative sign in the current. The photocurrent at the end of the

experiment is calculated as 0.1 mA/cm^2. The average hydrogen production rate is 2.7 mg/h and 6.5 mg/h for no-light and concentrated light measurements, respectively.

Table 5.21 Model fitting parameters of 1.3 V measurements for concentrated light and no-light.

Parameter	No-light	Concentrated light	Unit
a10	0.5128	0.6237	
a14	0.9053	0.6180	
B14	0.0342	15.9000	$s^{0.5}$
CPE-A	0.0557	0.0004	S s^a/cm^2
CPE-C	0.0011	0.0024	S s^a /cm^2
L	0.0018	0.0017	H cm^2
R-A	631.4000	49.9500	ohm cm^2
R-C	305.4000	170.8000	ohm cm^2
R-Co	87.8000	74.4000	ohm cm^2
W-M	0.0020	0.0090	S $s^{0.5}$ /cm^2
Goodness of Fit	0.0002	0.0002	

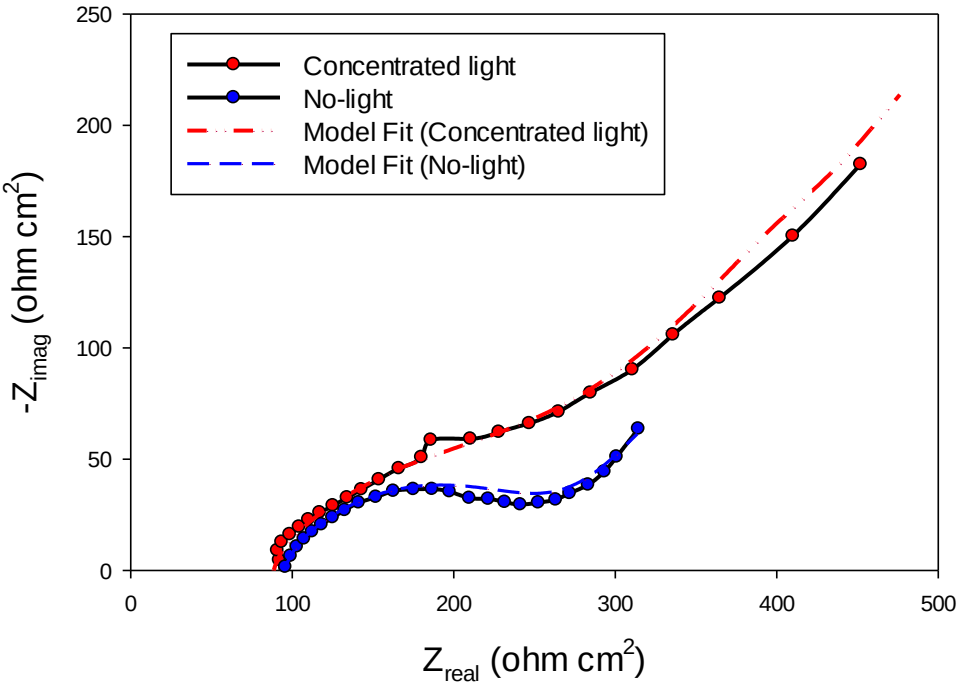

Fig. 5.50 Nyquist plot of concentrated light and no-light measurements with equivalent circuit fit curves at 1.7 V applied potential.

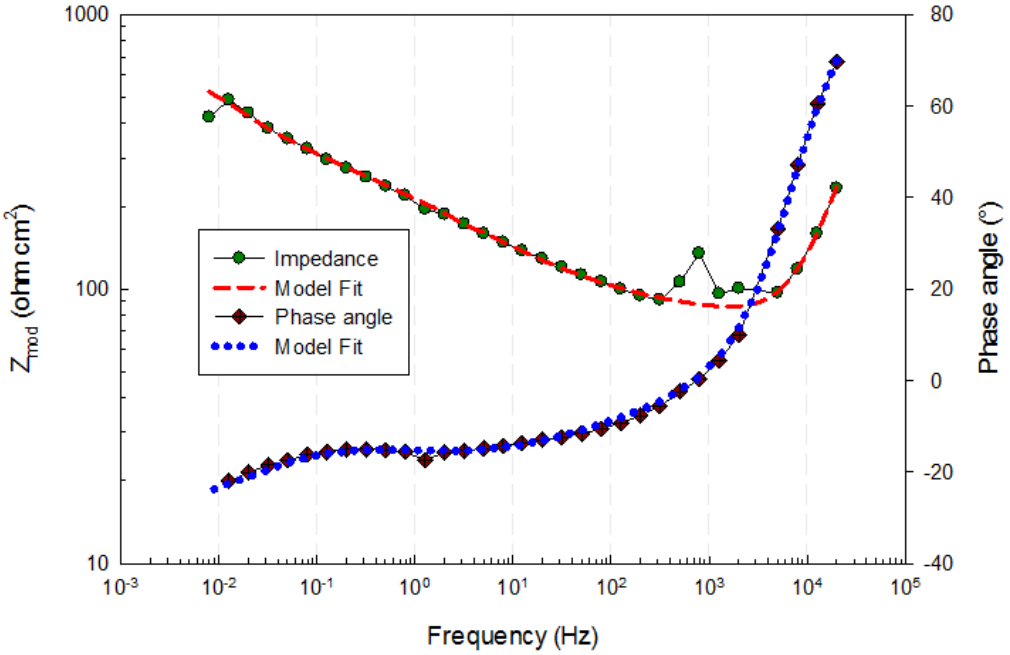

Fig. 5.51 Bode plot of concentrated light measurements with equivalent circuit fit curves at 1.7 V applied potential

No-light impedance spectra represent a 45° line at low frequencies or the impedance can have a second semicircle in Nyquist plots. It is explained that if there is no arc in the graph, it corresponds to no diffusion. However, if diffusion is available and finite, two arcs are present in the graph. For the diffusion which is infinite, a 45° straight line is present at the low frequency region [197]. The impedance spectra at low frequencies always reflects the impedance due to mass transport limitations [247]. The electrolyzer is an electrochemical system with reactions at the electrodes and at the electrode/membrane interface.

These reactions consist of membrane resistance charge transfer at the electrode interface and mass transport. Each process can be presented by an electrical circuit element. At high frequencies the imaginary impedance is zero which results in a pure resistance representing ohmic losses. At low frequencies, the resistance is the summation of R-Co, R-A and R-C, from which the charge transfer resistance can be calculated. The resistance of the conductors, membrane and the contact resistance are measured with the EIS technique. The inductance of the conductors is presented with an inductor L.

The activation losses occur due to the kinetics of the two reactions at the anode and cathode. The oxygen yielding reaction at the anode is slower than the hydrogen generating reaction at the cathode and therefore the losses at the cathode are considered to be negligible. The parameters of CPE and *a* are responsible for the shape of the semicircles in the Nyquist plots.

The total current through the PEC cell and generated hydrogen mass flow rates at 1.7 V applied voltage are comparatively shown in Fig. 5.52. The hydrogen production rate for the concentrated light is about 8.7 mg/h whereas it is about 5.1 mg/h on average.

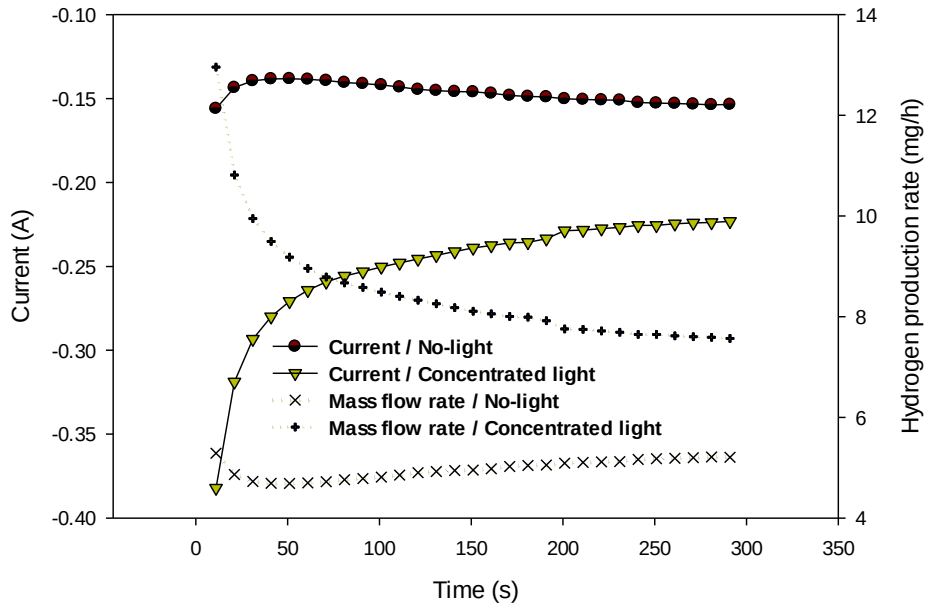

Fig. 5.52 Comparison of hydrogen production rate and current in the PEC reactor at 1.7 V applied potential under concentrated light and no-light.

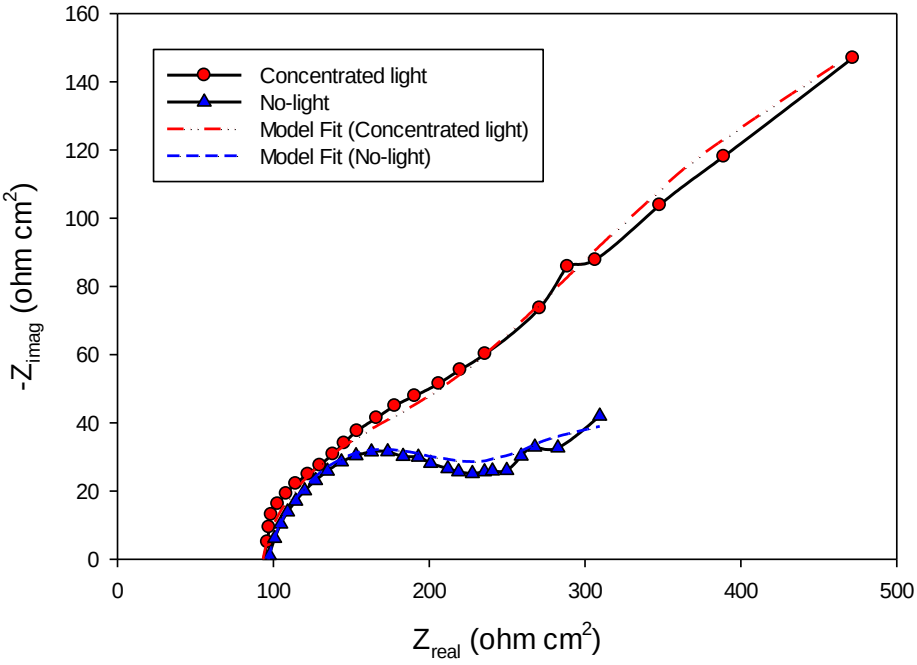

Fig. 5.53 Nyquist plot of concentrated light and no-light measurements with equivalent circuit fit curves at 1.9 V applied potential.

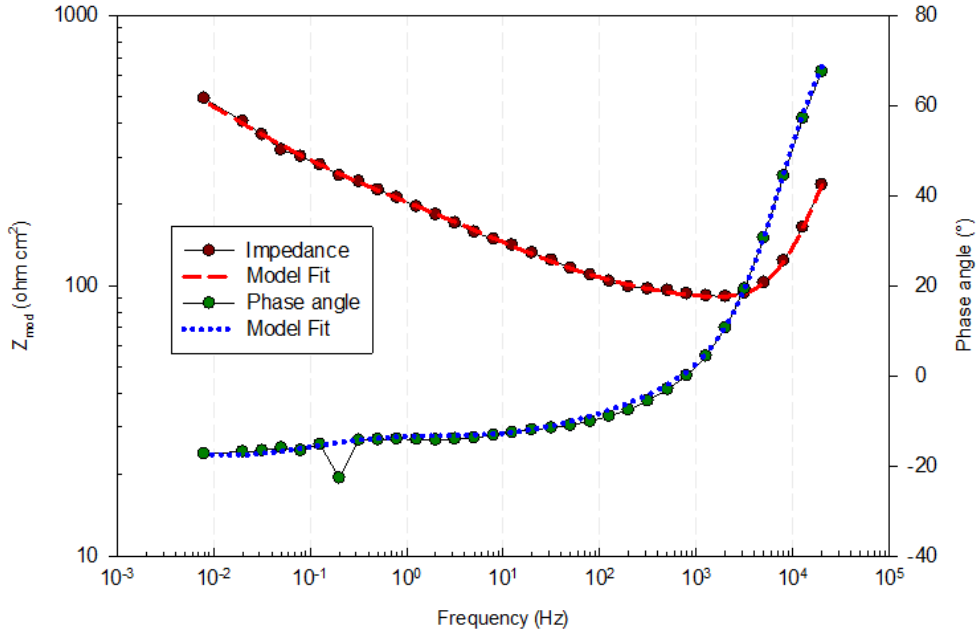

Fig. 5.54 Bode plot of concentrated light measurements with equivalent circuit fit curves at 1.9 V applied potential.

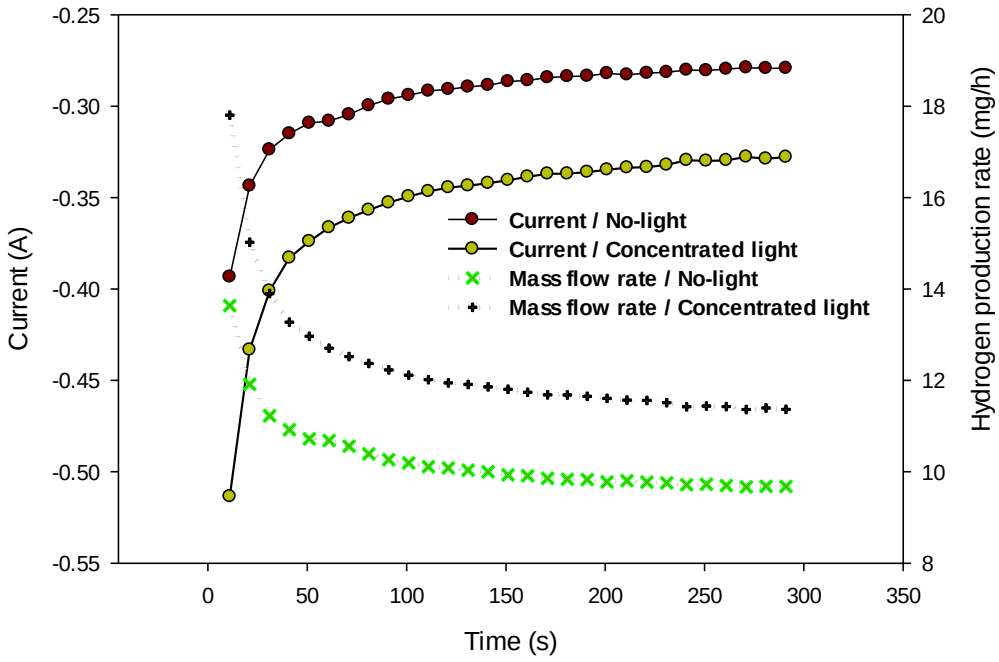

Fig. 5.55 Comparison of hydrogen production rate and current in the PEC reactor at 1.9 V applied potential under concentrated light and no-light.

The total current through the PEC cell and generated hydrogen mass flow rates at 1.9 V applied voltage are comparatively shown in Fig. 5.55. Higher applied voltage yields higher

total current and hydrogen production rates. On average, the hydrogen evolution rate is 12.5 mg/h for concentrated light measurement.

Table 5.22 Model fitting parameters of 1.5 V measurements for concentrated light and no-light.

Parameter	No-light	Concentrated light	Unit
a10	0.4491	0.4410	
a14	0.8175	0.1983	
B14	0.0311	17.6600	$s^{0.5}$
CPE-A	0.0738	0.0022	S s^{a} /cm^2
CPE-C	0.0013	0.0296	S s^{a} /cm^2
L	0.0018	0.0018	H cm^2
R-A	366.9000	210.0000	ohm cm^2
R-C	241.4000	116.4000	ohm cm^2
R-Co	79.4100	66.2700	ohm cm^2
W-M	0.0056	0.0121	S $s^{0.5}$ /cm^2
Goodness of Fit	0.0003	0.0003	

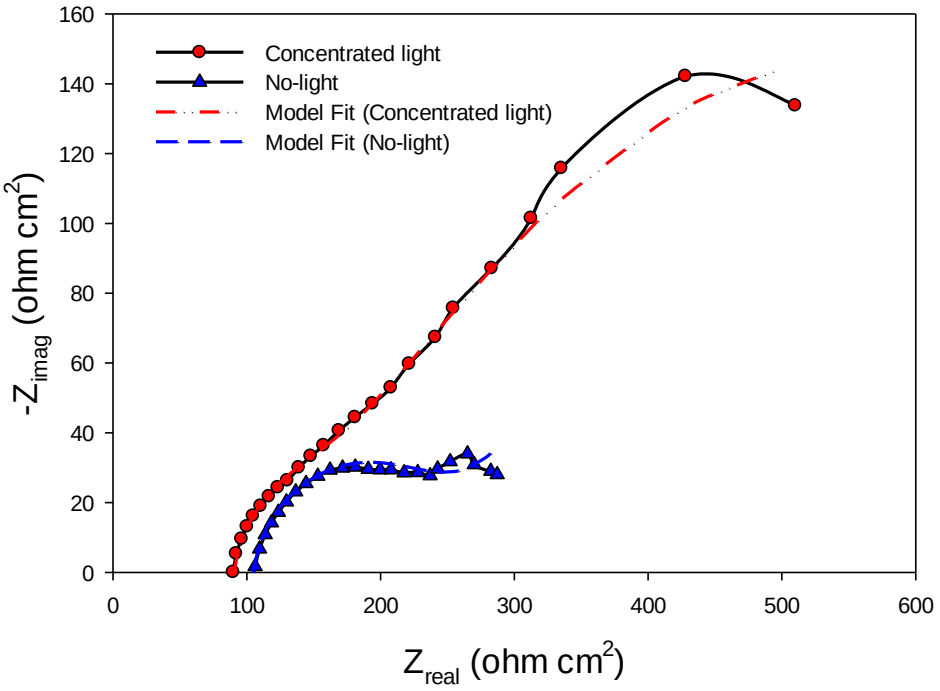

Fig. 5.56 Nyquist plot of concentrated light and no-light measurements with equivalent circuit fit curves at 2.1 V applied potential.

The corresponding numbers of the circuit elements are found by fitting the resulting impedance of the circuit with real experimental impedance information. A clear change in the activation resistance is recorded when applied voltage is changed. At low voltages, a high activation resistance is observed.

The activation resistance declines as the applied voltage increases. This is explained as the reaction necessities a definite amount of energy to drive it. Hence, in low voltages, if a small amount of electrons is present, a larger resistance is available for driving the reaction. However, at high applied voltages which means higher current densities, this resistance that drives the reaction is lesser. The imaginary part of the impedance is maximum about 35 ohm cm^2 and 275 ohm cm^2 for 3 V and 1.3 V, respectively in no light measurements.

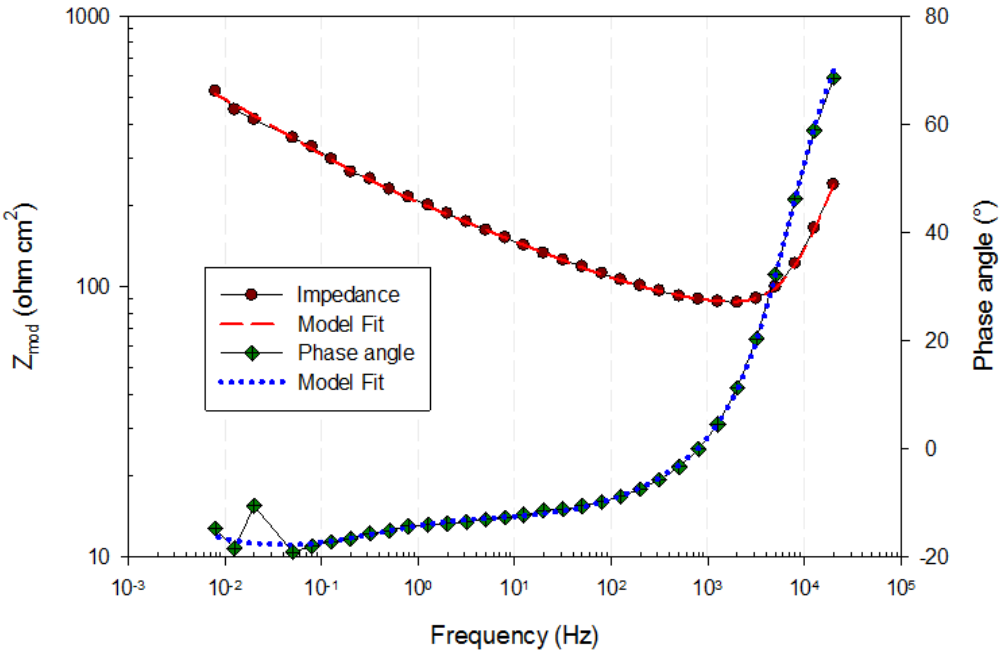

Fig. 5.57 Bode plot of concentrated light measurements with equivalent circuit fit curves at 2.1 V applied potential.

Table 5.23 Model fitting parameters of 1.7 V measurements for concentrated light and no-light.

Parameter	No-light	Concentrated light	Unit
a10	0.4667	0.4431	
a14	0.9349	2.0060	
B14	15.0800	11.0300	$s^{0.5}$
CPE-A	0.0012	0.0020	S s^a /cm^2
CPE-C	0.0001	0.0210	S s^a /cm^2
L	0.0018	0.0018	H cm^2
R-A	182.7000	203.0000	ohm cm^2
R-C	3.6590	0.1250	ohm cm^2
R-Co	82.4700	78.4200	ohm cm^2
W-M	0.0469	0.0145	S $s^{0.5}$ /cm^2
Goodness of Fit	0.0001	0.0005	

The inductance is mainly caused by the wirings which are not changed during concentrated light and no-light experiments. The series inductance, L is typically attributed to

the connection wires between the electrodes and the measuring instrument. L almost assume constant value of independent of the applied potential. Therefore, the inductance values are almost same for all voltage levels corresponding to about 0.0018 H cm^2. At higher frequencies, an imaginary part of admittance yields negative values. The presence of this results indicate the inductance effects. Though the graphs start with zero which do not show the impact of the inductance.

A capacitor is present in case a non-conducting medium splits two conducting plates. The rate of the capacitance is based on the dimension of the plates, the space among the plates, and the characteristics of the dielectric structure. If a coated metal dipped in an electrolyte, the metal is one plate, the coating is the dielectric, and the electrolyte is the second plate. CPE-C values rise from no-light to concentrated light measurements.

Table 5.24 Model fitting parameters of 1.9 V measurements for concentrated light and no-light.

Parameter	No-light	Concentrated light	Unit
a10	0.1968	0.3970	
a14	0.5779	4.3300	
B14	17.2600	2194.0000	$s^{0.5}$
CPE-A	0.0082	0.0024	S s^a /cm^2
CPE-C	0.0011	95.7200	S s^a /cm^2
L	0.0019	0.0018	H cm^2
R-A	341.6000	228.9000	ohm cm^2
R-C	77.5600	62.0000	ohm cm^2
R-Co	73.0900	81.6100	ohm cm^2
W-M	0.1940	0.0227	S $s^{0.5}$ /cm^2
Goodness of Fit	0.0001	0.0004	

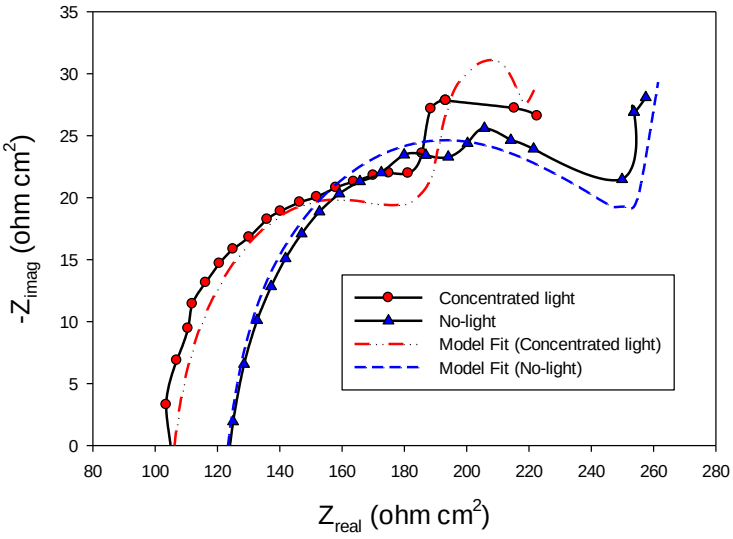

Fig. 5.58 Nyquist plot of concentrated light and no-light measurements with equivalent circuit fit curves at 2.5 V applied potential.

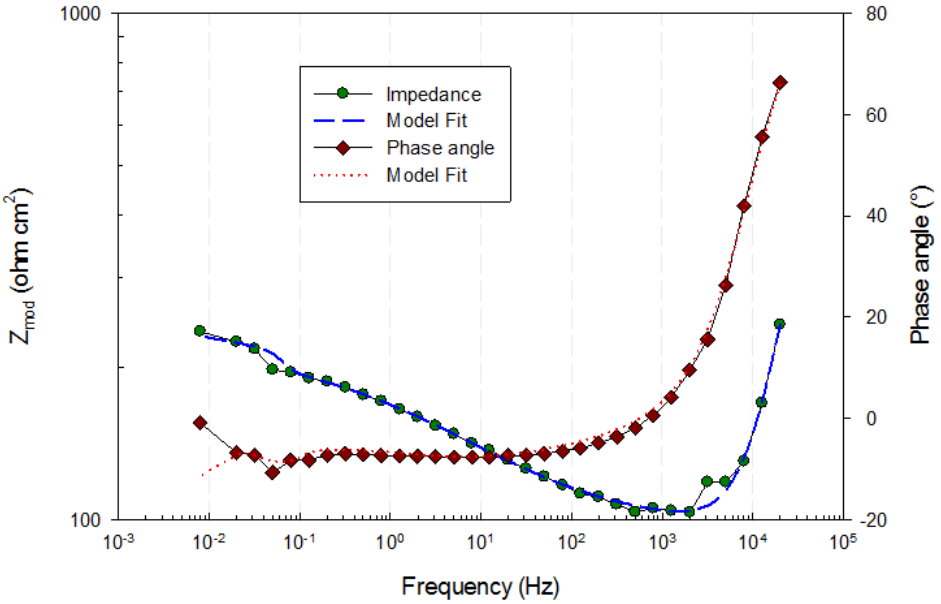

Fig. 5.59 Bode plot of concentrated light measurements with equivalent circuit fit curves at 2.5 V applied potential.

The ohmic resistances of cell elements contain resistance of the membrane, photocatalyst layer, cathode and anode plates, and contact resistance between the plates. The total resistances (R-A, R-C and R-Co) are lower in concentrated light measurements as listed in Tables 5.20 to 5.24. For instance, cathode resistance (R-C) decreases from 241 ohm cm^2 to 116.4 ohm cm^2 as the light is concentrated for 1.5 V case.

This phenomena explains the photo-current generation in the PEC cell because higher current densities lower the activation losses. The space charge width decreases in case of concentrated light of the semiconductor-electrolyte interface because of excitation of charge carriers from the valence band to the conduction band. Intercept of the high-frequency impedance loop with the real axis designates an ohmic resistance representing ohmic losses within the PEC cell.

The decreasing of ohmic losses under concentrated light are also visible in the Nyquist graphs as the graph starts left shifted in lower frequency region converts smaller on concentrate light illumination. This is due to an increase in conductivity caused by higher number of charge carriers in the bands. R-Co represents the mass transfer resistances including the coating pf the cathode plate. Furthermore, if the low-frequency arc moves toward real axis, this shows that a finite diffusion in the PEC cell.

Operating at higher current densities decreases the activation resistance but increase the effect of mass transfer. As illustrated in Nyquist plots of Figs. 45-62, the mass transfer process is more dominant in concentrated light measurements. In addition, semicircles are not dominant because constant phase elements do not affect the process significantly. The high impact of mass transfer processes is noticeable after the semicircles with Warburg element and 45° angle in the Nyquist plots although the semi-circle diameters are quite low for concentrated light results.

The total current through the PEC cell and generated hydrogen mass flow rates at 3 V applied voltage are comparatively shown in Fig. 5.60. At 3 V, the total current is quite high compared to other potentials. The average hydrogen production rate is 60.5 mg/h whereas it is 82.2 mg/h for no-light and concentrated light measurements, respectively.

Table 5.25 Model fitting parameters of 2.1 V measurements for concentrated light and no-light.

Parameter	No-light	Concentrated light	Unit
a10	286.2000	0.2775	
a14	0.3908	0.0004	
B14	6.8640	13.6000	$s^{0.5}$
CPE-A	0.1086	0.0039	S s^a /cm^2
CPE-C	0.0014	1.8910	S s^a /cm^2
L	0.0018	0.0018	H cm^2
R-A	4.7700	890.8000	ohm cm^2
R-C	186.6000	161.0000	ohm cm^2
R-Co	86.6500	69.2800	ohm cm^2
W-M	0.0730	0.0525	S $s^{0.5}$ /cm^2
Goodness of Fit	0.0001	0.0006	

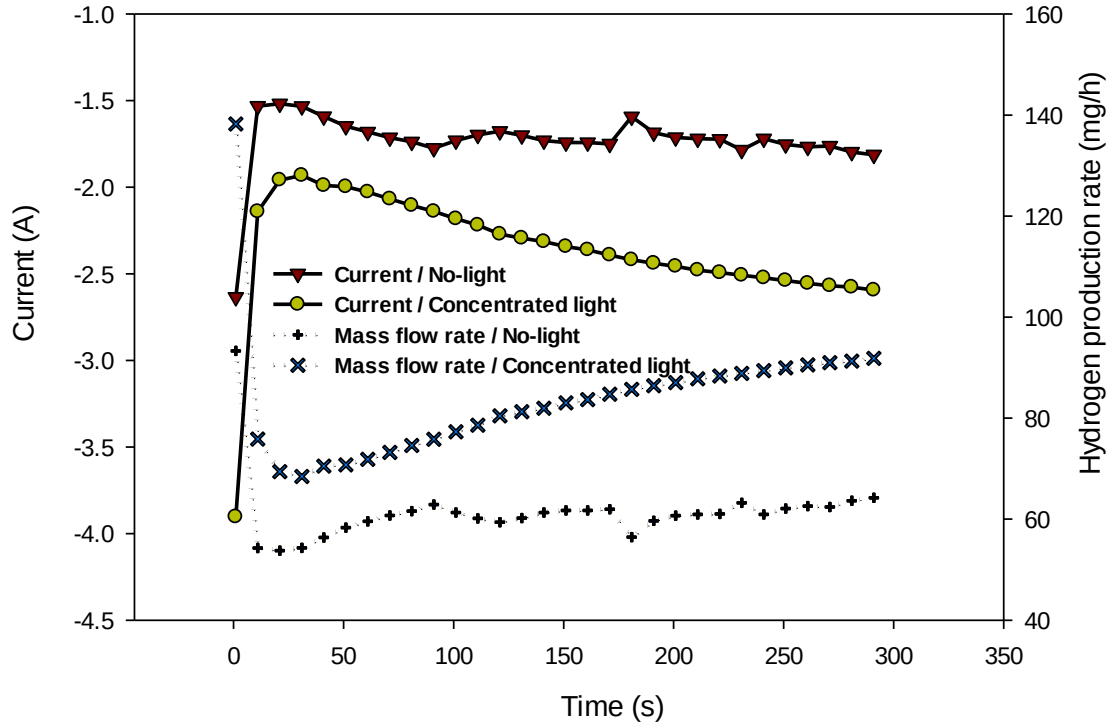

Fig. 5.60 Comparison of hydrogen production rate and current in the PEC reactor at 3 V applied potential under concentrated light and no-light.

Table 5.26 Model fitting parameters of 2.5 V measurements for concentrated light and no-light.

Parameter	No-light	Concentrated light	Unit
a10	0.3451	0.4357	
a14	0.0000	1.5040	
B14	3.0590	6.2650	$s^{0.5}$
CPE-A	0.0018	0.0024	S s^{a} /cm^2
CPE-C	0.0390	0.4957	S s^{a} /cm^2
L	0.0018	0.0018	H cm^2
R-A	172.9000	100.6000	ohm cm^2
R-C	180.3000	8.2710	ohm cm^2
R-Co	79.3500	97.3700	ohm cm^2
W-M	0.2095	0.0835	S $s^{0.5}$ /cm^2
Goodness of Fit	0.0007	0.0007	

The mass transport impedance is typically detected at low frequencies since it is longer time for the reactants to move and penetrate farther into the electrocatalyst and gas diffusion layers at both electrodes resulting in a higher diffusion resistance value. For all voltage results except for 1.3 V and 1.5 V, the Warburg element values decrease for concentrated light. The Warburg parameter decreases from 0.0469 S $s^{0.5}$ /cm^2 to 0.0145 S $s^{0.5}$ /cm^2 as the light is concentrated for 1.7 V.

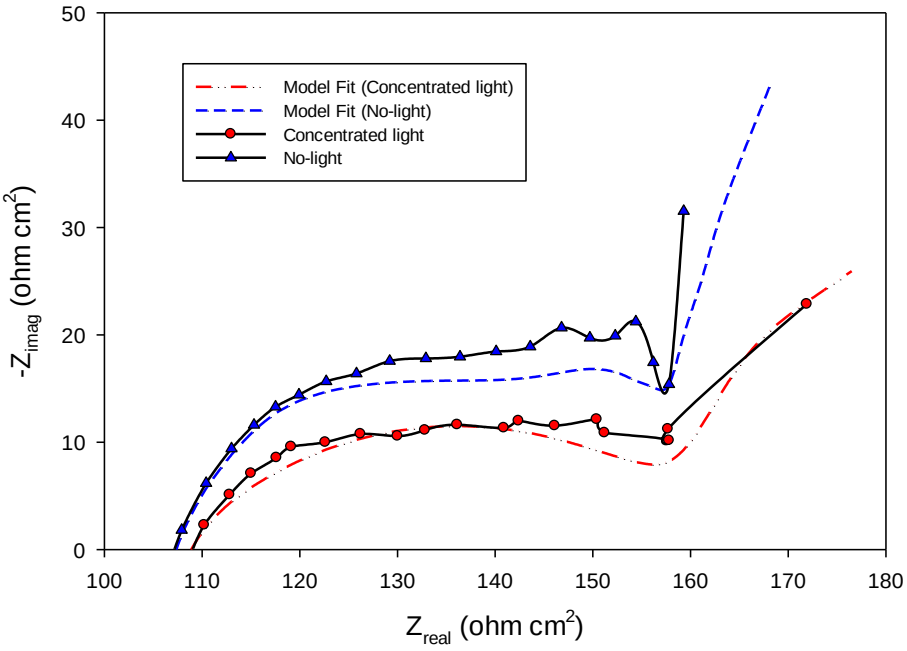

Fig. 5.61 Nyquist plot of concentrated light and no-light measurements with equivalent circuit fit curves at 3 V applied potential.

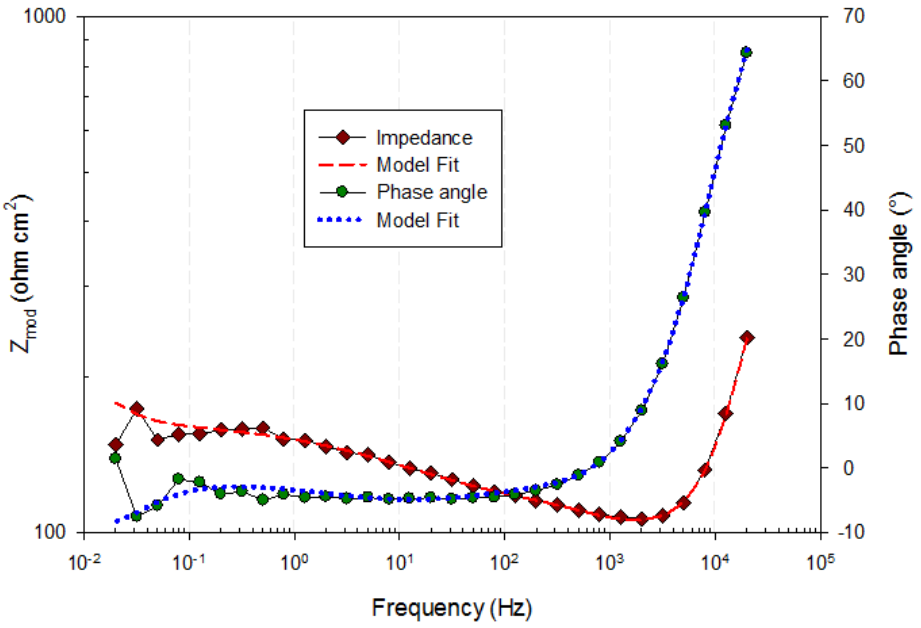

Fig. 5.62 Bode plot of concentrated light measurements with equivalent circuit fit curves at 3 V applied potential.

Table 5.27 Model fitting parameters of 3 V measurements for concentrated light and no-light.

Parameter	No-light	Concentrated light	Unit
a10	0.7972	0.4905	
a14	0.3639	1.0000	
B14	0.6284	0.0248	$s^{0.5}$
CPE-A	0.0015	0.2405	S s^{a} /cm^2
CPE-C	0.1137	0.0025	S s^{a} /cm^2
L	0.0018	0.0017	H cm^2
R-A	98.5000	54.2800	ohm cm^2
R-C	370.0000	56.3900	ohm cm^2
R-Co	102.0000	99.5800	ohm cm^2
W-M	0.0503	0.0032	S $s^{0.5}$ /cm^2
Goodness of Fit	0.0002	0.0003	

Similarly, the Warburg parameter declines from 0.2095 S $s^{0.5}$ /cm^2 to 0.0835 S $s^{0.5}$ /cm^2. It is explained that a lower Warburg parameter value designates a larger amount of mass transfer occurring. In this regard, it can be seen in Figs. 5.45 to 5.62 that concentrating the light enhances the mass transport in the PEC cell. However, in higher applied voltages such as 2.5 V and 3 V, the activation and mass transport processes yield quite similar patterns for concentrated light and no-light measurements as illustrated in Figs. 5.58 to 5.62. Different than lower voltages, the Nyquist curves of concentrated light measurements also have semi-circular patterns at higher voltages. Furthermore, the impact of photocurrents are not much distinguishable at higher voltages.

5.4 Electrochemical Ammonia Production Results

Using the equations given in the analyses section, the results obtained from ammonia production process are presented here. Some of the main input parameters used in the calculations are tabulated in Table 5.28. Here, a few of the parameters such as reaction temperature, measured voltage, and current are taken from the measurements which cause uncertainties. Therefore, the uncertainties are also calculated and depicted in the figures.

There are fundamentally two important parameters in the ammonia synthesis reaction; reaction temperature and pressure. In the selected electrochemical ammonia synthesis, the reactants gases are not pressurized. They are directly sent to the ammonia reactor. However, both the effects of the temperature and pressure are investigated here. As mentioned in the analyses section, the ammonia synthesis process is exothermic meaning that temperature increase is not favored. As shown in Fig. 5.63, the lower reaction temperature levels are desired. The changes in the efficiencies are illustrated in Fig. 5.63. At 420 K, the coulombic efficiency is calculated as 21.1% which decreases down to 2.3% at 550 K.

Table 5.28 Some of the parameters used in the ammonia production model.

Parameter	**Value**	**Unit**
Nickel electrode area	50	cm^2
Higher heating value of hydrogen	141,800	kJ/kg
Higher heating value of ammonia	22,500	kJ/kg
Lower heating value of hydrogen	119,900	kJ/kg
Lower heating value of ammonia	18,646	kJ/kg
I (Current)	0.2	A
J (Current density)	40	A/m^2
P (Pressure)	1	atm
ρ_{H_2} (Density)	0.05122	kg/m^3
ρ_{N_2} (Density)	0.7118	kg/m^3
ρ_{NH_3} (Density)	0.4337	kg/m^3
T (Reaction temperature)	473.2	K
V (Voltage)	1.401	V
T_o (Ambient temperature)	298	K

The columbic efficiency depends on the ammonia production rate and supplied current. As shown in Fig. 5.64, the production rate of ammonia gradually decreases by increasing reaction temperature which causes a decrease in efficiencies. The ammonia production rate at 485 K is calculated as 7.25 mL/h corresponding to a mass flow rate of 3.072 mg/h. It is noted that under normal conditions, the molten salt electrolyte used in the system, which is a eutectic mixture of KOH and NaOH, melt approximately at 170°C (443.15 K). Below this temperature, this electrolyte may not function however, there are other salt mixtures such as $LiNO_3/KNO_3$ which melt at lower temperatures and can be used in the reactor as electrolyte or some additives can be used to lower the melting temperature of the eutectic mixture. Therefore, the temperatures below 443.15 K are also included in the parametric study.

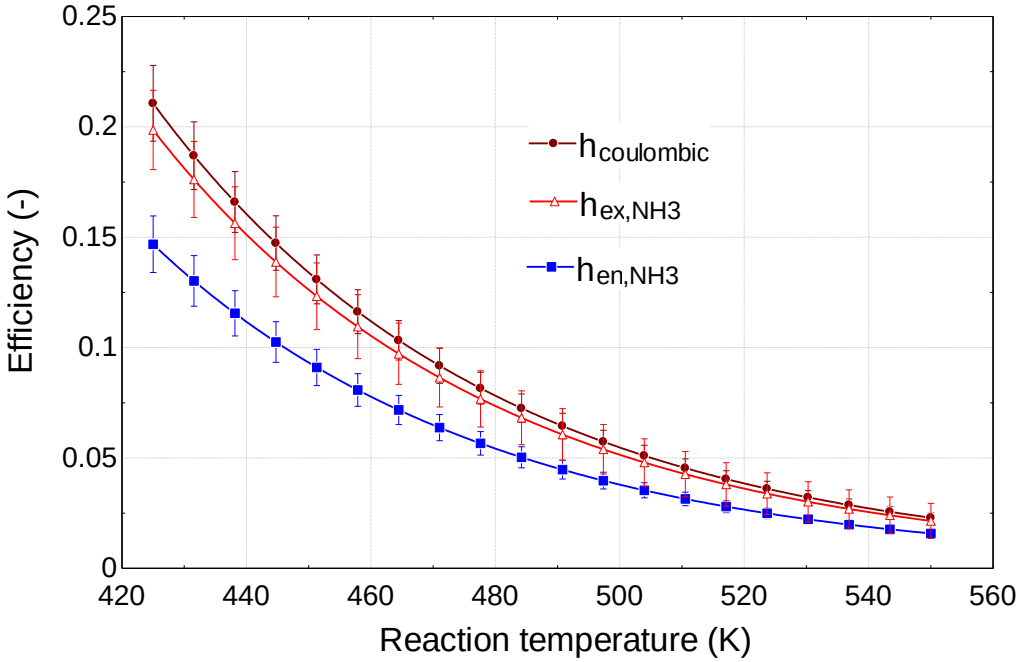

Fig. 5.63 The changes of the efficiencies by varying reaction temperature of the ammonia reactor.

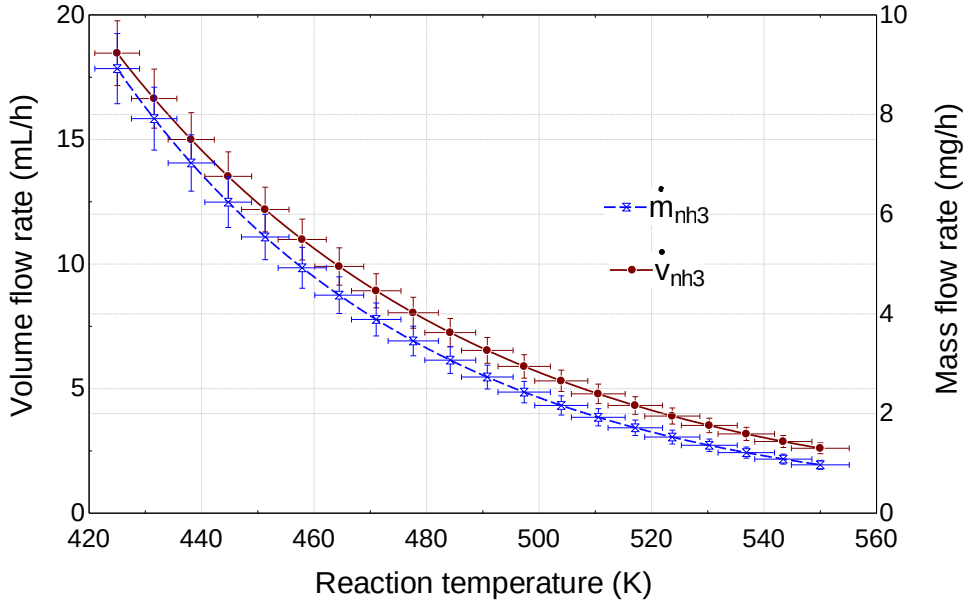

Fig. 5.64 The changes of the ammonia production rates by varying reaction temperature.

The changes in mole fractions by varying reaction temperature at chemical equilibrium are depicted in Fig. 5.65. Here, the pressures are atmospheric (1 atm). In commercial Haber-Bosch ammonia synthesis plants, the reaction temperatures are in the range of 350-550°C. As shown in Fig. 5.65, at higher temperatures, the conversion of nitrogen and hydrogen into ammonia is quite low. In the molten salt electrolyte electrochemical ammonia synthesis at 470 K, the ammonia conversion is about 0.33.

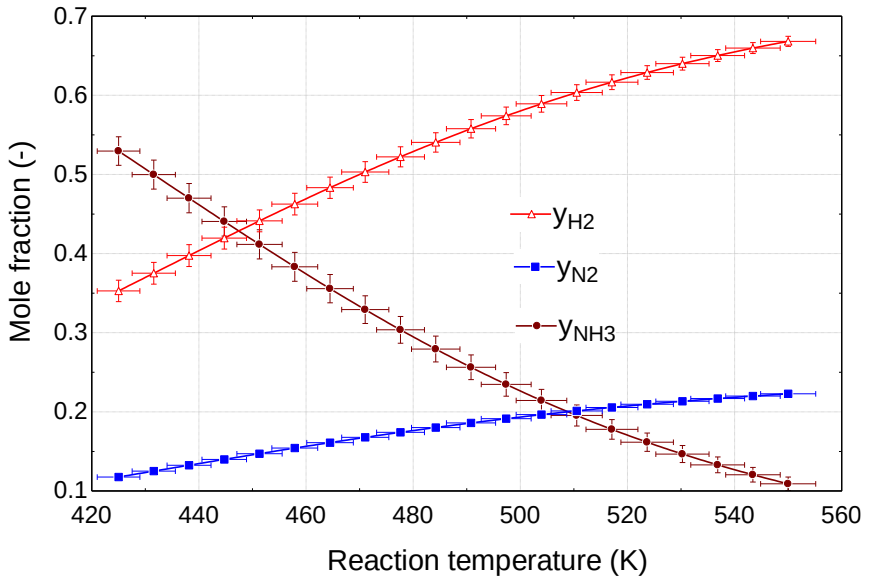

Fig. 5.65 The changes of the mole fractions in the ammonia production process by varying reaction temperature.

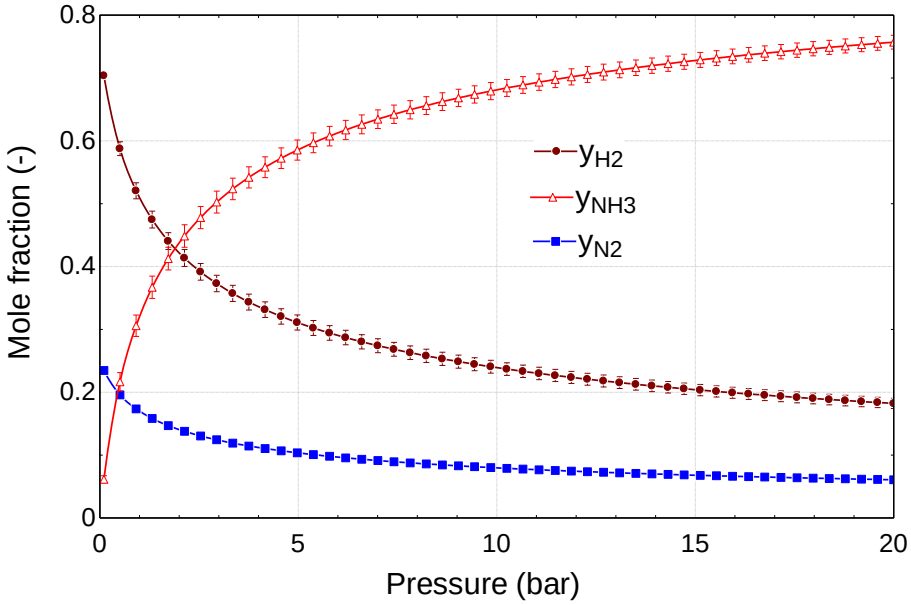

Fig. 5.66 The changes of the mole fractions in the ammonia production process by varying reaction pressure.

On the other hand, high pressures are more favorable for the ammonia synthesis as shown in Fig. 5.66. At set temperature of 473.2 K and 1 bar, the ammonia mole fraction is about 0.31 whereas it increases to 0.68 at 10 bar. In Haber-Bosch ammonia production plants, the pressures of the feed gases are quite high around 150-200 bar. Therefore, especially the gas compressors consume massive amounts of power. One of the main advantages of electrochemical ammonia synthesis is to have ambient pressure levels which eliminates the huge compressors. Although low pressures are not favored because of the reaction equilibrium, it can be compensated by lower temperatures and other catalysts.

Fig. 5.67 depicts the change of ammonia production rates by rising pressures. The pressure increase causes the density of ammonia to rise. Although the mass flow rate of ammonia production upsurges because of higher conversion rates, the rise of density is much higher causing less production volumes. At 2 bar, the volumetric flow rate of ammonia is 6.963 mL/h whereas the mass flow rate is 6.448 mg/h.

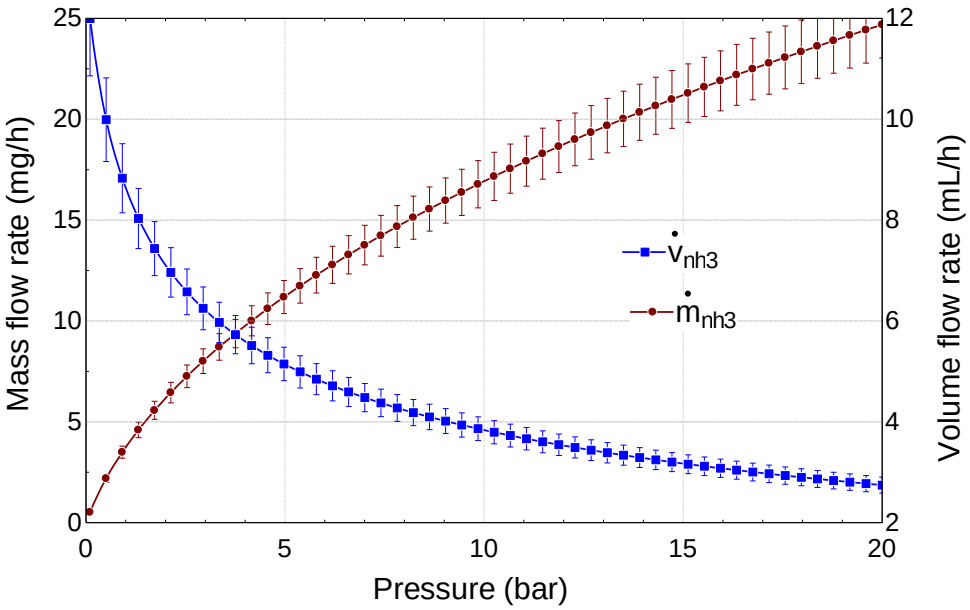

Fig. 5.67 The changes of the ammonia production rates by varying reaction pressure.

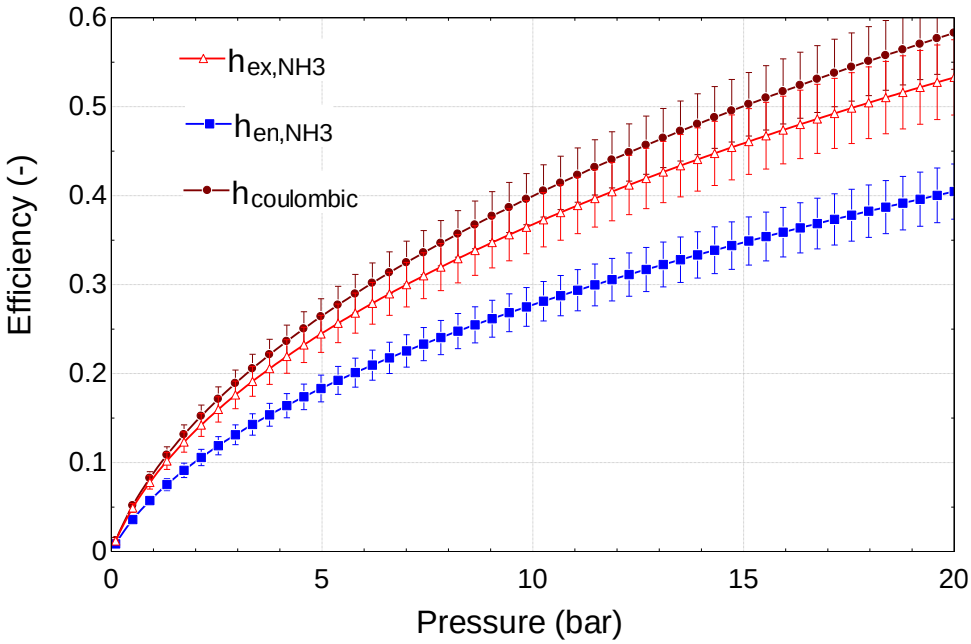

Fig. 5.68 The changes of the energy, exergy and coulombic efficiencies by varying reaction pressure.

As a result of higher conversion rates at elevated pressures, the efficiencies rise by increasing pressure as shown in Fig. 5.68. At 3.3 bar, the columbic, energy and exergy efficiencies of ammonia synthesis process are 20.56%, 14.27% and 19.12%, respectively.

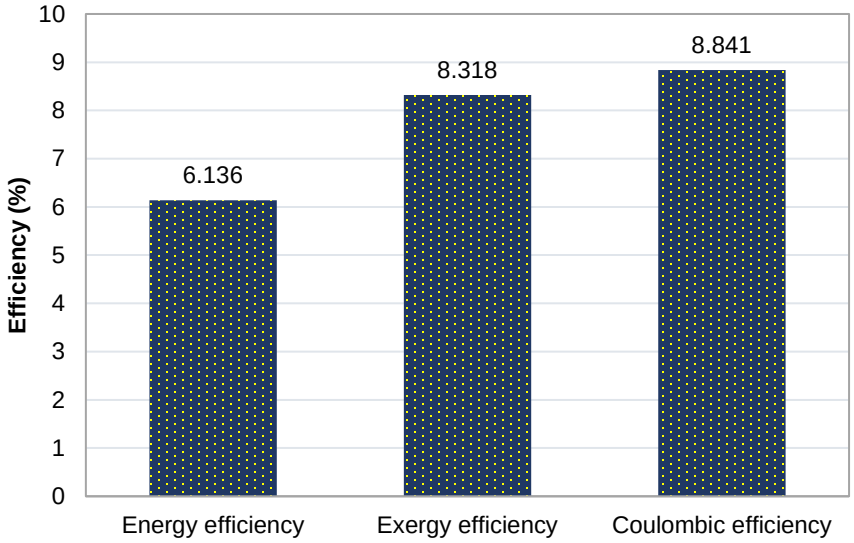

Fig. 5.69 The energy, exergy and coulombic efficiencies of the electrochemical ammonia synthesis process under given conditions.

In the given conditions at 1 atm and 473.15 K, the energy, exergy and coulombic efficiencies of the ammonia production are comparatively shown in Fig. 5.69. The exergy efficiencies are higher due to the consideration of chemical exergy of the fuels. The coulombic efficiency is calculated to be 8.8%.

The applied current is I=0.2 A ± 0.003973, the corresponding potential between the electrodes of the ammonia reactor is V=1.401±0.05545 V and the reaction temperature is set to T=473.2 K ± 4.426. The inlet mass flow rate of the nitrogen is set to 3.259 mg/h. The pressures are atmospheric pressures (1 atm). Under these conditions, the results shown in Table 5.29 are obtained from the model. The chemical equilibrium constant is calculated as 2.142 for the given temperature and pressure. The mole fractions at the chemical equilibrium are 0.51, 0.17 and 0.32, respectively for hydrogen y_{H_2}, nitrogen $y_{N_2}$and ammonia y_{NH_3}. This implies that not all hydrogen is reacted with nitrogen at once. Therefore, recycling the unreacted gases are commonly realized. The ammonia production rate is calculated to be 6.11×10^{-8} mol/s and volumetric flow rate is 8.63 mL/h. The electricity input is calculated based on the current and voltage of electrochemical reactor as 0.28 W. Using the EIS experimental data, the overpotentials are found and actual cell potential is obtained as 1.32 V.

In the experiments of ammonia synthesis, the pure alkali hydroxides NaOH and KOH each melt only at temperatures above 300°C. The individual melting temperatures of NaOH and KOH are 318°C and 406°C, respectively. Among various alternatives, these two salts melt at quite lower temperatures which is a highly desired property in order to decrease external heat energy input. Based on common materials, the NaOH-KOH eutectic is of particular attention and melts at 170°C. Ammonia synthesis rates increase when the molten hydroxide

(NaOH-KOH) electrolyte is mixed with high–surface area Fe_3O_4 to provide iron as a reactive surface and when nitrogen and hydrogen are present in the reactor. The molten salt medium is supplied electricity between two nickel anode and cathode electrodes. The mixture is prepared in the beginning by simply adding NaOH and KOH pellets in the reactor. After the salts melt, nano-Fe_3O_4 is added to the electrolyte and then stirred. When the mixture is ready, the lid is tightly closed and sealed. In order to yield NH_3 in the reactor, H_2, N_2 and nano-Fe_3O_4 are simultaneously needed.

Table 5.29 The calculated results of ammonia synthesis process including the uncertainties.

Parameter	Value	Uncertainty	Unit
$\eta_{coulombic}$	8.841	±0.7748	%
$\eta_{en_{NH3}}$	6.136	±0.5715	%
$\eta_{ex_{NH3}}$	8.318	±0.8001	%
$E_{actual_{cell_{EIS}}}$	1.323	±0.0263	V
$K_{T,P}$ (equilibrium constant)	2.142	±0.2246	-
$\dot{m}_{h2}$	0.7037	±0.02214	mg/h
$\dot{m}_{nh3}$	3.745	±0.3197	mg/h
$\dot{V}_{H_2}$	13.74	±0.4509	mL/h
$\dot{V}_{N_2}$	4.579	±0.1503	mL/h
$\dot{V}_{NH_3}$	8.635	±0.6621	mL/h
$\dot{W}_{in}$	0.2802	±0.01241	W
$\dot{n}_{H_2}$	9.70×10^{-8}	$\pm3.051\times10^{-9}$	mol/s
$\dot{n}_{N_2}$	3.23×10^{-8}	$\pm1.017E\times10^{-9}$	mol/s
$\dot{n}_{NH_3}$	6.11×10^{-8}	$\pm5.214E\times10^{-9}$	mol/s
y_{H_2}	0.5093	±0.01296	-
y_{N_2}	0.1698	±0.004321	-
y_{NH_3}	0.3209	±0.01729	-

Table 5.30 shows the experimental conditions for four different runs. Experiment 2 is performed at constant applied potential of 1.5 V whereas the others are performed at constant current in galvanostatic mode. The experimental runs have different durations because of the H_2SO_4 solution saturation which is changed every 15 minutes. Since, the production rates are given per second, the results are comparable.

Table 5.30 Experimental conditions for different runs for electrochemical ammonia synthesis.

Experiment #	Temperature (°C)	Duration (min)	Current density (mA/cm^2)	Voltage (V)
1	210	15	2	1.4
2	255	30	3	1.5
3	215	45	2	1.3
4	220	25	2.5	1.55

The temperatures given in the table are average temperatures because, the temperature controller is the on/off type and keeping the temperature constant causes fluctuations. For each run, different ammonia trapping H_2SO_4 solution is used. The unreacted H_2 is also measured using a hydrogen sensor embedded to Arduino board which shows the portion of H_2 which does not react. Note that water is not preferred to be added into the molten salt mixture because NH_3 is soluble in water which may cause some of the formed ammonia to be dissolved in the eutectic mixture before arriving the ammonia collection tank.

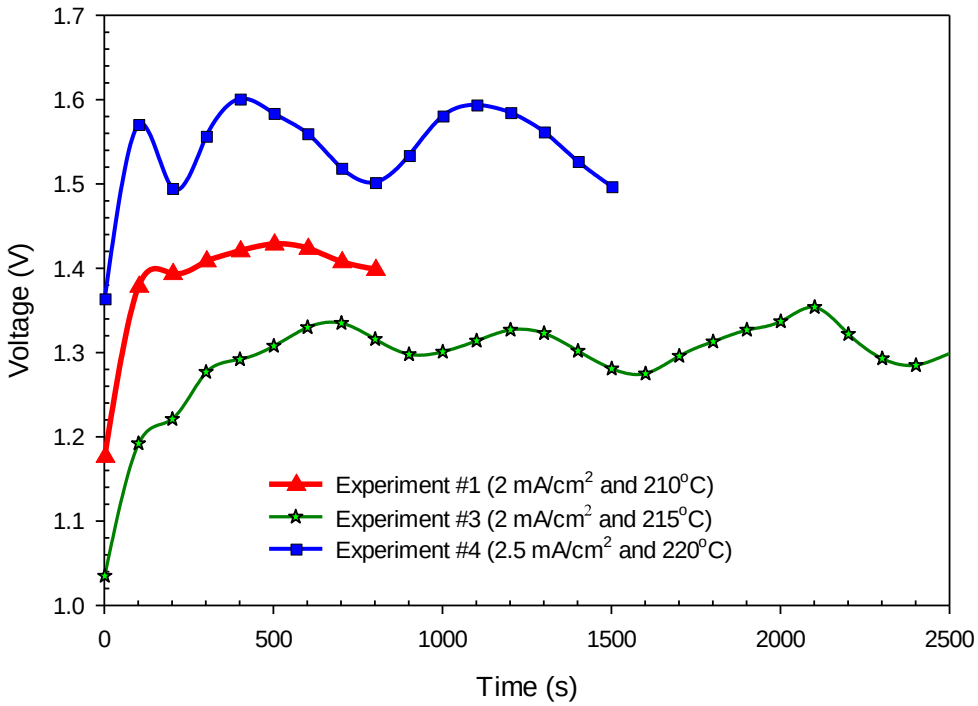

Fig. 5.70 The relationship between voltage and time during several experimental runs at different applied currents and temperatures for electrochemical synthesis of NH_3 using N_2 and H_2 with nano-Fe_3O_4 in a molten salt hydroxide electrolyte.

The required cell voltage to initiate the reaction of nitrogen and hydrogen in molten hydroxide at 210°C in the existence of nano-Fe_3O_4 is measured to be on average 1.4 V when the applied current is 200 mA between the 100 cm^2 Ni electrodes in the molten NaOH-KOH electrolyte. The potential increases to 1.54 V when the current density is increased to 2.5 mA/cm^2 at 220°C as shown in Fig. 5.70.

At 2 mA/cm^2 and 210°C, ammonia is synthesized at a rate of 6.54×10^{-10} mol/s cm^2. At 2.5 mA/cm^2 and 220°C, the ammonia evolution rate decreased to 4.9×10^{-11} mol NH_3/s cm^2. At 215°C in a eutectic $Na_{0.5}K_{0.5}OH$ electrolyte with suspended nano-Fe_3O_4, it is observed that at 2 mA/cm^2 applied current, NH_3 is generated at a coulombic efficiency of about 6.3%, which declines to about 0.56% at 2.5 mA cm^2 in the reactor temperature of 220°C. Constant current electrolysis at 2 mA/cm^2 and 2.5 mA/cm^2 are driven at 1.3 V and 1.54 V, respectively at different temperatures as depicted in Fig. 5.70.

It is also observed in the experiments that even though the reactor temperature is below 200°C, ammonia is generated with a similar production rate to above 200°C. The fluctuations in the potentials are caused by the temperature on/off processes to keep the temperature constant during the experiments. When the heater is on, the required potential to drive the reaction decreases as seen in Fig. 5.70. The potential gradually declines from 1.6 V to 1.5 V during the experiment at constant current density of 2.5 mA/cm^2. It is observed in the experiments that lower current density and lower temperature improve the stability of the rate of NH_3 evolution. Fig. 5.71 shows the current density across the electrodes of the reactor when constant voltage of 1.5 V is applied.

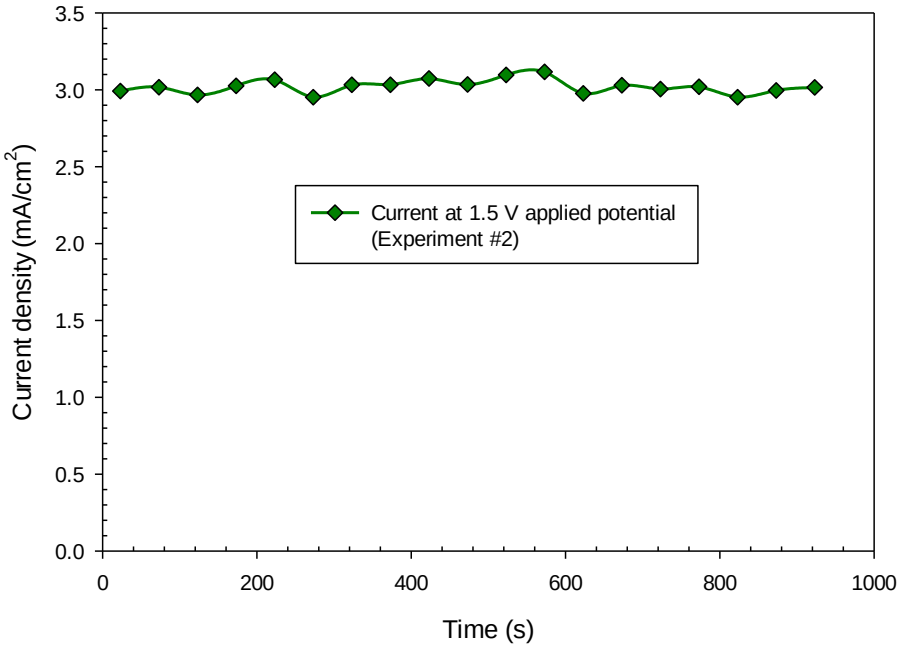

Fig. 5.71 Current density at 1.5 V applied voltage for 100 cm^2 Ni electrodes of electrochemical NH_3 synthesis reactor.

In this case, on average 3 mA/cm^2 current density is measured where the reaction temperature is considerably higher than other experiments which is about 255°C. The greater ammonia generation rate at lower voltages can be because of the lower hydrogen ion stream at the cathode which provides more time for generation of ammonia according to reaction.

Higher NH_3 synthesis rates are obtained within the first hour of the experiments as seen in Fig. 5.72. By the end of the experiment which is close to about two hours, 5.69 mL of NH_3 is formed. The measured columbic and energetic efficiencies of ammonia evolution in time at different temperature levels and conditions in NaOH-KOH molten electrolyte are comparatively illustrated in Fig. 5.73. The generated NH_3 is trapped and measured in a room temperature dilute H_2SO_4 trap. A non-dilute H_2SO_4 trap is also tried before the experiments reported here to understand the absorptivity of the solution. However, the ammonia readings are not successful in this case. Hence, dilute H_2SO_4 solutions are utilized for the reported experiments. The conversion efficiency is not only dependent on the hydrogen amount but also

amount of catalyst available to stimulate the conversion of N_2 and H_2 into NH_3. In order to make sure that there is enough N_2 to be reacted with supplied H_2, the supplied volume of N_2 is kept quite higher than H_2.

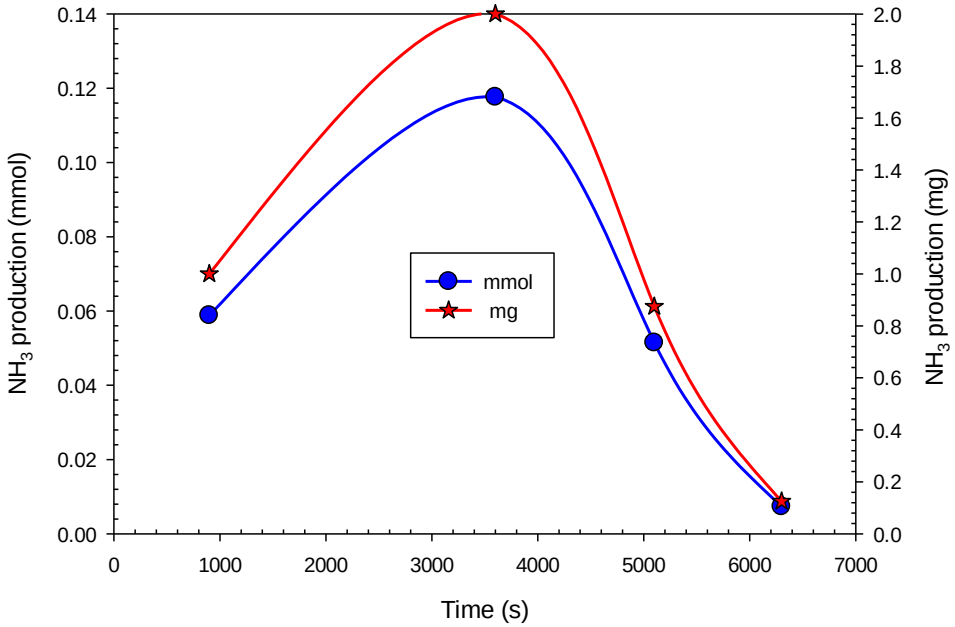

Fig. 5.72 Cumulative NH_3 production amount by electrochemical synthesis using N_2 and H_2 with nano-Fe_3O_4 in a molten salt hydroxide electrolyte.

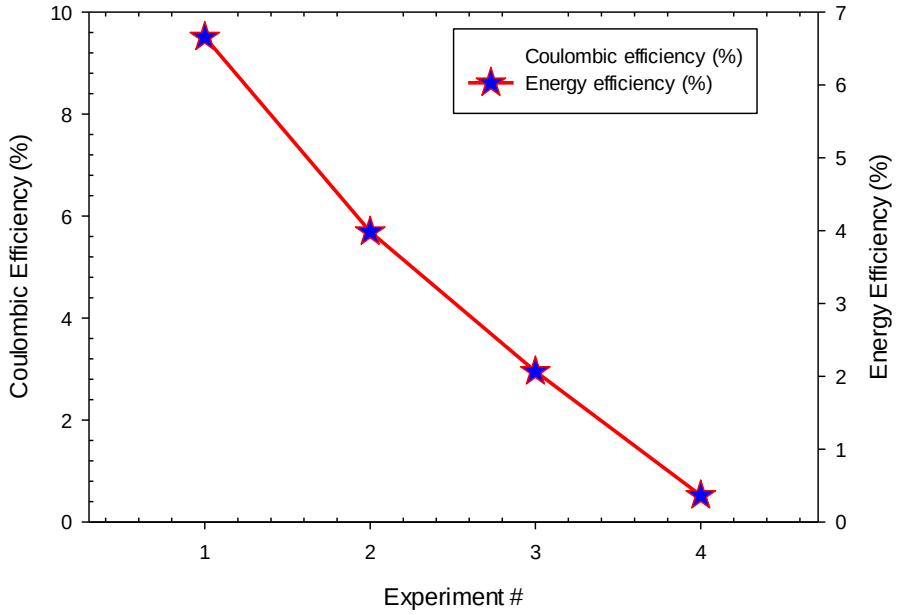

Fig. 5.73 Coulombic and energy efficiencies of several experimental runs for electrochemical NH_3 synthesis using N_2 and H_2 with nano-Fe_3O_4 in a molten salt hydroxide electrolyte.

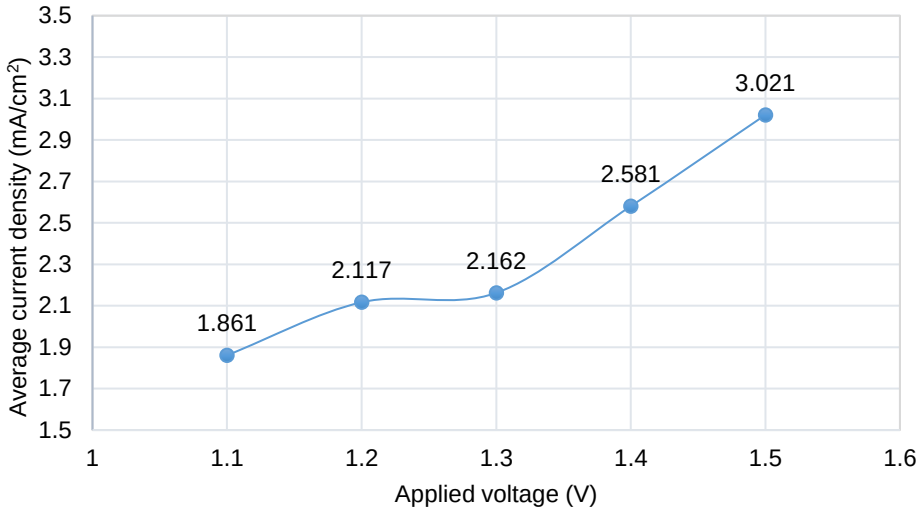

Fig. 5.74 Applied potential-current density relations at 200°C for electrochemical NH_3 formation using N_2 and H_2 with nano-Fe_3O_4 in a molten salt hydroxide electrolyte.

In order to understand the current-voltage characteristics at lower temperature levels such as 200°C, the applied potentials are varied between 1.1 V and 1.5 V as shown in Fig. 5.74. At 200°C and 1.3 V, the average current density is 2.16 mA/cm^2 whereas it is about 2 mA/cm^2 at 215°C. Note that this is not recorded using the linear voltage sweeping. Rather, at different applied current densities, the corresponding voltage values are recorded. The given temperatures and current densities are the average values where there are fluctuations because of the temperature controller.

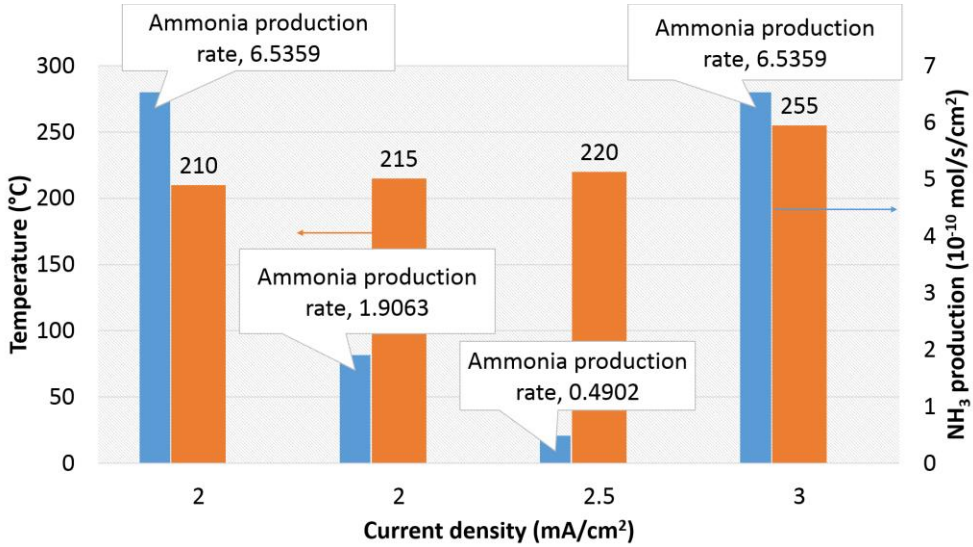

Fig. 5.75 Change of electrochemical NH_3 formation rates depending on the applied current densities and reactor temperature using N_2 and H_2 with nano-Fe_3O_4 in a molten salt hydroxide electrolyte.

The variations of NH_3 formation rates at different current densities and temperature levels are comparatively shown in Fig. 5.75. The figure reveals that the temperature and current density are not the sole parameters effecting the performance of the reaction. Although the temperature is high at 2.5 mA/cm^2 current density, the NH_3 formation rate is low. The summary of the ammonia synthesis experiment results are tabulated in Table 5.31.

Table 5.31 Summary of the experimental results showing the NH_3 formation rates and efficiencies.

Experiment #	NH_3 formation rate (mol s^{-1} cm^{-2})	NH_3 mass flow rate (g/min)	Coulombic efficiency (%)	Energy efficiency (%)
1	6.54×10^{-10}	6.67×10^{-5}	9.45	6.65
2	6.54×10^{-10}	6.67×10^{-5}	6.30	3.98
3	1.91×10^{-10}	1.94×10^{-5}	2.75	2.06
4	4.90×10^{-11}	5.00×10^{-6}	0.56	0.36

In contrast, at higher current densities at 3 mA/cm^2 (although there is higher temperature levels about 255°C), the NH_3 formation rate is high corresponding to about 6.6×10^{-10} mol s^{-1} cm^{-2}. The differentiations might be caused by the catalyst saturations as well as the changes in supplied H_2 rates.

After this step, the electrochemical ammonia synthesis reactor is integrated to photoelectrochemical hydrogen production cell to develop a clean and environmentally friendly ammonia production technique.

5.5 Integrated System Results

The integrated system consists of mainly 5 sub-systems as illustrated in Fig. 5.76. Each unit is individually analyzed and evaluated previously. In this section, the results combining all these units are presented and discussed.

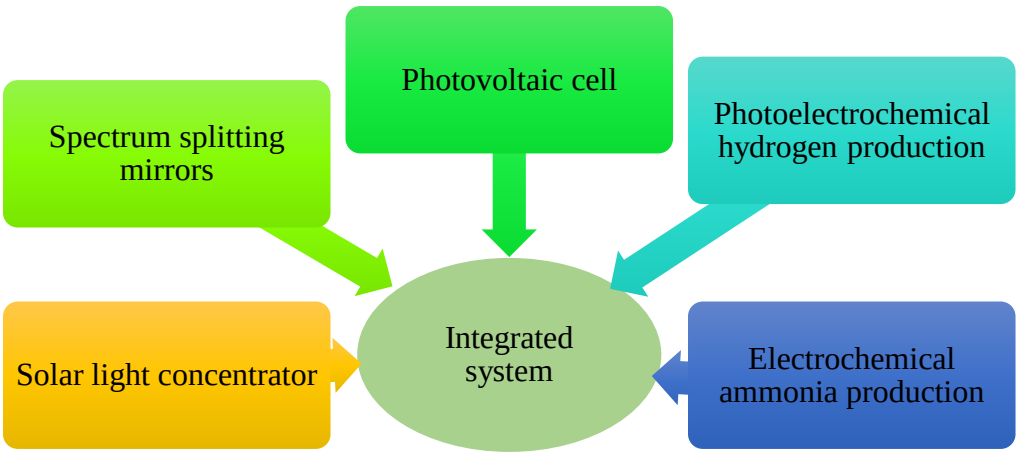

Fig. 5.76 The sub-system constituting the integrated system.

The dielectric mirror is characterized using the spectrometer and solar simulator under artificial light. The dielectric mirror is placed 45°. The transmitted and reflected spectra are measured as illustrated in Fig. 5.77 and 5.78.

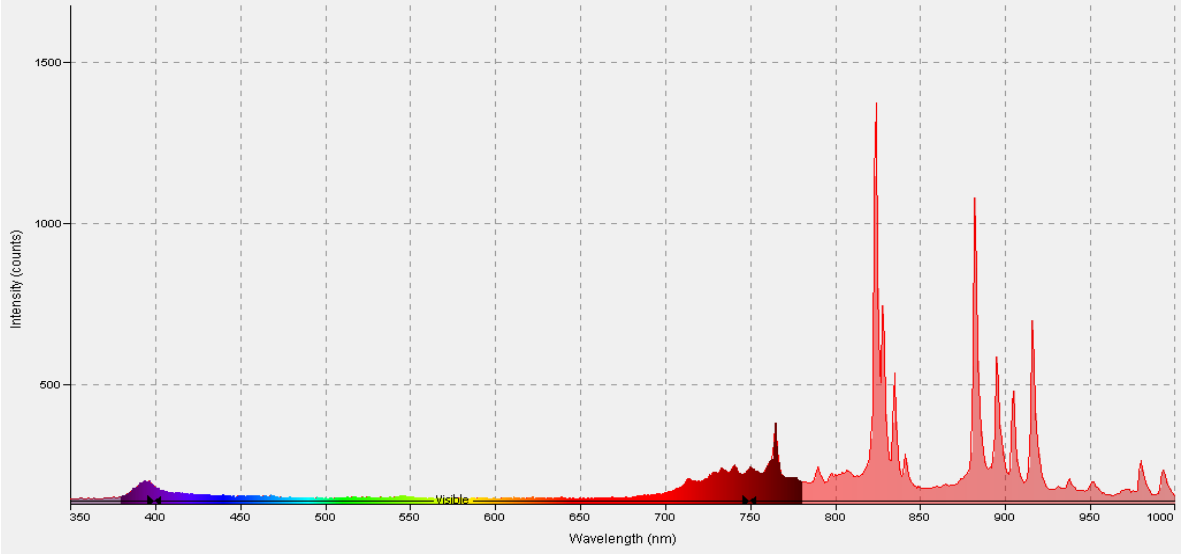

Fig. 5.77 Transmitted beam of the cold mirror at 45° under artificial light.

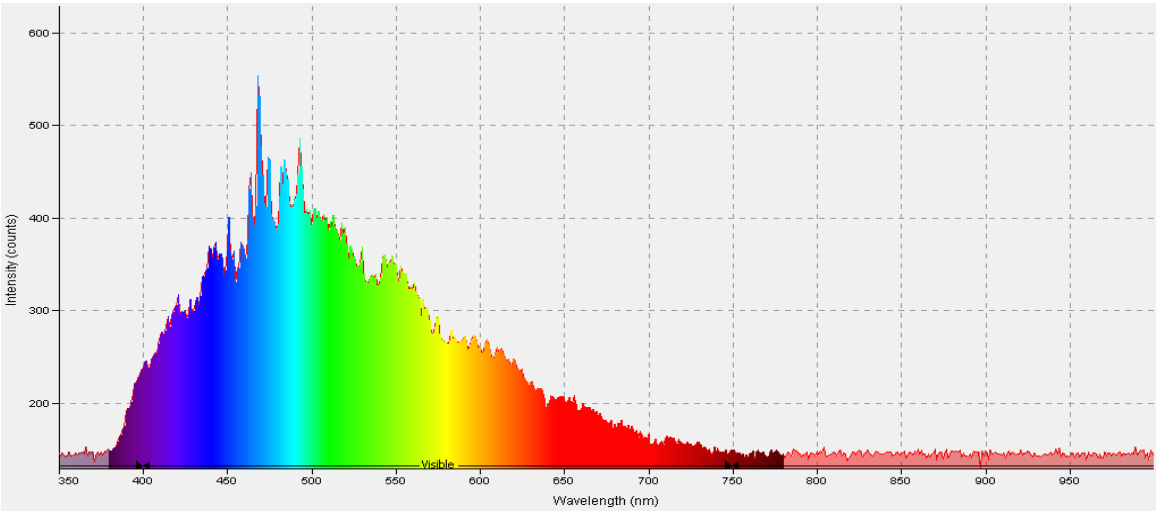

Fig. 5.78 Reflected beam of the cold mirror at 45° under artificial light.

From Figs. 5.77 and 5.78, it is observed that when the mirror is placed at 45 degrees the shape of the spectrum is very similar to the reference spectrum, but the intensity of light decreases as the wavelengths >700 nm are divided. This is the behavior expected from the graph provided by the manufacturer. In the 45° angle, a very small part of the spectrum below 400 nm is transmitted confirming the specifications given by the manufacturer. These measurements are taken using the solar simulator as the source of light and revealed the behavior of the spectrum through the mirror with the manufacturer's specifications. These results are used in the following analyses to model the spectrum splitting mirror.

In Fig. 5.79, the solar light intensities and spectral distribution within the integrated system are illustrated. As mentioned earlier, the spectrum is split below 700 nm which is utilized for photoelectrochemical hydrogen production. Since the PEC system has Cu_2O as the

photocathode, above 650 nm is not captured. Reception of above 700 nm for the PEC reactor would result in unnecessary heating as well as higher degradation. As shown in Fig. 5.79, the concentration ratio from ambient irradiance to dielectric mirrors is about 6.2. Above 700 nm, the PV cell receives the solar light spectrum and generated electricity.

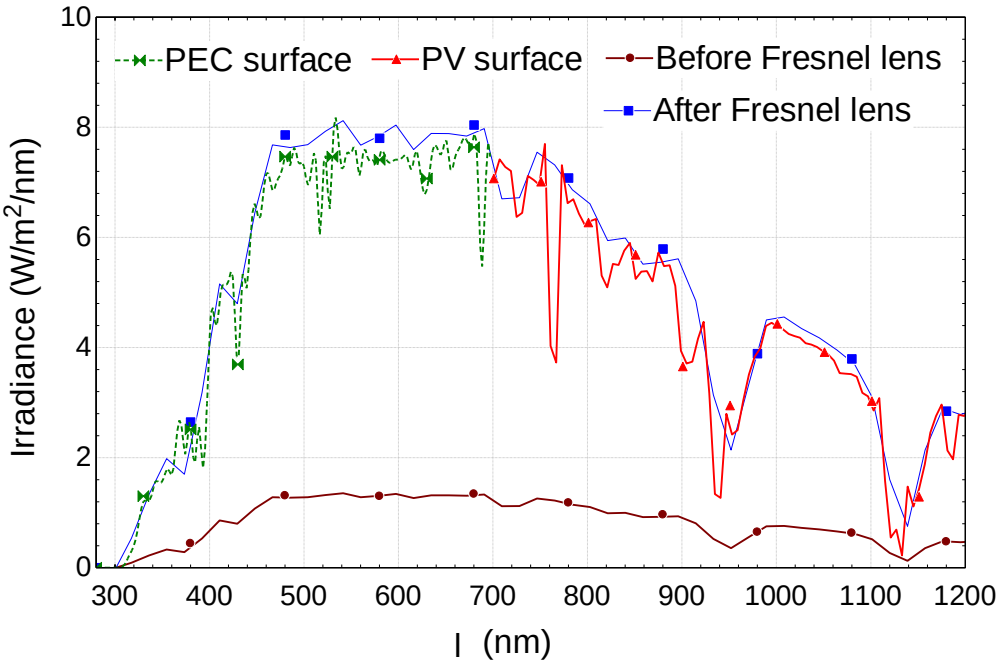

Fig. 5.79 The spectrum distribution within the system showing the portions received by each component.

The total currents including the externally supplied and photogenerated current are shown in Table 5.32. The external current is supplied by potentiostat device. The photocurrent increases to 3.75 mA/cm^2 under concentrated and split spectrum light.

Table 5.32 Photogenerated current and total current values for the integrated system.

Current	Value	Unit
Photogenerated current (J_{ph})	18.76	A/m^2
Photogenerated current under concentrated light ($J_{ph_{Conc}}$)	37.51	A/m^2
Total current (J)	98.76	A/m^2
Total current under concentrated light (J_{Conc})	117.5	A/m^2

Based on the received solar spectrum by the PEC reactor, the calculated hydrogen production rates are shown in Table 5.33. The light absorption processes are named based on the state points within the system. The solar light firstly hits on the Fresnel lens (#1) and concentrated on the dielectric mirrors (#2). The efficiency of this process is calculated based on the surface areas of these components as 52.71% as shown in Fig. 5.80.

Table 5.33 The hydrogen production rates in the PEC reactor under ambient and concentrated light conditions.

Parameter	Value	Unit
Hydrogen volumetric flow rate	19.77	mL/min
Hydrogen volumetric flow rate under concentrated light	24.27	mL/min

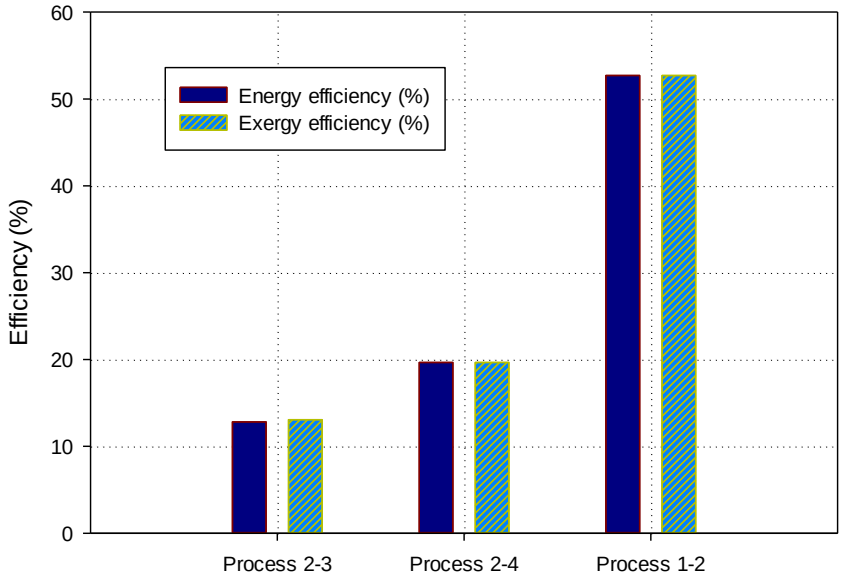

Fig. 5.80 The overall energy and exergy efficiencies of light conversion processes in the integrated system.

After the dielectric mirror, a portion of the light is reflected to the PEC reactor surface (#3) and some portion is transmitted to the PV cell surface (#4). The exergy efficiencies of process 2-3 and process 2-4 are respectively calculated as 13.1% and 19.7%. The efficiencies are lower compared to process 1-2 because the spectrum is separated. These efficiencies represent only the light conversion processes. The overall integrated system efficiency considers the products as useful outputs which are photoelectrochemically produced hydrogen and photovoltaic electricity production. On the other hand, the input is the ambient irradiance on the Fresnel lens.

The overall energy and exergy efficiencies of the integrated system for hydrogen production are found to be 6.7% and 7.5%, respectively as illustrated in Fig. 5.81. It is emphasized that even though the sole PEC photocurrent production energy efficiency is 2.7% and solar-to-hydrogen efficiency is 5.5%, the integrated hydrogen production system efficiency is higher because of mainly the following facts:

- Solar light is concentrated, hence more energy is absorbed by each component,
- The spectrum is divided into two portions in which only useful parts are used (which would be wasted otherwise),
- Photocurrent generation hence hydrogen production is higher in concentrated light,
- Photovoltaic cell efficiency and electricity production is higher.

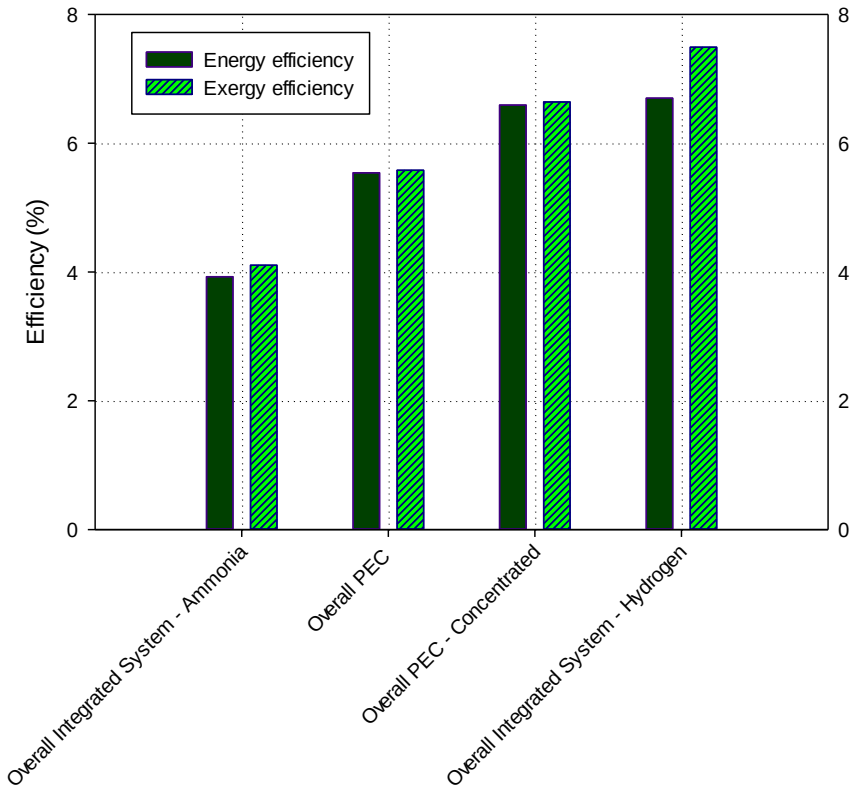

Fig. 5.81 The overall energy and exergy efficiencies of integrated hydrogen and ammonia production processes.

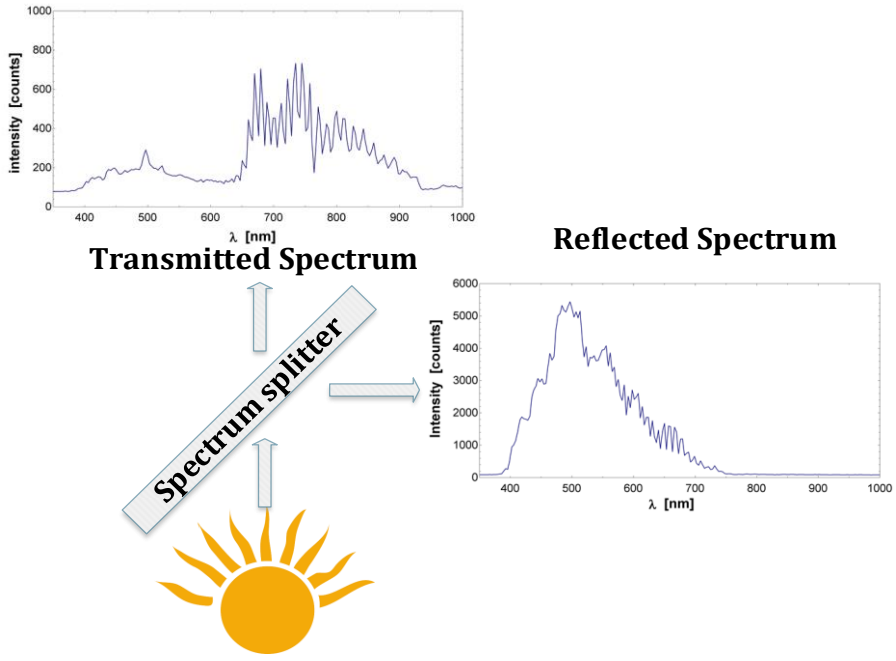

Fig. 5.82 The reflected and transmitted spectrum by the cold mirror under actual sunlight.

Furthermore, the overall ammonia production system energy and exergy efficiencies are found to be 3.92% and 4.1%, respectively shown in Fig. 5.81. It is expected to be lower than PEC hydrogen production efficiency since hydrogen is reacted with nitrogen in another reactor which causes additional losses.

After modeling results, in this section, the experimental results of the integrated system including the electrochemical ammonia production are presented. First of all, the performance and behavior of the dielectric mirrors are evaluated under actual sunlight which is previously performed under solar simulator light. The incident angle of the ray of light that hits the mirror has an impact on the reflected and transmitted beam. It is observed that to mount the mirror at an angle of 45° provides better results (transmittance and reflectance) as shown in Fig. 5.82. The behavior of the cold mirrors are similar to what is given by the manufacturer. It is noted the mirrors does not absorb a significant amount of light's energy and hence their temperatures are not expected to rise to critical levels for concentrated light measurements.

The spectral irradiance per wavelength of the components in the system is determined. The total irradiance received by each sub-system are calculated. The results obtained are presented in Table 5.34 and Fig. 5.83.

Table 5.34 Measurement results of irradiance at each state and corresponding incoming energy rates on each unit.

	Ambient (#1)	**Concentrated (#2)**	**Reactor (#3)**	**PV (#4)**
Measured Irradiance (W/m^2)	676.6	9330	6113	1075
Area (m^2)	0.8761	0.0266	0.02	0.04085
Energy rate (W)	592.8	248.2	122.3	43.93
Exergy rate (W)	563.0	235.7	116.2	42.6

The measurements with the spectrometer are based on the spectrum range from 400 to 1000 nm (because of spectrometer limit), and this portion of the spectrum represents almost 75% of the entire energy in light. The energy received by the concentrated area and the PV are in fact higher since infrared spectrum is not considered, however the energy on the reactor remains same since the cold mirror only reflects wavelengths from 400 to 700 nm as shown in Fig. 5. 83. The solar light is concentrated more than ten times using the Fresnel lens. The PEC reactor receives the higher amount of energy corresponding to 116.2 W. In case the PEC reactor is used without any concentration and spectrum splitter, the amount of exergy rate would be about 64.22 W. This implies almost two times higher power.

Fig. 5.84 shows the ambient and module temperatures measured during the PV characterization experiment under non-concentrated light. The temperatures are measured to remain fairly constant throughout the test. The average PV temperature(T_{PV}) is 54.5°C and the average ambient temperature ($T_{ambient}$) is 28.0°C.

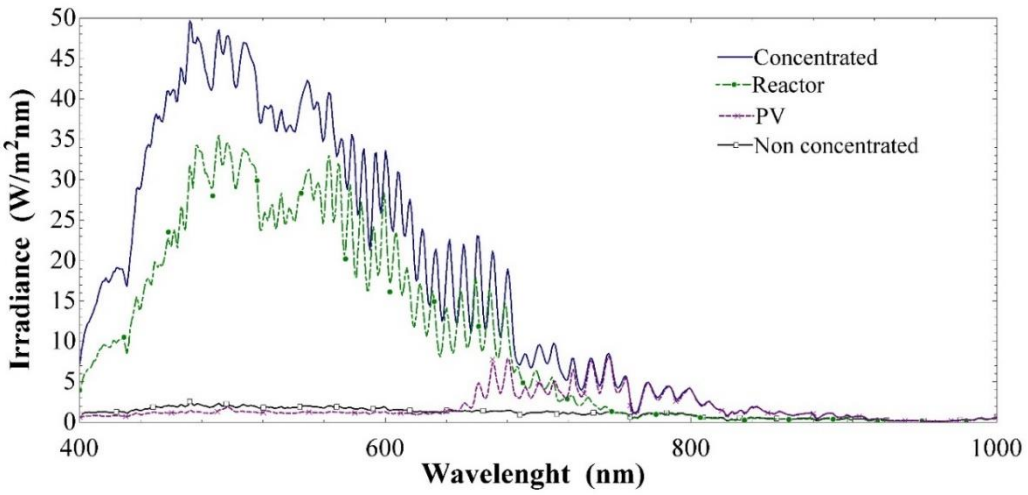

Fig. 5.83 Measured irradiance at each state point of the system under actual sunlight.

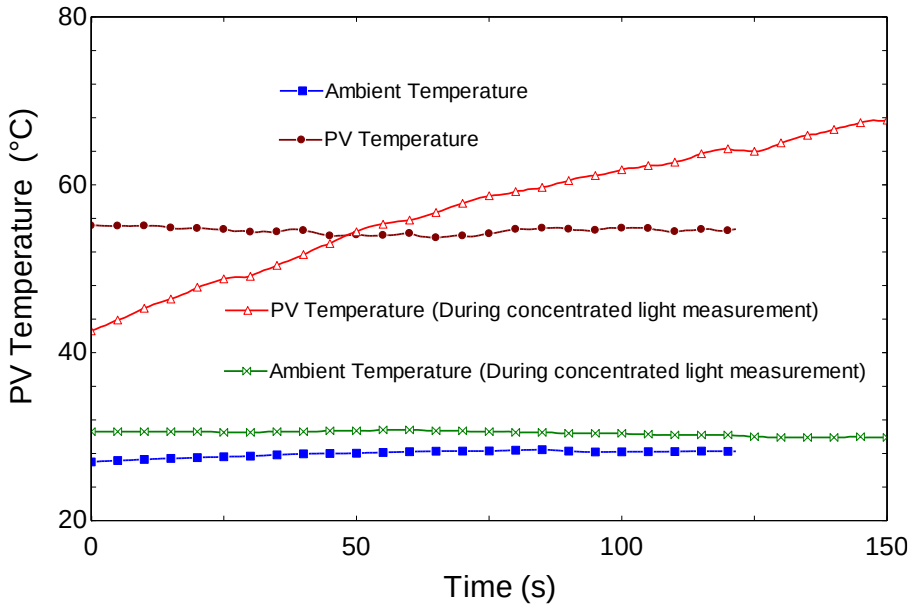

Fig. 5.84 Temperature measurement under non-concentrated sunlight and concentrated light during larger PV characterization.

As shown in Fig. 5.85, the current-voltage and power characteristics of the PV module are measured. The open circuit voltage is about 20 V and the short circuit current is about 0.35 A. The ambient and module temperatures are also measured under concentrated light. However the module temperature does not reach steady-state before the end of the experiment as shown in Fig. 5.84. The average ambient temperature ($T_{ambient}$) is measured as 30.4°C. The maximum module temperature is 70.8°C. The operating temperature of PV cell is quite important aspect because usage of solar concentrator can rise the PV temperatures up to 80°C which would lower the long term performance. The resulting efficiencies are listed in Table 5.35 including the total solar power input.

Table 5.35 The results of the PV cell performance under ambient and concentrated light.

Parameter	Ambient	Concentrated light	
Irradiance (W/m^2)	916	865	
Maximum Power Output (W)	4.56	7.27	
Open-Circuit Voltage (V)	19.84	19	
Short-Circuit Current (A)	0.353	0.716	
Fill Factor (%)	0.652	0.534	
Energy Input (W)	37.42	56.16	
Efficiency (%)	12.2	η_{PV}=12.8	η_{CPV} = 16.5

Under the concentrated light, the power output of the PV module increases although the higher energy spectrum is not utilized by the PV. The short circuit current is about 0.7 A and open circuit voltage is about 19 V as shown in Fig. 5.85. It is observed in the results that it is succeeded to obtain higher energy in every component by concentrating and splitting the light. In addition, the splitting of the spectrum by the mirror helps to achieve higher efficiencies with a low cost cold mirrors. Fig. 5.85 presents the voltage-current characteristics of the PV module under concentrated and ambient conditions.

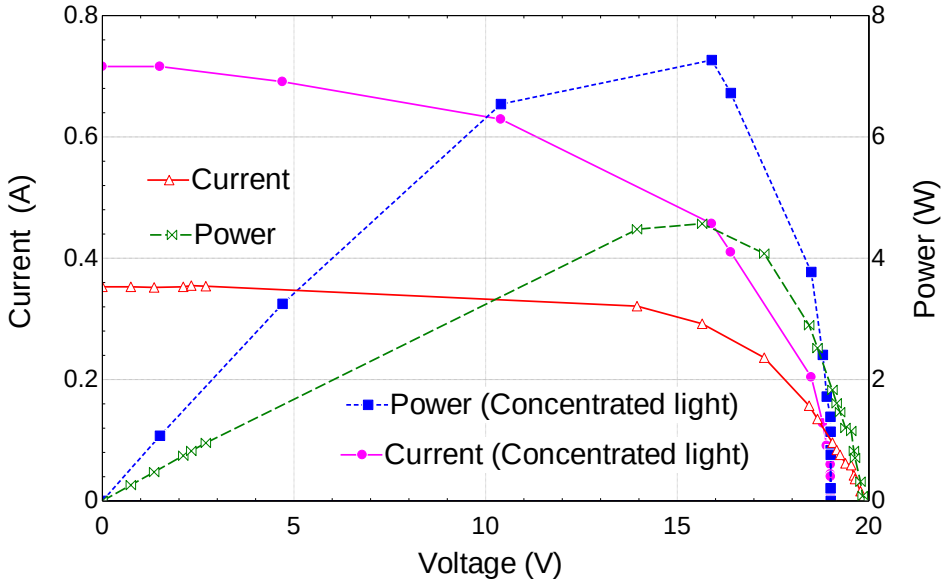

Fig. 5.85 Current-voltage and power curve under concentrated sunlight and ambient conditions for larger PV.

In the concentrated light measurements, the energy input into the entire system (E_1) is now the irradiance (I_{rad}) multiplied by the area of the lens ($A_{lens} = 0.8761\ m^2$). In order to calculate the efficiency of the PV under concentrated sunlight (η_{CPV}) the incoming energy at state 4 is required (E_4). As the results illustrate, the maximum power output of the PV module increases from 4.56 W in ambient irradiance to 7.27 W in concentrated sunlight at state 4. The power output under concentrated sunlight is measured under lower solar irradiance (865 W/m^2) than the ambient test (916 W/m^2). This increase in power output is mainly due to the increase

in current at maximum power output which almost doubled between the two tests. The voltage at maximum power output is approximately constant. The energy efficiency of the PV module also increases from 12.2% to 16.5% for concentrated sunlight case.

The energy and exergy efficiency values of all sub processes are illustrated in Fig. 5.86. The energy efficiencies from non-concentrated condition to dielectic mirror and dielectric mirror to the PEC are calculated to be 41.9% and 49.3%, respectively. In addition, the energy efficiency after dielectric mirror to photovoltaic module is about 17.7%. Note that that in this experiment, only one dielectric mirror is used which means that the energy received by the mirror is lower than the one which uses six mirrors in total. This results in a higher process 2-3 efficiency than six mirrors. As noted before, these are light conversion efficiencies. In addition, due to the limited spectrum considered in the model where it is set up to 1200 nm, the variations are possible. However, in the experiments, the wavelengths above 1200 nm can also be absorbed together with diffuse radiation which can affect the light conversion efficiency.

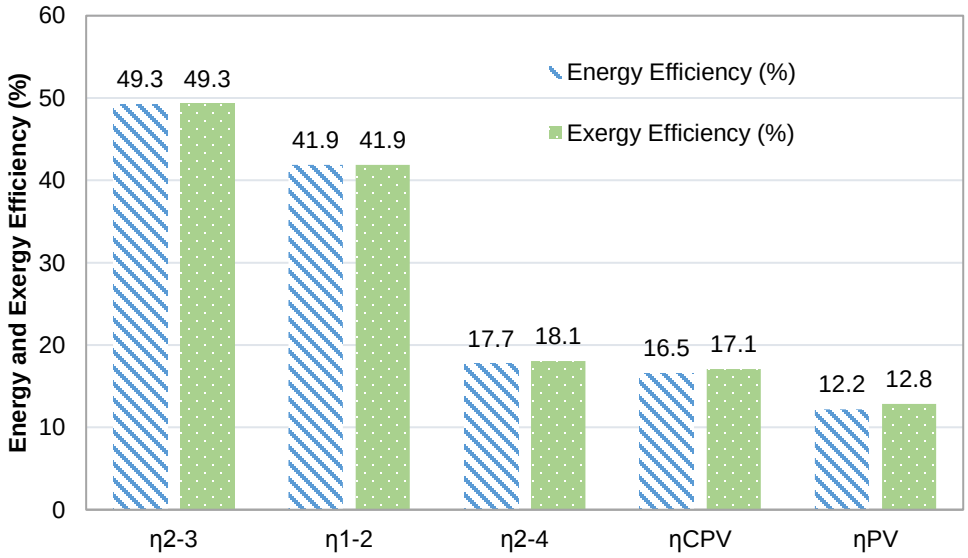

Fig. 5.86. Energy and exergy efficiency values of sub-processes, PV and CPV.

After the characterization of the light and system components, the hydrogen production tests are conducted. The photoelectrochemical cell having Cu_2O coated cathode plate is tested for photoelectrochemical characterization at 1.7 V to 3 V as shown in Fig. 5.87. It is observed that at higher applied voltages, the effect of photocurrent diminishes. The hydrogen evolution rate improves by rising voltage.

Furthermore, the obtained photocurrent densities are shown in Figs. 5.88 and 5.89 for 1.7 V and 3 V, respectively under concentrated and non-concentrated light conditions.The accumulated charges during the hydrogen production experiment at 1.7 V are calculated to be 89.9 C and 108.1 C, respectively for concentrated light and non-concentrated light. Similarly, for 3 V measurements, the accumulated charge is 555 C for concentrated light and 547 C for non-concentrated light. The maximum photocurrent densities for 1.7 V and 3 V are observed

to be 0.5 mA/cm^2 and 0.25 mA/cm^2, respectively. During electrochemical ammonia synthesis, to satisfy high hydrogen feed rates, the applied potential is selected to be 3 V.

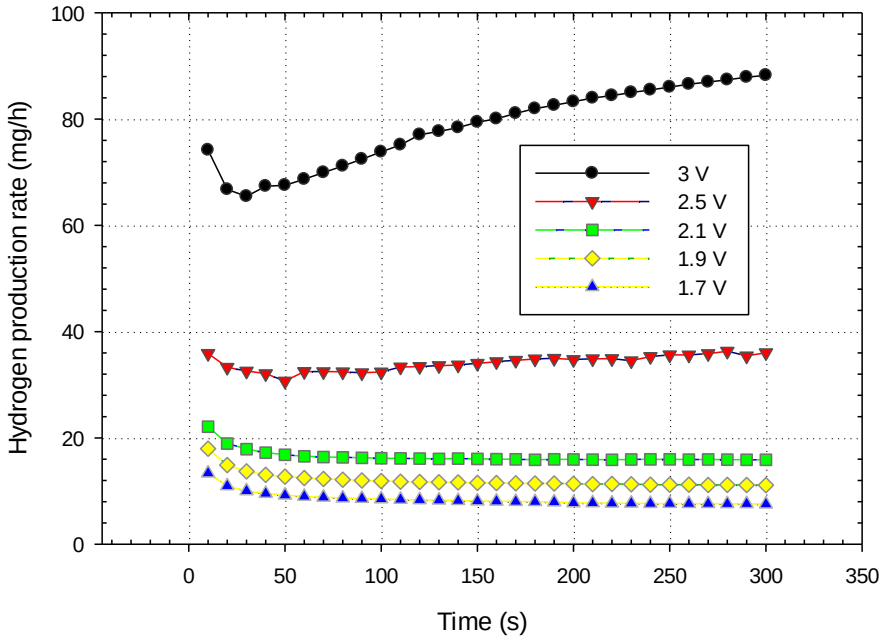

Fig. 5.87 The comparison of hydrogen evolution rates at different applied potentials under concentrated light in the integrated system.

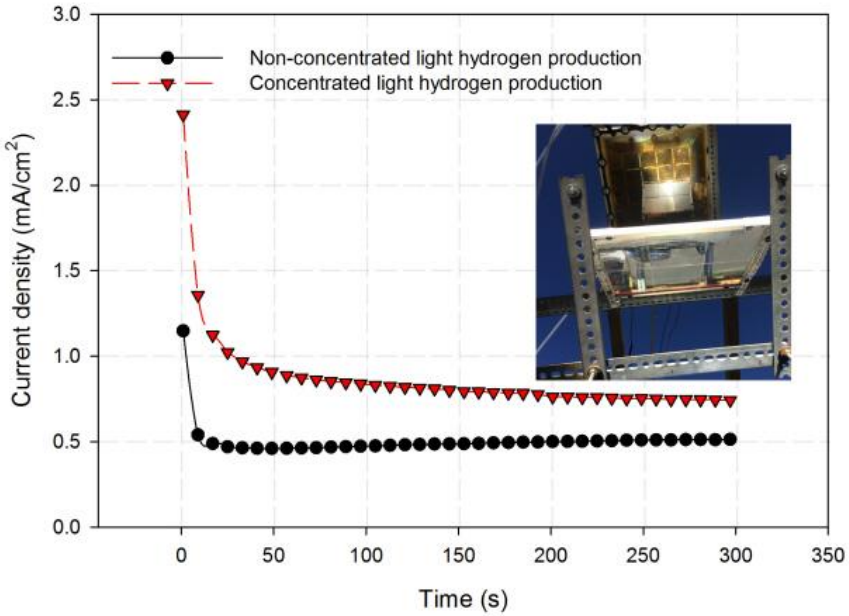

Fig. 5.88 Photocurrent densities obtained during photoelectrochemical hydrogen production under concentrated light and solar light splitting at 1.7 V applied potential.

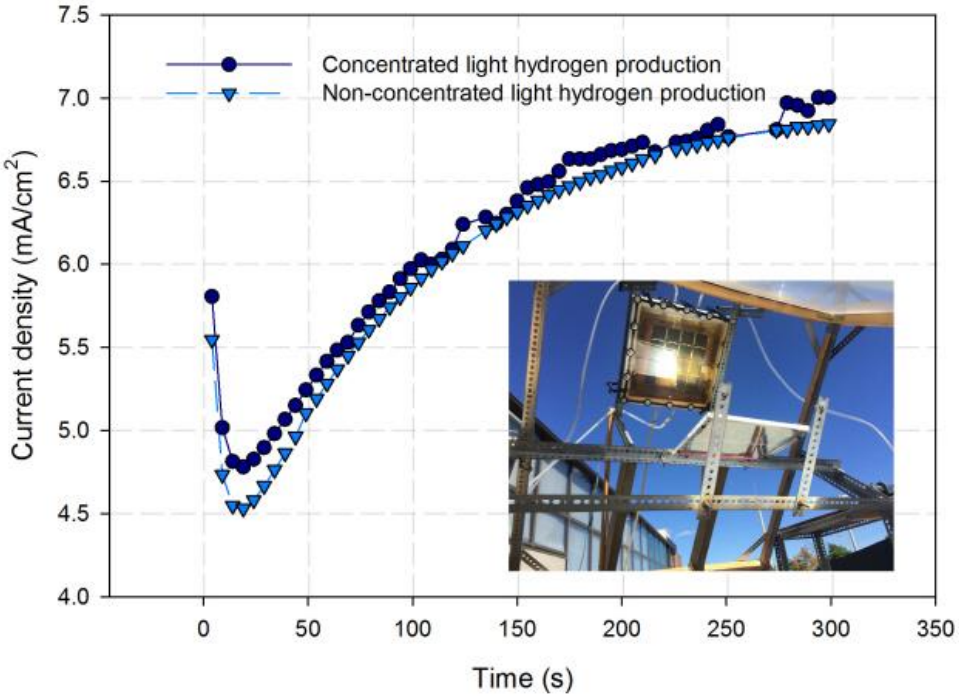

Fig. 5.89 Photoelectrochemical hydrogen production using concentrated light and solar light splitting at 3 V applied potential during electrochemical ammonia synthesis.

The average current and hydrogen evolution rate at 3 V are measured as 1.85 A and 14.2 mL/min and 1.82 A and 13.8 mL/min for concentrated and non-concentrated light measurements, respectively. The supplied hydrogen to the ammonia reactor is measured to be 10 mL/min on average because of possible losses in tubing.

Table 5.36 tabulates the experimental conditions and yielded results for two different runs which are performed at constant current modes. Test 1 is performed at current density of 9 mA/cm^2 (0.225 A in total) and Test 2 is performed at 6.2 mA/cm^2 (0.155 A in total) current density. The temperatures are average temperatures because, the temperature controller is the on/off type and hence trying to keep the temperature constant causes fluctuations. For Test 1, the reactor temperature is 200°C on average and for Test 2, the temperature is about 240°C. For each run, different ammonia trapping H_2SO_4 solution is used. The total duration of the experiments are different because of the saturation of H_2SO_4 solution for capturing the produced ammonia. However, the ammonia formation rate results are given per second as well as the efficiencies are calculated based on the ammonia formation rate. The unreacted H_2 is also measured using a hydrogen sensor embedded to Arduino board which shows the portion of H_2 which remains unreacted. One of the significant advantages of this electrochemical process is having ambient pressures in the reaction. Since there is no compression in the cycle, the gas pressures are equal to ambient pressure. Therefore, the pressures are not measured and reported in the experiments.

Table 5.36 Summary of the experimental results showing the NH_3 formation rates and efficiencies.

Parameter	Test #1	Test #2
Experiment time (s)	1000	600
NH_3 mass flow rate (g/min)	0.0001125	0.00001875
NH_3 volume flow rate (mL/min)	0.16011	0.02668
NH_3 mole flow rate (mol/s)	1.10×10^{-7}	1.83×10^{-8}
NH_3 production rate (mol s^{-1} cm^{-2})	4.41×10^{-9}	7.35×10^{-10}
Reactor temperature (°C)	200°C	240°C
Current density (mA/cm^2)	9	6.2
Voltage (V)	1.75	1.2
Current (A)	0.225	0.155
Coulombic Efficiency (%)	14.17	3.43
Energy Efficiency (%)	5.50	2.45

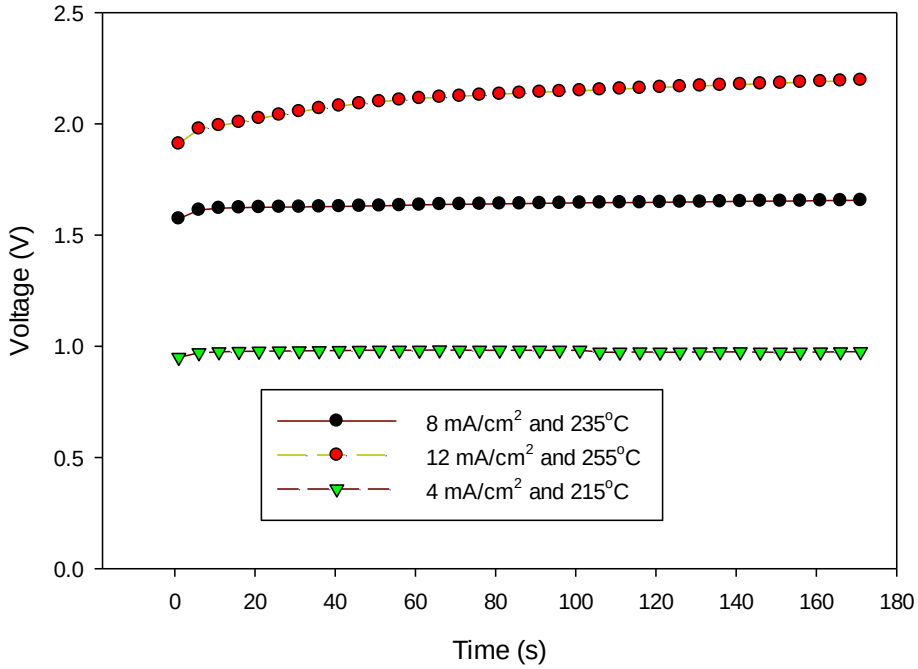

Fig. 5.90 The relationship between voltage and time during several experimental runs at different applied currents and temperatures for electrochemical synthesis of NH_3 using N_2 and H_2 with nano-Fe_3O_4 in a molten salt hydroxide electrolyte.

The required cell voltage to initiate the reaction of nitrogen and hydrogen in molten hydroxide for Test 1 at 200°C in the existence of nano-Fe_3O_4 is measured to be on average 1.75 V when the applied current is 225 mA between the 25 cm^2 Ni electrodes in the molten NaOH-KOH electrolyte. The potential decreases to 1.2 V when the current density is to 6.2 mA/cm^2 at 240°C. In Test 1, ammonia is synthesized at a rate of 4.41×10^{-9} mol s^{-1} cm^{-2} whereas in Test 2, the ammonia evolution rate decreased to 7.35×10^{-10} mol NH_3 s^{-1} cm^{-2}. NH_3 is generated at a coulombic efficiency of about 14.2% at 9 mA/cm^2, which declines to about 3.4%

at 6.2 mA/cm^2 at 240°C. Constant current electrochemical ammonia synthesis at different applied current densities and temperature levels are comparatively shown in Fig. 5.90.

The potential gradually declines from 2.1 V to 1 V for the applied current densities from 12 mA/cm^2 to 4 mA/cm^2. It is observed in the experiments that lower current density and lower temperature improve the stability of the rate of NH_3 evolution.

The measured coulombic and energetic efficiencies of ammonia evolution in time at different temperature levels and conditions in NaOH-KOH molten electrolyte are comparatively illustrated in Fig. 5.91. The generated NH_3 is trapped and measured in a room temperature dilute H_2SO_4 trap. A non-dilute H_2SO_4 trap is also tried before the experiments reported here to understand the absorptivity of the solution. However, the ammonia readings are not successful in this case. Hence, dilute H_2SO_4 solutions are utilized for the reported experiments. The conversion efficiency is not only dependent on the hydrogen amount but also amount of catalyst available to stimulate the conversion of N_2 and H_2 into NH_3. In order to make sure that there is enough N_2 to be reacted with supplied H_2, the supplied volume of N_2 is kept quite higher than H_2. The greater ammonia generation rate at lower voltages can be because of the lower hydrogen ion stream at the cathode which provides more time for generation of ammonia according to reaction. Higher NH_3 synthesis rates are obtained for Test 1 as illustrated in Fig. 5.91 which can be due to the improved ammonia conversion rate at lower temperature according to the chemical equilibrium. In addition, the coulombic efficiency is higher for Test 1. At higher current density of 9 mA/cm^2, the NH_3 formation rate yields about 4.41×10^{-9} mol s^{-1} cm^{-2}.

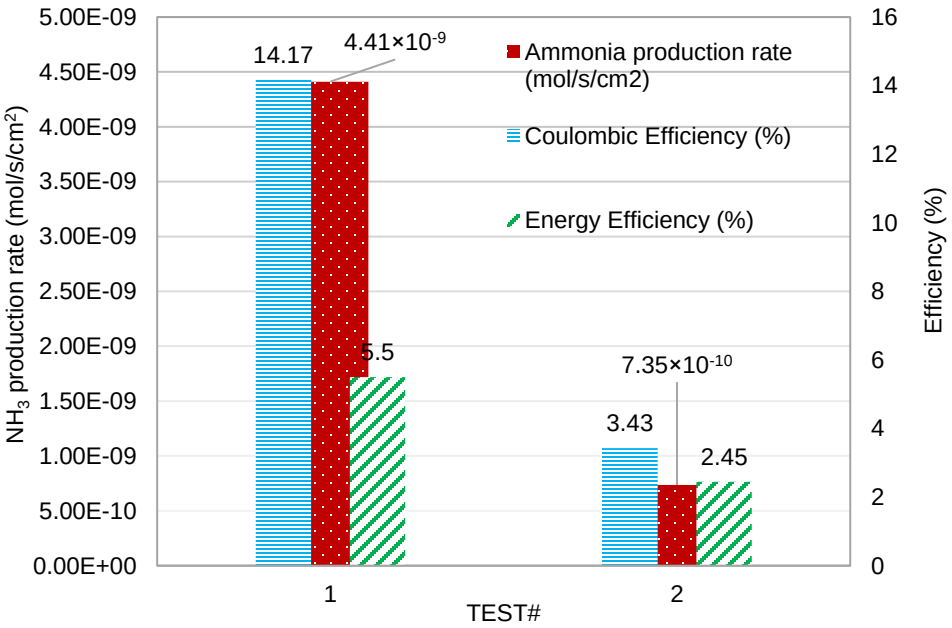

Fig. 5.91 Coulombic and energy efficiencies of two experimental runs for electrochemical NH_3 synthesis using N_2 and H_2 with nano-Fe_3O_4 in a molten salt hydroxide electrolyte.

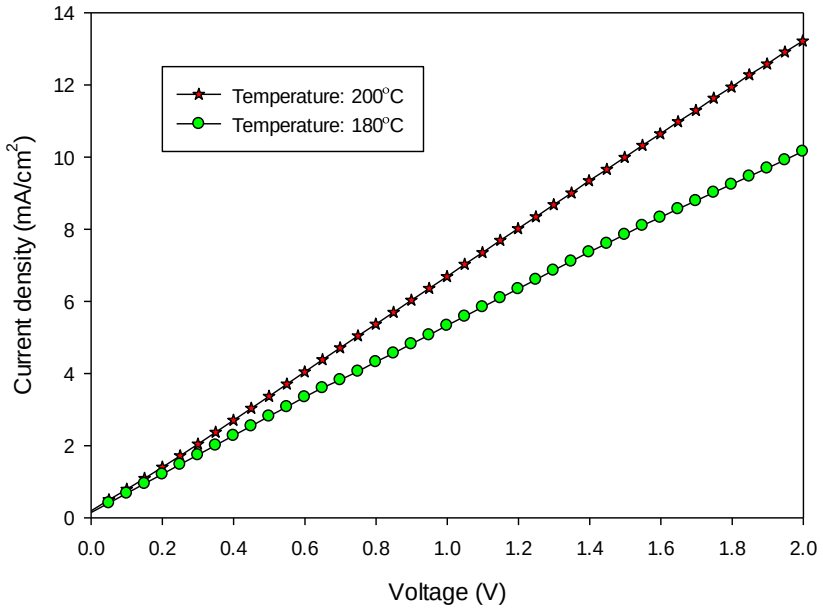

Fig. 5.92 Applied potential-current density relations at 200°C and 180°C for electrochemical NH_3 formation using N_2 and H_2 with nano-Fe_3O_4 in a molten salt hydroxide electrolyte.

In order to understand the current-voltage characteristics at lower temperature levels such as 180°C and 200°C, linear sweep voltagram of the reactor is collected between 0 V and 2 V as shown in Fig. 5.92. At 200°C and 1.2 V, the obtained current density is 8 mA/cm^2 whereas it is about 6.1 mA/cm^2 at 180°C. Hence, higher temperatures lowers the required voltage at constant supplied current.

The differentiations might be caused by the catalyst saturations as well as the changes in supplied H_2 rates. The effects of catalyst quantity and type of electrodes are likely to be investigated in the future designs. The results prove that ammonia synthesis can be achieved using photoelectrochemical hydrogen.

5.6 Exergoeconomic Analysis Results

The main findings of the exergoeconomic assessment is based on stream exergy rates and corresponding exergy destruction ratios. Thus, exergy destruction rates of the system components is illustrated in Fig. 5.93. In the Fresnel lens and dielectric mirror, only light interactions occur. Therefore, the exergy destruction rates are quite higher than other components. In addition, inlet irradiance is about 946 W/m^2 and it is concentrated about 6 to 10 times. The concentration and light splitting processes destruct more exergy than PV and PEC processes.

The cost rates and costs of exergy destructions for each component are tabulated in Table 5.37. The highest capital cost is observed in PEC reactor because of high purchased cost and electricity input. Secondly, ammonia reactor has highest cost rate as shown in Fig. 5.94. These two reactors are the only electricity consuming devices resulting in a larger cost rates.

Furthermore, since PV generates electricity, the total cost rate is quite lower than other components.

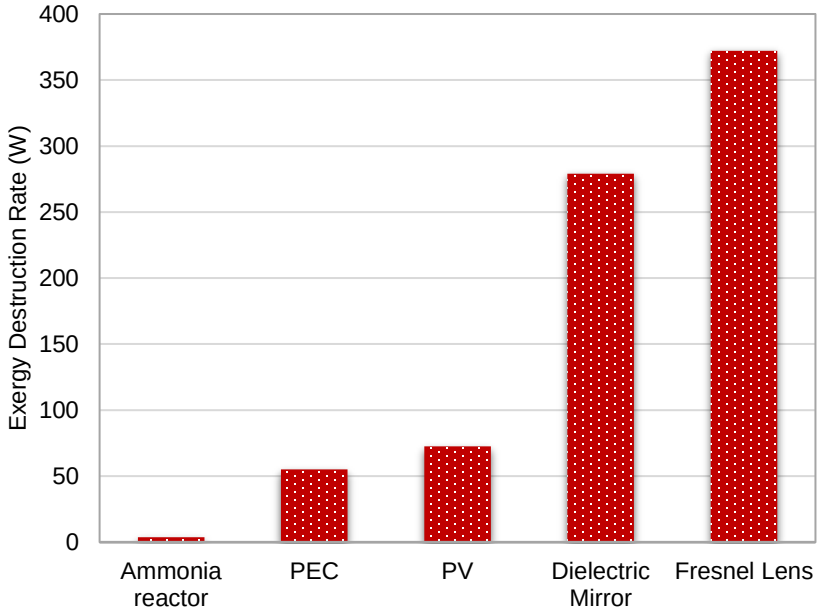

Fig. 5.93 The exergy destruction rates of the integrated system components.

Table 5.37 The exergoeconomic results of the components in the integrated system

Component	**Cost Rate of Exergy Destruction - $\dot{C}_D$ ($/h)**	**Exergoeconomic Factor - f (%)**	**Total Cost Rate - $\dot{C}_{total}$ ($/h)**	**Annual Investment Cost Rate - $\dot{Z}$ ($/h)**
Ammonia reactor	0.07295	42.46	0.1268	0.05384
Fresnel Lens	0.004365	50	0.008731	0.004365
Dielectric Mirror	0.03911	50	0.07823	0.03911
PEC	0.1596	59.27	0.3918	0.2322
PV	0.003902	54.4	0.008559	0.004656
TOTAL	0.2799	54.42	0.6141	0.3342

Since the PEC reactor capital cost is the highest contributor to the system cost, a parametric study is conducted to investigate the effect on the total cost rates as shown in Fig 5.95. In case the PEC reactor can be built in a more cost effective way corresponding to about 2000$, the total exergy destruction cost rate decreases to 0.1641 $/h whereas total exergoeconomic factor increases to 57.1%. Also, the exergoeconomic factor of PEC reactor component increases to 72.7 % from 54.41%.

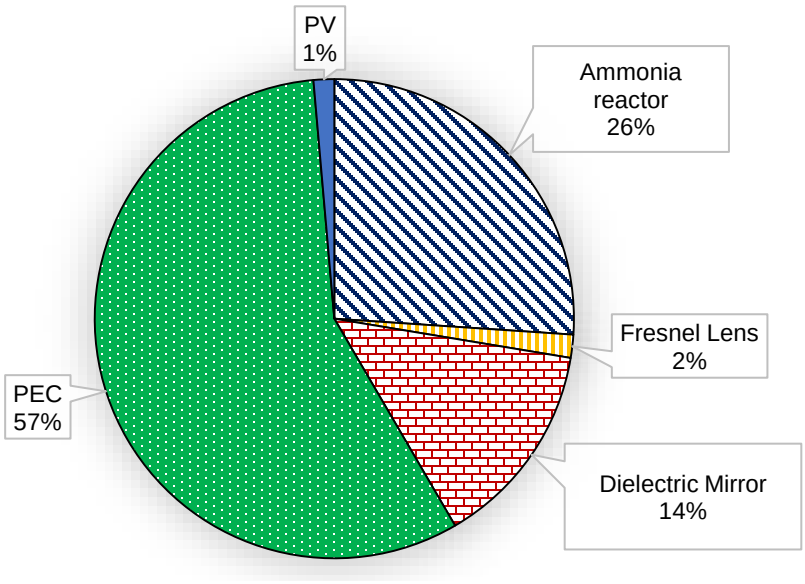

Fig. 5.94 The cost rate of exergy destruction in each component of the integrated system.

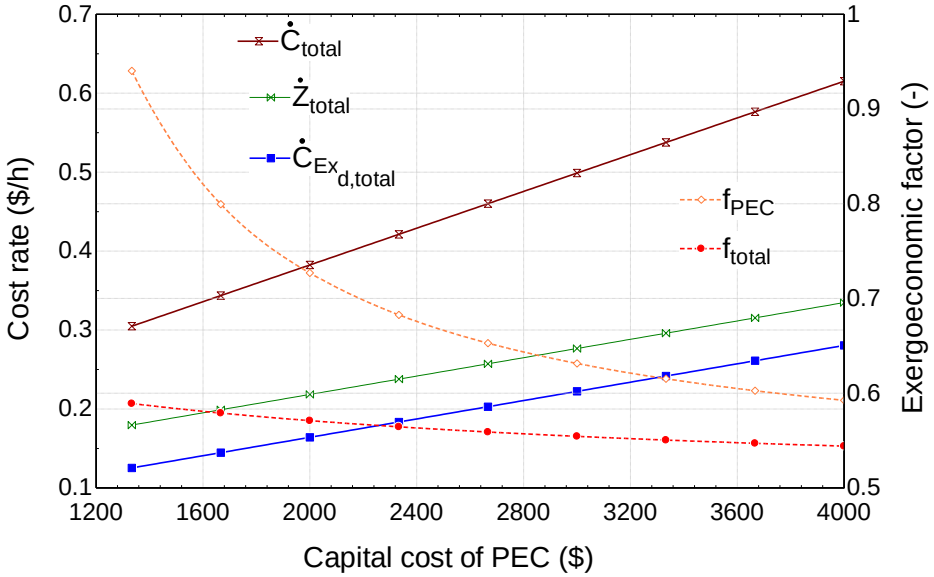

Fig. 5.95 The effects of PEC reactor capital cost on the system cost rates and exergoeconomic factors.

Fig 5.96 clearly shows that interest rate has a negative impact on the system cost rates. Although the total cost rate of the system is 0.4801 $/h at 2% interest rate, it rises to 0.702 $/h at 10% interest. The lifetime of the system and components has also important role in the total cost rate as shown in Fig. 5.97. Each component can have different lifetime periods. For example, the PEC electrodes may need to be replaced in two years whereas the solar concentrator may have up to ten years operation. In the base case, the system lifetime is taken to be 10 years for the experimental system that is about 0.6141 $/h total cost rate. However, in case the lifetime can be increased up to 40 years, the total cost rate can be decreased down to 0.3233 $/h.

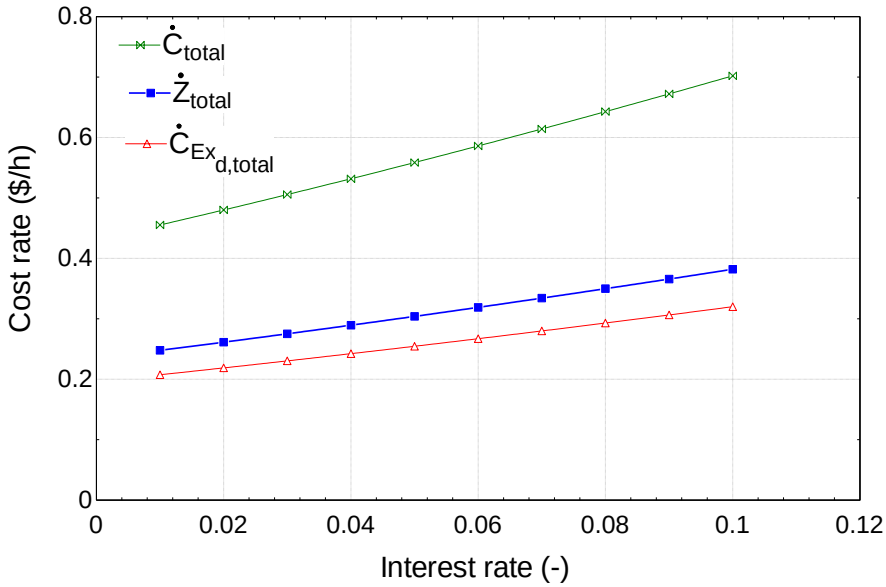

Fig. 5.96 The effects of increasing interest rate on the total system cost rates.

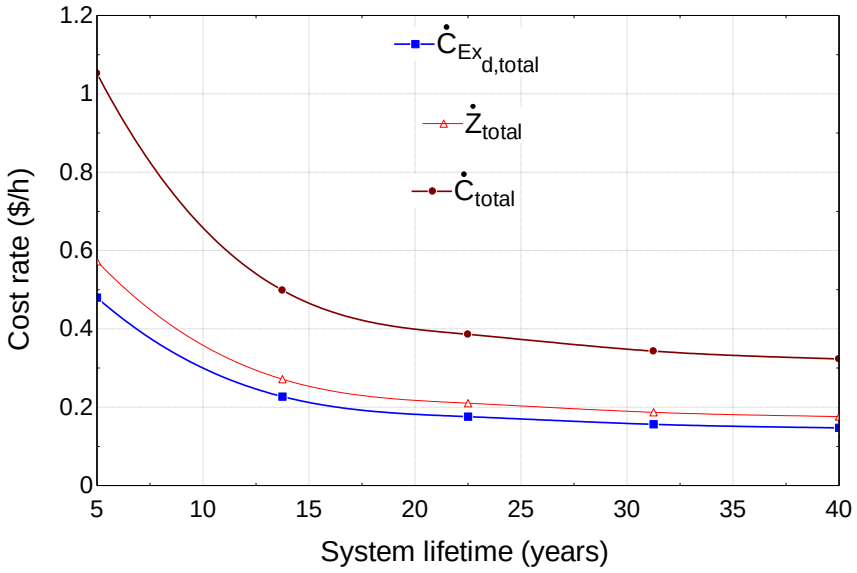

Fig. 5.97 The effects of system total lifetime on the system cost rates.

Annual operation time of the systems are also critical for the solar energy applications. The intermittency of the solar energy decreases the total annual operation time. The availability of the sunshine depends on the season and location. This is also named as capacity factor. In general, the capacity factor of the solar energy applications range between 10-30% corresponding to about 876 to 2628 hours annually. In the base case of the system, the operation time is set to 2500 hours. However, if the operation time diminishes to 1000 hours, the total cost rate rises to approximately 1 $/h as shown in Fig. 5.98. The operation time of the solar energy based systems strongly depend on the solar irradiation and seasonal changes. For the locations where the yearly irradiance is quite constant and high (such as Middle East and Central Africa), the annual operation time of the solar energy systems can be significantly increased.

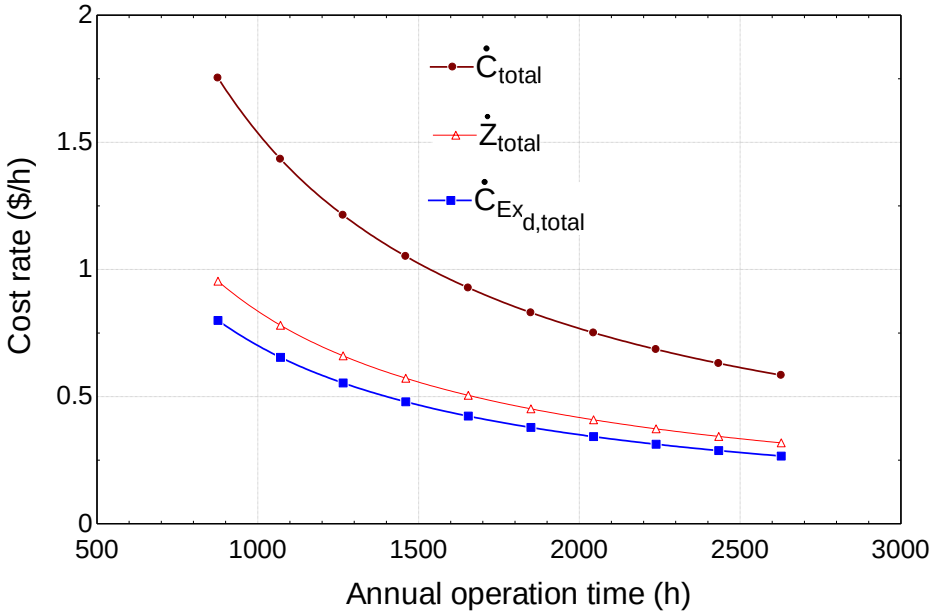

Fig. 5.98 The effects of annual operation time on total cost rates.

5.6.1 Scale-up analysis results

The economic analyses results scale-up study are presented in this section. The plant is scaled-up to 1000 kg/day. The capital costs, operation/maintenance costs etc. are considered in the analyses. Table 5.38 shows the total capital costs of the hydrogen production plant with cost breakdown of indirect and direct capital costs. The total capital cost of the concentrated light PEC hydrogen production plant is calculated as $6,428,852.03.

Table 5.38 The direct and indirect depreciable capital costs.

Indirect Depreciable Capital Costs	**2017$**
Site Preparation ($)	$98,690.81
Engineering and Design ($)	$370,089.69
Project Contingency ($)	$493,452.92
Up-Front Permitting Costs ($)	$370,089.69
Total Depreciable Capital Costs (Including direct capital costs)	$6,266,851.18
Cost of Land ($/acre)	$7,256.69
Land Required (acres)	22.32
Land Cost ($)	$162,001.32
Total Non-Depreciable Capital Costs	$162,000.85
Total Capital Costs	$6,428,852.03

Total Variable Operating Costs per year is estimated as $4,800 because of unpredicted Replacement Capital Cost. The fixed operating costs are tabulated in Table 5.39. Production maintenance and repair costs are predicted to 4% of the overall cost excluding the replacement parts which are mainly electrodes and lens. The state, federal taxes and after-tax real rate of return are taken as 6.0%, 35.0% and 1%, respectively in the cost analysis. The after-tax real

rate of return affects the cost considerably which would increase the cost of hydrogen. The after-tax real rate of return is the actual financial benefit of an investment after accounting for inflation and taxes. The calculations include the replacement of the PEC reactor electrodes every two years and replacement of the PEC cells including the Fresnel lens solar concentrator every ten years as tabulated for 40 year operation in Table 5.40. The other components are allocated for 20 years.

Table 5.39 The fixed operating costs of the PEC hydrogen production plant.

Fixed Operating Costs	**2017$**
Burdened labor cost, including overhead ($/man-hour)	$45.20
Labor cost ($/year)	$24,444.16
General and administrative expense ($/year)	$4,888.38
Licensing, permits and fees ($/year)	$589.11
Property tax and insurance rate (% of total capital investment per year) (In Ontario)	1.45%
Property taxes and insurance ($/year)	$93,218.22
Production maintenance and repairs ($/year)	$19,973.88
Total fixed operating costs	$143,114.50

The capital cost of the system components including the control unit, PEC cell, pumps and other components are shown in Table 5.41. Here, the PEC cell reactor body cost is taken as $145.23/m^2 including the concentrating and containment system. In addition, the PEC electrodes are taken as $234.24/m^2 unit cost. For a 1 tonne/day hydrogen production plant, an overall solar capturing area of 21,615 m^2 and electrode area of about 2162 m^2 are required. Based on these values, the installed costs of the major components in the PEC hydrogen production plant are tabulated in Table 5.41. The highest cost is the PEC cell with the concentrators which is followed by the PEC electrodes.

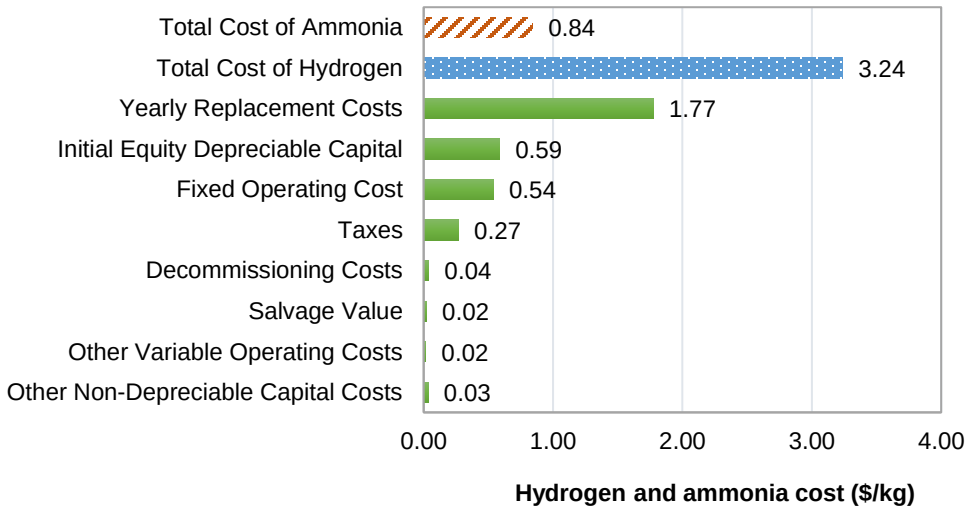

Fig. 5.99 The calculated cost of hydrogen and ammonia with contributing factors for a 1000 kg/day concentrated PEC hydrogen production plant.

Table 5.40 The cost of material replacements of the system components.

Operations Year	Total Yearly Replacement Costs (2017$)	Replacement
1	$35,061	
2	$632,966	Replacement of PEC electrodes every 2 years.
3	$35,061	
4	$632,966	Replacement of PEC electrodes every 2 years.
5	$35,061	
6	$632,966	Replacement of PEC electrodes every 2 years.
7	$35,061	
8	$632,966	Replacement of PEC electrodes every 2 years.
9	$35,061	
10	$4,997,679	Replacement of PEC electrodes every 2 years and replacement of PEC cell including solar concentrator, windows and sealing every 10 years plus installation
11	$35,061	
12	$632,966	Replacement of PEC electrodes every 2 years.
13	$35,061	
14	$632,966	Replacement of PEC electrodes every 2 years.
15	$35,061	
16	$632,966	Replacement of PEC electrodes every 2 years.
17	$35,061	
18	$632,966	Replacement of PEC electrodes every 2 years.
19	$35,061	
20	$4,997,679	Replacement of PEC electrodes every 2 years and replacement of PEC cell including solar concentrator, windows and sealing every 10 years plus installation
21	$35,061	
22	$632,966	Replacement of PEC electrodes every 2 years.
23	$35,061	
24	$632,966	Replacement of PEC electrodes every 2 years.
25	$35,061	
26	$632,966	Replacement of PEC electrodes every 2 years.
27	$35,061	
28	$632,966	Replacement of PEC electrodes every 2 years.
29	$35,061	
30	$4,997,679	Replacement of PEC electrodes every 2 years and replacement of PEC cell including solar concentrator, windows and sealing every 10 years plus installation
31	$35,061	
32	$632,966	Replacement of PEC electrodes every 2 years.
33	$35,061	
34	$632,966	Replacement of PEC electrodes every 2 years.
35	$35,061	
36	$632,966	Replacement of PEC electrodes every 2 years.
37	$35,061	
38	$632,966	Replacement of PEC electrodes every 2 years.
39	$35,061	
40	$35,061	

Table 5.41 The direct capital costs of the components in 1000 kg/day PEC concentrated light hydrogen production plant.

Major components/systems	Installed Costs (2017$)
PEC cell body, concentrating and containment system	$ 3,139,192
PEC Electrodes	$ 506,321
Make-up Water Pump	$ 237
Manifold Piping	$ 18,062
Collection Piping	$ 4,475
Column Collection Piping	$ 2,111
Final Collection Piping	$ 481
Condenser	$ 7,924
Manifold Piping (diameter)	$ 18,062
Collection Piping (diameter)	$ 4,475
Column Collection Piping (diameter)	$ 2,111
Final Collection Piping (diameter)	$ 481
PLC	$ 3,349
Control Room building	$ 19,567
Control Room Wiring Panel	$ 3,349
Computer and Monitor	$ 1,675
LabVIEW Software	$ 4,799
Water Level Controllers	$ 78,902
Pressure Sensors	$ 6,933
Hydrogen Area Sensors	$ 152,725
Hydrogen Flow Meter	$ 6,140
Instrument Wiring	$ 453
Power Wiring	$ 227
Conduit	$ 6,771
Piping Installation	$ 8,870
Reactor Foundation & Erection	$ 556,953
Reactor feed install	$ 71
Gas processing Subassembly install	$ 2,377
Control System Install	$ 85,467
TOTAL DIRECT CAPITAL COST	$ 4,675,618

The hydrogen and ammonia costs calculated based on the model are shown in Fig. 5.99. Moreover, the breakdown of the hydrogen cost are illustrated. Yearly replacement costs are about 1.77 $/kg hydrogen. This implies that if the durability and stability of the PEC electrodes and solar concentrators can be improved, the unit cost of hydrogen would decrease considerably. The hydrogen cost per kg is calculated to be 3.24 $/kg. The cost of ammonia is found to be 0.84 $/kg. The fixed operation and maintenance costs represent about 14% of the overall hydrogen cost whereas the capital cost of the plant has about 84% share as shown in Fig. 5.100. The cost of hydrogen is expected to decrease with higher concentration ratio. The bars within the tornado chart in Fig. 5.101 show the range of minimum hydrogen cost values

obtained by entering a base value for each specified variable, a reducing value, and an increasing value while holding all other variables constant at their base values. The operating capacity is chosen as 85% in the base case.

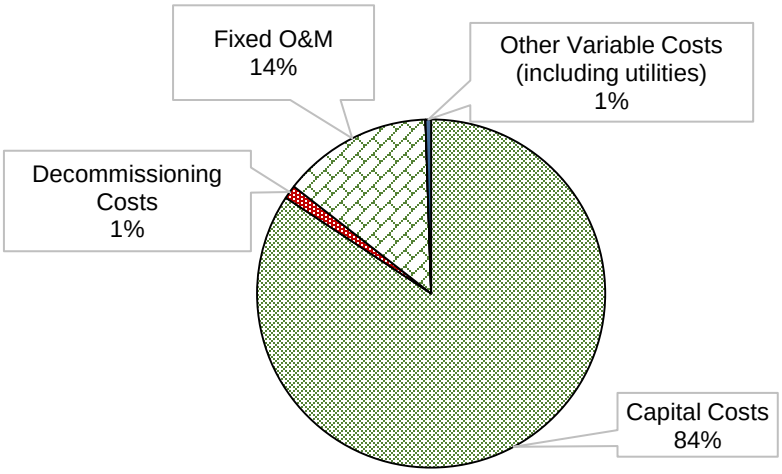

Fig. 5.100 The cost breakdown of hydrogen production plant.

As shown in Fig. 5.101, when operating capacity is increased to 94%, the cost of hydrogen can decrease down to 2.94 $/kg. On the other hand, if there is 10% lower capital investment, the cost of hydrogen can drop by 0.1 $/kg.

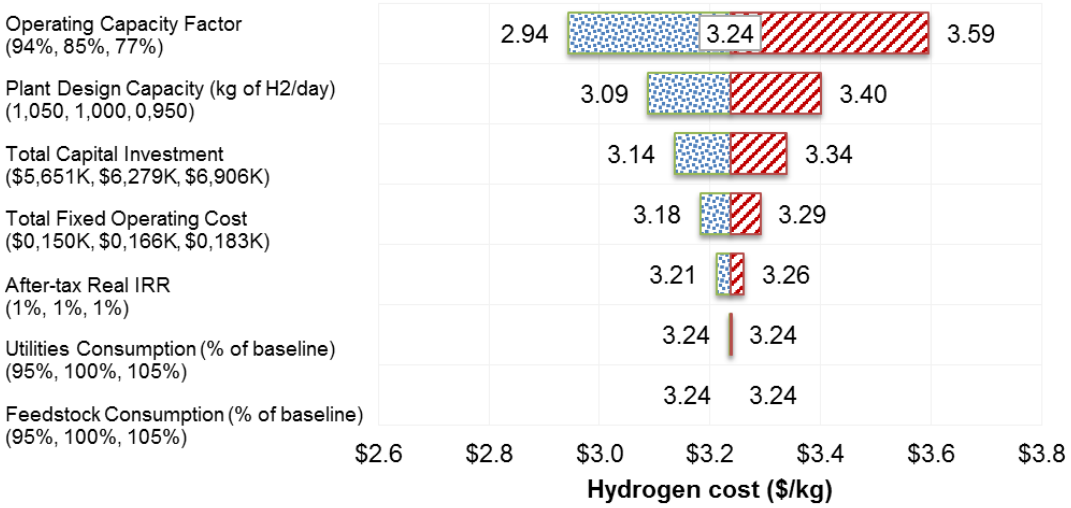

Fig. 5.101 The sensitivity of the hydrogen cost based on different parameters.

The plant capacity factor is increased 10%, the capital investment and fixed operating costs are lowered 10% and utilities consumption is decreased by 5%. Under these conditions, the adjusted hydrogen cost can decrease down to 2.82 $/kg and ammonia cost in this case is found to be 0.73$/kg as shown in Fig. 5.103. The waterfall diagram of the hydrogen cost by increasing the operating conditions is shown in Fig. 5.102. Here, multiple improvements are considered.

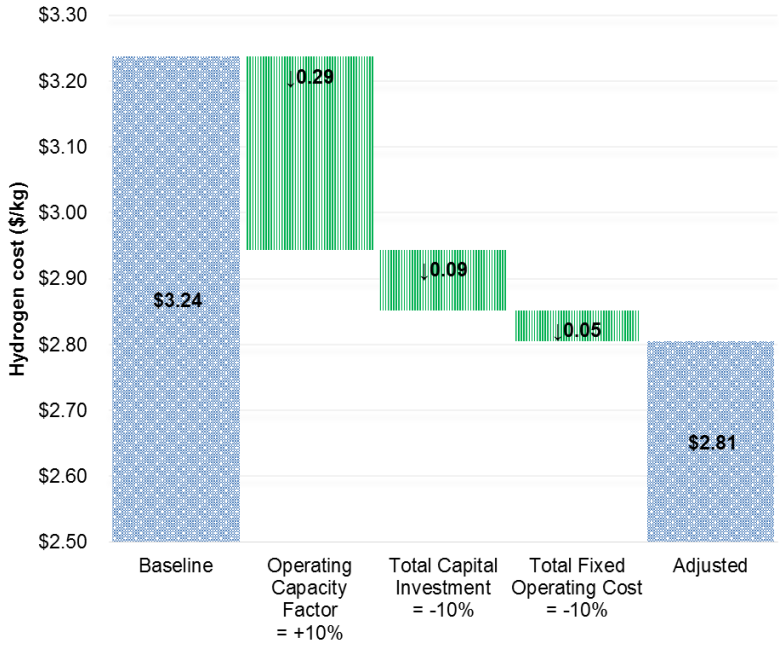

Fig. 5.102 Waterfall diagram for hydrogen cost considering better plant operating capacity and lower capital, operating costs.

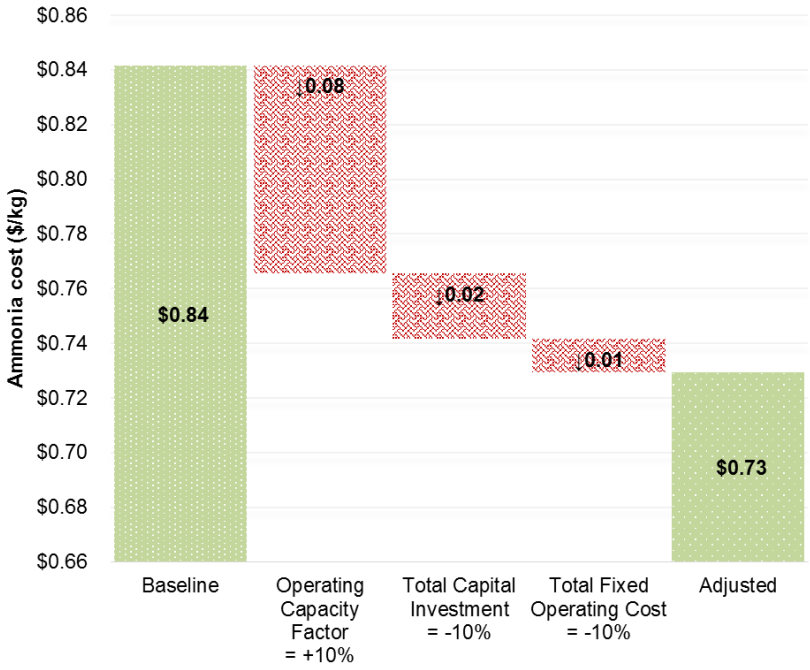

Fig. 5.103 Waterfall diagram for ammonia cost considering better plant operating capacity and lower capital, operating costs.

5.7 Optimization Study Results

The exergy efficiencies of the integrated hydrogen and ammonia production systems are maximized whereas the total cost rates are minimized using the optimization toolbox of

Engineering Equation Solver. The genetic algorithm optimization is performed for 64 generations where the maximum mutation rate is 0.2625 and number of individuals (populations) is 16. Larger values for the maximum mutation rate cause the algorithm to search more aggressively for an optimum at locations distant from the current optimum. Smaller values focus the search more around the current optimum. There are other parameters in the genetic algorithm however they are set to default and not adjustable in Engineering Equation Solver software.

At first, the exergy efficiencies for hydrogen and ammonia production systems are individually optimized to be maximized. The total cost rate obtained from the exergoeconomic analyses is then optimized to be minimized. Finally, the exergy efficiency of integrated ammonia production system (since it is the complete process) and total cost rate are combined in the function having same weighting factors of 0.5. Since the total cost rate is requested to be minimized, there is a negative sign assigned to the cost factor.

The single objective optimization results for the integrated ammonia production system are shown in Table 5.42. In addition, the sensitivity of the results are shown by changing the values of the decision parameters by 20%. In this case, the optimum efficiency for the integrated ammonia production system is found to be 6.96%. The optimum PEC cell area is very close to lower bound. However, the optimum PV cell area is very close to upper bound due to higher power generation. As the sensitivity results show that the system performance is mostly affected by the ambient temperature and irradiation on the PV cell.

Table 5.42 Single objective optimization results for the overall ammonia production system exergy efficiency including the sensitivities.

Decision Parameter	**-20%**	**Overall Exergy Efficiency (Ammonia)**	**Optimum**	**+20%**	**Overall Exergy Efficiency (Ammonia)**
A_{PEC} (m^2)	0.025	6.985	0.02542	0.0302	6.254
A_{PV} (m^2)	0.04591	6.669	0.04991	0.05	6.967
Interest rate (%)	0.02431	6.96	0.04231	0.06031	6.96
Irradiation on PV (W/m^2)	2528	6.449	2828	3000	10.68
Irradiation on PEC (W/m^2)	1500	6.984	1523	1823	6.667
Lifetime (year)	24.6	6.96	31.6	38.6	6.96
T_o (K)	290	6.961	290.8	294.8	10.44

The single objective optimization results for the hydrogen production system are shown in Table 5.43. In addition, the sensitivity of the results are shown by changing the values of the decision parameters by 20%. In this case, the optimum efficiency for the hydrogen production system is calculated as 9.69%. The optimum PEC cell area is equal to lower bound. However, the optimum PV cell area is very close to upper bound due to higher power

production. As the sensitivity results show that the hydrogen production system performance is mostly affected by the ambient temperature and irradiation on the PV cell and then PEC cell.

Table 5.43 Single objective optimization results for the overall hydrogen production system exergy efficiency including the sensitivities.

Decision Parameter	**-20%**	**Overall Exergy Efficiency (Hydrogen)**	**Optimum**	**+20%**	**Overall Exergy Efficiency (Hydrogen)**
A_{PEC} (m^2)	0.025	9.697	0.025	0.0386	9.112
A_{PV} (m^2)	0.04591	9.588	0.04991	0.05	9.699
Interest rate (-)	0.07277	9.697	0.09077	0.1	9.697
Irradiation on PV (W/m^2)	2547	9.444	2847	3000	13.34
Irradiation on PEC (W/m^2)	1500	9.697	1500	1800	9.294
Lifetime (year)	20.99	9.697	27.99	34.99	9.697
T_o (K)	290	9.697	290.9	294.9	13.68

The single objective optimization results for the total cost rate of the overall system are shown in Table 5.44. In addition, the sensitivity of the results are shown by changing the values of the decision parameters by 20%. Here, the optimum total cost flow rate is found to be 0.131 \$/h. The irradiances on the PEC cell and PV cell are desired to be higher in this case to lower the unit cost for energy production. Furthermore, the area of the PEC cell is close to upper bound and PV cell area is close to lower bound implying the higher efficiency for power production. As the sensitivity results show that the total cost rate of the system is mostly affected by the interest rate and lifetime of the system. These are the two critical parameters used in the exergoeconomic analysis to define the system cost. The lifetime is maximized and interest rate is minimized to yield the optimum cost rate.

Table 5.44 Single objective optimization results for the total cost rate of the overall system including the sensitivities.

Decision Parameter	**-20%**	**Total Cost Rate (\$/h)**	**Optimum**	**+20%**	**Total Cost Rate (\$/h)**
A_{PEC} (m^2)	0.07075	0.131	0.08435	0.093	0.1311
A_{PV} (m^2)	0.03185	0.1311	0.03585	0.0399	0.1309
Interest rate (-)	0.01	0.131	0.01	0.028	0.1803
Irradiation on PV (W/m^2)	2340	0.1312	2640	2940	0.1308
Irradiation on PEC (W/m^2)	2450	0.131	2750	3000	0.131
Lifetime (year)	33	0.1538	40	40	0.131
T_o (K)	290	0.131	290.3	294.3	0.131

Table 5.45 shows the summary of the optimization results for each objective function. The obtained values are optimum for the specific objective whereas the in the last column, the optimum parameters for the multi-objective function are presented combining the exergy efficiency of the ammonia and hydrogen production system and total cost rate of the overall system.

Table 5.45 Comparison of optimized values and base case values for design parameters of the integrated system.

Decision Parameter	**Base Case**	**Best Exergy Efficiency (Ammonia)**	**Best Exergy Efficiency (Hydrogen)**	**Best Total Cost Rate**	**Multi-Objective Best Exergy Efficiency (Ammonia) and Best Total Cost Rate**	**Multi-Objective Best Exergy Efficiency (Hydrogen) and Best Total Cost Rate**
A_{PEC} (m^2)	0.025	0.02542	0.025	0.08435	0.02609	0.02554
A_{PV} (m^2)	0.040	0.04991	0.04991	0.03585	0.04971	0.04572
Interest rate (-)	0.07	0.04231	0.09077	0.01	0.01046	0.01652
Irradiation on PV (W/m^2)	2238	2828	2847	2640	2018	2103
Irradiation on PEC (W/m^2)	2102	1523	1500	2750	1516	1542
Lifetime (year)	10	31.6	27.99	40	24.56	27.95
T_o (K)	298	290.8	290.9	290.3	299.7	300.7

The irradiance levels on the PEC cell and PV cell are in the range of 1500 W/m^2 to 3000 W/m^2. The overall efficiencies are mainly affected by the PV and PEC cell areas and solar light illumination. The lower area of the PEC cell results in higher efficiencies because the increasing the cell area does not increase the hydrogen production significantly. On the other hand, the less Fresnel lens area is favored because the illuminated area on the dielectric mirrors remain similar to the base case (caused by the distance of the mirror from to the focal area of the Fresnel lens). In this way, there is less power input to the system, however, the amount of generated useful products remain constant or decrease slightly.

The optimum values in Table 5.42 for the lifetime is the highest for multi-objective case and best total cost rate whereas the lower interest rates are favored. As explained in the exergoeconomic analyses, increasing the lifetime of the system enhances the total cost rate.

As shown in Fig. 5.104, the optimized values for exergy efficiency of the integrated systems range between 5% to 9.6%. The optimum efficiency is found to be 8.7% for the multi-objective optimization of hydrogen production system although it is 9.69% for single-objective optimization. On the other hand, the best total cost rate of the system is found to be 0.131 $/h in single optimization. However, when the exergy efficiency of the ammonia production system is maximized and total cost rate is minimized at the same time, the total cost rate of the system increases to 0.2 $/h. Similarly, it increases to 0.194 $/h for the multi-objective optimization of hydrogen production efficiency and total cost rate. In the base case, it is

calculated to be 0.61 $/h. In the multi-objective optimization, the total cost rate in lower whereas the exergy efficiency is slightly higher revealing that there is an optimum range between the best efficiency and best total cost rate.

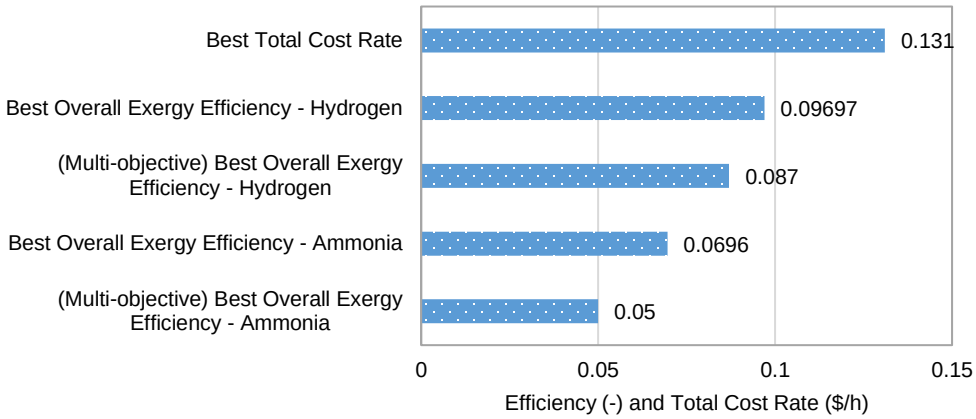

Fig. 5.104 The resulting overall best efficiencies and total cost rate in the system including the multi-objective optimization.

5.8 Environmental Impact Assessment Results

The LCA results are obtained using SimaPro LCA software. The LCA is performed using two different methods; CML 2001 and Eco-indicator 99. The Eco-Indicator method uses the standard step by step procedure: classification, characterization, normalization and weighting, respectively. In this method, the results are mainly presented as single score and relative damage assessment level under human health, ecosystem quality and resources categories.

CML 2001 method presents the results based on the environmental impact categories such as global warming, human toxicity and abiotic depletion. In this method, the results are mostly presented per equivalent substance amount such as kg CO_2 equivalent and kg SO_2 equivalent. Here, the environmental impact assessment results of 25 different ammonia production routes are comparatively presented.

The single score of ammonia production from coal electrolysis based methods correspond to 0.3905 and 0.4393 Pt for bituminous coal and hard coal, respectively in human health category. It is followed by heavy oil and natural gas based electrolysis methods as illustrated in Fig. 5.105. With respect to ecosystem quality, municipal waste, biomass and hydropower routes (except pumped storage) yield the lowest environmental damage. In the category of resources, heavy oil electrolysis option has a single score of 0.4353 as the highest one. PEC electrochemical route has slightly higher single scores than PV electrolysis route however, it is considerably lower than any other fossil fuel based ammonia production options. The single scores of PEC electrochemical route are 0.0728, 0.0103 and 0.046 Pt, respectively for human health, ecosystem quality and resources categories. In relative damage assessment, the method which yields the highest score is considered as 100% in each category. The other methods are ranked accordingly. For human health and ecosystem category, the coal electrolysis based method has the highest damage whereas heavy oil electrolysis based method has the highest damage in resources category corresponding to 100% as shown in Fig. 5.106.

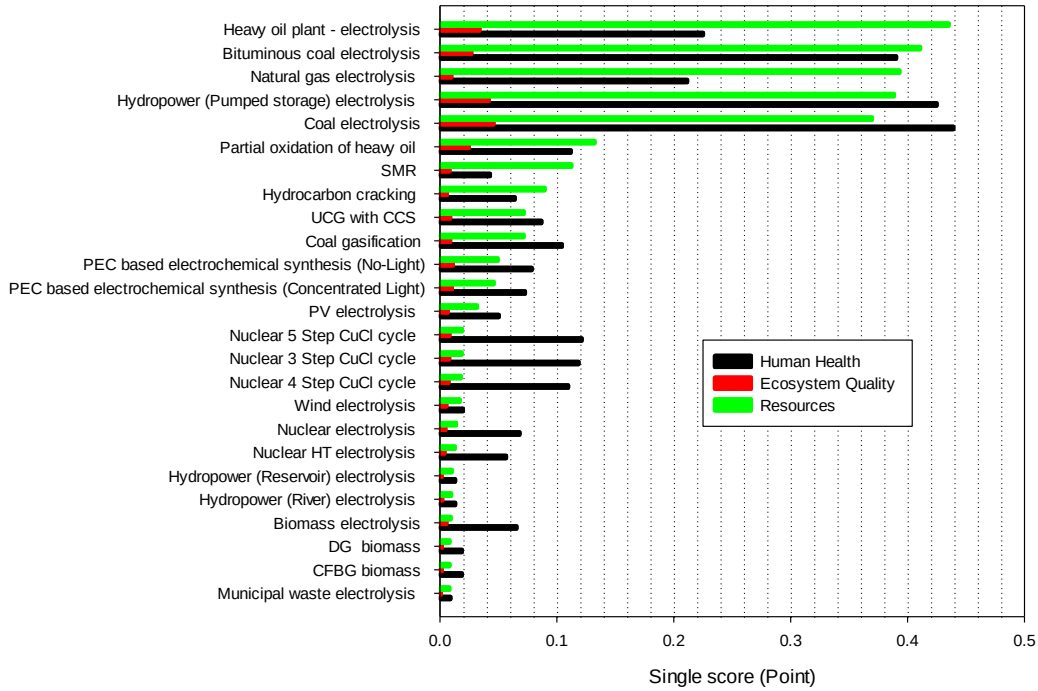

Fig. 5.105 Overall single score comparison of ammonia production methods according to Eco-Indicator 99.

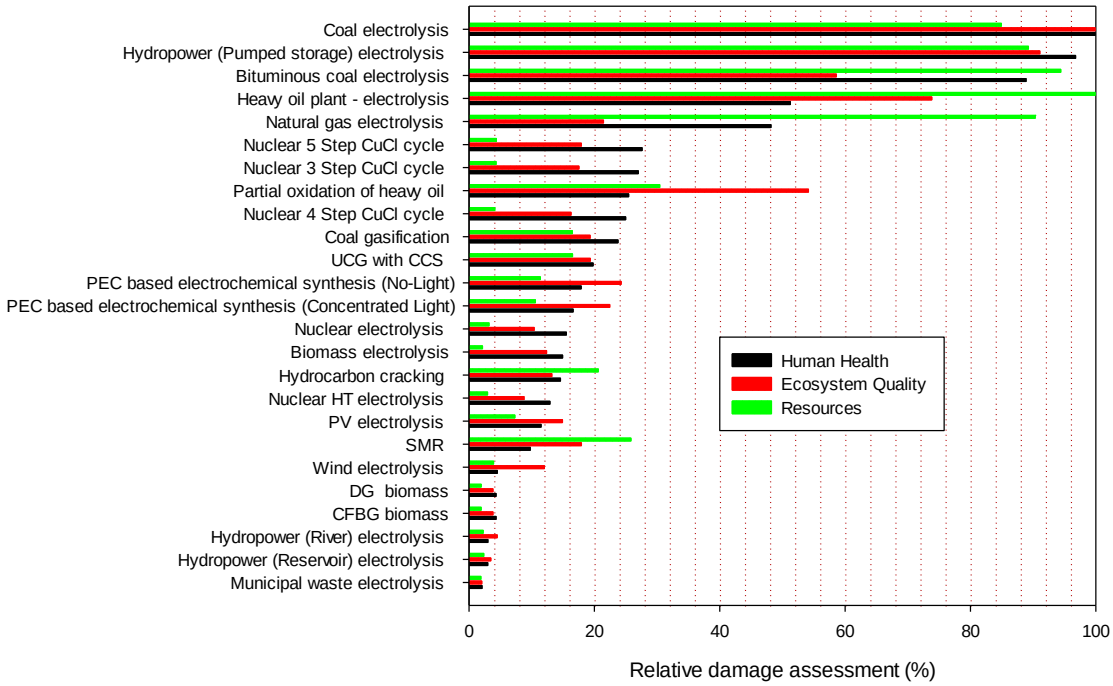

Fig. 5.106 Overall relative damage assessment comparison of ammonia production methods according to Eco-Indicator 99.

Except hydrocarbon cracking, coal gasification based ammonia production options including UCG have the lowest impact on human well-being, ecology quality and resources among fossil fuel based methods. Nuclear thermochemical methods have similar damages with other fossil fuel methods however, nuclear electrolysis options are more environmentally friendly. PV electrolysis option yields 11.46%, 14.89% and 7.29% relative damage in human health, ecosystem quality and resources categories. The global warming results obtained using CML 2001 method are shown in Fig. 5.107.

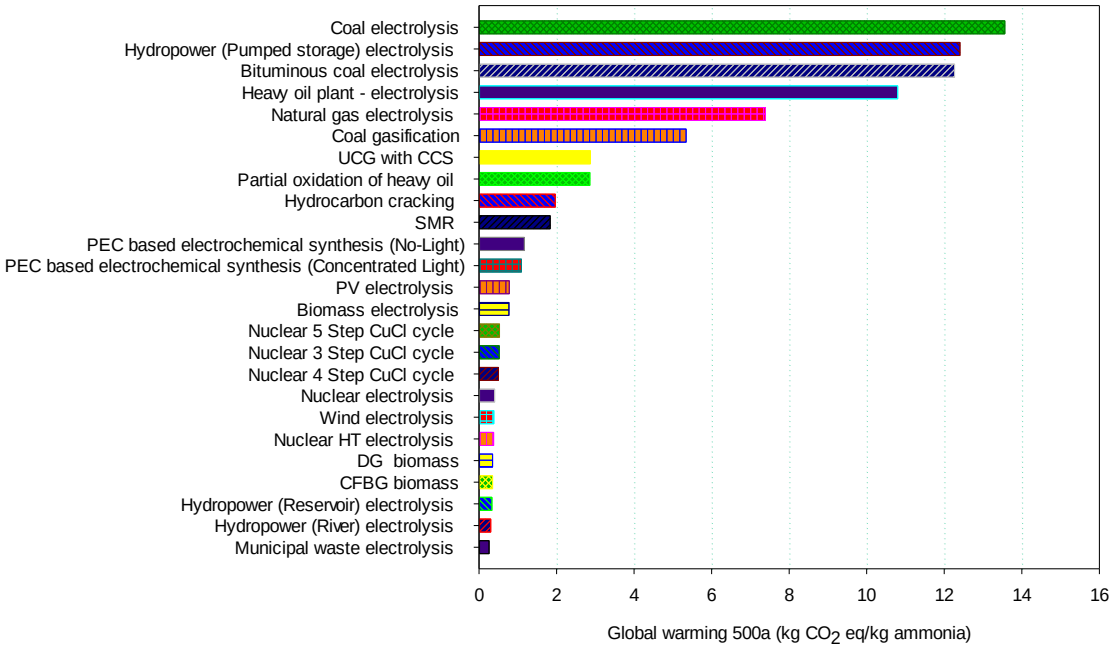

Fig. 5.107 Global warming values of all ammonia production methods.

The high GWP results for pumped storage hydropower route is mainly caused by the electricity mix usage in the construction of the system. Since hard coal is one of the common electricity supply in US grid mix and pumped storage construction consumes high amount of electricity, the overall environmental impact of this method is quite high compared to other renewables as shown in Fig. 5.108. The amounts of GHG emitted from SMR based ammonia production process are mainly caused by the fuel gas combustion during the primary and secondary reformers of process gas and by the compressors used to transport natural gas. Furthermore, the generation of electricity using bituminous coal is found to be the fundamental contributor to the global warming potential of ammonia production from bituminous coal.

Municipal waste, hydropower and biomass options emit the least amount of GHG emission. Although, PEC electrochemical ammonia production method has slightly higher GHG emissions than other renewable methods, it is significantly lower than the mostly used SMR method. In addition, it is observed that gasification routes of coal and biomass for ammonia production emit lower GHG emissions.

PEC based electrochemical synthesis (concentrated light) yields about 1.09 kg CO_2 eq. whereas PEC based electrochemical synthesis (no-light) yields about 1.16 kg CO_2 eq. per kg ammonia. Among fossil fuel based routes, the global warming potential is highest for the ammonia production from coal based electrolysis method (13.56 kg CO_2 eq.) followed by heavy oil electrolysis based ammonia production (10.79 kg CO_2 eq.) as shown in Fig. 5.107. The municipal waste and hydropower (run-of-river) based ammonia production have lowest global warming potential of 0.26 and 0.30 kg CO_2 eq per kg of ammonia, respectively.

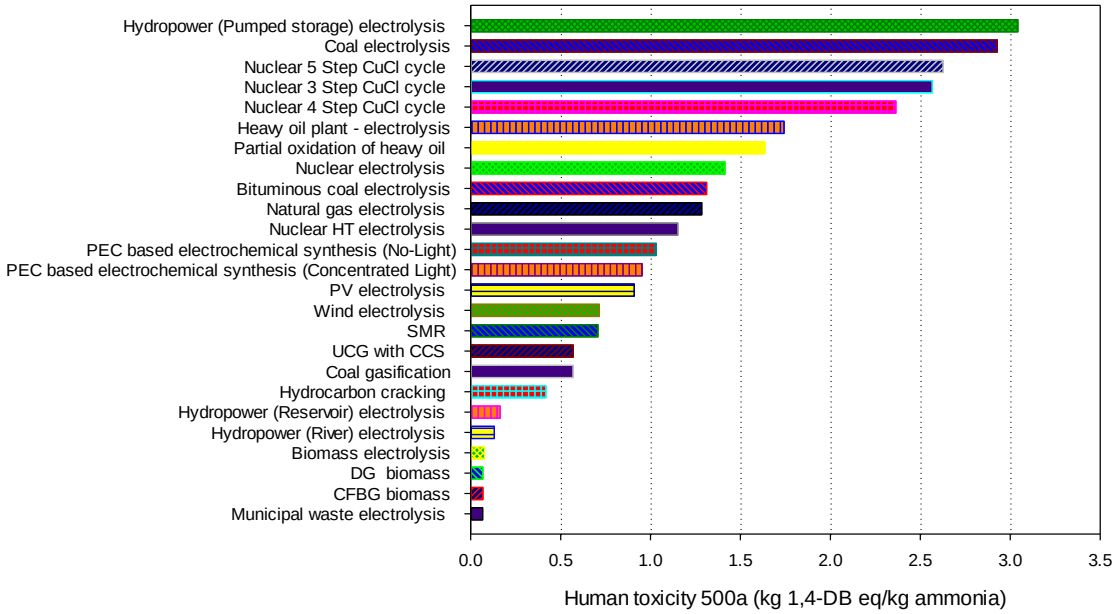

Fig. 5.108 Human toxicity values of all ammonia production methods.

The impact on human health due to human toxicity is maximum for the ammonia production from pumped hydro, coal electrolysis and nuclear thermochemical based methods where the maximum is found to be 3.0427 kg 1,4-DB-eq per kg of ammonia for pumped hydro electrolysis method. Ammonia from municipal waste, biomass gasification and hydropower electrolysis based methods yield lowest human toxicity values as seen in Fig. 5.108. Note that hydrocarbon (naphtha) cracking and coal gasification have slightly lower human toxicity values compared to some renewable options such as PV electrolysis.

This is due to the production process of aluminum support construction materials used in PV systems, hence can be lowered by using alternative options. Among conventional methods, ammonia from both underground coal gasification and normal coal gasification based methods yield lowest human toxicity values as seen in Fig. 5.109.

Abiotic resources are natural resources including energy resources, such as natural gas and crude oil, which are considered as non-living. The abiotic depletion is highest for fossil fuel based electrolysis methods followed by coal gasification, hydrocarbon cracking and SMR methods as it is illustrated in Fig. 5.109. This is because of fossil fuels are major basis of energy and feed resource, it shows the huge intake of coal and heavy oil for unit quantity of ammonia generated.

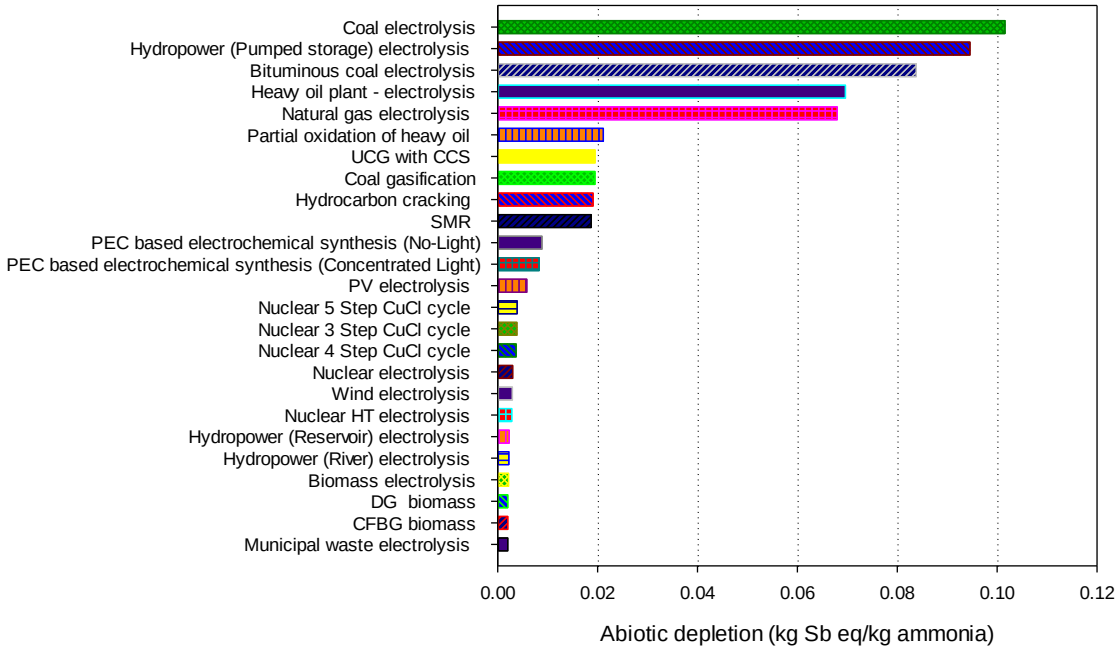

Fig. 5.109 Abiotic depletion values of all ammonia production methods.

The crude oil production is considered to be responsible about 89% of abiotic depletion value for heavy oil electrolysis and partial oxidation of heavy oil based methods. Municipal waste electrolysis, CFBG biomass and DG biomass have the lowest abiotic depletion corresponding to about 0.0019 kg Sb eq/kg ammonia.

Acidification which is caused by acidifying substances is represented by the equivalent amount of SO_2. Nuclear electrolysis options have similar acidification values with biomass gasification and hydropower options. The acidification values of SMR and nuclear 4 Step CuCl cycle are found to be 0.0036 kg SO_2 eq. and is 0.0037 kg SO_2 eq., respectively as shown in Fig. 5.110.

The highest polluting methods in this category are coal and natural gas electrolysis methods together with pumped storage hydro option. Transport of the substances is considered the main factor for the acidification impact category. The combustion of diesel fuel has high impact hence, particularly transportation processes with agricultural machinery and trucks create high emissions leading to higher acidification values. The variation in this impact category is fairly high because of considerable different type of transportation options such as pipelines, trucks, ships etc.

The terrestrial ecotoxicity value is maximum for partial oxidation of heavy oil method corresponding to about 0.021 kg 1,4 DB eq per kg ammonia as shown in Fig. 111. This is due to the refinery process of heavy oil. The lowest values in this category are calculated for biomass and hydropower based routes.

PEC based electrochemical ammonia production which is the method experimentally tested in this thesis uses photovoltaic cells for electricity requirements of the system. Among renewable options, PV electrolysis for ammonia production has higher environmental effects

because of mainly the production phase of the PV cells and aluminum support mechanism. Therefore, for PEC based electrochemical ammonia synthesis option, the environmental effects are higher than some renewable routes such as hydropower, municipal waste and wind. However, it is important to note that the environmental effects are quite lower than mostly used SMR method especially in global warming potential.

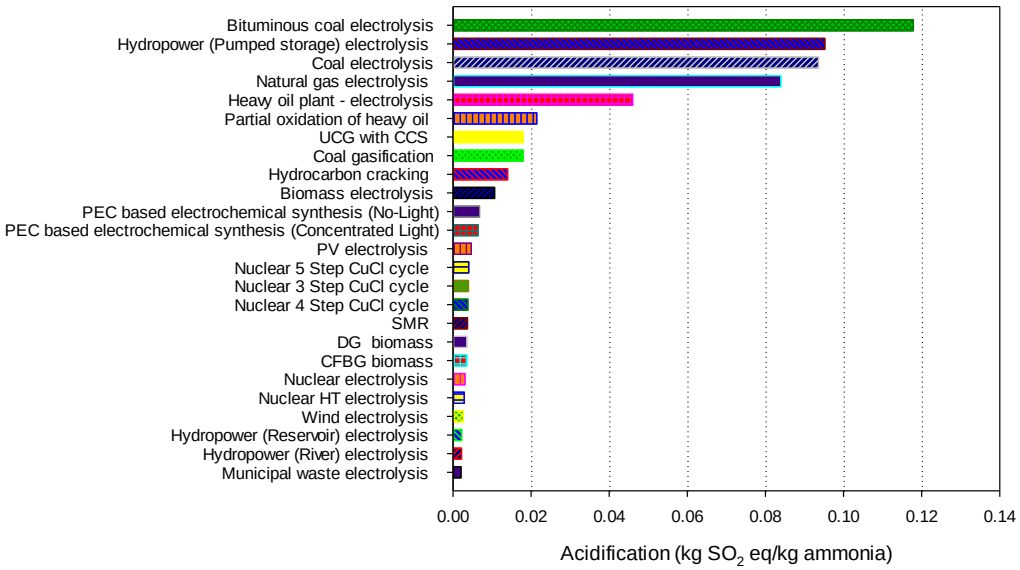

Fig. 5.110 Acidification values of all ammonia production methods.

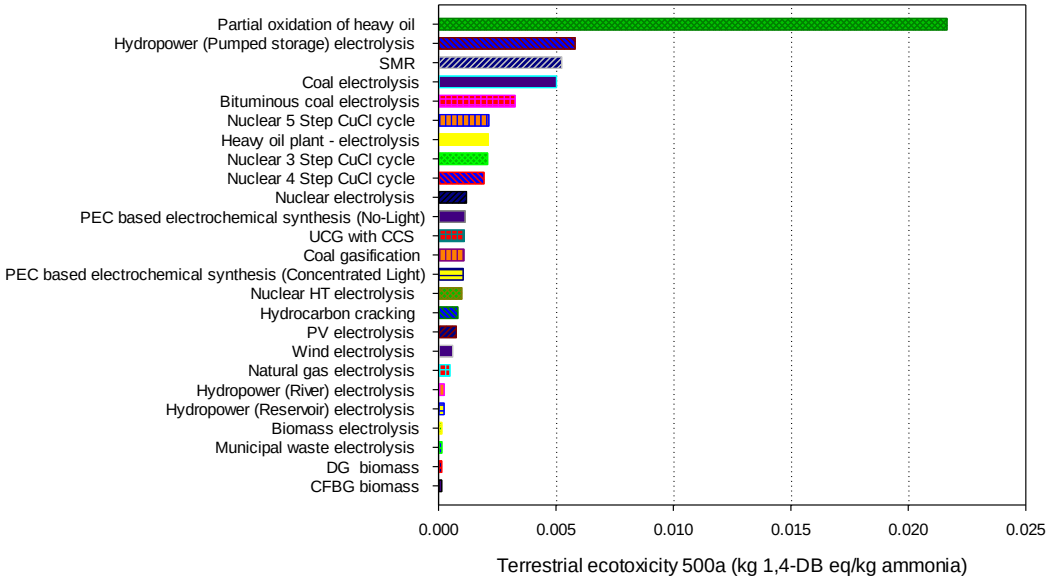

Fig. 5.111 Terrestrial ecotoxicity values of all ammonia production methods.

As the average GHG emission from commercial ammonia plants range between 2 to 2.5 kg CO_2. Eq per kg ammonia, using PEC based electrochemical ammonia production can reduce the GHG emissions more than 50%. The main reason of having higher environmental effects

in PEC electrochemical route than some renewable routes is that this process still consumes more energy than Haber-Bosch process. Because, the pressure is the ambient pressure, the conversion rate is lower. However, the technology and materials are improving quite quickly which will decrease the energy required for electrochemical ammonia synthesis and contribute the less environmental impact.

5.8.1 Life cycle assessment of PEC (concentrated light) based electrochemical ammonia synthesis results

In this section, the LCA results obtained for PEC based electrochemical ammonia production method using concentrated light are given in detail to reveal the contribution of various sub-processes. When reporting the contribution of different processes to overall impact category, 1% cut-off is applied. There are mainly three processes in the PEC based ammonia synthesis namely; hydrogen production from photoelectrochemical reactor, nitrogen production from air separation and electricity production from PV cells for energizing the process.

The main contributor in all categories is the electricity production from PV cell as shown in Tables 5.43 to 5.45. 6.9% of total human toxicity is caused by nitrogen production process whereas 29.9% is due to hydrogen production from PEC system as listed in Table 5.43. Electricity production from PV is mainly responsible for remaining. There are numerous substances causing toxicity for human health such as arsenic and nickel as shown in Fig. 5.112. Arsenic and polycyclic aromatic hydrocarbons are the two fundamental toxic substances (about 64% in total) released to the environment in this method. There are mainly caused by copper and aluminum production processes for PV and support structures as shown in Fig. 5.113. Polycyclic aromatic hydrocarbons are released due to nitrogen production from air separation plant since mix grid electricity is used.

Table 5.46 The shares of different sub-processes in human toxicity category for PEC (concentrated light) based electrochemical ammonia synthesis.

Inflows	Flow	Unit
Total	100	%
Electricity, production photovoltaic, multi-Si	63.2	%
Hydrogen, PEC cell, PV, Concentrated Light-Integrated System	29.9	%
Nitrogen, gas, at plant	6.9	%
Potassium hydroxide	0.000102	%
Sodium hydroxide	6.96E-05	%
Iron oxide	7.06E-06	%

Table 5.44 shown the shares of main processes contributing to abiotic depletion. Almost half of the total abiotic depletion is because of PV electricity production whereas 25% is due to hydrogen production. The molten salt electrolyte and reaction catalyst have quite small shares in total impact. Furthermore, as shown in Fig. 5.114, coal and natural gas are two main substances depleting in this method due to high electricity consumption in the PV cell factory and aluminum needed for support mechanism. Crude oil and brown coal have shares of 14% and 7%, respectively as shown in Fig. 5.115.

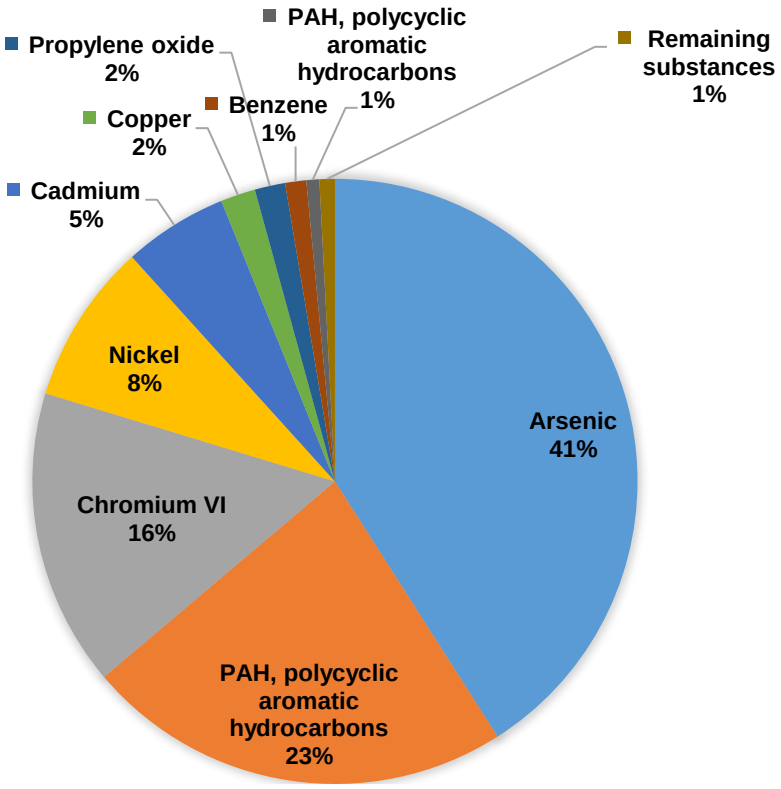

Fig. 5.112 The share of toxic substances for PEC (concentrated light) based electrochemical ammonia synthesis.

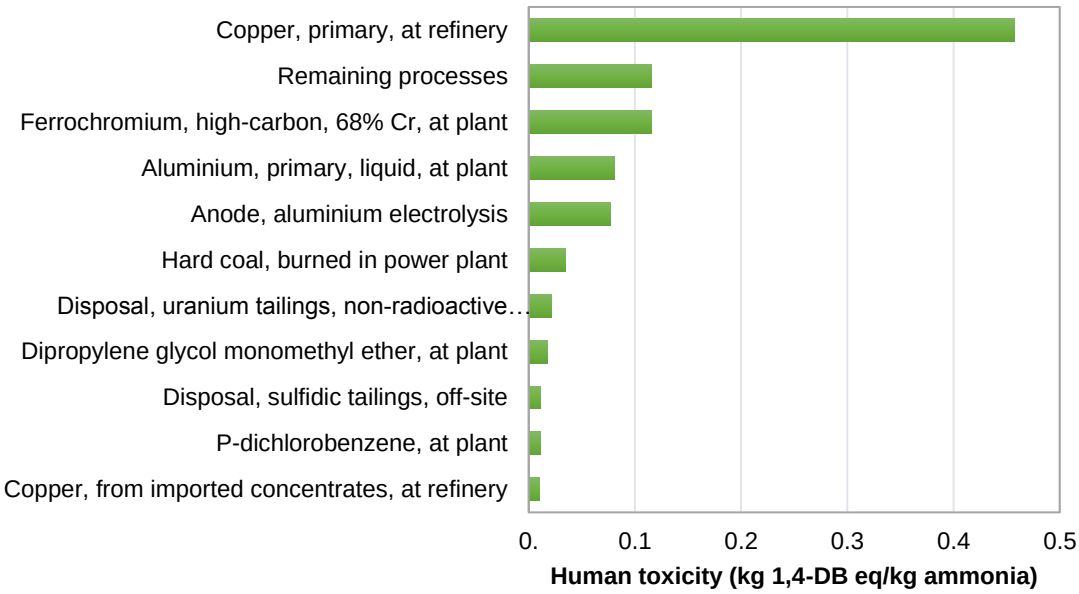

Fig. 5.113 Contribution of various sub-processes to human toxicity potential of PEC (concentrated light) based electrochemical ammonia synthesis.

Table 5.47 The shares of different sub-processes in abiotic depletion category for PEC (concentrated light) based electrochemical ammonia synthesis.

Inflows	Flow	Unit
Total	100	%
Electricity, production photovoltaic, multi-Si	51.7	%
Hydrogen, PEC cell, PV, Concentrated Light-Integrated System	24.5	%
Nitrogen, gas, at plant	23.8	%
Potassium hydroxide	0.000256	%
Sodium hydroxide	0.000141	%
Iron oxide	1.83E-05	%

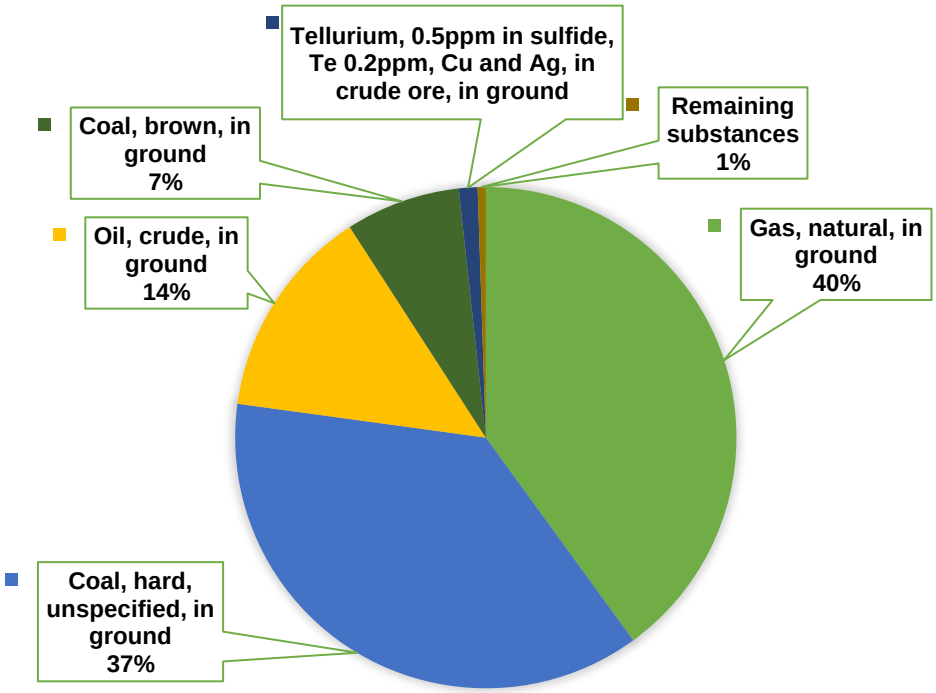

Fig. 5.114 The share of depleting abiotic sources for PEC (concentrated light) based electrochemical ammonia synthesis.

The global warming potential of PV electricity production is responsible for almost 50% of total GHG emissions where almost 76% of PV electricity is because of PV cell production process in the factory. The shares of main processes for global warming potential are tabulated in Table 5.45. Global warming category includes all greenhouse gas emissions however, CO_2 is the main gas emitted to the environment corresponding to about 93% of total in the method as shown in Fig. 5.116. Sulfur hexafluoride (3%) and methane (2%) are the other gases contributing to total GHG emission. Sulfur hexafluoride emission is mainly due to magnesium production in the plant required for PV cell production. Shown in Fig. 5.117, electricity production in cogeneration plant and hard coal burned in power plant are mainly because of silicon production required for PV cells.

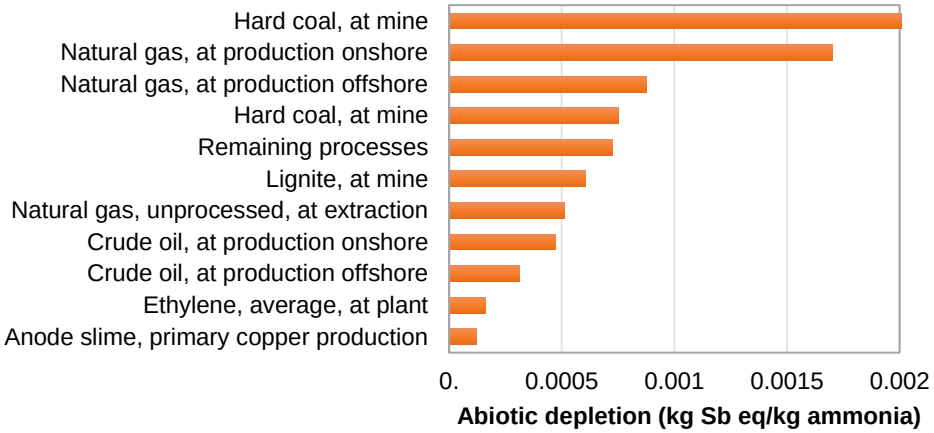

Fig. 5.115 Contribution of various sub-processes to abiotic depletion potential of PEC (concentrated light) based electrochemical ammonia synthesis.

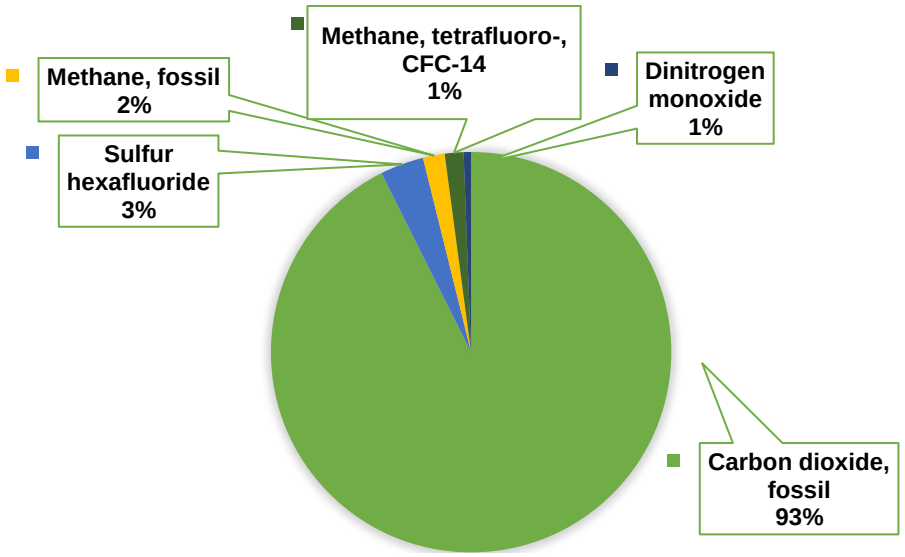

Fig. 5.116 The share of greenhouse gas emissions for PEC (concentrated light) based electrochemical ammonia synthesis.

Table 5.48 The shares of different sub-processes in global warming category for PEC (concentrated light) based electrochemical ammonia synthesis.

Inflows	Flow	Unit
Total	100	%
Electricity, production photovoltaic, multi-Si	51.9	%
Hydrogen, PEC cell, PV, Concentrated Light-Integrated System	24.5	%
Nitrogen, gas, at plant	23.6	%
Potassium hydroxide	0.000248	%
Iron oxide	0.000143	%
Sodium hydroxide	0.000143	%

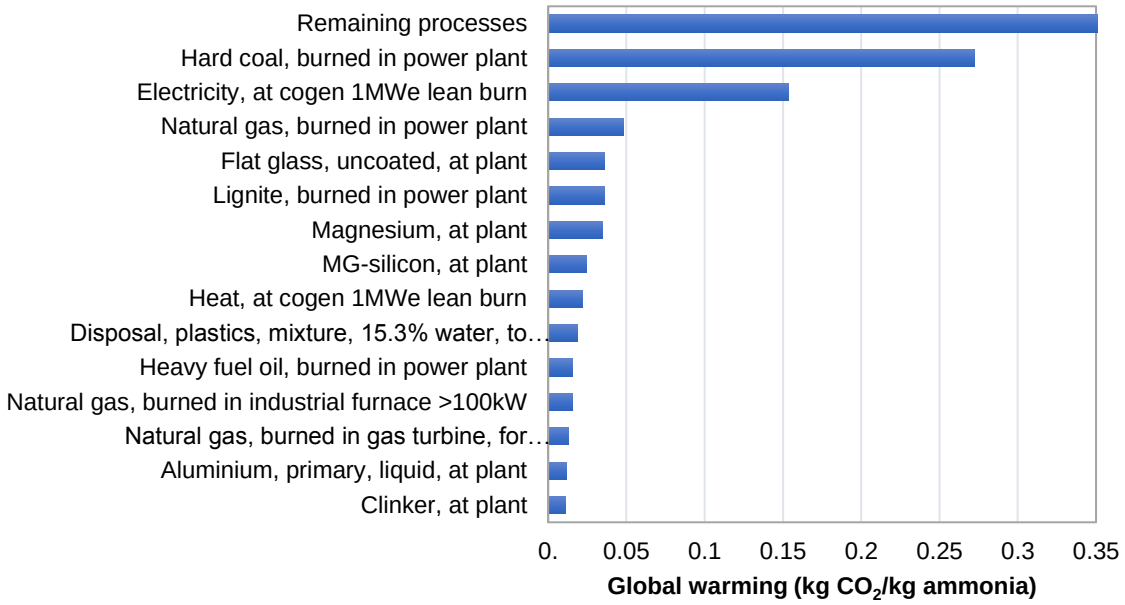

Fig. 5.117 Contribution of various sub-processes to global warming potential of PEC (concentrated light) based electrochemical ammonia synthesis.

5.8.1.1 LCA uncertainty analyses results

Defining the uncertainties within the LCA study brings more reliability of the results. The uncertainty analyses are performed in SimaPro software using Monte Carlo technique. The presented results here are only for PEC based (concentrated light) electrochemical ammonia production method using the experimental system defined in the modeling section.

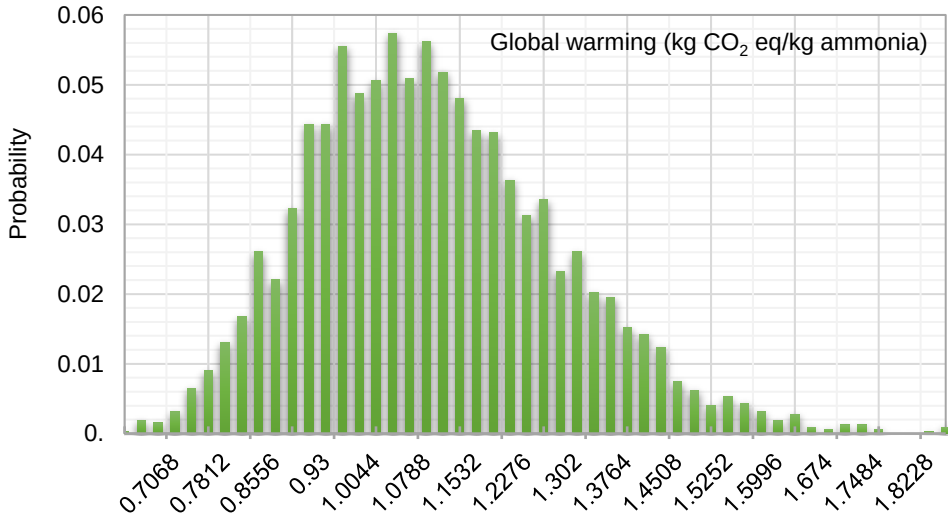

Fig. 5.118 Probability distribution of global warming potential for PEC based (concentrated light) electrochemical ammonia production method.

The confidence interval is 95% for the results. The number of runs performed for the results is 3224. The uncertainty analyses results are shown in Table 5.46 for the selected environmental impact categories. The mean of global warming value is 1.09 kg CO_2 eq. and standard error of mean is 0.00301 kg CO_2 eq. corresponding to 17.1% coefficient of variation which is the lowest among other categories. The highest coefficient of variance is found to be 43.9% for abiotic depletion category

Table 5.49 Uncertainty analyses results of PEC based (concentrated light) electrochemical ammonia production method.

Impact category	**Unit**	**Mean**	**Median**	**SD**	**CV (Coefficient of Variation)**	**Std.err.of mean**
Abiotic depletion	kg Sb eq	0.00822	0.00746	0.00361	43.90%	0.00773
Acidification	kg SO_2 eq	0.00637	0.00623	0.00121	19%	0.00335
Global warming 500a	kg CO_2 eq	1.09	1.07	0.187	17.10%	0.00301
Human toxicity 500a	kg 1,4-DB eq	0.949	0.884	0.302	31.80%	0.0056
Land competition	m^2a	0.0523	0.0495	0.0167	32%	0.00564
Ozone layer depletion 40a	kg CFC-11 eq	2.75E-07	2.63E-07	7.65E-08	27.80%	0.00489
Terrestrial ecotoxicity 500a	kg 1,4-DB eq	0.00104	0.000999	0.000269	25.70%	0.00453

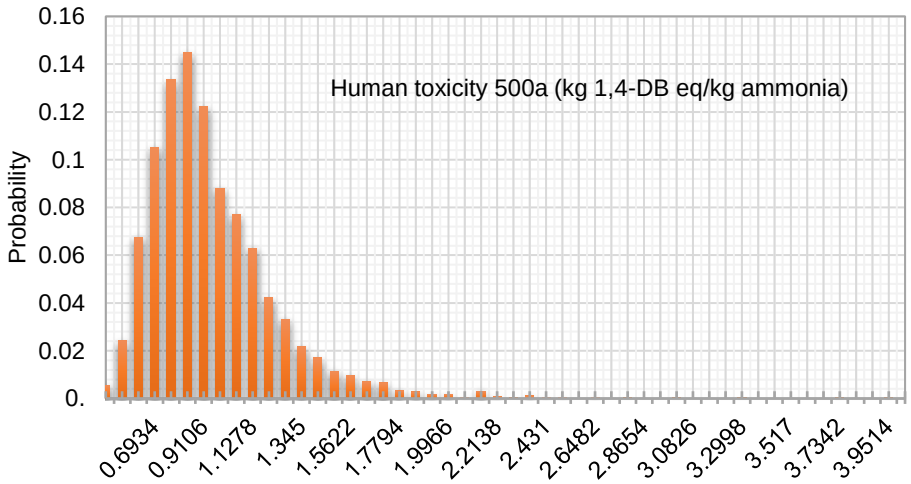

Fig. 5.119 Probability distribution of human toxicity potential for PEC based (concentrated light) electrochemical ammonia production method.

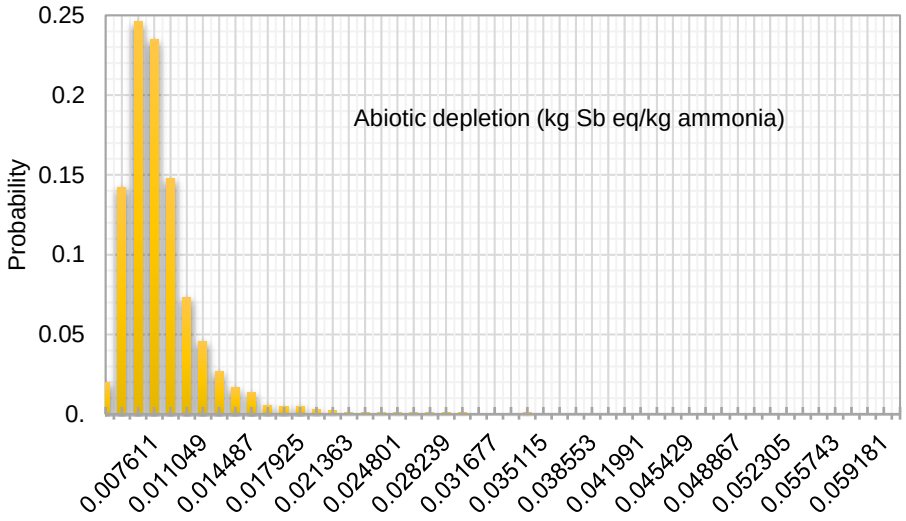

Fig. 5.120 Probability distribution of abiotic depletion potential for PEC based (concentrated light) electrochemical ammonia production method.

The probability distributions of the selected environmental impact categories are shown in Figs. 5.118 to 5.120. Fig. 5.121 shows the comparison of uncertainty ranges for the different categories. This method is still in early investigation phase resulting in less reliable data for LCA inventory step. Taking into account the uncertainties of LCA results for PEC based electrochemical ammonia production method, this process can be more environmentally benign than other renewable routes.

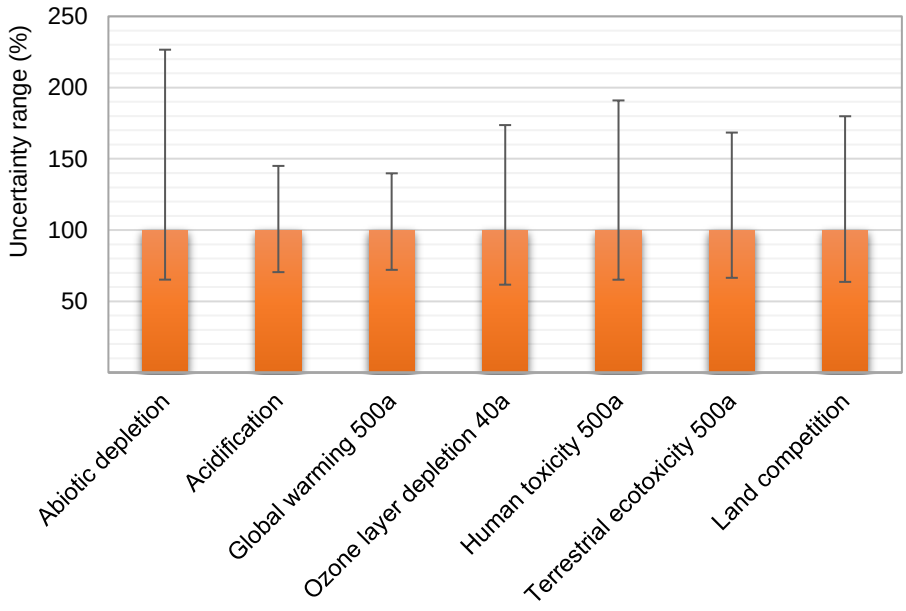

Fig. 5.121 Uncertainty ranges of the selected impact categories for PEC based (concentrated light) electrochemical ammonia production method.

CHAPTER 6: CONCLUSIONS AND RECOMMENDATIONS

In this chapter, the main findings derived from this thesis are summarized and shortly explained. Based on the attained experience and obtained results, further recommendations are also presented for future studies in this research area.

6.1 Conclusions

Maximum utilization of solar energy plays an important role in the photo-conversion processes. In this thesis, both theoretical and experimental investigation of photoelectrochemical hydrogen based electrochemical ammonia synthesis are presented. The spectrum of solar light can be concentrated and separated for various applications to improve the overall system performance for solar energy conversion processes. In this way, multiple products such as electricity, fuels, heating and cooling can be produced within the same system. The underlying motivation of this thesis is the potential for combining photoelectrochemical hydrogen production system with electrolytic ammonia synthesis processes to increase the solar spectrum utilization and ammonia production yield. This thesis demonstrates the integration of photoelectrochemical hydrogen into electrochemical ammonia synthesis for the first time. The concluding remarks are written for each sub-system and integrated system as follows.

The PV cell is modeled and analyzed in detail for determining the occurring losses. The internal processes of a PV cell include: transmission, reflection and absorption of photons through wafer, background (blackbody) radiation emission at cell temperature, electron excitation to generate a photocurrent, electron-hole recombination, internal heat generation by shunt and series resistances, heat dissipation by conduction-convection, and electrical power transmission to a load.

The main findings obtained from the photovoltaic system can be summarized as follows:

- Two different PV modules under concentrated or non-concentrated beams and with or without solar light splitting are characterized. The received portion of the wavelengths by the PV modules decrease considerably, which corresponds to about 19% of the total spectrum when solar spectrum splitters are used. However, when the light is concentrated about 5 to 15 times than ambient irradiance, the loss of power caused by the lack of incoming photons could be compensated and, then, the overall efficiency could be increased.
- The efficiency of the measured PV modules under concentrated and divided solar light range between 13% and 16.5%, which are quite similar to the ones obtained by the modeling results. Moreover, the total power outputs from one of the PV modules are found in the range of 5 W and 7 W under concentrated and divided spectrum.
- The heat transfer rate from cell casing to environment is quite high corresponding to about 90% of the overall input. Hence, this heat can be utilized using photovoltaic/thermal systems. For the long-term operation of the PV panels under split spectrum concentrated light, the temperature is one of the key factors that should be continuously monitored and

controlled to avoid deficiencies. The heat from the PV can be recovered for PV/T and PEM electrolyzer for higher overall efficiency and lesser applied potential of water splitting.

- The velocity of wind and the cell temperature have significant effects on the overall PV performance as well as the atmospheric conditions such as aerosol type, turbidity and gaseous absorption/pollution vaguely affect the performance. Albedo and ground reflectance conditions contribute to irradiance levels received by the PV cell and eventually affect the efficiency.
- PV generator-photo current generation process has the highest exergy destruction rate corresponding to about 65 W among the sub-processes whereas the total exergy destruction rate is about 72 W. The wafer absorption is also important in which the photonic current is determined.

Furthermore, the lower wavelengths of the spectrum is used for photoelectrochemical hydrogen production system which has copper oxide photocathode. The newly built PEC cell is a membrane electrode assembly using photosensitive copper oxide (Cu_2O) material as photocathode. The copper oxide material is deposited on the large area stainless steel cathode plate electrochemically using $CuSO_4 \cdot 5H_2O$ and lactic acid solution. From the electrodeposition of the semiconductor, the followings concluding remarks can be written:

- The impacts of various electrodeposition conditions on the photocurrent density and photoelectrochemical hydrogen production for Cu_2O coated steel plates are presented.
- On the source of the cathodic photo current observed and the equivalent hydrogen generation, the results in this thesis proves that the photo-induced charges in the conduction band of p-type Cu_2O are capable of reducing water to hydrogen.
- The magnitude of the photocurrent produced or hydrogen generated is a consequence of the electrodeposition temperature, duration, pH and surface area which impacted the overall performance.
- The electrodeposited plates present high photo-response under both solar simulator and concentrated light conditions. Using Fresnel lenses, the photocurrent generations and hydrogen evolution are tested under concentrated light yielding higher photocurrent densities and hydrogen production rates.
- In concentrated light characterization at the ambient irradiance of 605 W/m^2 and the concentrated irradiance of 1900 $W/m^{2,}$ the average photocurrent density is measured about 1.5 mA/cm^2. The produced hydrogen is about 160 mL/h hydrogen production under concentrated illumination whereas it decreases to about 65 mL/h as a consequence of lower current in dark measurements.

The electrochemical impendence spectroscopy (EIS) of a newly developed photoelectrochemical (PEC) cell in no-light and concentrated light illuminations is also performed. EIS analyses reveal the fundamental internal charge transfer resistances which limit the performance of the PEC cell. The following remarks are noted from the electrochemical model and EIS measurements of the PEC hydrogen production system:

- The photocurrent generation in the PEC cell is more distinguishable in lower voltages. At higher applied voltages and concentrated light illumination, the activation losses decrease.

- Operating at concentrated light conditions increase the effect of mass transfer which causes the Warburg element values decrease under concentrated light measurements implying a larger amount of mass transfer occurring in the cell.
- The actual cell voltage under concentrated light is calculated to be 1.589 V based on experimental EIS data whereas it is 1.545 V in the model results. This shows that in practice, the experimentally yielded results may differ from model results.

The electrochemical synthesis of NH_3 is a promising alternative to conventional energy intensive NH_3 production plants. Using renewable energy resources to drive the electrochemical NH_3 synthesis, the carbon footprint of current NH_3 production industry can be lowered significantly. Electrochemical NH_3 synthesis routes offer higher integrability to stand alone and distributed NH_3 production which is a carbon free fuel for various sectors. The following results can be derived from the electrochemical ammonia production system:

- NH_3 is electrochemically generated at ambient pressure without a necessity of huge compressors using H_2 and N_2 in a molten hydroxide medium with nano-Fe_3O_4 catalyst.
- The reaction temperature is varied in the range of 180°C to 255°C to investigate the impact of temperature on NH_3 production rates. Having non-corrosive and high surface area nickel mesh electrodes allowed to generate more NH_3. The maximum coulombic efficiency is calculated as 14.17 % corresponding to NH_3 formation rate of 4.41×10^{-9} mol s^{-1} cm^{-2}.
- The lower current densities succeeded to generate higher NH_3 and increasing the reaction temperature lowers the ammonia production rate. At 2 mA/cm^2 and 210°C, ammonia is synthesized at a rate of 6.54×10^{-10} mol/s cm^2. At 2.5 mA/cm^2 and 220°C, the ammonia evolution rate decreased to 4.9×10^{-11} mol NH_3/s cm^2.
- The possible issues being faced in the liquid electrolyte based electrochemical NH_3 synthesis is expected to further be resolved by way of not only the addition of more appropriate additives but also the continuous optimization of reactor configuration.

In the integrated system using solar concentrators and solar spectrum splitters for hydrogen, ammonia and electricity production, the following concluding remarks can be extracted from this thesis:

- Solar light can be split using appropriate devices for a more effective solar energy harvesting. It is succeeded to obtain higher energy rates in each component by concentrating the light although the spectrum is split into two portions.
- The overall solar-to-hydrogen energy and exergy efficiencies of the integrated system for hydrogen production are found to be 6.7% and 7.5%, respectively.
- The overall ammonia production system energy and exergy efficiencies are found to be 3.92% and 4.1%, respectively.
- Even though the sole PEC photocurrent production exergy efficiency is 2.9% and solar-to-hydrogen efficiency is 5.5% in ambient conditions, under the concentrated and split spectrum light, they are enhanced to and 5.6% and 6.2%, respectively.

From the exergoeconomic analyses, the following remarks are noted:

- The system capital cost is mainly dominated by the photoelectrochemical reactor and electrodes.

- In case the system lifetime is taken to be 10 years for the experimental system, the total calculated cost rate is about 0.6141 $/h. However, in case the lifetime can be increased up to 40 years, the total cost rate can be decreased down to 0.3233 $/h.
- In the scale-up analyses, the concentrated light based photoelectrochemical hydrogen production plant is considered to have about 21,615 m^2 solar capturing area for 1,000 kg/day hydrogen production plant.
- In the large capacity plant, which is assumed to start operation in 2020, the hydrogen cost per kg is calculated to be 3.24 $/kg whereas the cost of ammonia is found to be 0.84 $/kg.

The following concluding remarks are noted for LCA analyses conducted for one kg ammonia production from various methods:

- In terms of human toxicity, coal, pumped hydro, heavy oil fired power plant based electrolysis and nuclear CuCl thermochemical methods have highest values. Municipal waste, biomass and hydropower routes have lower abiotic depletion, global warming and human toxicity values respectively among all methods. Coal gasification based ammonia production methods have lower acidification/ eutrophication values among conventional ammonia production methods.
- Nuclear electrolysis and naphtha cracking based ammonia production methods have least effect on climate change among conventional methods while hydropower and biomass based methods are the most environmentally benign method in terms of climate change and global warming.
- PEC based electrochemical ammonia synthesis under concentrated light yields about 1.09 kg CO2 eq./kg ammonia whereas PEC based electrochemical synthesis under no-light yields about 1.16 kg CO2 eq. per kg ammonia. These values are considerably lower than conventional steam methane reforming.

Through the developed system, it is achieved to demonstrate a competitive hydrogen and ammonia production pathway with a design that harmoniously integrates: low-cost sun-tracking system with azimuth pivot-on-rollers, cost effective Fresnel lens concentrator, small-surface dielectric spectral splitting mirror, concentrated PV, photoelectrochemical hydrogen reactor and electrochemical ammonia reactor.

6.2 Recommendations

This thesis investigates the photoelectrochemical hydrogen production and electrochemical ammonia synthesis under various conditions. In order to expand the study to a wider perspective and increase the utilization opportunities, the following recommendations are listed:

- For the photoelectrochemical hydrogen production, various photoactive materials other than copper oxide need to be tested for increasing the photoactivity and photocurrent generation. In addition, various doping materials to make composite photocatalysts/photoelectrodes can be investigated to enhance the photo absorption and total solar-to-hydrogen efficiency. This is required in order to capture a larger portion of the solar spectrum by the photoelectrochemical cell. Eventually, the absorption of the larger spectrum improves the photocurrent generations and hydrogen evolution.

- A larger scale integrated system for electricity, heat, hydrogen and ammonia production providing above 100 mL/h ammonia and 2.5 L/h hydrogen can be built and experimentally tested. The practicability of the solar energy based hydrogen and ammonia production options is needed to be further confirmed in larger scales. This enables utilization of large scale applications for decentralized energy production and storage.
- Thermal imaging of the experimental system can be performed to investigate the temperature distribution over the system components. In this way, the possible heat losses can be determined and the waste heat utilization techniques can be implemented. Since, the system has waste heat from different components, the recovery of this heat can enhance the overall system efficiency.
- Specific concentrated photovoltaic (CPV) modules can be used in the experiments which are more appropriate for concentrated solar light applications since they are more resistive to higher temperatures. CPV technology has been developing in recent years. Especially, CPV power plants can be integrated to hydrogen and ammonia production plants for energy storage applications.
- Different solar light concentration and splitting mechanisms can be tested to investigate the most efficient method having less exergy destruction rates and higher efficiencies. In the designed system, most of the exergy destruction occurs in Fresnel lens. Therefore, a better apparatus having higher energy absorption and transmission rates would improve the overall system performance.
- For the electrochemical ammonia synthesis, the effects of various catalysts, various molten salts and various electrodes can be investigated to find the optimal materials required to increase the ammonia formation rate. The catalyst stability is also important for the reaction occurrence. Furthermore, the long-term operation of electrodes used in the experiments need to be confirmed because of corrosivity of the molten salt medium.
- The possible storage techniques of hydrogen and ammonia can be investigated which can be integrated to the current experimental setup for further utilization. As well as, the produced hydrogen can be integrated to other synthetic fuel production technologies such as methanol and ethanol.
- Thermoelectric generators (TEG) can be integrated to the current system for recovering the excess heat and increasing the overall system efficiency. TEG systems work based on the temperature gradient. Since there are high temperature levels in the current system, this temperature differences could be utilized by employing TEGs for direct electricity production. The produced electricity can either be used for hydrogen and ammonia production or directly used by the consumer.
- The phase change materials (PCM) can be used as a storage medium. Employing PCMs can enhance the system operation in the nighttime or at low irradiation levels. In this way, continuous operation of the system can further be satisfied.
- The developed system for ammonia production can be applied in various sectors ranging from solar fields to remote communities for multiple commodities such as heating, cooling, power generation, energy storage, etc.

- Other renewable energy options can be easily integrated to this system to produce clean ammonia. The electrochemical process for ammonia synthesis is not restricted to solar energy. Any type of renewable electricity would make the process environmentally friendly. Therefore, there is a high potential for utilization of renewable energy in electrochemical ammonia synthesis applications for energy conversion and storage.
- Comprehensive CFD, flow modeling and ASPEN Plus modeling of the integrated system can be performed. In the continuous operation of the photoelectrochemical reactor, the product gases and water flow in the same channel. Therefore, a study of multi-phase flow within the reactor and tubing would reveal the losses and behavior of the flow. In this way, the system performance can further be confirmed.
- Wastewater treatment can be integrated to hydrogen production system for multi-product generation. In addition, saline water is a significant candidate for hydrogen production applications. Especially, considering the massive amount of industrial wastewater and saline water in the world, the integration of the current system into waste water and saline water applications is critical.
- Direct solar to ammonia conversion technologies could be investigated which can include the nitrogen bond cracking at concentrated sunlight. If the required nitrogen for the ammonia synthesis reaction can be produced from an environmentally benign and small/medium scale method rather than massive air separation plants, the de-centralized ammonia production and utilization opportunities can be further developed.

REFERENCES

1. REN21. *renewables 2016 global status report - REN21*. 2016. Paris: REN21 Secretariat.
2. Hydrogen Analysis Resource Center, Energy Information Administration (EIA), U.S. Department of Energy (DOE). [cited 8 March 2017]. Available from http://hydrogen.pnl.gov/.
3. Brown LC, Besenbruch GE, Schultz KR, Showalter SK, Marshall AC, Pickard PS, *et al.* High efficiency generation of hydrogen fuels using thermochemical cycles and nuclear power. *AIChE 2002 Spring Natl. Meet. New Orleans, Louisiana*, 2002.
4. Naterer GF, Suppiah S, Stolberg L, Lewis M, Ferrandon M, Wang Z, *et al.* Clean hydrogen production with the Cu-Cl cycle-Progress of international consortium, I: Experimental unit operations. *Int. J. Hydrogen Energy*, 2011. 36:15472–15485.
5. Jennings JR. *Catalytic Ammonia Synthesis : Fundamentals and Practice*. 1991. Springer US.
6. Holladay JD, Hu J, King DL, Wang Y. An overview of hydrogen production technologies. *Catal. Today*, 2009. 139:244–260.
7. Avery W. Hydrogen generation by OTEC electrolysis, and economical energy transfer to world markets via ammonia and methanol. *Int. J. Hydrogen Energy*, 1985. 10:727–736.
8. Joshi AS, Dincer I, Reddy B V. Solar hydrogen production: A comparative performance assessment. *Int. J. Hydrogen Energy*, 2011. 36:11246–11257.
9. Bolton JR, Strickler SJ, Connolly JS. Limiting and realizable efficiencies of solar photolysis of water. *Nature*, 1985. 316:495.
10. Archer MD, Bolton JR. Requirements for ideal performance of photochemical and photovoltaic solar energy converters. *J. Phys. Chem.*, 1990. 94:8028–8036.
11. Weber MF, Dignam MJ. Efficiency of Splitting Water with Semiconducting Photoelectrodes. *J. Electrochem. Soc.*, 1984. 131:1258.
12. Gálvez ME, Halmann M, Steinfeld A. Ammonia Production via a Two-Step Al2O3/AlN Thermochemical Cycle. 1. Thermodynamic, Environmental, and Economic Analyses. *Ind. Eng. Chem. Res.*, 2007. 46:2042–2046.
13. Kool A, Marinussen M, Blonk H. LCI data for the calculation tool Feedprint for greenhouse gas emissions of feed production and utilization. *GHG Emiss. N, P K Fertil. Prod. Gravin Beatrixstraat*, 2012. 34:2805.
14. Canadian Ammonia Producers. *Benchmarking Energy Efficiency and Carbon Dioxide Emissions*. 2008. Canada.
15. Bicer Y, Dincer I, Vezina G, Raso F. Impact Assessment and Environmental Evaluation of Various Ammonia Production Processes. *Environ. Manage.*, 2017.:1–14. doi:10.1007/s00267-017-0831-6.
16. Yara Fertilizer Industry Handbook. 2017. [cited 7 January 2017]. Available from http://yara.com/investor_relations/reports_presentations/.
17. Ammonia | Industrial Efficiency Technology Database; Measures. [cited 7 January 2017]. Available from http://ietd.iipnetwork.org/content/ammonia#key-data.
18. International Energy Agency. *Energy Technology Perspectives 2012*. *Energy Technol. Perspect. 2012*, 2012. OECD Publishing, FRANCE. doi:10.1787/energy_tech-2012-en.
19. Smith AR, Klosek J. A review of air separation technologies and their integration

with energy conversion processes. *Fuel Process. Technol.*, 2001. 70:115–134.
20. Bartels J. A feasibility study of implementing an Ammonia Economy. *Grad. Theses Diss.*, 2008.
21. Appl M. *Ammonia: principles and industrial practice*. 1999. Vch Verlagsgesellschaft Mbh.
22. Appl M. Chemical Reactions and Uses of Ammonia. *Ammonia*, 2007. Wiley-VCH Verlag GmbH, pp 231–234. doi:10.1002/9783527613885.ch12.
23. Appl M, Appl, Max. Ammonia, 3. Production Plants. *Ullmann's Encycl. Ind. Chem.*, 2011. Wiley-VCH Verlag GmbH & Co. KGaA, Weinheim, Germany. doi:10.1002/14356007.o02_o12.
24. Appl M. Complete Ammonia Production Plants. *Ammonia*, 2007. Wiley-VCH Verlag GmbH, pp 177–204. doi:10.1002/9783527613885.ch05.
25. Rossetti I, Pernicone N, Forni L. Graphitised carbon as support for Ru/C ammonia synthesis catalyst. *Catal. Today*, 2005. 102–103:219–224.
26. Erisman JW, Sutton MA, Galloway J, Klimont Z, Winiwarter W. How a century of ammonia synthesis changed the world. *Nat. Geosci.*, 2008. 1:636–639.
27. Marnellos G, Stoukides M. Ammonia Synthesis at Atmospheric Pressure. *Science (80-.).*, 1998. 282:98–100.
28. Liu R, Xu G. Comparison of Electrochemical Synthesis of Ammonia by Using Sulfonated Polysulfone and Nafion Membrane with Sm1.5Sr0.5NiO4. *Chinese J. Chem.*, 2010. 28:139–142.
29. Xu G, Liu R. Sm1.5Sr0.5MO4 (M=Ni, Co, Fe) Cathode Catalysts for Ammonia Synthesis at Atmospheric Pressure and Low Temperature. *Chinese J. Chem.*, 2009. 27:677–680.
30. Appl M. Material Considerations for Equipment Fabrication. *Ammonia*, 2007. Wiley-VCH Verlag GmbH, pp 209–212. doi:10.1002/9783527613885.ch08.
31. Ganley JC, Holbrook JH, McKinley DE. Solid State Ammonia Synthesis. *Ammon. Fuel Netw. Conf.*, 2007.
32. ecoinvent v3 | High-Quality LCI Database Integrated in SimaPro.
33. Makhlouf A, Serradj T, Cheniti H. Life cycle impact assessment of ammonia production in Algeria: A comparison with previous studies. *Environ. Impact Assess. Rev.*, 2015. 50:35–41.
34. Hasler K, Bröring S, Omta SWF, Olfs H-W. Life cycle assessment (LCA) of different fertilizer product types. *Eur. J. Agron.*, 2015. 69:41–51.
35. Kahrl F, Li Y, Su Y, Tennigkeit T, Wilkes A, Xu J. Greenhouse gas emissions from nitrogen fertilizer use in China. *Environ. Sci. Policy*, 2010. 13:688–694.
36. PotashCorp Integrated Annual Report. *2015 Annu. Integr. Rep.*, 2015. [cited 7 January 2017]. Available from http://www.potashcorp.com/irc/nitrogen.
37. Home - Industry Overview - PotashCorp. [cited 7 January 2017]. Available from http://www.potashcorp.com/overview/introduction/company/potashcorp-profile.
38. Olson NK, Holbrook J. NH3 - 'The Other Hydrogen'. *Ammon. Fuel Netw.*, 2007.
39. Lovegrove K, Luzzi A, Soldiani I, Kreetz H. Developing ammonia based thermochemical energy storage for dish power plants. *Sol. Energy*, 2004. 76:331–337.
40. Dincer I, Zamfirescu C. *Advanced power generation systems*. 2014. Elsevier.
41. Dincer İ. *Refrigeration Systems and Applications*. 2003. Wiley.

42. Zamfirescu C, Dincer I. How much exergy one can obtain from incident solar radiation? *J. Appl. Phys.*, 2009. 105:44911.
43. He Y-R, Yan F-F, Yu H-Q, Yuan S-J, Tong Z-H, Sheng G-P. Hydrogen production in a light-driven photoelectrochemical cell. *Appl. Energy*, 2014. 113:164–168.
44. Tseng C-L, Tseng C-J, Chen J-C. Thermodynamic analysis of a photoelectrochemical hydrogen production system. *Int. J. Hydrogen Energy*, 2010. 35:2781–2785.
45. Lopes T, Dias P, Andrade L, Mendes A. An innovative photoelectrochemical lab device for solar water splitting. *Sol. Energy Mater. Sol. Cells*, 2014. 128:399–410.
46. Abe R. Recent progress on photocatalytic and photoelectrochemical water splitting under visible light irradiation. *J. Photochem. Photobiol. C Photochem. Rev.*, 2010. 11:179–209.
47. Minggu LJ, Wan Daud WR, Kassim MB. An overview of photocells and photoreactors for photoelectrochemical water splitting. *Int. J. Hydrogen Energy*, 2010. 35:5233–5244.
48. Gibson TL, Kelly NA. Optimization of solar powered hydrogen production using photovoltaic electrolysis devices. *Int. J. Hydrogen Energy*, 2008. 33:5931–5940.
49. Ismail AA, Bahnemann DW. Photochemical splitting of water for hydrogen production by photocatalysis: A review. *Sol. Energy Mater. Sol. Cells*, 2014. 128:85–101.
50. Gibson TL, Kelly NA. Predicting efficiency of solar powered hydrogen generation using photovoltaic-electrolysis devices. *Int. J. Hydrogen Energy*, 2010. 35:900–911.
51. Shi Z, Wen X, Guan Z, Cao D, Luo W, Zou Z. Recent progress in photoelectrochemical water splitting for solar hydrogen production. *Ann. Phys. (N. Y).*, 2015. 358:236–247.
52. Kelly NA, Gibson TL. Solar energy concentrating reactors for hydrogen production by photoelectrochemical water splitting. *Int. J. Hydrogen Energy*, 2008. 33:6420–6431.
53. Jacobsson TJ, Fjallstrom V, Edoff M, Edvinsson T. Sustainable solar hydrogen production: from photoelectrochemical cells to PV-electrolyzers and back again. *Energy Environ. Sci.*, 2014. 7:2056–2070.
54. Tseng C-J, Tseng C-L. The reactor design for photoelectrochemical hydrogen production. *Int. J. Hydrogen Energy*, 2011. 36:6510–6518.
55. James BD, Baum GN, Perez J, Baum KN. *Technoeconomic Analysis of Photoelectrochemical (PEC) Hydrogen Production*. 2009.
56. Acar C, Dincer I. Experimental investigation and analysis of a hybrid photoelectrochemical hydrogen production system. *Int. J. Hydrogen Energy*, 2017. 42:2504–2511.
57. Acar C, Ghosh S, Dincer I, Zamfirescu C. Evaluation of a new continuous type hybrid photo-electrochemical system. *Int. J. Hydrogen Energy*, 2015. 40:11112–11124.
58. Shi X, Jeong H, Oh SJ, Ma M, Zhang K, Kwon J, *et al.* Unassisted photoelectrochemical water splitting exceeding 7% solar-to-hydrogen conversion efficiency using photon recycling. *Nat. Commun.*, 2016. 7:11943.
59. Döscher H, Young JL, Geisz JF, Turner JA, Deutsch TG, Gaillard N, *et al.* Solar-to-hydrogen efficiency: shining light on photoelectrochemical device performance.

Energy Environ. Sci., 2016. 9:74–80.
60. Li J, Wu N, Wang Z, Zhong Z, Xu R, Fujita T, *et al.* Semiconductor-based photocatalysts and photoelectrochemical cells for solar fuel generation: a review. *Catal. Sci. Technol.*, 2015. 5:1360–1384.
61. Reece SY, Hamel JA, Sung K, Jarvi TD, Esswein AJ, Pijpers JJH, *et al.* Wireless Solar Water Splitting Using Silicon-Based Semiconductors and Earth-Abundant Catalysts. *Science (80-.).*, 2011. 334:645–648.
62. Brillet J, Yum J-H, Cornuz M, Hisatomi T, Solarska R, Augustynski J, *et al.* Highly efficient water splitting by a dual-absorber tandem cell. *Nat. Photonics*, 2012. 6:824–828.
63. Fernando CAN, Bandara TMWJ, Wethasingha SK. H2 evolution from a photoelectrochemical cell with n-Cu2O photoelectrode under visible light irradiation. *Sol. Energy Mater. Sol. Cells*, 2001. 70:121–129.
64. de Jongh PE, Vanmaekelbergh D, Kelly JJ. Cu2O: a catalyst for the photochemical decomposition of water? *Chem. Commun.*, 1999.:1069–1070. doi:10.1039/a901232j.
65. Matsuzaki K, Nomura K, Yanagi H, Kamiya T, Hirano M, Hosono H. Epitaxial growth of high mobility Cu2O thin films and application to p-channel thin film transistor. *Appl. Phys. Lett.*, 2008. 93:202107.
66. Fernando CA., Wetthasinghe S. Investigation of photoelectrochemical characteristics of n-type Cu2O films. *Sol. Energy Mater. Sol. Cells*, 2000. 63:299–308.
67. Khan KA, Leung YK, Kos JF. Quantum efficiency of Cu2O electrode in photoelectrochemical cells with and without bias. *Renew. Energy*, 1997. 11:293–298.
68. Jeong SS, Mittiga A, Salza E, Masci A, Passerini S. Electrodeposited ZnO/Cu2O heterojunction solar cells. *Electrochim. Acta*, 2008. 53:2226–2231.
69. Korzhavyi PA, Johansson B. Literature review on the properties of cuprous oxide Cu2O and the process of copper oxidation. *Swedish Nucl. Fuel Waste Manag. Co*, 2011. Technical.
70. Zhang D., Liu Y., Liu Y., Yang H. The electrical properties and the interfaces of Cu2O/ZnO/ITO p–i–n heterojunction. *Phys. B Condens. Matter*, 2004. 351:178–183.
71. Akimoto K, Ishizuka S, Yanagita M, Nawa Y, Paul GK, Sakurai T. Thin film deposition of Cu2O and application for solar cells. *Sol. Energy*, 2006. 80:715–722.
72. Bornoz P, Abdi FF, Tilley SD, Dam B, van de Krol R, Graetzel M, *et al.* A Bismuth Vanadate–Cuprous Oxide Tandem Cell for Overall Solar Water Splitting. *J. Phys. Chem. C*, 2014. 118:16959–16966.
73. Acar C, Dincer I. A review and evaluation of photoelectrode coating materials and methods for photoelectrochemical hydrogen production. *Int. J. Hydrogen Energy*. doi:http://dx.doi.org/10.1016/j.ijhydene.2015.11.160.
74. Zhao W, Fu W, Yang H, Tian C, Li M, Li Y, *et al.* Electrodeposition of Cu2O films and their photoelectrochemical properties. *CrystEngComm*, 2011. 13:2871–2877.
75. Amano F, Ebina T, Ohtani B. Enhancement of photocathodic stability of p-type copper(I) oxide electrodes by surface etching treatment. *Thin Solid Films*, 2014. 550:340–346.

76. Georgieva V, Ristov M. Electrodeposited cuprous oxide on indium tin oxide for solar applications. *Sol. Energy Mater. Sol. Cells*, 2002. 73:67–73.
77. Bao M, Wang D, Liu S, Kuang L, Sun J, Wang F, *et al.* Electrodeposition and electrocatalytic activity of Cu2O film on stainless steel substrate. *Appl. Surf. Sci.*, 2012. 258:8008–8014.
78. Chiang C-Y, Shin Y, Aroh K, Ehrman S. Copper oxide photocathodes prepared by a solution based process. *Int. J. Hydrogen Energy*, 2012. 37:8232–8239.
79. Haller S, Jung J, Rousset J, Lincot D. Effect of electrodeposition parameters and addition of chloride ions on the structural and optoelectronic properties of Cu2O. *Electrochim. Acta*, 2012. 82:402–407.
80. Casallas C, Dincer I, Zamfirescu C. Experimental investigation and analysis of a novel photo-electrochemical hydrogen production cell with polymeric membrane photocathode. *Int. J. Hydrogen Energy*, 2016. 41:7968–7975.
81. Juodkazytė J, Šebeka B, Savickaja I, Jagminas A, Jasulaitienė V, Selskis A, *et al.* Study on copper oxide stability in photoelectrochemical cell composed of nanostructured TiO2 and CuxO electrodes. *Electrochim. Acta*, 2014. 137:363–371.
82. Tran PD, Batabyal SK, Pramana SS, Barber J, Wong LH, Loo SCJ. A cuprous oxide-reduced graphene oxide (Cu2O-rGO) composite photocatalyst for hydrogen generation: employing rGO as an electron acceptor to enhance the photocatalytic activity and stability of Cu2O. *Nanoscale*, 2012. 4:3875–3878.
83. Zyoud A, Saadeddin I, Khurduj S, Mari'e M, Hawash ZM, Faroun MI, *et al.* Combined electrochemical/chemical bath depositions to prepare CdS film electrodes with enhanced PEC characteristics. *J. Electroanal. Chem.*, 2013. 707:117–121.
84. Zyoud A, AlKerm RS, Alkerm RS, Abdelhadi DH, Park D, Helal MHS, *et al.* Enhanced PEC characteristics of pre-annealed CuS film electrodes by metalloporphyrin/polymer matrices. *Sol. Energy Mater. Sol. Cells*, 2016. 144:429–437.
85. Mao Y, He J, Sun X, Li W, Lu X, Gan J, *et al.* Electrochemical synthesis of hierarchical Cu2O stars with enhanced photoelectrochemical properties. *Electrochim. Acta*, 2012. 62:1–7.
86. Mitra S, Poizot P, Finke A, Tarascon J -M. Growth and Electrochemical Characterization versus Lithium of Fe3O4 Electrodes Made by Electrodeposition. *Adv. Funct. Mater.*, 2006. 16:2281–2287.
87. Dubal DP, Dhawale DS, Salunkhe RR, Jamdade VS, Lokhande CD. Fabrication of copper oxide multilayer nanosheets for supercapacitor application. *J. Alloys Compd.*, 2010. 492:26–30.
88. Daltin A-L, Addad A, Chopart J-P. Potentiostatic deposition and characterization of cuprous oxide films and nanowires. *J. Cryst. Growth*, 2005. 282:414–420.
89. Zhou YC, Switzer JA. Galvanostatic electrodeposition and microstructure of copper (I) oxide film. *Mater. Res. Innov.*, 1998. 2:22–27.
90. Gomadam PM, Weidner JW. Analysis of electrochemical impedance spectroscopy in proton exchange membrane fuel cells. *Int. J. Energy Res.*, 2005. 29:1133–1151.
91. Lopes T, Andrade L, Ribeiro HA, Mendes A. Characterization of photoelectrochemical cells for water splitting by electrochemical impedance spectroscopy. *Int. J. Hydrogen Energy*, 2010. 35:11601–11608.

92. Siracusano S, Baglio V, Lufrano F, Staiti P, Aricò AS. Electrochemical characterization of a PEM water electrolyzer based on a sulfonated polysulfone membrane. *J. Memb. Sci.*, 2013. 448:209–214.
93. Bohra D, Smith WA. Improved charge separation via Fe-doping of copper tungstate photoanodes. *Phys. Chem. Chem. Phys.*, 2015. 17:9857–9866.
94. Dedigama I, Angeli P, Ayers K, Robinson JB, Shearing PR, Tsaoulidis D, *et al.* In situ diagnostic techniques for characterisation of polymer electrolyte membrane water electrolysers - Flow visualisation and electrochemical impedance spectroscopy. *Int. J. Hydrogen Energy*, 2014. 39:4468–4482.
95. Rong Y, Han H. Monolithic quasi-solid-state dye-sensitized solar cells based on graphene-modified mesoscopic carbon-counter electrodes. *J. Nanophotonics*, 2013. 7:73090.
96. Yi JS, Song T. Performance Characterization of PEM Fuel Cells Using AC Impedance Spectroscopy: I. Model-Based Analysis. *J. Electrochem. Soc.*, 2013. 160:F141–F152.
97. Cho EA, Jeon US, Hong SA, Oh IH, Kang SG. Performance of a 1 kW-class PEMFC stack using TiN-coated 316 stainless steel bipolar plates. *J. Power Sources*, 2005. 142:177–183.
98. Jia R, Chen J, Zhao J, Zheng J, Song C, Li L, *et al.* Synthesis of highly nitrogen-doped hollow carbon nanoparticles and their excellent electrocatalytic properties in dye-sensitized solar cells. *J. Mater. Chem.*, 2010. 20:10829–10834.
99. Faine P, Kurtz SR, Riordan C, Olson JM. The influence of spectral solar irradiance variations on the performance of selected single-junction and multijunction solar cells. *Sol. Cells*, 1991. 31:259–278.
100. Nagae S, Toda M, Minemoto T, Takakura H, Hamakawa Y. Evaluation of the impact of solar spectrum and temperature variations on output power of silicon-based photovoltaic modules. *Sol. Energy Mater. Sol. Cells*, 2006. 90:3568–3575.
101. Minemoto T, Toda M, Nagae S, Gotoh M, Nakajima A, Yamamoto K, *et al.* Effect of spectral irradiance distribution on the outdoor performance of amorphous Si//thin-film crystalline Si stacked photovoltaic modules. *Sol. Energy Mater. Sol. Cells*, 2007. 91:120–122.
102. Nann S, Emery K. Spectral effects on PV-device rating. *Sol. Energy Mater. Sol. Cells*, 1992. 27:189–216.
103. Gottschalg R, Betts TR, Infield DG, Kearney MJ. The effect of spectral variations on the performance parameters of single and double junction amorphous silicon solar cells. *Sol. Energy Mater. Sol. Cells*, 2005. 85:415–428.
104. Saloux E, Teyssedou A, Sorin M. Analysis of photovoltaic (PV) and photovoltaic/thermal (PV/T) systems using the exergy method. *Energy Build.*, 2013. 67:275–285.
105. Sudhakar K, Srivastava T. Energy and exergy analysis of 36 W solar photovoltaic module. *Int. J. Ambient Energy*, 2013. 35:51–57.
106. Duran Sahin A, Dincer I, Rosen MA. Thermodynamic analysis of solar photovoltaic cell systems. *Sol. Energy Mater. Sol. Cells*, 2007. 91:153–159.
107. Rabady RI. Solar spectrum management for effective hydrogen production by hybrid thermo-photovoltaic water electrolysis. *Int. J. Hydrogen Energy*, 2014. 39:6827–6836.

108. Khamooshi M, Salati H, Egelioglu F, Hooshyar Faghiri A, Tarabishi J, Babadi S. A Review of Solar Photovoltaic Concentrators. *Int. J. Photoenergy*, 2014. 2014:17.
109. Kumar V, Shrivastava RL, Untawale SP. Fresnel lens: A promising alternative of reflectors in concentrated solar power. *Renew. Sustain. Energy Rev.*, 2015. 44:376–390.
110. Wu Y, Eames P, Mallick T, Sabry M. Experimental characterisation of a Fresnel lens photovoltaic concentrating system. *Sol. Energy*, 2012. 86:430–440.
111. Dincer I, Zamfirescu C. Chapter 7 - Renewable-Energy-Based Power Generating Systems. In Zamfirescu, ID, ed., *Adv. Power Gener. Syst.*, 2014. Elsevier, Boston, pp 369–453. doi:http://dx.doi.org/10.1016/B978-0-12-383860-5.00007-9.
112. Mojiri A, Taylor R, Thomsen E, Rosengarten G. Spectral beam splitting for efficient conversion of solar energy—A review. *Renew. Sustain. Energy Rev.*, 2013. 28:654–663.
113. An W, Wu J, Zhu T, Zhu Q. Experimental investigation of a concentrating PV/T collector with Cu9S5 nanofluid spectral splitting filter. *Appl. Energy*, 2016. 184:197–206.
114. Stanley C, Mojiri A, Rahat M, Blakers A, Rosengarten G. Performance testing of a spectral beam splitting hybrid PVT solar receiver for linear concentrators. *Appl. Energy*, 2016. 168:303–313.
115. Crisostomo F, Taylor RA, Surjadi D, Mojiri A, Rosengarten G, Hawkes ER. Spectral splitting strategy and optical model for the development of a concentrating hybrid PV/T collector. *Appl. Energy*, 2015. 141:238–246.
116. Kim JP, Lim H, Song JH, Chang YJ, Jeon CH. Numerical analysis on the thermal characteristics of photovoltaic module with ambient temperature variation. *Sol. Energy Mater. Sol. Cells*, 2011. 95:404–407.
117. Vorndran S, Russo JM, Wu Y, Gordon M, Kostuk R. Holographic diffraction-through-aperture spectrum splitting for increased hybrid solar energy conversion efficiency. *Int. J. Energy Res.*, 2015. 39:326–335.
118. Willars-Rodríguez FJ, Chávez-Urbiola EA, Vorobiev P, Vorobiev Y V. Investigation of solar hybrid system with concentrating Fresnel lens, photovoltaic and thermoelectric generators. *Int. J. Energy Res.*, 2016.:n/a-n/a. doi:10.1002/er.3614.
119. Xu Y, Xuan Y, Yang L. Full-spectrum photon management of solar cell structures for photovoltaic–thermoelectric hybrid systems. *Energy Convers. Manag.*, 2015. 103:533–541.
120. Akyuz E, Coskun C, Oktay Z, Dincer I. A novel approach for estimation of photovoltaic exergy efficiency. *Energy*, 2012. 44:1059–1066.
121. Ceylan İ, Gürel AE, Ergün A, Tabak A. Performance analysis of a concentrated photovoltaic and thermal system. *Sol. Energy*, 2016. 129:217–223.
122. Cotfas DT, Floroian L, Cotfas PA, Floroian D, Rubin R, Lieberman D. The study of the photovoltaic cells parameters in concentrated sunlight. *2014 Int. Conf. Optim. Electr. Electron. Equip.*, 2014. IEEE, pp 707–712. doi:10.1109/OPTIM.2014.6850916.
123. Rawat R, Kaushik SC, Sastry OS, Singh YK, Bora B. Energetic and exergetic performance analysis of CdS/CdTe based photovoltaic technology in real operating conditions of composite climate. *Energy Convers. Manag.*, 2016. 110:42–50.

124. Green MA, Emery K, Hishikawa Y, Warta W, Dunlop ED, Levi DH, *et al.* Solar cell efficiency tables (version 49). *Prog. Photovoltaics Res. Appl.*, 2017. 25:3–13.
125. Wu S-Y, Guo F-H, Xiao L. A Review on the Methodology for Calculating Heat and Exergy Losses of a Conventional Solar PV/T System. *Int. J. Green Energy*, 2014. 12:379–397.
126. Royne A, Dey CJ, Mills DR. Cooling of photovoltaic cells under concentrated illumination: a critical review. *Sol. Energy Mater. Sol. Cells*, 2005. 86:451–483.
127. Zamfirescu C, Dincer I. Using ammonia as a sustainable fuel. *J. Power Sources*, 2008. 185:459–465.
128. Verma A, Kumar A. Life cycle assessment of hydrogen production from underground coal gasification. *Appl. Energy*, 2015. 147:556–568.
129. Kalinci Y, Hepbasli A, Dincer I. Life cycle assessment of hydrogen production from biomass gasification systems. *Int. J. Hydrogen Energy*, 2012. 37:14026–14039.
130. Koroneos C, Dompros A, Roumbas G, Moussiopoulos N. Life cycle assessment of hydrogen fuel production processes. *Int. J. Hydrogen Energy*, 2004. 29:1443–1450.
131. Granovskii M, Dincer I, Rosen MA. Life cycle assessment of hydrogen fuel cell and gasoline vehicles. *Int. J. Hydrogen Energy*, 2006. 31:337–352.
132. Hacatoglu K, Rosen MA, Dincer I. Comparative life cycle assessment of hydrogen and other selected fuels. *Int. J. Hydrogen Energy*, 2012. 37:9933–9940.
133. Utgikar V, Thiesen T. Life cycle assessment of high temperature electrolysis for hydrogen production via nuclear energy. *Int. J. Hydrogen Energy*, 2006. 31:939–944.
134. Acar C, Dincer I. Impact assessment and efficiency evaluation of hydrogen production methods. *Int. J. Energy Res.*, 2015. 39:1757–1768.
135. Ozbilen A, Dincer I, Rosen MA. Life cycle assessment of hydrogen production via thermochemical water splitting using multi-step Cu–Cl cycles. *J. Clean. Prod.*, 2012. 33:202–216.
136. Ozbilen A, Dincer I, Rosen MA. A comparative life cycle analysis of hydrogen production via thermochemical water splitting using a Cu–Cl cycle. *Int. J. Hydrogen Energy*, 2011. 36:11321–11327.
137. Ozbilen A, Dincer I, Rosen MA. Exergetic life cycle assessment of a hydrogen production process. *Int. J. Hydrogen Energy*, 2012. 37:5665–5675.
138. Cetinkaya E, Dincer I, Naterer GF. Life cycle assessment of various hydrogen production methods. *Int. J. Hydrogen Energy*, 2012. 37:2071–2080.
139. Bicer Y, Dincer I, Zamfirescu C, Vezina G, Raso F. Comparative life cycle assessment of various ammonia production methods. *J. Clean. Prod.*, 2016. 135:1379–1395.
140. Bicer Y, Dincer I. Life cycle evaluation of hydrogen and other potential fuels for aircrafts. *Int. J. Hydrogen Energy*. doi:http://dx.doi.org/10.1016/j.ijhydene.2016.12.119.
141. Bicer Y, Dincer I. Life cycle assessment of nuclear-based hydrogen and ammonia production options: A comparative evaluation. *Int. J. Hydrogen Energy*, 2017. doi:10.1016/j.ijhydene.2017.02.002.
142. Xu G, Liu R, Wang J. Electrochemical synthesis of ammonia using a cell with a Nafion membrane and SmFe0.7Cu0.3−x Ni x O3 (x = 0−0.3) cathode at atmospheric pressure and lower temperature. *Sci. China Ser. B Chem.*, 2009. 52:1171–1175.

143. Giddey S, Badwal SPS, Kulkarni A. Review of electrochemical ammonia production technologies and materials. *Int. J. Hydrogen Energy*, 2013. 38:14576–14594.
144. Tsuyoshi Murakami, Tokujiro Nishikiori, Toshiyuki Nohira and, Ito* Y. Electrolytic Synthesis of Ammonia in Molten Salts under Atmospheric Pressure. 2002. doi:10.1021/JA028891T.
145. Fanning JC. The chemical reduction of nitrate in aqueous solution. *Coord. Chem. Rev.*, 2000. 199:159–179.
146. Bockris JOM, Conway BE, White RE. *Modern aspects of electrochemistry Vol. 29*. 1995. Springer.
147. Li F-F, Licht S. Advances in Understanding the Mechanism and Improved Stability of the Synthesis of Ammonia from Air and Water in Hydroxide Suspensions of Nanoscale Fe2O3. *Inorg. Chem.*, 2014. 53:10042–10044.
148. Lan R, Irvine JTS, Tao S. Synthesis of ammonia directly from air and water at ambient temperature and pressure. *Sci. Rep.*, 2013. 3:1145.
149. Licht S, Cui B, Wang B, Li F-F, Lau J, Liu S. Ammonia synthesis by N2 and steam electrolysis in molten hydroxide suspensions of nanoscale Fe2O3. *Science (80-.).*, 2014. 345:637–640.
150. Garagounis I, Kyriakou V, Skodra A, Vasileiou E, Stoukides M. Electrochemical Synthesis of Ammonia in Solid Electrolyte Cells. *Front. Energy Res.*, 2014. 2.
151. Skodra A, Stoukides M. Electrocatalytic synthesis of ammonia from steam and nitrogen at atmospheric pressure. *Solid State Ionics*, 2009. 180:1332–1336.
152. Serizawa N, Miyashiro H, Takei K, Ikezumi T, Nishikiori T, Ito Y. Dissolution Behavior of Ammonia Electrosynthesized in Molten LiCl–KCl–CsCl System. *J. Electrochem. Soc.*, 2012. 159:E87–E91.
153. Kyriakou V, Garagounis I, Vasileiou E, Vourros A, Stoukides M. Progress in the Electrochemical Synthesis of Ammonia. *Catal. Today*. doi:http://dx.doi.org/10.1016/j.cattod.2016.06.014.
154. Shipman MA, Symes MD. Recent progress towards the electrosynthesis of ammonia from sustainable resources. *Catal. Today*. doi:http://dx.doi.org/10.1016/j.cattod.2016.05.008.
155. Pappenfus TM, Lee K, Thoma LM, Dukart CR. Wind to Ammonia: Electrochemical Processes in Room Temperature Ionic Liquids. *ECS Trans.*, 2009. 16, ECS, pp 89–93.
156. Kim K, Yoo C-Y, Kim J-N, Yoon HC, Han J-I. Electrochemical synthesis of ammonia from water and nitrogen catalyzed by nano-Fe2O3 and CoFe2O4 suspended in a molten LiCl-KCl-CsCl electrolyte. *Korean J. Chem. Eng.*, 2016. 33:1777–1780.
157. Kim K, Kim J-N, Yoon HC, Han J-I. Effect of electrode material on the electrochemical reduction of nitrogen in a molten LiCl–KCl–CsCl system. *Int. J. Hydrogen Energy*, 2015. 40:5578–5582.
158. Di J, Chen M, Wang C, Zheng J, Fan L, Zhu B. *Samarium doped ceria–(Li/Na)2CO3 composite electrolyte and its electrochemical properties in low temperature solid oxide fuel cell*. *J. Power Sources*, 2010. 195.
159. Amar IA, Lan R, Petit CTG, Arrighi V, Tao S. Electrochemical synthesis of ammonia based on a carbonate-oxide composite electrolyte. *Solid State Ionics*,

2011. 182:133–138.
160. Malavasi L, Fisher CAJ, Islam MS. Oxide-ion and proton conducting electrolyte materials for clean energy applications: structural and mechanistic features. *Chem. Soc. Rev.*, 2010. 39:4370–4387.
161. Tillement O. Solid state ionics electrochemical devices. *Solid State Ionics*, 1994. 68:9–33.
162. Norby T. Solid-state protonic conductors: principles, properties, progress and prospects. *Solid State Ionics*, 1999. 125:1–11.
163. Iwahara H, Esaka T, Uchida H, Maeda N. Proton conduction in sintered oxides and its application to steam electrolysis for hydrogen production. *Solid State Ionics*, 1981. 3:359–363.
164. Zhai Y, Ye C, Xiao J, Dai L. A microwave-induced solution-polymerization synthesis of doped LaGaO 3 powders. *J. Power Sources*, 2006. 163:316–322.
165. Nowick AS, Du Y, Liang KC. Some factors that determine proton conductivity in nonstoichiometric complex perovskites. *Solid State Ionics*, 1999. 125:303–311.
166. Skodra A, Ouzounidou M, Stoukides M. NH3 decomposition in a single-chamber proton conducting cell. *Solid State Ionics*, 2006. 177:2217–2220.
167. Kordali V, Kyriacou G, Lambrou C. Electrochemical synthesis of ammonia at atmospheric pressure and low temperature in a solid polymer electrolyte cell. *Chem. Commun.*, 2000.:1673–1674. doi:10.1039/B004885M.
168. Badwal SPS, Ciacchi FT. Oxygen-ion conducting electrolyte materials for solid oxide fuel cells. *Ionics (Kiel).*, 2000. 6:1–21.
169. Katahira K, Kohchi Y, Shimura T, Iwahara H. Protonic conduction in Zr-substituted BaCeO 3. *Solid State Ionics*, 2000. 138:91–98.
170. Solar Simulators - Class AAA Solar Simulators - CPV Solar Simulators - Photovoltaic Cell Solar Light Simulators. doi:http://www.oainet.com/.
171. Gamry Reference 3000 Potentiostat/Galvanostat/ZRA. [cited 21 February 2017]. Available from https://www.gamry.com/potentiostats/reference-3000/.
172. USB-650 Red Tide Spectrometers - Ocean Optics. [cited 21 February 2017]. Available from https://oceanoptics.com/product/usb-650-red-tide-spectrometers/.
173. Surface Temperature Sensor; Vernier Software Technology. [cited 16 January 2017]. Available from https://www.vernier.com/products/sensors/temperature-sensors/sts-bta/.
174. Pyranometer ; Products; Vernier Software Technology. [cited 16 January 2017]. Available from https://www.vernier.com/products/sensors/solar-radiation-sensors/pyr-bta/.
175. Portable Handheld Data Logger OM-DAQPRO-5300. [cited 3 March 2017]. Available from http://www.omega.ca/pptst_eng/OM-DAQPRO-5300.html.
176. Mass and Volumetric Flow Meters - FMA-1600A Series Mass Flowmeters display Flow, Pressure and Temperature. [cited 3 March 2017]. Available from http://www.omega.ca/pptst_eng/FMA1600.html.
177. FMA1700A/1800A Series eletronic gas mass flowmeters. [cited 3 March 2017]. Available from http://www.omega.com/pptst/FMA1700A_1800A.html.
178. SainSmart MQ137 Ammonia detection sensor NH3 Gas Sensor Module. [cited 3 March 2017]. Available from https://www.sainsmart.com/sainsmart-mq137-ammonia-detection-sensor-nh3-gas-sensor-module.html.

179. Protisen Hydrogen Sensor Fuel Cell Store. [cited 3 March 2017]. Available from http://www.fuelcellstore.com/protisen-hydrogen-sensor.
180. High Performance Cold Mirrors - Edmund Optics Inc. [cited 16 January 2017]. Available from http://www.edmundoptics.com/optics/optical-mirrors/hot-cold-mirrors/high-performance-cold-mirrors/3149/.
181. Nafion 115 - FuelCellsEtc. [cited 3 March 2017]. Available from http://www.fuelcellsetc.com/store/Nafion/N115.
182. McMaster-Carr Clear Acrylic Sheets and Bars. [cited 3 March 2017]. Available from https://www.mcmaster.com/#acrylic-sheets/=16lnw5f.
183. McMaster-Carr HDPE Sheets, Bars, and Strips. [cited 3 March 2017]. Available from https://www.mcmaster.com/#hdpe/=16lnwig.
184. McMaster-Carr Rubber Sheets. [cited 3 March 2017]. Available from https://www.mcmaster.com/#standard-rubber-sheets/=16lnx9w.
185. Bicer Y, Chehade G, Dincer I. Experimental investigation of various copper oxide electrodeposition conditions on photoelectrochemical hydrogen production. *Int. J. Hydrogen Energy*, 2017. 42:6490–6501.
186. Bicer Y, Dincer I. Experimental investigation of a PV-Coupled photoelectrochemical hydrogen production system. *Int. J. Hydrogen Energy*, 2017. 42:2512–2521.
187. Appl M. Ammonia, 2. Production Processes. *Ullmann's Encycl. Ind. Chem.*, 2011. Wiley-VCH Verlag GmbH & Co. KGaA, Weinheim, Germany. doi:10.1002/14356007.o02_o11.
188. Smolinka T, Ojong E, Lickert T. Fundamentals of PEM Water Electrolysis. *PEM Electrolysis Hydrog. Prod.*, 2015. CRC Press, pp 11–33. doi:10.1201/b19096-3.
189. Mench MM. *Fuel cell engines*. 2008. John Wiley & Sons.
190. Berger A. Integrated Modeling and Design of Photoelectrochemical Water-Splitting Cells. 2014.
191. Ahn J, Holze R. Bifunctional electrodes for an integrated water-electrolysis and hydrogen-oxygen fuel cell with a solid polymer electrolyte. *J. Appl. Electrochem.*, 1992. 22:1167–1174.
192. Bessarabov D, Wang H, Li H, Zhao N. *PEM Electrolysis for Hydrogen Production*. 2015. CRC Press. doi:10.1201/b19096.
193. Radecka M, Wierzbicka M, Rekas M. Photoelectrochemical cell studied by impedance spectroscopy. *Phys. B Condens. Matter*, 2004. 351:121–128.
194. Orazem ME, Tribollet B. *Electrochemical impedance spectroscopy*. 2011. 48, John Wiley & Sons.
195. Orazem ME, Tribollet B. Electrochemistry. *Electrochem. Impedance Spectrosc.*, 2008. John Wiley & Sons, Inc., pp 73–96. doi:10.1002/9780470381588.ch5.
196. Orazem ME, Tribollet B. Diffusion Impedance. *Electrochem. Impedance Spectrosc.*, 2008. John Wiley & Sons, Inc., pp 183–210. doi:10.1002/9780470381588.ch11.
197. Wagner N. Characterization of membrane electrode assemblies in polymer electrolyte fuel cells using ac impedance spectroscopy. *J. Appl. Electrochem.*, 2002. 32:859–863.
198. Chen Z, Mo S, Hu P. Recent progress in thermodynamics of radiation—exergy of radiation, effective temperature of photon and entropy constant of photon. *Sci.*

China Ser. E Technol. Sci., 2008. 51:1096–1109.
199. Dincer I, Zamfirescu C. Sustainable hydrogen production. 2016.:494.
200. American Society for Testing and Materials (ASTM) Terrestrial Reference Spectra for Photovoltaic Performance Evaluation. Solar Spectral Irradiance: Air Mass 1.5. [cited 17 January 2017]. Available from http://rredc.nrel.gov/solar/spectra/am1.5/.
201. Baumeister PW. Optical Absorption of Cuprous Oxide. *Phys. Rev.*, 1961. 121:359–362.
202. Cendula P, Tilley SD, Gimenez S, Bisquert J, Schmid M, Grätzel M, *et al*. Calculation of the Energy Band Diagram of a Photoelectrochemical Water Splitting Cell. *J. Phys. Chem. C*, 2014. 118:29599–29607.
203. Abbas T, Ahmed Bazmi A, Waheed Bhutto A, Zahedi G, Abbasi T, Abbasi SA, *et al*. No Title. In Zamfirescu, ID, ed., *Int. J. Hydrogen Energy*, 2013. 39:1–5.
204. McIntosh KR, Baker-Finch SC. OPAL 2: Rapid optical simulation of silicon solar cells. *2012 38th IEEE Photovolt. Spec. Conf.*, 2012. IEEE, pp 000265–000271. doi:10.1109/PVSC.2012.6317616.
205. Equivalent circuit calculator-PV lighthouse. [cited 16 January 2017]. Available from https://www.pvlighthouse.com.au/.
206. Bouzidi K, Chegaar M, Bouhemadou A. Solar cells parameters evaluation considering the series and shunt resistance. *Sol. Energy Mater. Sol. Cells*, 2007. 91:1647–1651.
207. Palik ED. *Handbook of optical constants of solids*. 1998. 3, Academic press.
208. Chen Z, Mo S, Hu P. Recent progress in thermodynamics of radiation—exergy of radiation, effective temperature of photon and entropy constant of photon. *Sci. China Ser. E Technol. Sci.*, 2008. 51:1096–1109.
209. Gueymard CA. Parameterized transmittance model for direct beam and circumsolar spectral irradiance. *Sol. Energy*, 2001. 71:325–346.
210. Gueymard CA, duPont WC. Spectral effects on the transmittance, solar heat gain, and performance rating of glazing systems. *Sol. Energy*, 2009. 83:940–953.
211. Shettle EP, Fenn RW. *Models for the aerosols of the lower atmosphere and the effects of humidity variations on their optical properties*. 1979. DTIC Document.
212. WMO A. Preliminary Cloudless Standard Atmosphere for Radiation Computation. *Radiat. Comm. WCP*, 1986. 112.
213. Gmehling J. *Chemical thermodynamics for process simulation*. 2012. Wiley-VCH.
214. Gannouni M, Ben Assaker I, Chtourou R. Photoelectrochemical cell based on n-CuIn5S8 film as photoanodes for photocatalytic water splitting. *Int. J. Hydrogen Energy*, 2015. 40:7252–7259.
215. Kay A, Cesar I, Grätzel M. New benchmark for water photooxidation by nanostructured α-Fe2O3 films. *J. Am. Chem. Soc.*, 2006. 128:15714–15721.
216. Gamry Reference 3000 Potentiostat/Galvanostat/ZRA. [cited 16 January 2017]. Available from https://www.gamry.com/potentiostats/reference-3000/.
217. Reference 30k Booster/Reference 3000 Potentiostat. [cited 21 February 2017]. Available from https://www.gamry.com/potentiostats/reference-30k-booster/.
218. Barry N. Taylor, Chris E. Kuyatt. Guidelines for Evaluating and Expressing the Uncertainty of NIST Measurement Results. *Natl. Inst. Stand. Technol. Gaithersburg, MD.*, 2007. [cited 7 March 2017]. Available from https://www.nist.gov/pml/nist-technical-note-1297.

219. Lazzaretto A, Tsatsaronis G. SPECO: A systematic and general methodology for calculating efficiencies and costs in thermal systems. *Energy*, 2006. 31:1257–1289.
220. Bejan A, Tsatsaronis G (George), Moran MJ. *Thermal design and optimization*. 1996. Wiley.
221. DOE Hydrogen and Fuel Cells Program: DOE H2A Production Analysis. *H2A Cent. Hydrog. Prod. Model. Version 3.1*. [cited 7 January 2017]. Available from https://www.hydrogen.energy.gov/h2a_production.html.
222. Comparison of Electricity Prices in Major North American Cities | Publications | Hydro-Québec. [cited 7 January 2017]. Available from http://www.hydroquebec.com/publications/en/corporate-documents/comparaison-electricity-prices.html.
223. Inflation Calculator | Find US Dollar's Value from 1913-2017. [cited 3 March 2017]. Available from http://www.usinflationcalculator.com/.
224. Morgan E. Techno-Economic Feasibility Study of Ammonia Plants Powered by Offshore Wind. *Dissertations*, 2013.
225. ISO 14040:2006 - Environmental management -- Life cycle assessment -- Principles and framework. [cited 7 January 2017]. Available from http://www.iso.org/iso/catalogue_detail?csnumber=37456.
226. ISO 14044:2006 - Environmental management -- Life cycle assessment -- Requirements and guidelines. [cited 7 January 2017]. Available from http://www.iso.org/iso/catalogue_detail?csnumber=38498.
227. Curran MA. Life cycle assessment: Principles and Practice. 2006.
228. Consultants P. SimaPro Life Cycle Analysis version 7.2 (software).
229. Acero AP, Rodríguez C, Ciroth A. Impact assessment methods in Life Cycle Assessment and their impact categories'. *GreenDelta, Berling, Ger.*, 2014.
230. Boyano A, Blanco-Marigorta AM, Morosuk T, Tsatsaronis G. Exergoenvironmental analysis of a steam methane reforming process for hydrogen production. *Energy*, 2011. 36:2202–2214.
231. Morgan ER, McGowan JG. Techno-economic feasibility study of ammonia plants powered by offshore wind. 2013. 3556272.
232. Taghvaei H, Jahanmiri A, Rahimpour MR, Shirazi MM, Hooshmand N. Hydrogen production through plasma cracking of hydrocarbons: Effect of carrier gas and hydrocarbon type. *Chem. Eng. J.*, 2013. 226:384–392.
233. Łamacz A, Krztoń A. Hydrogen production by catalytic decomposition of selected hydrocarbons and H2O dissociation over CeZrO2 and Ni/CeZrO2. *Int. J. Hydrogen Energy*, 2013. 38:8772–8782.
234. Taghvaei H, Shirazi MM, Hooshmand N, Rahimpour MR, Jahanmiri A. Experimental investigation of hydrogen production through heavy naphtha cracking in pulsed DBD reactor. *Appl. Energy*, 2012. 98:3–10.
235. Muradov NZ, Veziroğlu TN. From hydrocarbon to hydrogen–carbon to hydrogen economy. *Int. J. Hydrogen Energy*, 2005. 30:225–237.
236. Canada GA. *Invest In Canada, 2016-2017 Edition*. 2016. Ottowa.
237. Hydro-Québec. Annual Report 2010. 2010. [cited 8 March 2017]. Available from http://www.hydroquebec.com/publications/en/docs/annual-report/annual-report-2010.pdf.
238. REED CL, KUHRE CJ. Hydrogen Production from Partial Oxidation of Residual

Fuel Oil. *Hydrog. Prod. Mark.*, 1980. 116, AMERICAN CHEMICAL SOCIETY, pp 95–121.
239. Steinberg M, Cheng HC. Modern and prospective technologies for hydrogen production from fossil fuels. *Int. J. Hydrogen Energy*, 1989. 14:797–820.
240. Fujiwara S, Kasai S, Yamauchi H, Yamada K, Makino S, Matsunaga K, *et al.* Hydrogen production by high temperature electrolysis with nuclear reactor. *Prog. Nucl. Energy*, 2008. 50:422–426.
241. Acar C, Dincer I. Comparative assessment of hydrogen production methods from renewable and non-renewable sources. *Int. J. Hydrogen Energy*, 2014. 39:1–12.
242. Bicer Y, Dincer I, Zamfirescu C, Vezina G, Raso F. Comparative life cycle assessment of various ammonia production methods. *J. Clean. Prod.* doi:http://dx.doi.org/10.1016/j.jclepro.2016.07.023.
243. Ozbilen A, Aydin M, Dincer I, Rosen MA. Life cycle assessment of nuclear-based hydrogen production via a copper–chlorine cycle: A neural network approach. *Int. J. Hydrogen Energy*, 2013. 38:6314–6322.
244. Naterer GF, Suppiah S, Stolberg L, Lewis M, Ferrandon M, Wang Z, *et al.* Clean hydrogen production with the Cu–Cl cycle – Progress of international consortium, I: Experimental unit operations. *Int. J. Hydrogen Energy*, 2011. 36:15472–15485.
245. Jeong SS, Mittiga A, Salza E, Masci A, Passerini S. Electrodeposited ZnO/Cu2O heterojunction solar cells. *Electrochim. Acta*, 2008. 53:2226–2231.
246. Fuel Cells Etc Commercial Fuel Cell Components, Electrolyzer Design Helper. [cited 2 March 2017]. Available from http://fuelcellsetc.com/helpful-tools/electrolyzer-design-helper/.
247. Wu J, Yuan XZ, Wang H, Blanco M, Martin JJ, Zhang J. Diagnostic tools in PEM fuel cell research: Part I Electrochemical techniques. *Int. J. Hydrogen Energy*, 2008. 33:1735–1746.